

**High Speed Rotary PWM On/Off Valves for Digital
Control of Hydraulic Pumps and Motors**

**A DISSERTATION
SUBMITTED TO THE FACULTY OF THE GRADUATE SCHOOL
OF THE UNIVERSITY OF MINNESOTA
BY**

Haink Cheng Tu

**IN PARTIAL FULFILLMENT OF THE REQUIREMENTS
FOR THE DEGREE OF
DOCTOR OF PHILOSOPHY**

**Perry Y. Li, Adviser
Thomas R. Chase, Adviser**

August, 2014

© Haink Cheng Tu 2014
ALL RIGHTS RESERVED

Acknowledgements

Many thanks to the outstanding individuals who contributed to my development and growth as an engineer and human being: Professors Perry Li and Tom Chase for teaching me how to think like an engineer; My parents for only asking for my best and teaching me not to borrow tomorrow's time; My wife Nicole for teaching me how to live life adventurously and for not giving up on me when times were rough; The Center for Compact and Efficient Fluid Power (CCEFP) and National Science Foundation (NSF) for funding the research presented in this dissertation under grants ENG/CMS-0409832 and EEC-0540834 and for recruiting great minds that enriched and stimulated my graduate school experience; Mel Chapin and Peter Zimmermann of the student machine shop for teaching me how to machine and transform raw metal into useful parts; Mike Gandrud, Jake Williams, and Eric Bretey of Sauer-Danfoss for the long hours (weekends included) spent setting up, testing, troubleshooting, and rebuilding the prototype 4-way rotary valve; And lastly, The Angry Carrots for teaching me to play smart, work smarter, and never give up. From flop to top in 5 years!

Dedication

Do good.

ABSTRACT

The research described in this dissertation focuses on the development of innovative on/off valves for high performance, high efficiency control of fixed displacement hydraulic pumps and motors. On/off valves, the hydro-mechanical equivalent of transistors, enable the application of digital control techniques found in electrical systems to hydraulics. These techniques, such as pulse-width-modulation (PWM), have the potential of combining the low cost, high bandwidth characteristics of valve control with the efficiency of variable displacement machines.

Effective control of hydraulic systems using PWM requires that the on/off valve simultaneously exhibits fast switching speed, large flow area, and low actuation power. The valves developed in this dissertation exploit continuous rotary motion to achieve the desired, and traditionally competing, operating characteristics. A helical land is used to mechanically embed the desired PWM functionality into the valve spool. The rotary motion of the valve performs the switching functionality while its axial motion determines the PWM duty ratio.

Several unique rotary valve concepts are presented in this dissertation for switched-mode pump and pump/motor circuits. An analysis framework is developed that predicts valve performance and typical losses which can be used for design and optimization. Physics based dynamic models of switched-mode pump and motor circuits are also developed for simulating system pressures and flow rates and for validating the analytical models. In addition, guidelines for sizing the valve sleeve based on fatigue considerations are formulated to aid prototype design. Prototype hardware is fabricated and extensively tested to validate the analysis, performance, and predicted efficiency of the proposed valves. The research in this dissertation verifies that helical land rotary valves used in switched-mode hydraulic circuits are capable of exceeding the efficiency of comparable metering valve circuits at moderate PWM frequencies. In two comparable systems, the switched-mode circuit achieved 84% efficiency at 50% output flow compared to 50% efficiency in the bleed off circuit. Analysis also shows that substantial gains in efficiency and switching frequency can be attained with improvements in valve configuration, circuit configuration, and valve geometry. Additional suggestions for further improving efficiency in switched-mode hydraulic systems are also discussed.

Contents

Acknowledgements	i
Dedication	ii
Abstract	iii
List of Tables	viii
List of Figures	x
1 Introduction	1
1.1 Review of existing on/off valves	4
1.1.1 Linear valves	4
1.1.2 Rotary valves	9
1.1.3 Valve summary	12
1.2 Rotary valve concept and initial UMn efforts	14
1.3 Dissertation overview and structure	16
2 3-way self-spinning rotary valve for virtually variable displacement pumps	20
2.1 VVDP Concept	21
2.2 3-way Valve Embodiment for Pumps	23
2.3 Design and Performance Analysis	26
2.3.1 Valve Throttling Losses	27
2.3.2 Compressibility Losses	31

2.3.3	Leakage	32
2.3.4	Self-spinning Velocity Analysis	34
2.3.5	Output Flow Analysis	39
2.3.6	Trade Off and Design Summary	41
2.4	Dynamic System Model	43
2.5	Experimental Hardware	44
2.6	Simulation and Experimental Results	46
2.6.1	Pressure Profiles	47
2.6.2	Self-spinning Validation	49
2.6.3	Flow Modulation	51
2.6.4	Hydraulic Efficiency	52
2.6.5	Volumetric Efficiency	56
2.7	Conclusions	57
3	Extension of rotary valve to pump/motors and high pressure	59
3.1	HHPV Application	60
3.2	Proposed VVDPM and Rotary Valve Concept	63
3.3	Mechanical Design for High Pressure	66
3.3.1	Review of Stress Concentration Factors	68
3.3.2	Stress-Life Analysis	71
3.4	Updated Design Analysis	74
3.4.1	4-way Valve Throttling Losses	74
3.4.2	4-way Valve Leakage	78
3.4.3	4-way Valve Switched Volumes	79
3.4.4	4-way Valve Bearing Surface Area	79
3.4.5	4-way Self-spinning	80
3.5	Drive Cycle Optimization and Actuation Trade Study	80
3.6	Externally Actuated Valve	86
3.6.1	Drive Mechanism for Realizing External Actuation	88
3.7	VVDPM Dynamic Model and Simulation Results	93
3.7.1	VVDPM Pressure Profiles	95
3.7.2	VVDPM Efficiency Maps	96

3.7.3	Efficiency Comparison with Bent Axis Pump/motor	97
3.8	Prototype Hardware and Preliminary Testing	100
3.8.1	Full Open Pressure Drop	103
3.9	Conclusions	106
4	Ring valve concept and other ideas for improving efficiency	112
4.1	Trade Study	113
4.1.1	Valve Configuration	113
4.1.2	Four Quadrant Circuit Configuration	116
4.1.3	Valve Geometry	117
4.1.4	Trade Study Conclusions	119
4.2	Ring Valve Concept	121
4.2.1	Preliminary Sizing and Design Trade Offs	122
4.3	Simulation Comparison	126
4.3.1	Pressure Profile Comparison	128
4.3.2	Efficiency Map Comparison	129
4.4	Other Ideas	131
4.4.1	Underlap	132
4.4.2	Soft-switching	134
4.4.3	Surface Texturing	136
4.4.4	High Bulk Modulus Oil	137
4.5	Conclusions	137
5	Conclusions	140
5.1	Review	140
5.2	Contributions	142
5.3	Recommendations for Future Work	142
	References	144
	Appendix A. Baseline fixed displacement pump efficiency testing	154
	Appendix B. 4-way rotary valve prototype drawings	163

Appendix C. Pilot operated disc directional valve **175**
C.1 Directional valve machining drawings 177

List of Tables

2.1	3-way self-spinning rotary valve parameters	43
2.2	Breakdown of VVDP losses using the parameters $P_{load} = 6.9MPa$, $Q_{in} = 40lpm$, $r = .10$. Total output power is $4.6kW$	44
2.3	Ratio of shear stresses due to fluid recirculation between the spool's helical lands and turbine structures. The ratio depends on spool section type and radial clearance. Refer to analysis in Section 2.3.4.	51
3.1	Leakage paths in 4-way rotary valve based on spool position. In Position I, $P_A \approx P_C$ and $P_B \approx P_D$. In Position II, $P_A \approx P_B \approx P_{fw}$. $P_C = P$ and $P_D = P_t$ or vice versa depending how the ports are connected. Using P and P_t in place of P_A and P_B provides a method of approximating the leakage without needing to calculate P_A and P_B which are flow rate dependent based on the spool's pressure drop.	78
3.2	Speeder valve parameters optimized for a $21MPa$ working pressure differential and PWM frequency of $40Hz$. $L_s = 120mm$, $A_{out} = 100mm^2$, and $c_r = .013mm$ were driven to their respective parameter bounds in both cases. All lengths in mm and volumes in cc	87
3.3	EPA combined Urban/Highway speeder cycle efficiency.	97
3.4	HHPV cycle fuel economy over combined EPA Urban/Highway cycle. B indicates bent axis while V indicates VVDPM. In all cases, both speeder and torquer sizes are optimized.	98
3.5	Measured pressure in MPa averaged over $0.5s$ immediately following each test run.	104

4.1	Comparison of valve parameters for $40Hz$ PWM frequency and $21MPa$ working pressure differential with $N = 3$. All lengths in mm and volumes in cc	125
4.2	Comparison of rotary valve losses at $40Hz$ PWM frequency, $21MPa$ working pressure differential, and $82lpm$ flow rate ($8400rpm$). Total hydraulic power is $28kW$. Loss percentages are based on the total hydraulic power. Ring Port A and B refer to the shorter and longer flow paths respectively as labeled in Fig. 4.6.	125
4.3	Preliminary CFD generated ring valve pressure drop relations for the fluid routing concept shown in Fig. 4.6. The flow rate Q must be in units of m^3/s and A_r is the fully open area of one rhombic port as given in Table 4.1. The pressure drop across the ring is due to the inner cavity connecting flow between Port C and Ports A or B . The pressure drop across Port A is modeled as an orifice with a least-squares fit to determine the equivalent discharge coefficient of $.704$ based on CFD simulations. The pressure drops across Ports B and C are the pressure drop across A with an additional term to account for the longer connecting pipe length.	127
A.1	Data collected during baseline pump testing at Sauer-Danfoss.	155

List of Figures

1.1	Two functionally equivalent hydraulic control circuits. The bleed off circuit (left) throttles excess flow across the load pressure, resulting in high energy loss if low flow is demanded. In contrast, the pulse-width-modulated virtually variable displacement pump (right) switches rapidly between supplying flow to load or bypassing flow to tank. In both situations, throttling losses across the on/off valve are minimal.	2
1.2	Comparison of flow area and average valve transition time for selected on/off valves found in the literature. Flow area is estimated from pressure drop and flow data assuming an orifice discharge coefficient of $C_d = .6$ and a fluid density of $\rho = 876kg/m^3$. Average transition time is the average of opening and closing times. Recall that the transition times for the helical land rotary valves studied in this dissertation are proportional to $\frac{1}{f_{PWM}}$. Therefore, running the valves at a higher PWM frequency will inherently reduce their transition times. The transition times at the frequencies presented are dictated by application.	13
1.3	Helical land rotary valve concept illustrating PWM functionality. The rotational velocity of the spool (ω) determines the valve's PWM frequency. The axial position of the spool (normalized as z) determines the valve's duty ratio.	15
1.4	Generation 1 helical rotary on/off valve spool designed by David Rajala at the University of Minnesota (2004).	16
1.5	Generation 2 helical rotary on/off valve spool and sleeve designed by Adrian Durand at the University of Minnesota (2006).	17

1.6	Generation 2.5 helical rotary on/off valve spool modified to demonstrate self-spinning functionality. Self-spinning is achieved by reversing the flow path of the generation 2 valve such that the inlet port of the valve is tangential to its axis of revolution.	18
2.1	Two VVDP implementations using a 3-way on/off control valve. Q_{vol} and Q_{acc} represent the net flows into the inlet volume and accumulator.	21
2.2	Top: Inlet pressure (P_{in}) profile over one PWM cycle ($\frac{2\pi}{N}rad$ spool rotation) for the two circuits in Fig. 2.1. Bottom: Corresponding profiles of the valve inlet orifice open areas ($A(\theta)$) to load or to tank.	22
2.3	3-way rotary valve spool, sleeve, and pump housing assembly.	24
2.4	Top: 3-way helical rotary valve concept for VVDPs. Internal passages connect the center section (responsible for PWM) to one of the two adjacent outlet turbines. The dark gray portions of the spool are hydraulically connected and permit flow from the inlet to the load. Similarly, the light gray sections connect the inlet to tank. Bottom: Open area profiles illustrating when Port A is connected to Port B or C	25
2.5	2D representation of the rotary valve's geometry including variable definitions used in Section 2.3.	26
2.6	Comparison of transition losses between the relief and check circuits. Results for the relief circuit are only valid when the load pressure is below the relief pressure.	31
2.7	Top: Yu pressure dependent bulk modulus for various fractions (r) of air entrainment and no dissolved air. Bottom: Unit compression energy required to compress fluid from P_{tank} to P_{load}	33
2.8	Inlet and outlet turbines with their control volumes.	34
2.9	Pocketed volume and corresponding CFD model.	37
2.10	Normalized pocket shear ($K = -0.653$)	39
2.11	Power required to overcome viscous friction. A curve fit of the data yields $f(x) = .003x^2 - 4.8 \times 10^{-16}x + 1.7 \times 10^{-14}$ where $f(x)$ is friction power in W and x is the PWM frequency in Hz . Thus, friction power is essentially proportional to PWM frequency squared even when accounting for the additional effects of fluid recirculation.	40

2.12	Prototype rotary valve hardware	45
2.13	Prototype VVDP test stand	46
2.14	15Hz pressure profiles: 50% travel	47
2.15	15Hz pressure profiles: $P_{load} = 2.8MPa$	48
2.16	75Hz pressure profiles: 50% travel	49
2.17	PWM frequency vs. Q_{in} (loglog)	50
2.18	Estimated friction (actuation) power used to match self-spinning velocity predictions with test stand data in Fig. 2.17	52
2.19	Output flow vs. axial position (15Hz)	53
2.20	Efficiency at 15Hz: Relief	54
2.21	Efficiency at 15Hz: Check	55
2.22	Efficiency at 75Hz: Relief	56
2.23	Leakage across helical land	57
3.1	Polaris Ranger hydraulic hybrid passenger vehicle test bed at the University of Minnesota based on an input coupled power-split drive train.	60
3.2	Schematic of Polaris Ranger input coupled power-split hydraulic hybrid passenger vehicle. Two variable displacement pump/motors enable full engine management: the torquer, connected to the engine via a fixed ratio, controls the engine torque. The speeder, connected to the engine and wheel via a planetary gearset, decouples the engine speed from the wheel speed.	61
3.3	Switched-mode pumping and motoring configurations based on 2-way, 3-way, and 4-way on/off valves. Other configurations are possible. Note: check valves for preventing cavitation and reducing transition pressure spikes are not included in these circuit diagrams.	63

3.4	Proposed VVDPM utilizing a 4-way tandem on/off control valve. One 4-way directional valve is needed to enable self-spinning by rectifying the flow direction when switching between pumping and motoring. The other is needed for four quadrant operation by controlling the shaft direction of the pump/motor. Check valves a and b prevent cavitation. Check valves A and B reduce pressure spikes when the on/off valve or directional valves are switching. V_A , corresponding to the bold black fluid volume between Port A of the pump/motor and on/off valve, represents the switched volume. P_A is the corresponding pressure in V_A . The volume associated with Port B of the pump/motor is similarly represented by the bold gray lines in the schematic.	64
3.5	Top: 4-way tandem helical rotary valve concept. Bottom: Open area profiles illustrating when Port D is connected to Port B or blocked and when Port A is connected to Port C or B.	65
3.6	Cyclic pressure loading on the valve sleeve occurs due to the switching nature of PWM. The pressure in the inlet rail is continuously switching between P_A and P_B as the valve spool rotates. One area of concern is the inlet nozzle, essentially a cross-hole, which introduces a stress concentration in the sleeve that is then repeatedly pressurized and depressurized. Another area of concern, labeled C , is effectively a thick-walled pressure vessel that switches between external pressure loading (A = high pressure) and internal pressure loading (B = high pressure).	67
3.7	Schematic of thick-walled pressure vessel representation of the valve sleeve showing variable definitions used in the Stress-Life analysis.	68
3.8	Comparison of hoop (tangential) stress concentration factors between several models for a closed-ended thick-walled cylinder with circular cross-hole. (A) denotes an analytical model whereas (C) denotes a computational model. Results from Gerdeen are estimated based on a figure within the paper.	69

3.9	Comparison of Von Mises equivalent stress concentration factors between several models for a closed-ended thick-walled cylinder with circular cross-hole. The values presented here are based off of the hoop stress concentration factors presented in Fig. 3.8. (A) denotes an analytical model whereas (C) denotes a computational model.	70
3.10	Comparison of the sleeve’s predicted fatigue safety factor assuming fluctuating external to internal pressure loading at $21MPa$ for two types of steel. The analysis assumes an uncorrected endurance limit that is half of the ultimate tensile strength of the material as well as a machined surface finish and 99.99% reliability.	75
3.11	Diagram of 4-way valve geometry illustrating variable names used in Section 3.4.	76
3.12	Speeder and torquer operating points for an input coupled power-split HHPV with $21MPa$ working pressure differential.	81
3.13	Comparison of rotary valve optimized drive cycle efficiencies between self-spinning and external actuation for different frequency bounds (lower bound on mean frequency for self-spinning and constant speed for external actuation). Friction/actuation losses are included for external actuation. P/M losses are not included in either case. The efficiencies correspond to the drive cycle operating points presented in Fig. 3.12. . .	83
3.14	Comparison of optimized rotary valve losses between self-spinning (Top) and external actuation (Bottom) for different frequency bounds (lower bound on mean frequency for self-spinning and constant speed for external actuation). Friction/actuation losses are included for external actuation. P/M losses are not included in either case.	84
3.15	Comparison between optimized self-spinning and externally actuated spool geometries. Diameter (Top), inlet and outlet flow areas (Middle), and overall spool length (Bottom) are presented.	85
3.16	Top: VVDPM overall efficiency, defined as $\eta_h = \frac{\sum_{cycle} \tau_{pm} \omega_{pm} dt}{\sum_{cycle} (\tau_{pm} \omega_{pm} + \pi_{tot}) dt}$, optimized and plotted with respect to PWM frequency for $21MPa$ vehicle working pressure differential. Losses attributed to the fixed displacement P/M are included. Bottom: Breakdown of losses.	86

3.17	Pressure drops across the valve orifice, spool, and toroidal pressure rail based on the 30mm 4-way valve geometry presented in Table 3.2. Note that the traces are additive to elucidate the combined drop as well as the individual contributions.	88
3.18	Schematic of proposed 2 DOF rotary valve driving mechanism for enabling external actuation. The rotary motion is actuated using an electric motor that is coupled to the spool via a splined shaft and double u-joint. The axial motion is actuated hydraulically by leveraging the area difference between the spool and translating piston using a control valve.	89
3.19	Assembled and exploded views of the drive mechanism illustrating its various components. The mechanism shown in this figure uses a magnetic linear encoder to sense the spool’s axial position. A boss protruding from the side of the translating piston enables the attachment of a magnetic code strip that is read by the sensor mounted on the sleeve extension.	90
3.20	Short-time Fourier transform of the VVDP test stand’s inlet pressure (P_{in}) showing its frequency content compared to the commanded PWM frequency trajectory. The PWM frequency ramp trajectory in this figure was commanded concurrently with the step duty ratio trajectory shown in Fig. 3.21. This shows that PWM frequency and duty ratio are independently controllable.	91
3.21	VVDP test stand load pressure (top) and flow rate (middle) corresponding to the commanded step change in duty ratio (bottom). The duty ratio trajectory in this figure was commanded concurrently with the ramp PWM frequency trajectory shown in Fig. 3.20. This shows that PWM frequency and duty ratio are independently controllable.	92
3.22	Flow diagram describing the VVDPM model including the fixed displacement pump/motor and on/off valve. Arrowheads indicate positive flow directions. Solid dots indicate flow junctions or pressure connections. Inset illustrates leakage paths that affect the pressure dynamics in volumes A and B	94

3.23	Speeder VVDPM pressure profiles for motoring and pumping (one cycle). VVDPM is operating at $4000rpm$ and 50% axial travel.	95
3.24	Speeder VVDPM efficiency maps for motoring.	97
3.25	Speeder VVDPM efficiency maps for pumping.	98
3.26	Speeder VVDPM overall efficiency maps overlaid with drive cycle oper- ating points from Fig. 3.12.	99
3.27	Assembled and exploded renders of the 4-way prototype rotary valve. . .	100
3.28	From left to right: Prototype 4-way rotary valve sleeve housing, sleeve, and spool.	101
3.29	Left: Custom 4-way P/M housing compared to stock housing. Center: Fixed displacement bent axis P/M disassembled to replace housing and insure correct timing. Right: Fully re-assembled P/M with custom hous- ing installed.	102
3.30	Initial benchtop setup for running in the 4-way rotary valve. Port plates enable running the valve as a standalone unit for troubleshooting pur- poses. The fixed displacement P/M is connected to the valve via hoses.	103
3.31	Left: Casting defects led to internal voids in the spool which resulted in cross port leakage. Right: Voids were repaired using 3M acrylic adhesive.	104
3.32	VVDPM pump test circuit used in test cell at Sauer-Danfoss in Ames, IA. The 4-way check allows testing both shaft directions of the pump without the need to reconfigure the circuit.	105
3.33	Left: Baseline testing of the modified P/M as a standalone unit in test cell at Sauer-Danfoss in Ames, IA. Right: VVDPM assembled for testing with the 4-way rotary valve mounted on the P/M.	106
3.34	Scanning electron microscope analysis of filtered solvent used to clean the prototype valve revealed numerous contaminants.	107
3.35	Flow direction and position convention used to describe 4-way VVDPM experimental data.	108

3.36	4-way valve Position I pressures. When the P/M is spinning CCW, Port <i>A</i> of the valve coincides with the the inlet side of the P/M and Port <i>B</i> the outlet side. The 4-way check directs the flow such that Port <i>C</i> is connected to low pressure and Port <i>D</i> is connected to high pressure. When the P/M is spinning CW, Port <i>A</i> coincides with the outlet side of the P/M and Port <i>B</i> the inlet side. Port <i>C</i> is connected to high pressure and Port <i>D</i> is connected to low pressure. The cavitation preventing check valves are active on the inlet side of the P/M.	109
3.37	4-way valve Position II pressures. Ports <i>C</i> and <i>D</i> of the valve are blocked in this position. When the P/M is spinning CCW, Port <i>A</i> of the valve coincides with the inlet side of the P/M and Port <i>B</i> the outlet side. Flow is sent through the valve from Port <i>B</i> back to Port <i>A</i>	110
3.38	Predicted pressure drop across the valve orifice, spool, and toroidal pressure rail compared to measured data from the prototype valve. While the measured data is inaccurate due to inappropriately sized sensors, the pressure drops are qualitatively within the range of the analysis.	111
4.1	Comparison of 3-way and 4-way pumping and motoring circuits showing where check valves can be effectively used to reduce transition losses. Note that check valves are ineffective for reducing losses when motoring in the 4-way configuration.	114
4.2	Comparison of 3-way and 4-way pumping and motoring transition losses using the 30mm diameter 4-way valve parameters presented in Table 3.2.	115
4.3	Conventional 3-way on/off valve based four quadrant VVDPM. Note that the 4-way directional valve needed for four quadrant operation contributes to the switched volume of the device. Check valves for preventing cavitation etc. are omitted for simplicity.	116
4.4	Comparison of internal switched volume between ring valve concept and 4-way rotary spool valve for varying valve diameters using the 30mm diameter spool parameters listed in Table 3.2 for $N = 3$. The 4-way valve is assumed to have a wall thickness ratio of $K = 3$. V_{pm} , the volume between the P/M and the valve, is not included in the comparison.	117

4.5	Critical end land width \bar{L}_1 with respect to spool diameter (D) for fixed rhombus width ($R_w = 7.85mm$) and height ($R_h = 8.94mm$) using the 30mm diameter spool parameters in Table 3.2. End land widths greater than \bar{L}_1 will result in the spool valve having less leakage than the ring valve.	120
4.6	The 3-way ring valve consists of a stationary cylindrical boss with internal fluid routing and three sets of rhombic ports on its outer surface corresponding to Ports A , B , and C . A ring with two helical lands on its inner diameter rotates and translates on the boss's surface. Port C , located at the center of the boss, is connected to high (accumulator) pressure at all times. Ports A and B , on either side of Port C , are nominally connected to tank via an open bath of fluid that surrounds the ring. When the ring shifts left or right axially, Port A or B will be pulse-width-modulated between tank and high pressure via the internal cavity formed by the two helical lands. Switching of Port A is shown.	122
4.7	Port switching functionality embedded into the axial travel of the ring valve. Note that Port C is connected to high (accumulator) pressure at all times. When the ring is centered in its axial travel (top), Port C is always blocked. Ports A and B are connected to each other and to tank by the volume around the rotating ring. Once the ring shifts to the left (middle), the helical land on the left begins to PWM Port A between Port C at high pressure and tank. When the ring shifts past center to the right (bottom), it begins to PWM Port B	123
4.8	Diagram illustrating concept ring valve geometry used in the trade study in Section 4.1.	124

4.9	Flow diagram describing the ring VVDPM model including the fixed displacement pump/motor and on/off valve. Arrowheads indicate positive flow directions. Solid dots indicate flow junctions or pressure connections. To represent the port switching functionality of the valve, only one switch is active at a time with the other connected to tank when inactive. PWM of Port <i>A</i> is shown including check valves for preventing cavitation and reducing transition pressure spikes. The corresponding check valves for Port <i>B</i> are omitted for clarity.	126
4.10	Comparison of VVDPM pressure profiles for motoring and pumping (one cycle) between the 4-way tandem valve and the ring valve. The VVDPM is operating at 4000rpm and 50% axial travel in both cases.	128
4.11	Comparison of VVDPM valve efficiency maps for motoring between the 4-way valve and ring valve at 40Hz PWM frequency for a system working pressure differential of 21MPa. Losses from the fixed displacement P/M are not included.	129
4.12	Comparison of VVDPM valve efficiency maps for pumping between the 4-way valve and ring valve at 40Hz PWM frequency for a system working pressure differential of 21MPa. Losses from the fixed displacement P/M are not included.	130
4.13	Comparison of VVDPM valve efficiency for motoring and pumping between the 4-way valve and ring valve at selected P/M speeds when operating at 40Hz PWM frequency for a system working pressure differential of 21MPa. Losses from the fixed displacement P/M are not included. . .	131
4.14	Comparison of 4-way tandem valve VVDPM pressure profiles for motoring and pumping (one cycle) with different valve lapping configurations. The VVDPM is operating at 4000rpm and 50% axial travel in both cases.	132
4.15	Comparison of VVDPM four quadrant overall efficiency maps (including P/M losses) for the 4-way valve with different lapping conditions at 40Hz PWM frequency for a system working pressure differential of 21MPa. .	133

4.16	Comparison of VVDPM overall efficiency for motoring and pumping between a critically lapped 4-way valve and one with 5% underlap at selected P/M speeds when operating at 40Hz PWM frequency for a system working pressure differential of 21MPa. Fixed displacement P/M losses are included.	134
4.17	Soft-switching concept for 3-way motoring circuit. The soft-switch piston supplies flow rapidly during the two high pressure transitions (open/close Position I) to minimize throttling. The cavitation preventing check valve supplies flow to bypass the on/off valve during the two tank transitions (open/close Position II).	135
A.1	Sample of raw data collected. This data set corresponds to the first counter-clockwise experiment.	156
A.2	Volumetric efficiency, counter-clockwise shaft rotation, first data set. . .	156
A.3	Mechanical efficiency, counter-clockwise shaft rotation, first data set. . .	157
A.4	Overall efficiency, counter-clockwise shaft rotation, first data set.	157
A.5	Volumetric efficiency, counter-clockwise shaft rotation, second data set. .	158
A.6	Mechanical efficiency, counter-clockwise shaft rotation, second data set.	158
A.7	Overall efficiency, counter-clockwise shaft rotation, second data set. . . .	159
A.8	Volumetric efficiency, clockwise shaft rotation, first data set.	159
A.9	Mechanical efficiency, clockwise shaft rotation, first data set.	160
A.10	Overall efficiency, clockwise shaft rotation, first data set.	160
A.11	Volumetric efficiency, clockwise shaft rotation, second data set.	161
A.12	Mechanical efficiency, clockwise shaft rotation, second data set.	161
A.13	Overall efficiency, clockwise shaft rotation, second data set.	162
B.1	4-way rotary valve spool	164
B.2	4-way rotary valve sleeve	165
B.3	Sleeve housing	166
B.4	Manifold	167
B.5	Pump port plate adapter for stand-alone testing	168
B.6	Valve port plate adapter for stand-alone testing (Ports A and B)	169
B.7	Valve port plate adapter for stand-alone testing (Ports C and D)	170
B.8	Valve drive mechanism shaft	171

B.9	Valve drive mechanism piston	172
B.10	Valve drive mechanism housing	173
B.11	Valve drive mechanism guide	174
C.1	Disc valve sealing and actuation concepts.	176
C.2	Switching concept for the disc directional control valve.	177
C.3	Preliminary prototype disc valve seal friction. Disc moment arm is $83.3mm$.178	
C.4	Disc valve housing base	179
C.5	Disc valve housing cover	180
C.6	Valve disc with initial o-ring seal geometry	181
C.7	Modified valve disc with Teflon seal geometry	182

Chapter 1

Introduction

Valves are the primary control devices used in hydraulic systems. A typical hydraulic valve consists of one or more orifices that allow the passage of flow. Depending on the type of valve, flow restriction and/or direction can be manipulated, thereby enabling the control of force, speed, and direction of actuators in a hydraulic system. A typical proportional valve controlled system driven by a fixed displacement pump, such as the bleed off circuit shown in Fig. 1.1(a), is compact, inexpensive, and provides good control bandwidth. However, due to the resistive nature of valve control, these systems suffer from poor efficiency since some or all of the flow produced by the pump is throttled by the control valve.

A more efficient approach is displacement control where the pump displacement is controlled directly. Control of the pump displacement, or fluid volume displaced per revolution of the pump shaft, allows variation of the pump's output flow rate regardless of input shaft speed. Using this approach, the pump can be controlled to produce only the flow demanded by the system, thus eliminating throttling losses associated with excess flow. Several methods have been developed to vary pump displacement. Mechanical variation methods include varying the eccentricity of the pump rotor or cylinder block with respect to a cam driving the pumping elements (vane and radial piston pumps), changing the angle between pump drive shaft and cylinder block (bent axis pumps), or altering the angle of a swash plate used to drive the pumping elements (axial piston pumps) [1]. The disadvantage of variable displacement pumps (VDPs) is that conventional electronic displacement control (EDC) piston pumps typically require 3-4 times

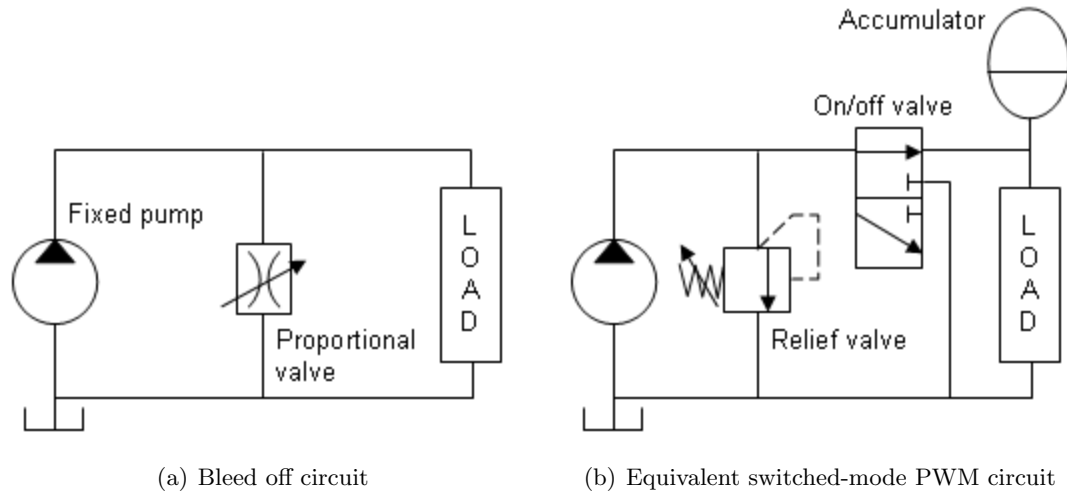


Figure 1.1: Two functionally equivalent hydraulic control circuits. The bleed off circuit (left) throttles excess flow across the load pressure, resulting in high energy loss if low flow is demanded. In contrast, the pulse-width-modulated virtually variable displacement pump (right) switches rapidly between supplying flow to load or bypassing flow to tank. In both situations, throttling losses across the on/off valve are minimal.

the volume and weight of a fixed displacement gear pump of equal displacement [2]. The power required to actuate the displacement varying mechanism at high bandwidths can be substantial as well. This is because the cam or swash plate driving the pumping elements typically has considerable mass since it must support forces generated by the working pressure of the fluid. The added complexity of the EDC unit also increases the cost of VDPs over their fixed displacement counterparts.

Digital displacement piston pumps [3] eliminate the mechanical effort of varying pump displacement by replacing the pump valve plate with one or more active valves for each piston. By controlling the opening of the valves for each piston independently, selected pistons can be deactivated entirely or at partial stroke to vary the overall displacement of the pump. Since small high speed valves are used to vary the pump displacement, high control bandwidth is attainable. The disadvantage of this approach is that one or more active valves are required for each piston, thus increasing the size, complexity, and cost of the pump. Suitable high speed valves are also a barrier and

timing becomes an issue as well since the valves must switch quickly, precisely, and repeatably.

Another form of displacement control, which will be investigated in this dissertation, is to pulse-width-modulate (PWM) the entire output flow of the pump using a single high speed on/off valve. This technique is analogous to switched-mode power supplies found in power electronics [2, 4, 5]. The switched-mode pump/valve system, shown in Fig. 1.1(b), is referred to as a virtually variable displacement pump (VVDP) [2, 6, 7, 8] since the mean output flow of the system is varied instead of the pump displacement itself. With this approach, only a single on/off valve is needed to control the effective displacement of a fixed displacement pump including traditionally fixed architectures such as check ball and gear pumps. The fundamental principle behind this concept is to use the on/off valve to rapidly switch the pump between delivering full power to the system (on) or letting the pump idle (off) instead of restricting the flow using an orifice. In both circumstances, there is minimal throttling loss across the control valve since the valve is either fully open (low pressure drop) or fully closed (no flow). The average system output power is controlled by varying the fraction of each switching cycle that the system is in the on state, known as the PWM duty ratio. Because valve losses are additive to pump losses in a VVDP, the overall efficiency of a VVDP may not meet or exceed the efficiencies of mechanical and digital variable displacement pumps. However, these devices have the potential of offering similar efficiency while maintaining the compact, simple, robust, and cost effective attributes of valve control. In addition, pump architectures that are inherently efficient, such as check ball and bent axis pumps, can be used to compensate for the additional losses in VVDPs.

A current barrier to switched-mode PWM hydraulic systems is the lack of suitable on/off valves, the hydro-mechanical analogue of transistors in electrical systems. For PWM control of hydraulic systems to be effective, the on/off control valve must meet the following three requirements simultaneously: 1) high switching speed, 2) large flow area, and 3) low actuation power. Fast valves are required for high control bandwidth since bandwidth is proportional to PWM frequency in switched-mode systems. As a rule of thumb, the PWM frequency should be 4-10 times faster than the desired control bandwidth [9]. Fast valves are also desirable since pressure ripple and system noise/vibration/harshness (NVH) are reduced as the PWM frequency increases. Large

flow area is needed to transmit high levels of power and flow with minimal throttling losses. However, the requirements of high speed and large flow area typically conflict with the third requirement of low actuation power. The goal of the research presented in this dissertation is to develop a new class of high speed on/off valves that can better achieve the three requirements needed to enable effective PWM control of hydraulic pumps and motors.

1.1 Review of existing on/off valves

A survey of the literature regarding high speed valves reveals that designs generally fall into one of two categories: valves that switch position based on linear motion, discussed in Section 1.1.1, and valves that utilize rotary motion, discussed in Section 1.1.2.

1.1.1 Linear valves

Conventional high speed on/off valves, typically spool or poppet types, rely on linear motion that must be reversed when the valve switches position. High switching speeds have been achieved using piezoelectric actuators. Yokota and Akutu at the Tokyo Institute of Technology proposed a poppet valve driven directly by multi-layered piezoelectric actuators [10]. A pair of coaxially opposed poppets are connected in series to pressure balance the valve. The valve, sized for 7.2 lpm flow at 10 MPa , was able to achieve a transition time of 0.1 ms . Another piezoelectric poppet valve was developed at Gifu University by Yamada et al. [11]. This valve used a hydraulic amplifier to magnify the displacement of the piezoelectric actuator. A 0.7 ms on-to-off time and 0.4 ms off-to-on time were demonstrated. The valve was approximately sized for 3 lpm at 10 MPa .

Solenoid actuators have also been used. Topcu et al. at the University of Uludag proposed a disc type pneumatic valve actuated using an electromagnet [12]. The valve is nominally closed by a return spring and opens when the electromagnet is activated. Flow forces are used to aid the magnet in keeping the valve open. The valve featured a flow area of 12.5 mm^2 and exhibited an opening time of 3 ms and closing time of 6 ms . Mahrenholz and Lumkes from Purdue University developed a solenoid actuated poppet valve based on a multi-domain coupled model [13]. The lumped parameter model

included coupling between the electromagnetic, fluidic, and mechanical domains. During dry testing, the prototype valve achieved a transition time of $1.6ms$ for a stroke of $0.3mm$. This corresponded to a flow area of $17mm^2$. At Johannes Kepler University, Plöckinger et al. [14] proposed a low cost solenoid valve with custom integrated electronics. The prototype, designed for a nominal flow rate of $10lpm$ at a pressure drop of $.5MPa$, achieved a $1.5-2ms$ transition time. However, the valve required a high starting current of up to $50A$. Fast switching magnetically actuated ball valves have also been proposed. Mansfeld proposed a valve capable of $1ms$ switching times that utilized a tilting armature [15]. The armature would act on push rods that would open and close the ball elements when energized.

Numerous concepts have been proposed to improve the responsiveness of linear valves. Kajima and Kawamura of Kawasaki Heavy Industries proposed an experimentally verified mathematical model to explore the effects of different design parameters on solenoid performance [16]. The authors explored the effects of weight, flow force and plunger area, applied voltage, stroke and magnetic path length, and number of coil turns. They found that high applied voltage (around $300V$), low stroke, low conductivity magnetic materials, and short magnetic path length are beneficial for improving solenoid performance. Similarly, researchers at the Beijing Institute of Technology proposed the use of computational models to optimally select magnetic materials and design valve geometry to maximize the magnetic force of solenoid actuators [17]. Pellikka et al. [18] of the Tampere University of Technology proposed the use of a genetic optimization algorithm to design an optimal solenoid actuator based on the metrics of fast response and low energy consumption. Using a finite element electromagnet model and varying the dimensions of the plunger, coil, and their relative positions, the optimal solenoid actuated a commercial valve body sized for $100lpm$ at $1MPa$ pressure differential in $3ms$ while consuming $1.1J/switch$ at $24V$, a significant improvement in comparison to the commercial actuator's response time of $17ms$ for $1J/switch$. Other researchers, such as Lee at Pukyong National University, have proposed the use of alternate driving circuits for solenoid valves to reduce time delays in the driving circuitry [19].

Another approach, investigated at the University of Minnesota, is the exploitation of transient and steady flow forces to improve the agility of spool valves. Krishnaswamy

and Li [20] proposed an open loop unstable hydraulic spool valve. By geometrically designing a 4-way valve's meter in port spacing to be longer than the meter out spacing, net unstable transient flow forces are produced which can be used to overcome steady flow forces. By reducing the effect of steady flow forces, the net force required by the actuator to stroke the spool is decreased. Simulation results predicted a 24% improvement in step response time for the unstable valve in comparison to a stable valve when using the same actuator. The benefit of instability was found to have greater effect in situations where the actuator force is more limited.

Yuan and Li proposed also manipulating steady flow forces via viscosity effects and non-metering flux to improve spool agility [21]. Fluid viscosity creates a dependence of the steady flow forces on the damping length, i.e. port spacing, of the valve. Also, the non-metering flux can be influenced by changing the port angle of the non-metering orifices. Experimental results showed that the transition time of a prototype valve could be reduced by 40% simply by tuning the port spacing and port angles of the valve. Using concepts from robust control theory, Yuan and Li [22] proposed a design algorithm for optimally choosing valve parameters to minimize the steady flow force in the presence of uncertainty. A prototype valve was fabricated that demonstrated improved step response using a smaller size three solenoid compared to a similar commercial valve driven by a larger size five solenoid.

Another concept, proposed by Garstenauer and Scheidl [23] at Johannes Kepler University, is the use of a buckling beam as a displacement magnifier for driving spool valves using piezoelectric actuators. The valve spool, which is attached to the mid-point of the beam, switches position as the beam moves between its two buckled positions. Two actuators, one on either end of the beam, hold the beam in its buckled state. Switching of the valve is initiated by setting the actuator forces to zero. Potential energy, stored in the beam when it is buckled, causes the beam to straighten. Once the beam goes over center, the actuators are activated to keep the beam buckled. The initial prototype achieved switching times of $5ms$. Researchers improved the switching time to $2.5ms$ by making the spool hollow to reduce mass and using hydraulic pistons as actuators. Simulation results show that $1ms$ switching time is possible using piezoelectric actuators although this was not experimentally demonstrated in the paper.

Manhartsgruber [24], also at Johannes Kepler University, proposed a linear PWM

valve based on a spool oscillating at its resonant frequency. Taking advantage of the spool's resonant frequency enables higher switching speeds with lower actuation power. The valve consists of a symmetric critically lapped 3-way spool with a center application port flanked by pressure and tank ports. When the spool's sinusoidal zero point is centered about the application port, flow will be ported from pressure to application for positive spool displacements and from tank to application for negative spool displacements (i.e. 50% duty ratio). By shifting the zero point of the spool's sinusoidal motion, the fraction of each oscillation that the spool is connected to the pressure port can be varied. This enables control of the valve's PWM duty ratio. A prototype valve sized for 400Hz PWM frequency and a flow rating of 100lpm with a pressure drop of 0.5MPa at a designed spool stroke amplitude of 1.15mm only achieved an amplitude of 0.5mm in practice. The authors attribute the lower than expected amplitude (and flow area) to excessive eddy-current damping. A simulation study predicted a valve hydraulic efficiency (not including driving power) of 66% for 1mm spool amplitude and 76% efficiency for 4mm spool amplitude.

The hammer valve concept, proposed by Uusitalo et al. [25, 26] at Tampere University of Technology, is another approach that improves the response time of linear valves by using the impulse generated during a collision to actuate the valve. A small accelerating part within the valve is first accelerated by an electromagnet. The kinetic energy from the accelerating part is then transferred to a larger valve poppet via an impulse as it collides. The poppet is pressure balanced once it becomes unseated, thus reducing the forces required to open the poppet. Researchers quote an experimentally measured response time of 2ms with a pressure drop of 1MPa for 3.3lpm flow and 21MPa for 17lpm . Actuation power is published to be less than 20W .

The Sturman digital valve of Sturman Industries [27] utilizes balanced flow paths to reduce net flow forces on the valve spool. By reducing valve flow forces, residual magnetism can be exploited to decrease actuation power requirements by eliminating holding current when the valve is fully open or closed. Another benefit of eliminating steady-state actuation requirements is that coil forces are no longer constrained by thermally limited current densities, thus enabling high switching speeds. Three valve designs are presented that illustrate the performance capabilities of the design: 1) a valve with flow area of $.75\text{mm}^2$ is capable of $.19\text{ms}$ transition time while requiring

.011J/switch, 2) a valve with flow area of 10mm^2 is capable of $.45\text{ms}$ transition time while requiring $.3\text{J/switch}$, and 3) a valve with flow area of 23mm^2 is capable of 1ms transition time while requiring $.7\text{J/switch}$.

Pilot operation is a technique to overcome the force limitations of electro-mechanical actuators. By using a small pilot stage valve to hydraulically actuate a larger main stage valve, both fast transition time and large flow rate can be realized. Typically, the pilot pressure used to actuate the main stage is the working or load pressure of the system minus the pressure drop across the pilot valve. A pilot operated poppet valve, proposed by Ma et al. at the University of Wisconsin-Madison, used a small, high speed diesel injector valve as the pilot stage [28]. The main stage, with a 322.6mm^2 flow area, features pressure balanced poppets that are designed to fit within the housing of a conventional cartridge valve. An opening time of 3.8ms is reported for a working pressure of 21MPa .

Researchers at Johannes Kepler University have proposed several novel main stage positive sealing valve designs that rely on a parallel array of metering elements. One design, proposed by Winkler and Scheidl [29], uses the Hörbiger plate principle where multiple metering edges are formed by two opposing valve plates each with several offset annular rings. The hydraulically piloted valve experimentally achieved a flow rate of 90rpm at 0.5MPa pressure differential. An opening time of 4ms - 6ms was achieved at low pressures with a pilot opening time of 1.6ms while the time decreased to 1.1ms as the pressure, including pilot pressure, was increased to 20MPa . Another Hörbiger plate valve design proposed by Branson et al. [30] at the University of Bath uses a piezoelectric stack to directly actuate the valve plate. The prototype achieved an opening or closing time of less than 1.5ms for a designed flow rate of 65rpm at a pressure drop of 2MPa .

Due to the complex structure of the Hörbiger plate and its high corresponding manufacturing costs, Winkler et al. proposed a unique alternative multi poppet pilot valve to reduce costs. The main stage of the valve consists of 14 parallel small diameter (3mm), low stroke (0.675mm), poppets to achieve a large flow area [31, 32]. The authors propose the use of inexpensive needle bearing rollers as the poppet elements. The poppets are evenly spaced in a circular arrangement around the circumference of the pilot stage solenoid valve. Experimentally, the main stage valve achieved 85rpm flow rate for a pressure drop of 0.5MPa . The main stage was measured to open in

0.44ms for a valve and pilot pressure differential ranging from 2.5MPa to 4MPa while the pilot stage opened in roughly 1ms. Thus, the total transition time of the valve is approximately 1.5ms for opening. In contrast, the closing transition time was reported around 14ms.

A common trend among the linear valves surveyed is the requirement of short stroke and small mass to achieve fast switching times. These requirements typically result in small flow areas which limit flow rate and yield large pressure drop. Linear valves reflect the conventional trade off between speed, flow area, and actuation power that is a consequence of the inertial forces that must be overcome to switch the valve's position. Power due to inertial effects alone is proportional to the switching frequency cubed.

1.1.2 Rotary valves

Several high speed valves found in the literature have been proposed based on rotary motion. Cui et al. [33] from the University of Saskatchewan developed a bidirectional integrated two stage rotary spool valve. As the spool is rotated a set angle, machined ports on the spool align with ports on the sleeve, thus porting either supply pressure or tank pressure to one end of the spool. Pressure at the spool end creates an axial pressure imbalance that causes the spool to slide. A second stage poppet is machined on the other end of the spool that opens or closes as the spool slides. This valve achieved transition times of 2.5ms with a pressure drop of 9MPa for 18lpm of flow.

Continuous rotary motion is exploited by other valves to reduce the actuation power requirement by eliminating oscillating motion. Since the switching elements no longer undergo acceleration or deceleration, actuation power is reduced to a square dependence on frequency, required to overcome viscous friction. These valves are inherently well-matched to the continuous switching nature of PWM. The rotational velocity of the switching element typically determines the PWM switching frequency. Modulation of the duty ratio is accomplished using one of two methods.

The first method of duty ratio variation is based on the principle of altering the phase angle between different valve components. Brown et al. [34] at Lehigh University proposed a design capable of 500Hz PWM frequency. The concept consisted of a concentric control shaft, hollow rotor, and stator. The angular velocity of the rotor sets the PWM frequency while the angle between the control shaft and stator determines

the duty ratio. Leakage across the inner and outer sliding interfaces of the rotor was considerable and measured to be 2.1 lpm in the prototype valve. The authors attribute the high leakage to larger than desired clearances.

A similar valve, used in a digital flow divider application, was proposed by Lu et al. [35] from the University of Saskatchewan. The valve design consists of an inner rotor that is housed within two layers of concentric stators. The intermediate stator contains two or more plates that can rotate. The number of plates corresponds to the number of circuits the flow is to be divided between. The angle of the plates determines the fraction of each rotation that flow is divided between the various circuits.

Royston and Singh [36] at The Ohio State University developed a pneumatic rotary PWM valve capable of 80 Hz . The valve concept was based on a rotating inner shaft with supply and return ports machined into a fixed outer stator. A third load port is located on an outer rotor that rotates with respect to the stator. The duty ratio is set by the angular position of the load port relative to the supply port.

Researchers at Worcester Polytechnic Institute (WPI) have applied the phase angle concept to a dual tier phase-shift disc valve structure. The initial design proposed by Van de Ven and Katz [37] consisted of two valve tiers rotating at the same velocity. The first tier contains two subsections that connect to load and tank pressure out of phase. The two outputs from the first tier connect to the inputs of the second tier. The phase angle between the two tiers determines the ratio of the two inputs that the second tier connects to the output, thus achieving PWM with variable duty ratio. The flow path through the proposed valve is axial in nature to reduce centrifugal pumping effects and a hydrodynamic thrust bearing is used to support axial loads induced by pressure and flow forces. An analytical study of the valve operating at 6.9 MPa load pressure and 10 lpm flow rate predicted a valve efficiency of 73% at full duty ratio and 64% at 0.75 duty ratio. The modeled losses include throttling, compressibility, friction, and leakage. Friction and leakage were the main losses.

Katz and Van de Ven [38] proposed a kinematic inversion of the original phase-shift disc valve, thus simplifying the concept. In the inverted design, the phase angle between two tiers of stationary valve discs determines the duty ratio while a continuously rotating valve plate between the two tiers performs the switching. A prototype valve optimized for a lab power supply capable of delivering 8 lpm at 6.9 MPa achieved a full duty ratio

efficiency of 38%, far lower than the predicted efficiency of 79%. The authors attribute the poor efficiency to higher than expected leakage and friction.

An extension of the phase-shift valve to four quadrant operation was proposed by Wu and Van de Ven [39]. Four quadrant operation was enabled by the addition of a directional control valve integrated into the second valve tier that modulates the phase-shift. Custom disc check valves, which reduce moving mass in comparison to ball check valves, are integrated into the phase-shift valve to prevent cavitation and limit pressure spikes during transition. Predicted optimized valve efficiencies of 85% at full duty ratio and 50% at 0.25 duty ratio are cited.

The second method of achieving PWM with variable duty ratio is the use of a helical land embedded into a valve spool that rotates and translates inside of a sleeve. The rotational velocity of the spool determines the PWM frequency and the duty ratio is determined by the axial position of the spool with respect to stationary ports on the sleeve. The benefit of the helical land approach is that a single moving element generates the switching and varies the duty ratio. Thus, the number of valve components that experience relative motion is reduced. The number of leakage paths is also potentially reduced. Cyphelly and Langen [40] proposed a 2-way motor-driven valve of this type sized for 182lpm of flow. The valve and gear pump are spun with the same motor at 1500rpm. Since the valve switches twice per revolution, this equates to a PWM frequency of 50Hz. The rotary valve acts as a bypass valve: when the valve is open, flow is bypassed to tank, and when the valve is shut, flow is forced through a check valve to the consumer. Peak measured and simulated overall efficiencies (including pump and rotary valve losses) for 25%, 50%, 75%, and 100% of total flow are presented. The peak reported efficiencies for these flow fractions are 58%, 71%, 75%, and 87.5% respectively between 10MPa to 15MPa pressure differential.

Rajala [41] at The University of Minnesota also designed a valve that employed this concept. A low cost motor-driven proof-of-concept prototype was tested at PWM frequencies ranging from 10Hz to 20Hz and pressures up to 2.1MPa. However, the valve experienced binding and leakage issues due to imprecise manufacturing and extensive testing was not performed.

Other applications

Related research on rotary valves arises from the field of dynamic calibration. High frequency square-wave pressure generators are used to study the frequency response of systems, components, and sensors. Unlike PWM valves, square-wave pressure generators typically do not incorporate methods of varying the pressure pulse-width. Kobata et al. at the National Research Laboratory of Metrology (NRLM) proposed a pneumatic square-wave generating valve with internal rotor designed for operation at 0.1MPa [42]. The rotor contained two cavities separating high pressure from low pressure. A partition plate in the center of the rotor contains grooves on each face that alternately switch the valve between high and low pressure. At the National Taipei University of Technology, Wang et al. proposed an eight port fixed pulse-width hydraulic valve [43]. The valve is similar to the one proposed by Brown et al. [34] with the exclusion of the central duty ratio varying control shaft. The prototype was used to generate a pressure wave with amplitude of 1.9MPa at frequencies of 10Hz and 30Hz . The valve was designed to generate a pressure wave only and was not designed to meter flow.

1.1.3 Valve summary

A summary of the valves reviewed in this section with published performance data is presented in Fig. 1.2. Ideally, Fig. 1.2 would include a third axis containing actuation power or energy per switch, however, this data is seldom published.

Several trends can be inferred from Fig. 1.2. The first is that piezo actuated valves are typically fast but possess small flow areas (Yokota [10] and Yamada [11]). This is most likely due to the high speed, low displacement nature of the actuators. The second trend is that pilot operated valves feature much larger flow areas, however, this comes at the expense of slower transition times (Ma [28] and Winkler [29, 31, 32]). Direct acting single stage solenoid valves typically provide a good balance between transition time and flow area (Mahrenholz [13] and the Sturman valve [27]).

Unfortunately, it is difficult to gage the relative performance of the rotary valves (Van de Ven [37], Katz [38], and Wu [39]) included in Fig. 1.2 without the third axis of actuation power/energy. While all of the rotary valves feature large flow areas, the transition times are average. This is because the transition time of a rotary valve depends

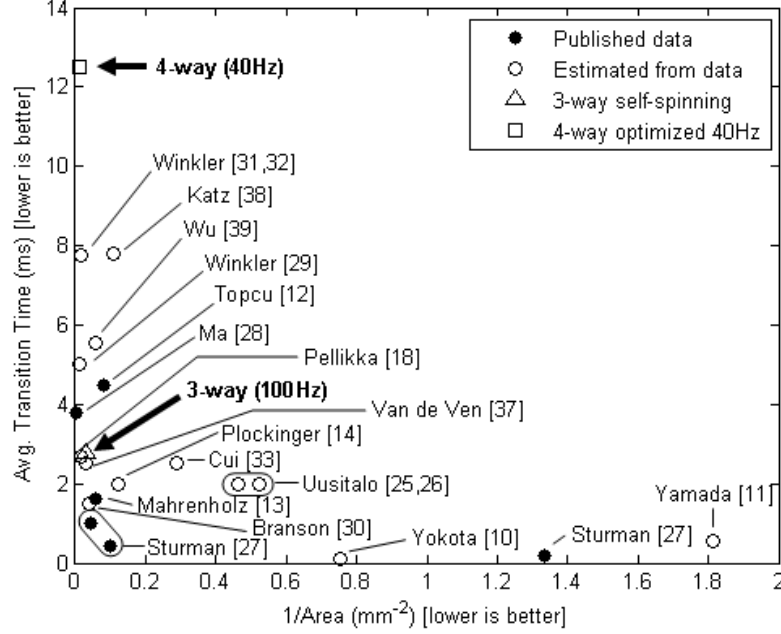


Figure 1.2: Comparison of flow area and average valve transition time for selected on/off valves found in the literature. Flow area is estimated from pressure drop and flow data assuming an orifice discharge coefficient of $C_d = .6$ and a fluid density of $\rho = 876 \text{ kg/m}^3$. Average transition time is the average of opening and closing times. Recall that the transition times for the helical land rotary valves studied in this dissertation are proportional to $\frac{1}{f_{PWM}}$. Therefore, running the valves at a higher PWM frequency will inherently reduce their transition times. The transition times at the frequencies presented are dictated by application.

on the PWM frequency, which is application dependent. Unlike linear valves where the transition time is fixed and the transition becomes a larger proportion of the PWM period as the frequency increases, the transition in a rotary valve is a fixed proportion of the PWM period (based on the valve's geometry) and transition time is proportional to $\frac{1}{f_{PWM}}$ where f_{PWM} is the PWM frequency. Therefore, the transition times of the rotary valves presented in Fig. 1.2 are determined by application requirements rather than limited by physical constraints. The true advantage of rotary valves (by design) is the low required actuation power. For instance, the 3-way self-spinning valve [44, 45, 46] (triangle in Fig. 1.2) presented in this dissertation is able to approach the performance of

state-of-the-art solenoid valves while requiring no externally supplied actuation power. The full rotary (switching) power is scavenged from the fluid flow through the valve itself in the form of fluid momentum and throttling energy.

1.2 Rotary valve concept and initial UMn efforts

The helical land concept is used to mechanically embed the desired variable PWM signal into a two degree-of-freedom rotating and translating valve spool. The rotational velocity of the spool determines the PWM frequency of the valve while its axial position determines the duty ratio. Figure 1.3 illustrates the land concept for a generic rotary valve. The helical land divides the spool surface into two regions. One region corresponds to the valve on state (gray) and the other the off state (white). As the spool rotates, the reference port (REF) is continuously switched between on and off, thus generating the PWM pulsing. The duty ratio, or fraction of each cycle that the valve is in the on state, is controlled by changing the axial position of the spool relative to the reference. Two duty ratios are shown in Fig. 1.3: 50% (Fig. 1.3(a)) and 25% (Fig. 1.3(b)).

The helical land concept permits multiple PWM sections along the circumference of the valve spool. This design flexibility can be exploited for balancing the spool and also for use as a design parameter for optimizing the valve's efficiency. For a N PWM section spool, the PWM frequency of the valve is N times the spool's rotational frequency.

Rotary valve development at the University of Minnesota began in 2004 with research by Rajala [41]. The first generation valve, shown in Fig. 1.4, was intended to be a low cost proof-of-concept prototype. A 2-way on/off valve configuration was selected with fluid flow entering the valve spool axially and exiting radially. The rotation of the spool was actuated using an electric hand drill and the axial position was controlled manually using a threaded sleeve cap. The spool was fabricated by press fitting the lands onto the spool shaft. The first generation prototype was tested at PWM frequencies ranging from $10Hz$ - $20Hz$ and pressures up to $2.1MPa$. The design validated the helical land concept, however, binding and leakage issues due to imprecise manufacturing limited the valve's performance and efficiency.

The second generation valve, shown in Fig. 1.5, was designed by Durand in 2006

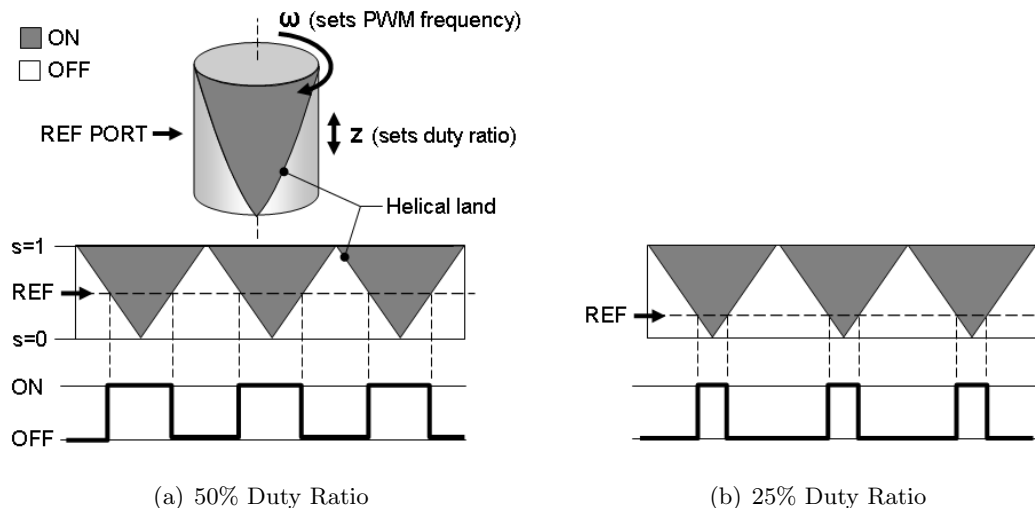


Figure 1.3: Helical land rotary valve concept illustrating PWM functionality. The rotational velocity of the spool (ω) determines the valve's PWM frequency. The axial position of the spool (normalized as z) determines the valve's duty ratio.

with the purpose of employing enhanced manufacturing techniques to overcome the binding and leakage issues that afflicted the previous valve. A 2-way configuration was retained along with the axial inlet and radial outlet ports. The spool and sleeve were CNC machined and precision ground in matched sets to maintain tight tolerances on the radial clearance. This valve was spun with an electric router capable of reaching PWM frequencies of up to $500Hz$, although the radial outlet ports led to centrifugal pumping effects that interfered with the PWM functionality of the valve.

To address the undesirable centrifugal pumping observed in the second generation valve as well as to explore the possibility of using fluid forces to spin the valve spool (i.e. self-spinning), a modification of the second generation rotary valve was proposed by the author in 2006 that reversed the flow path through the valve. By configuring the valve such that the inlets are tangential to the spool, angular momentum is produced in the fluid that is then transferred to the spool as the fluid exits axially (with no angular momentum). The prototype reached a self-spinning PWM frequency of $56Hz$ for an input flow rate of $13.3lpm$ at a pressure differential of $1.8MPa$. However, the 2-way

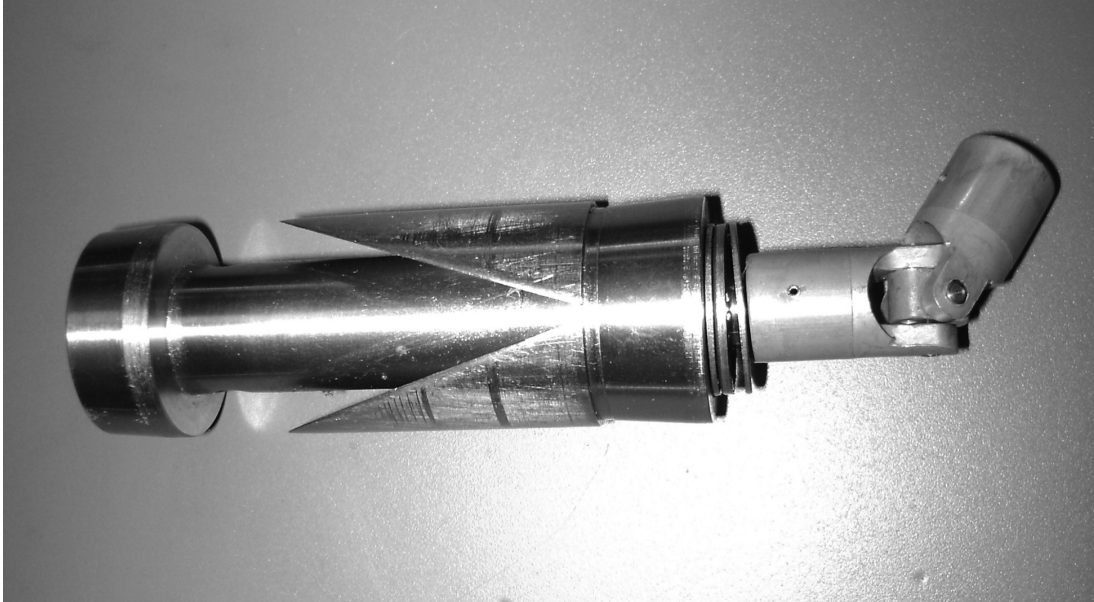


Figure 1.4: Generation 1 helical rotary on/off valve spool designed by David Rajala at the University of Minnesota (2004).

configuration of the valve proved less than ideal for self-spinning due to the fully blocked position where there is no flow through the spool.

1.3 Dissertation overview and structure

The research presented in this dissertation extends the helical land PWM concept proposed by Cyphelly et al. in several original directions and builds upon the initial studies performed at the University of Minnesota. The research can be generalized into three categories: 1) concept synthesis, 2) analysis, modeling, and simulation, and 3) hardware design, fabrication, and testing. Several unique rotary valve configurations are presented in this dissertation including a self-spinning 3-way valve for pump control, a 4-way self-spinning tandem valve for pump/motor control, and a 3-way ring valve that significantly improves efficiency. A rigorous design oriented analysis framework is developed for predicting the performance and typical losses in helical land style rotary valves. Physics based dynamic models of the valve in switched-mode pump and motor circuits



Figure 1.5: Generation 2 helical rotary on/off valve spool and sleeve designed by Adrian Durand at the University of Minnesota (2006).

are also developed for simulating system pressures and flow rates and for validating the analytical loss models. In addition, mechanical design guidelines are formulated to aid in prototype design. Lastly, prototype hardware is fabricated and extensively tested to validate the analysis, performance, and predicted efficiency of the proposed valves. The chapters in the dissertation are organized as follows:

Chapter 2 introduces the 3-way self-spinning rotary spool valve designed for implementation in virtually variable displacement pumps. Using the 3-way valve as a design example, a framework for investigating the primary losses in helical land based rotary valves is presented. Loss equations suitable for design purposes are derived and a dynamic VVDP model that captures the operation of the 3-way rotary valve is proposed. A proof-of-concept valve and VVDP prototype are fabricated to verify the valve's operation and supporting analysis. Analytical, simulated, and experimentally measured efficiencies are compared.

Chapter 3 extends the self-spinning rotary valve concept to pump/motor applications



Figure 1.6: Generation 2.5 helical rotary on/off valve spool modified to demonstrate self-spinning functionality. Self-spinning is achieved by reversing the flow path of the generation 2 valve such that the inlet port of the valve is tangential to its axis of revolution.

and to realistic operating pressures of up to 21MPa . A novel 4-way tandem valve is proposed. Fatigue design equations are formulated to size the valve sleeve for safety and longevity. The 3-way valve described in Chapter 2, designed for an operating pressure of 6.9MPa , only has a fatigue safety factor of .8 when the pressure is increased to 21MPa . A case study of implementing the proposed VVDPM as the speeder pump/motor in an input coupled power-split hydraulic hybrid passenger vehicle is conducted. Vehicle fuel economy is compared when replacing a variable displacement bent axis pump/motor with the VVDPM. A prototype VVDPM is constructed and preliminary findings are presented.

Chapter 4 revisits valve configurations, circuit configurations, and valve geometry in a holistic approach to improving on/off valve and VVDPM efficiency. A trade study is presented and a new valve structure based on a ring control element is introduced. The ring valve is predicted to significantly reduce two of the primary valve losses (transition

throttling and compressibility) with little increase in the remaining three losses (friction, leakage, and full open). A comparison is made via simulation to assess the efficiency of the ring valve in comparison to its spool valve predecessor. This chapter also explores other methods to further improve valve efficiency.

Chapter 5 includes concluding remarks and a review of the work and contributions presented in this dissertation. Recommendations for future research are also discussed.

Chapter 2

3-way self-spinning rotary valve for virtually variable displacement pumps

This chapter introduces a novel self-spinning 3-way rotary valve designed for switched-mode control of fixed displacement pumps. The combined valve/pump system, along with an accumulator, is referred to as a virtually variable displacement pump (VVDP) since it enables variable functionality using a fixed displacement base pump. Section 2.1 explains the operation of the VVDP and Section 2.2 introduces the rotary valve structure proposed to realize its operation. The analysis framework proposed to model the valve's primary losses, performance, and functionality is described in Section 2.3. A dynamic model is presented in Section 2.4. The prototype rotary valve and VVDP test stand are described in Section 2.5 and a comparison of the analysis and dynamic model with data taken from the prototype is made in Section 2.6 to validate the approach. Conclusions regarding the 3-way valve concept are discussed in Section 2.7. The work presented in this chapter has been published in several conference papers [44, 45] as well as a journal paper [46].

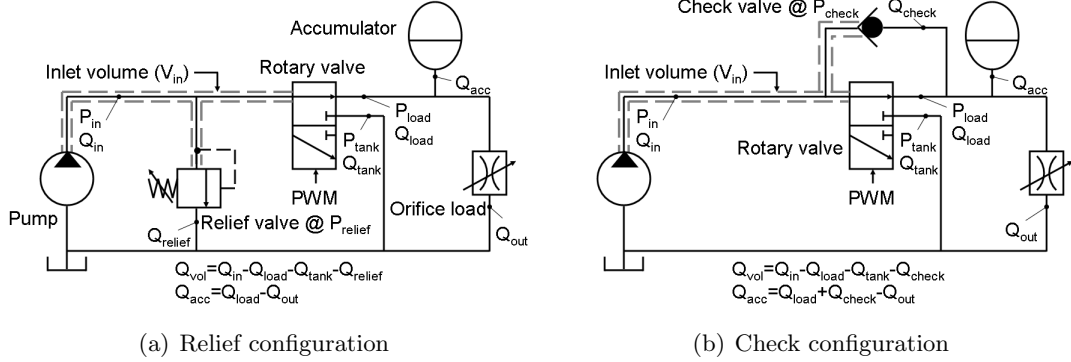


Figure 2.1: Two VVDP implementations using a 3-way on/off control valve. Q_{vol} and Q_{acc} represent the net flows into the inlet volume and accumulator.

2.1 VVDP Concept

The fundamental principle behind the VVDP is that a high speed on/off valve is used to pulse-width-modulate a fixed displacement pump between delivering full power to load and letting the pump idle. Two possible VVDP implementations using a 3-way on/off valve¹ are shown in Fig. 2.1. The system in Fig. 2.1(a) uses a relief valve with relief pressure P_{relief} to limit the inlet pressure P_{in} during valve transition. An alternate, potentially more efficient, approach is to use a check valve in parallel with the on/off valve, shown in Fig. 2.1(b). The cracking pressure of the check valve, P_{check} , should be sized higher than the full open pressure drop of the on/off valve ($P_{open} + P_{spool}$) when the valve is subject to the full flow rate Q_{in} . P_{open} and P_{spool} are the pressure drops across the valve sleeve's inlet orifices (when fully open) and the valve spool due to Q_{in} (see Section 2.2 for more details). This is needed to ensure that the check valve opens only during transition. The check valve circuit is potentially more efficient by reducing losses during transition in two ways: 1) limiting throttling losses to P_{check} above P_{load} in comparison to a fixed relief pressure which needs to be higher than any conceivable P_{load} , 2) porting the high pressure bypassed flow to load to do useful work instead of

¹ VVDP implementations based on 2-way valves are also possible [2, 6, 40, 41]. However, the 3-way valve implementation is studied here since there is fluid flow through the valve continuously regardless of valve position. This is needed for self-spinning rotation of the spool, which is discussed in Sections 2.2 and 2.3.4.

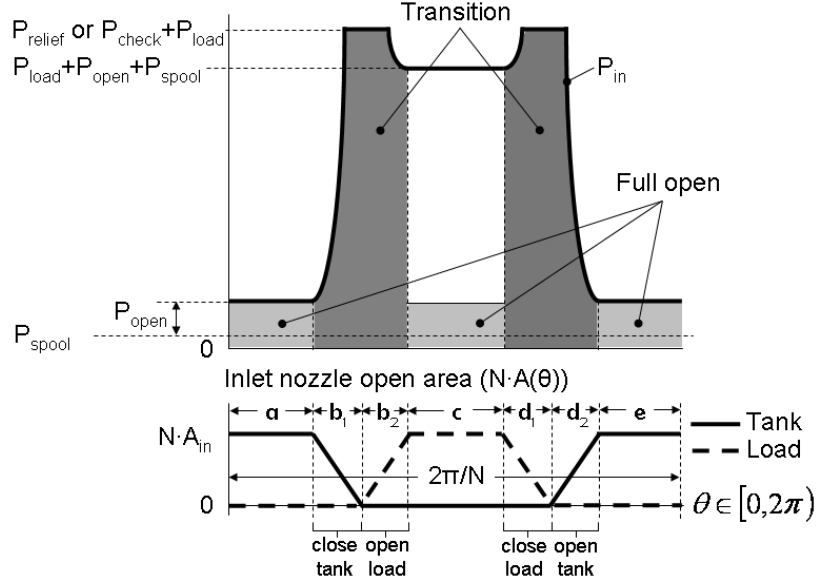


Figure 2.2: Top: Inlet pressure (P_{in}) profile over one PWM cycle ($\frac{2\pi}{N}$ rad spool rotation) for the two circuits in Fig. 2.1. Bottom: Corresponding profiles of the valve inlet orifice open areas ($A(\theta)$) to load or to tank.

dumping the fluid to tank. The latter achieves a *soft-switching* function that reduces losses when the on/off valve is switching [47, 48, 49].

For a VVDP based on a 3-way valve, full power is delivered when the on/off valve connects the pump output directly to load as shown in Fig. 2.1. In this state, the full pump flow Q_{in} is delivered to the load at pressure P_{load} . In idle mode, the valve connects the pump output directly to tank, thereby cycling Q_{in} at low pressure. When idling, the pump only supplies the pressure needed to overcome the full open pressure drop of the on/off valve ($P_{open} + P_{spool}$).

Figure 2.2 illustrates the inlet pressure profile of the VVDP over one PWM cycle along with the corresponding open orifice area profiles to tank (solid) or to load (dotted) assuming that $P_{tank} = 0$ for simplicity. In the proposed 3-way rotary valve, the orifices are rhombic shaped to match the helical land and to provide a faster transition time compared to a circular orifice of equal area [44]. With this configuration, the orifice opening varies linearly with the the spool rotation until either the orifice is completely open or closed. The full pump flow, Q_{in} , is supplied to the inlet volume V_{in} (Fig. 2.1)

throughout the entire PWM cycle.

Interval a in Fig. 2.2 represents the VVDP in the off state with the rotary valve completely open to tank. Since the pump is unloaded, P_{in} is low ($= P_{open} + P_{spool}$). The accumulator supplies flow to the load and Q_{in} is returned to tank.

Interval b is when the valve transitions from being open to tank to being open to load. First, the rhombic orifice closes to tank, causing P_{in} to rise (interval b_1). Once P_{in} reaches P_{relief} (in Fig. 2.1(a)) or $P_{check} + P_{load}$ (in Fig. 2.1(b)), the relief or check valve opens to regulate P_{in} at these levels. Since the valve is critically lapped (i.e. the helical lands and the rhombic orifices have equal widths), the instant the orifice closes completely to tank, it begins to open to load (interval b_2). The relief or check valve will close once the orifice is sufficiently open, thus causing P_{in} to decrease.

Interval c represents the period when the valve is completely open to load. The system is in the on state and the pressure drop across the rotary valve ($P_{in} - P_{load}$) becomes $P_{open} + P_{spool}$. Q_{in} from the pump is supplied to the accumulator and the load.

Interval d is when the valve transitions from being open to load to being open to tank. As the orifice closes to load (interval d_1), P_{in} rises until the relief or check valve opens. As the orifice is fully closed to load, it begins to open to tank (interval d_2). The relief or check valve closes once the orifice is sufficiently open. As the valve becomes fully open to tank, $P_{in} = P_{open} + P_{spool}$ and the system returns to the off state.

2.2 3-way Valve Embodiment for Pumps

The realization of the 3-way rotary valve required for the VVDP circuits shown in Fig. 2.1 is presented in Figs. 2.3 and 2.4. The rotary valve consists of a valve spool that rotates and translates inside of a stationary valve sleeve. The sleeve (Fig. 2.3) is designed to replace part of the pump housing in order to reduce the compressible dead volume between the pump outlet and spool. This is desirable in order to reduce compressibility losses and to improve bandwidth.

The flow trajectory through the 3-way valve is illustrated in Fig. 2.4. Helical lands on the center (inlet) section of the spool divide the spool into two flow paths, labeled B (dark gray) and C (light gray). Internal axial passages (see spool cutaway at top right of Fig. 2.4) port fluid from the center section of the spool to the two outlet sections.

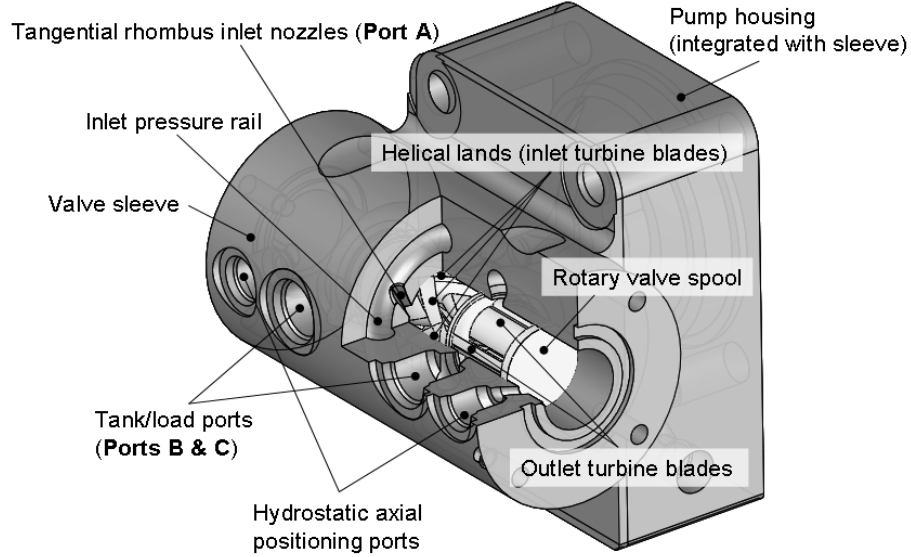


Figure 2.3: 3-way rotary valve spool, sleeve, and pump housing assembly.

Port *A*, the inlet port, is located on the valve sleeve shown in Fig. 2.3 and is tangential to the sleeve bore (used for self-spinning, see Section 2.3.4). There are N inlet ports corresponding to the N PWM sections on the spool. All inlet ports are supplied by a single toroidal pressure rail that is connected directly to the pump outlet.

As the spool rotates, Port *A* is continuously switched between Ports *B* and *C*, illustrated by the open orifice area profiles shown in the bottom of Fig. 2.4. This generates the PWM switching functionality of the rotary valve where the inlet pressure of the VVDP, P_{in} , is pulse-width-modulated between load pressure (P_{load}) and tank (P_{tank}). The PWM duty ratio, s , is defined as the fraction of each PWM period that the valve is in the on state or connected to load. s varies linearly with the spool's axial position due to its helical structure and controls the output flow fraction of the VVDP. When $s = 0$ (i.e. the zero duty ratio), flow is bypassed to tank during the entire revolution, thus sending no flow to load (i.e. no VVDP output flow). The opposite occurs at $s = 1$ (i.e. full duty ratio) where the VVDP output flow equals the full pump flow. In the prototype valve, the spool's axial position is controlled using an electro-hydraulic gerotor pump in a hydrostatic configuration, although other actuation methods are possible. The gerotor ports fluid to either side of the spool using the axial

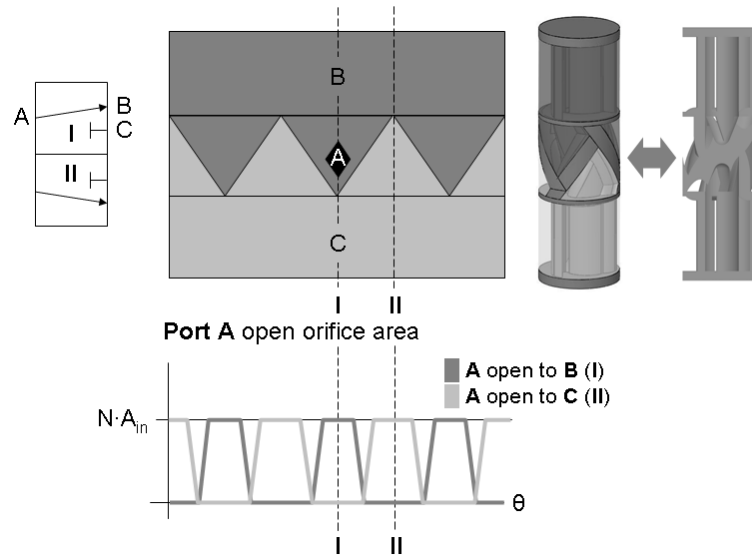


Figure 2.4: Top: 3-way helical rotary valve concept for VVDPs. Internal passages connect the center section (responsible for PWM) to one of the two adjacent outlet turbines. The dark gray portions of the spool are hydraulically connected and permit flow from the inlet to the load. Similarly, the light gray sections connect the inlet to tank. Bottom: Open area profiles illustrating when Port *A* is connected to Port *B* or *C*.

positioning ports shown in Fig. 2.3. Sensing of the axial and angular positions of the spool is accomplished using non-contact optical sensors. Refer to publications by Wang for details regarding the sensing (axial and rotary) and control (axial) of the rotary valve [50, 51, 52].

Self-spinning of the spool is accomplished by designing both the inlet and outlet sections of the spool as turbines to capture throttling energy and fluid momentum. The inlet section acts as an impulse turbine, where fluid is accelerated via nozzles tangential to the rotor (i.e. valve spool) [53]. As the fluid impinges on the turbine blades, angular momentum is transferred to the spool as it redirects flow to the center of the spool. Fluid then exits the inlet section axially with no angular momentum. In contrast, the outlet section is designed as a reaction turbine. Blades on the outlet section guide the fluid from the center of the spool outwardly and tangentially, thus imparting a reaction torque on the spool. Self-spinning is discussed in more detail in Section 2.3.4.

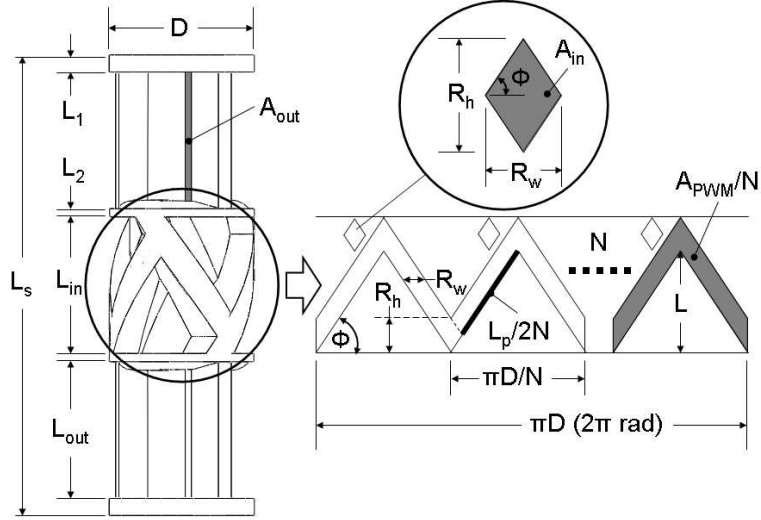


Figure 2.5: 2D representation of the rotary valve's geometry including variable definitions used in Section 2.3.

2.3 Design and Performance Analysis

A detailed analysis and resulting design equations for the rotary valve and the two VVDP configurations shown in Fig. 2.1 are presented in this section. Variables used in the analysis are defined in Fig. 2.5. Several simplifying assumptions are applied: 1) The fixed-displacement pump is assumed to be an ideal flow source with constant output flow Q_{in} . 2) The system pressure is assumed to be capped at P_{relief} for the relief circuit and $P_{check} + P_{load}$ for the check circuit when the relief valve or check valve is activated. 3) Variation of P_{load} (load/accumulator pressure) is assumed to be slow such that it can be considered a constant. 4) Tank pressure, P_{tank} , is assumed to be zero. Dynamic effects of the inlet and accumulator pressure will be discussed later in Section 2.4.

Section 2.3.1 investigates throttling losses. Section 2.3.2 examines compressibility losses. Valve leakage is explored in Section 2.3.3. The spool's self-spinning velocity is analyzed in Section 2.3.4 and the relationship between its axial position and the VVDP's output flow is studied in Section 2.3.5. Various design trade offs and a summary of the design are discussed in Section 2.3.6.

2.3.1 Valve Throttling Losses

Throttling losses through the rotary valve include sleeve losses from the variable rhombic orifices, losses through the spool itself, and losses due to the relief valve or check valve. Section 2.3.1 considers the losses when the rhombic orifices are fully open and Section 2.3.1 considers the losses when the valve is in transition.

Let the fraction of time that the valve is in transition or fully open be κ and $(1 - \kappa)$ respectively. Assuming the duty ratio s and the spool angular frequency ω are constant while the valve is transitioning, the helical land traverses the width of the rhombus R_w (Fig. 2.5) during each transition. The corresponding duration of each of the four transitions is:

$$T_{tran} = 2R_w / (D\omega) \quad (2.1)$$

and the PWM period is $2\pi / (\omega N)$. Thus,

$$\kappa = \frac{4NR_w}{\pi D} \quad (2.2)$$

Full Open Orifice Losses

When the rotary valve is fully open, the pressure drop across the N rhombic orifices is described by the orifice equation [54]:

$$P_{open} = \frac{\rho}{2} \left(\frac{Q_{in}}{C_d N A_{in}} \right)^2 \quad (2.3)$$

ρ is the density of hydraulic oil, C_d is the orifice discharge coefficient (assumed constant), and $A_{in} = 0.5R_w R_h$ is the cross-sectional area of one inlet with R_w and R_h being the rhombus width and height (see Fig. 2.5).

The pressure drop across the spool itself, P_{spool} , is estimated using a CFD generated semi-empirical formula [52, 55, 56] based on a scaled version of the prototype's geometry. For a given diameter (D) and flow rate (Q_{in}), P_{spool} is assumed to be constant regardless of whether the valve is connected to load or tank due to the symmetry of the flow paths. Thus, the rotary valve's full open power loss is:

$$\Pi_{open} = (1 - \kappa)(P_{open} + P_{spool})Q_{in} \quad (2.4)$$

Transition Losses

The transition throttling losses derived in this section include losses from blocking the inlet rhombic orifices, losses through the relief valve (Fig. 2.1(a)) or check valve (Fig. 2.1(b)), and losses through the spool. During each PWM cycle, the rotary valve undergoes four transitions: opening and closing to tank with equal energy losses (E_{tank}), and opening and closing to load also with equal energy losses (E_{load}).

For the relief circuit in Fig. 2.1(a), consider first the opening to tank transition (interval d_2 in Fig. 2.2). At the beginning of the transition, the rhombic inlet orifice is blocked and all flow goes through the relief valve to tank and $P_{in} = P_{relief}$. As the rhombic orifice opens to tank (with the relief valve still open), flow passes through both the relief and the on/off valve to tank with a pressure drop of P_{relief} . When the valve is sufficiently open, P_{in} falls below P_{relief} and all flow goes through the on/off valve to tank causing a pressure drop of P_{spool} across the spool.

Considering the problem in angular coordinates with $\Theta = \omega t$ where $\Theta = 0$ corresponds to the start of transition, let $P_i(\Theta)$ be the instantaneous pressure across the orifice with varying orifice area if the full flow Q_{in} passes through it:

$$P_i(\Theta) = \frac{\rho}{2} \left(\frac{Q_{in}}{C_d N A(\Theta)} \right)^2 = P_{open} \left(\frac{\Theta_{tran}}{\Theta} \right)^2 \quad (2.5)$$

where the definition in (2.3) has been employed and $A(\Theta)$ is the instantaneous open area of one rhombic inlet and Θ_{tran} is the total rotational angle for each transition:

$$A(\Theta) = \frac{R_h D}{4} \Theta = A_{in} \frac{\Theta}{\Theta_{tran}} \quad (0 \leq \Theta \leq \Theta_{tran}) \quad (2.6)$$

$$\Theta_{tran} = 2R_w/D \quad (2.7)$$

Let Θ_{crit} be the critical angle when the relief valve just begins to open or close coinciding with $P_i(\Theta_{crit}) = P_{relief}$. From (2.5) and (2.6), they are related by:

$$\frac{\Theta_{crit}}{\Theta_{tran}} = \sqrt{\frac{P_{open}}{P_{relief}}} \quad (2.8)$$

Therefore, considering whether the relief valve is open or closed and utilizing (2.5)-(2.8):

$$E_{tank} = \frac{Q_{in}}{\omega} \left[\underbrace{\int_0^{\Theta_{crit}} P_{relief} d\Theta}_{\text{relief open}} + \underbrace{\int_{\Theta_{crit}}^{\Theta_{tran}} (P_i(\Theta) + P_{spool}) d\Theta}_{\text{relief closed}} \right] \quad (2.9)$$

$$= \frac{Q_{in}}{\omega} \left[P_{relief} \Theta_{crit} + P_{open} \Theta_{tran} \left(\frac{\Theta_{tran}}{\Theta_{crit}} - 1 \right) + P_{spool} (\Theta_{tran} - \Theta_{crit}) \right] \quad (2.10)$$

$$= \frac{2Q_{in} R_w}{\omega D} \sqrt{P_{open}} \left[2\sqrt{P_{relief}} - \sqrt{P_{open}} + P_{spool} \left(\frac{1}{\sqrt{P_{open}}} - \frac{1}{\sqrt{P_{relief}}} \right) \right] \quad (2.11)$$

The energy lost when opening the inlet to load (interval b_2) is calculated similarly. The main difference is that when the relief valve is open, the flow through the relief valve is throttled across P_{relief} whereas the flow through the rotary valve is throttled across $P_{relief} - P_{load}$. In angular coordinates, the instantaneous flow through the rotary valve (Q_i) with varying orifice area when the relief valve is open is:

$$Q_i(\Theta) = Q_{in} \sqrt{\frac{P_{relief} - P_{load}}{P_{open}}} \frac{\Theta}{\Theta_{tran}} \quad (2.12)$$

The critical angle for the load transitions, Θ'_{crit} , occurs when $Q_i(\Theta'_{crit}) = Q_{in}$. Thus,

$$\frac{\Theta'_{crit}}{\Theta_{tran}} = \sqrt{\frac{P_{open}}{P_{relief} - P_{load}}} \quad (2.13)$$

The resulting energy loss during each load transition is:

$$E_{load} = \frac{1}{\omega} \left[\int_0^{\Theta'_{crit}} \{ (Q_{in} - Q_i(\Theta)) P_{relief} + Q_i(\Theta) (P_{relief} - P_{load}) \} d\Theta + \int_{\Theta'_{crit}}^{\Theta_{tran}} Q_{in} (P_i(\Theta) + P_{spool}) d\Theta \right] \quad (2.14)$$

$$= \frac{2Q_{in} R_w}{\omega D} \sqrt{P_{open}} \left[\frac{2P_{relief} - 1.5P_{load} - P_{spool}}{\sqrt{P_{relief} - P_{load}}} + \frac{P_{spool} - P_{open}}{\sqrt{P_{open}}} \right] \quad (2.15)$$

The average transition power loss is derived from the total energy loss per cycle (4 transitions) and the PWM frequency:

$$\Pi_{trans} = (2E_{load} + 2E_{tank}) \frac{N\omega}{2\pi} \quad (2.16)$$

Using the definition in (2.16), the loss for the relief circuit is:

$$\begin{aligned} \Pi_{trans,relief} = & \underbrace{\kappa\sqrt{P_{open}}}_{\text{optimizable}} \frac{Q_{in}}{2} \left[\frac{2P_{relief} - 1.5P_{load} - P_{spool}}{\sqrt{P_{relief} - P_{load}}} \right. \\ & \left. + \frac{2(P_{spool} - P_{open})}{\sqrt{P_{open}}} + \frac{2P_{relief} - P_{spool}}{\sqrt{P_{relief}}} \right] \end{aligned} \quad (2.17)$$

The loss for the check circuit is calculated similarly. The main difference is that the critical angle when the check valve first begins to open or close corresponds to a pressure of $(P_{check} + P_{load})$ for the tank transitions and P_{check} for the load transitions. The resulting loss is:

$$\begin{aligned} \Pi_{trans,check} = & \underbrace{\kappa\sqrt{P_{open}}}_{\text{optimizable}} \frac{Q_{in}}{2} \left[\frac{2P_{check} + 1.5P_{load} - P_{spool}}{\sqrt{P_{check} + P_{load}}} \right. \\ & \left. + \frac{2(P_{spool} - P_{open})}{\sqrt{P_{open}}} + \frac{2P_{check} - P_{spool}}{\sqrt{P_{check}}} \right] \end{aligned} \quad (2.18)$$

Remarks:

1. Equations (2.17) and (2.18) reveal that the average transition loss of the rotary valve is independent of PWM frequency. This is unlike linear valves with fixed transition time where transition losses increase with frequency.
2. Separating these equations into two parts reveals that the transition loss is dependent only on geometric and system parameters: $\kappa\sqrt{P_{open}}$ consists of rotary valve design parameters that can be optimized to reduce losses while the remaining terms consist mostly of system operating conditions and check and relief valve settings.
3. The last term in Eqs. (2.17) and (2.18) highlights the loss saving advantage of the check circuit. In Eq. (2.17), P_{relief} is constrained by the load pressure and is typically $\gg P_{spool}$. In contrast, the last term of Eq. (2.18) is independent of load pressure and P_{check} can be sized just slightly larger than $P_{open} + P_{spool}$. A comparison of how the transition losses compare between the two circuits is presented in Figure 2.6 when $P_{load} < P_{relief}$.

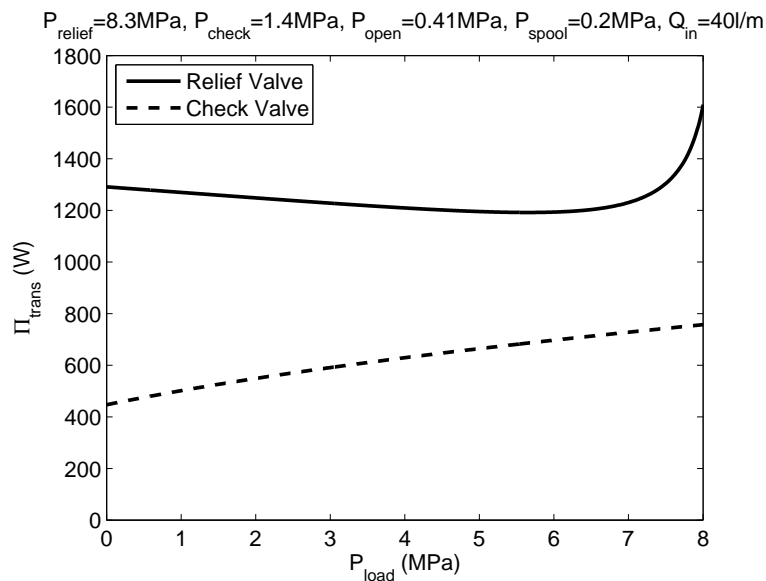


Figure 2.6: Comparison of transition losses between the relief and check circuits. Results for the relief circuit are only valid when the load pressure is below the relief pressure.

2.3.2 Compressibility Losses

Compressibility losses, which are frequency dependent, consist of the energy per cycle that is required to compress the fluid in the inlet volume, V_{in} (see Fig. 2.1), from tank to load pressure. This energy is lost when the valve re-opens to tank. Compressibility losses are especially important in switched-mode systems due to the high frequency repetitive switching nature of PWM. Because of the substantial variation of bulk modulus at low pressures ($< 7\text{MPa}$) due to the presence of air entrainment in the working fluid, the use of a pressure dependent bulk modulus model is proposed. A detailed review of fluid bulk modulus models performed by Gholizadeh et al. [57] at the University of Saskatchewan reveals two primary methods of modeling the effect of air in the working fluid. The first method considers compression of the air only while the second method also considers the volumetric reduction of the air due to it dissolving into the working fluid. Gholizadeh et al. [57] suggests that including the effect of compression alone is adequate for 'fast acting hydraulic systems in which the rate of increase in pressure is such that it does not allow for the air to dissolve in the oil'. Another motive for neglecting the effect of air dissolving arises from concerns that the physics of the dissolving process are not

adequately captured in the bulk modulus models reviewed [57]. Interestingly, several pressure dependent effective bulk modulus models found in the literature that consider only the compression of entrained air (Yu et al. [58], Cho et al. [59], and Nykanen et al. [60]) are essentially the same model once the definitions of volumetric air fraction and bulk modulus (secant, tangent) are made consistent [57]. A reduced version of Yu's model [58] that neglects the effect of air dissolving into solution, assumes the entrained air is compressed adiabatically (due to the fast switching of PWM), and is defined in terms of gage pressure² is used in this dissertation:

$$\beta_{eq}(P) = \frac{\left(\frac{P}{P_0} + 1\right)^{\frac{1}{\gamma}} \beta}{\frac{r\beta}{(P+P_0)\gamma} + \left(\frac{P}{P_0} + 1\right)^{\frac{1}{\gamma}} - r} \quad (2.19)$$

P is the gage pressure of the fluid, P_0 is atmospheric pressure, β is the bulk modulus of pure air free oil ($1.7GPa$), γ is the polytropic index for an adiabatic process (i.e. ratio of specific heats), and r is the volumetric air entrainment fraction. Equation (2.19) is plotted with respect to pressure and various amounts of air entrainment in the top portion of Fig. 2.7. Making use of this bulk modulus model, the energy lost per cycle is given by:

$$E_{comp} = V_{in} \int_{P_{tank}}^{P_{load}} \frac{P_{in}}{\beta(P_{in})} dP_{in} \quad (2.20)$$

P_{in} is the inlet volume pressure. The corresponding power lost due to compressibility is found using the compression energy described by Eq. (2.20), which is integrated numerically and plotted in the bottom of Fig. 2.7:

$$\Pi_{comp} = E_{comp} f_{PWM} \quad (2.21)$$

2.3.3 Leakage

Leakage paths exist in two locations (refer to Fig. 2.5): 1) across the helical land separating load pressure from tank, and 2) across the spool ends (L_1) separating working fluid from the hydrostatic axial control chambers.

² Equation (2.19) has been rearranged from its original form as presented in [58]. The effect of air dissolving into solution is neglected by setting $c_1 = 0$ in the full form of Yu's effective bulk modulus model.

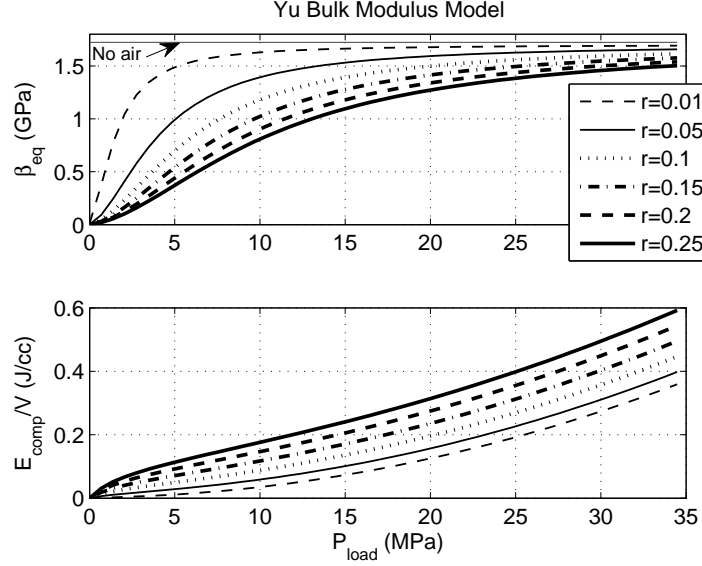


Figure 2.7: Top: Yu pressure dependent bulk modulus for various fractions (r) of air entrainment and no dissolved air. Bottom: Unit compression energy required to compress fluid from P_{tank} to P_{load} .

Because the outlet sections of the spool are always connected to load and tank pressure, the pressure differential across the helical land is nominally constant and equal to $P_{load} - P_{tank}$. Assuming laminar leakage flow [61], the leakage across the helical land is:

$$Q_{leak} = \frac{L_p c_r^3 (P_{load} - P_{tank})}{12 \mu R_w \sin \phi} \quad (2.22)$$

μ is the dynamic viscosity of hydraulic oil, c_r is the radial clearance between the spool and sleeve, $R_w \sin \phi$ is the thickness of the land normal to its edge, ϕ is the angle of the rhombus and L_p is the perimeter of the leakage path parallel to the land edges:

$$L_p = N \left(\frac{2L - R_h}{\sin(\phi)} \right) \quad (2.23)$$

$L = \frac{\pi D R_h}{2N R_w}$ is the total axial travel. The resultant power loss is:

$$\Pi_{leak} = \frac{L_p c_r^3 (P_{load} - P_{tank})^2}{12 \mu R_w \sin \phi} \quad (2.24)$$

Similarly, the power loss due to leakage across the spool end land assuming laminar

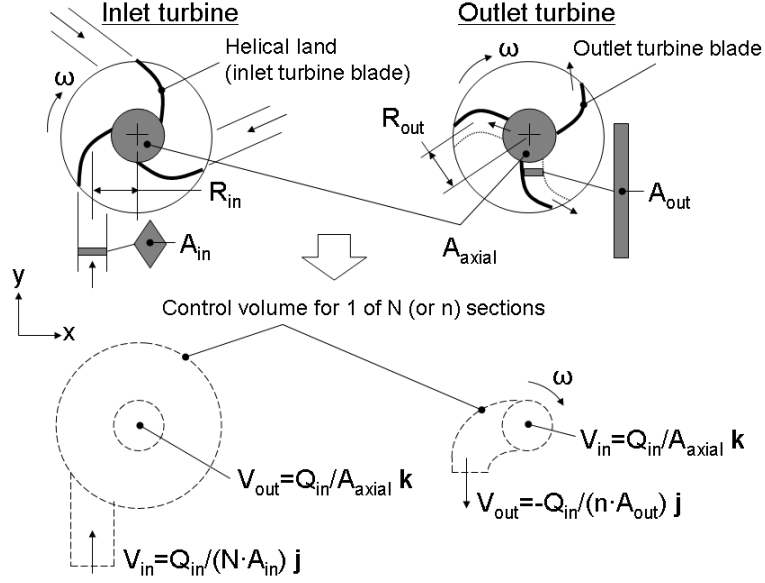


Figure 2.8: Inlet and outlet turbines with their control volumes.

leakage flow is:

$$\Pi_{leak,L1} = \frac{\pi D C_r^3 (P_{load} - P_{axial})^2}{12 \mu L_1} \quad (2.25)$$

P_{axial} is the pressure in the axial control chamber acting on the spool end adjacent to the load side. This pressure is used for axial positioning and is dependent on the method used.

2.3.4 Self-spinning Velocity Analysis

The rotary valve spool is designed to be self-spinning and requires no external rotary actuator. Self-spinning is accomplished by designing the inlet and outlet sections of the spool as turbines to capture momentum and kinetic energy from the fluid flow through the valve. The center inlet section of the spool is designed as an impulse turbine while the two outlet sections are designed as reaction turbines. In an impulse turbine, fluid is accelerated at the expense of pressure drop through stator nozzles that are tangential to the turbine rotor [53]. Blades on the rotor turn the accelerated flow, thus converting the linear momentum of the fluid into angular momentum, and therefore torque, to drive the rotor. The rotor and stator are analogous to the valve spool and tangential

inlet nozzles in the valve sleeve, shown in Fig. 2.3. In contrast, pressure drop occurs across the rotor of the turbine instead of the stator [53] in a reaction type turbine. Fluid enters the outlet turbine axially from the inlet turbine with no angular momentum. By turning and accelerating the fluid as it flows outward through the outlet turbine blades, a reaction torque is generated on the spool.

The dynamics of the spool rotation can be determined by summing torques on the spool. This consists of the torques generated by the inlet and outlet turbines that must counteract the resistive torque from viscous friction:

$$J\ddot{\theta} = \tau_{in} + \tau_{out} - \tau_f \quad (2.26)$$

where J is the mass moment of inertia of the spool, $\ddot{\theta}$ is the angular acceleration, τ_{in} and τ_{out} are the torques contributed by the inlet and outlet turbines, and τ_f is the resisting torque due to viscous friction. τ_f is estimated using Petroff's Law [62] which assumes Newtonian shear stress between concentric cylinders with relative rotary motion:

$$\tau_f = \frac{1}{4} A_{eff} \frac{\mu}{c_r} D^2 \omega \quad (2.27)$$

A_{eff} is the effective bearing surface area of the spool which is discussed in more detail in Section 2.3.4.

A diagram of the inlet and outlet turbines and their corresponding control volumes (CV) is shown in Fig. 2.8. The inlet turbine is modeled as a stationary CV that surrounds the spool and tangential rhombic sleeve ports (offset R_{in} from the axis of rotation). The tangential sleeve ports serve as the inlet to the CV and generate angular momentum in the fluid. The fluid exits the inlet turbine axially (with no angular momentum) through an internal channel with cross sectional area A_{axial} that leads to the outlet turbine. Thus all angular momentum generated by the inlets is transferred to the spool. Assuming steady incompressible flow and one dimensional inlets/outlets, the inlet turbine torque is:

$$\tau_{in} = \sum_1^N (R_{in} \times v)_{IN} \dot{m}_{in} = \frac{\rho R_{in}}{A_{in} N} Q_{in}^2 \quad (2.28)$$

ρ is the density of hydraulic oil, v is the mean velocity of the fluid as it exits the inlet and enters the spool, and \dot{m} is the corresponding mass flow rate. $(\dots)_{IN}$ refers to the conditions at the inlet of the CV.

The outlet turbine is modeled as a CV that rotates with the spool (Fig. 2.8). Sleeve effects on the fluid are assumed small since the sleeve/turbine interface allows the fluid to exit the turbine unguided before accumulating the fluid at the outlet port downstream. Fluid enters the CV axially from the inlet turbine with no angular momentum. As the fluid is turned by the curved turbine blades (n blades with $n = N$ in the current design for simplicity), a reaction torque is generated on the spool. Assuming A_{out} , the flow area through the blades (see Figs. 2.5 and 2.8), is constant and offset by R_{out} from the axis of rotation, the outlet turbine torque is:

$$\begin{aligned}\tau_{out} &= \sum_1^N (R_{out} \times (v - v_{CV}))_{OUT} \dot{m}_{out} \\ &= R_{out} \rho Q_{in} \left(\frac{Q_{in}}{A_{out} N} - R_{out} \omega \right)\end{aligned}\quad (2.29)$$

$v_{CV} = R_{out} \omega$ is the velocity of the CV at the tip of the blades where the fluid exits. Equating the inlet and outlet torques to the friction torque at steady state (Eq. (2.26)) produces the steady state angular spool velocity:

$$\omega = \frac{4\rho}{ND^2 \left(A_{eff} \frac{\mu}{c_r} + \frac{4R_{out}^2}{D^2} \rho Q_{in} \right)} \frac{R_{in}}{\bar{A}} Q_{in}^2 \quad (2.30)$$

where \bar{A} is an equivalent combined flow area:

$$\frac{1}{\bar{A}} = \frac{1}{A_{in}} + \frac{R_{out}}{R_{in} A_{out}} \quad (2.31)$$

Remarks:

1. Equation (2.29) illustrates competing effects in the outlet turbine. $\frac{Q_{in}}{A_{out} N}$ corresponds to the angular momentum generated by the fluid flow as it is turned by the turbine blades. However, this momentum is counteracted by the $R_{out} \omega$ term which reflects the angular momentum that must be transferred to the fluid as it is forced to rotate with the same circumferential velocity as the blades. Consequently, when the tip velocity of the outlet turbine exceeds the mean velocity of the fluid (i.e. $R_{out} \omega > \frac{Q_{in}}{A_{out} N}$) the turbine will act as a pump and require torque to maintain its velocity.
2. For applications where low throttling is desired and a slower PWM frequency is acceptable, the inlet turbine alone can be used for self-spinning and the outlet

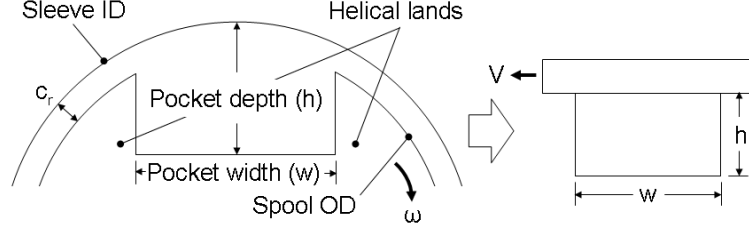


Figure 2.9: Pocketed volume and corresponding CFD model.

section can be designed to minimize pressure drop. Equation (2.30) can be simplified to this case by setting $R_{out} = 0$ which reduces Eq. (2.26) to $\tau_{in} = \tau_f$. The corresponding self-spinning velocity for the inlet turbine only case is:

$$\omega = \frac{4\rho}{ND^2 A_{eff} \frac{\mu}{c_r}} \frac{R_{in}}{A_{in}} Q_{in}^2 \quad (2.32)$$

Both designs will be verified experimentally in Section 2.6.2.

Effective Bearing Surface and Friction Analysis

A method is developed in this section for estimating the total friction effects on the valve spool. This is done by finding an equivalent spool bearing surface area A_{eff} that can be used in Eq. (2.27). The first type of friction present is the journal bearing friction which is due to the helical land and sealing lands, having axial widths L_1 and L_2 , which have a combined surface area of:

$$A_b = \pi D [R_h + 2(L_1 + L_2)] \quad (2.33)$$

The second type of friction is due to fluid recirculation in the pockets between the helical lands and the outlet turbine blades with surface areas πDL and $2\pi DL_{out}$ respectively (refer to Fig. 2.5). By using CFD to characterize the friction in the pockets, the effect of this friction can be combined with A_b to form an effective bearing surface area:

$$\begin{aligned} A_{eff} &= A_b + \lambda [\alpha_{in} \pi DL + \alpha_{out} 2\pi DL_{out}] \\ &= \pi D [R_h + 2(L_1 + L_2) + \lambda(\alpha_{in} L + 2\alpha_{out} L_{out})] \end{aligned} \quad (2.34)$$

α_{in} and α_{out} are the ratios of shear stress due to fluid recirculation (σ_p) to the bearing surface shear (σ_b) and λ is a correction factor on the fluid recirculation contribution to the effective bearing surface area that is used to match the predicted self-spinning velocity to experimental data. Test stand results presented in Section 2.6.2 show that $\lambda = 2$ provides a good fit to data. σ_p is estimated from a CFD code³ that assumes steady two-dimensional incompressible Newtonian flow. The spool geometry is approximated by a rectangular chamber with moving upper boundary (Fig. 2.9). The CFD analysis shows that a single trend line (Fig. 2.10) is able to capture the dependence of normalized shear ($\frac{\sigma_p}{\rho V^2}$) on aspect ratio ($\xi = \frac{w}{h}$) and Reynolds number ($Re = \frac{\rho V h}{\mu}$):

$$\frac{\sigma_p}{\rho V^2} = 10^b \xi^K \quad (2.35)$$

b is a function of Re and is defined at the bottom of Fig. 2.10 and $K = -0.653$. w is the chamber width, h is the chamber depth, and $V = R\omega$ is the sliding velocity of the upper boundary corresponding to the spool's rotational velocity ω .

Equation (2.35) is used to quantify the shear stress due to recirculation in the fluid pockets of the non-bearing surface area. Because the aspect ratio of the pocket between the helical lands of the inlet turbine varies with respect to the spool's axial position, an average shear stress is defined for the inlet turbines. Integrating the differential shear stress along the length of the pocket and then dividing by the total surface area ($.5\bar{w}L$, where $\bar{w} = \pi D/N$ is the widest portion of the pocket), and knowing that the aspect ratio varies linearly according to $\xi = \frac{\bar{w}}{L}l$ for $0 \leq l \leq L$ produces:

$$\begin{aligned} \sigma_{p,avg} &= \frac{\int_{l=0}^{l=L} \sigma_p w dl}{.5\bar{w}L} = \frac{\int_{l=0}^{l=L} 10^b \rho V^2 \xi^K \xi h dl}{.5\bar{w}L} \\ &= \frac{2}{K+2} \rho V^2 10^b \bar{\xi}^K \end{aligned} \quad (2.36)$$

$\bar{\xi} = \frac{\bar{w}}{h}$ is the largest aspect ratio corresponding to the widest portion of the pocket. Using Eq. (2.36), $\alpha_{in} = \frac{\sigma_{p,avg}}{\sigma_b}$. Conversely, because the aspect ratio of the fluid pocket between the outlet turbine blades is constant, the shear stress is calculated directly from Eq. (2.35) and $\alpha_{out} = \frac{\sigma_p}{\sigma_b}$.

³ The CFD simulations were performed by Meng Wang [46].

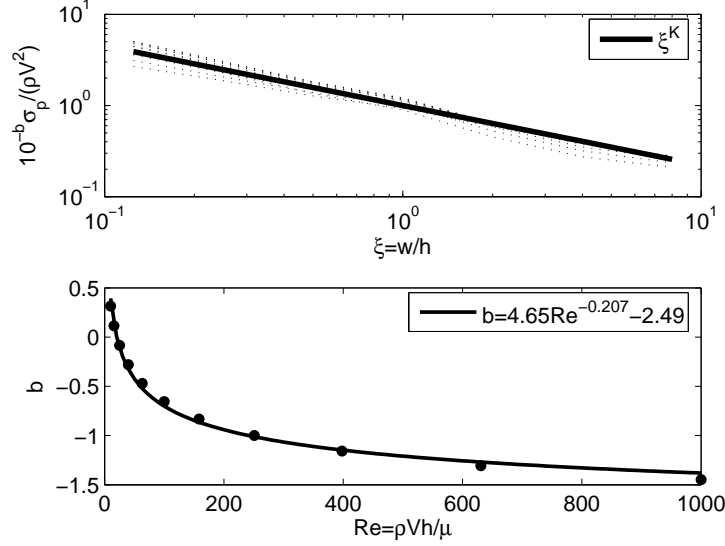


Figure 2.10: Normalized pocket shear ($K = -0.653$)

The journal bearing shear σ_b is estimated using the shear stress equation for Newtonian flow between two moving plates with constant relative velocity [63]:

$$\sigma_b = \mu \frac{R\omega}{c_r} \quad (2.37)$$

Figure 2.11 presents the predicted driving power needed to overcome viscous friction. A curve fit reveals that friction power is essentially proportional to the PWM frequency squared despite the additional frictional contributions from fluid recirculation. Only 30W is required to achieve 100Hz PWM frequency with the prototype valve described in Table 2.1 and Section 2.5. This confirms the low actuation power potential of uni-directional rotary valves. $\alpha_{in} \approx 0.05$ and $\alpha_{out} \approx 0.035$ for the prototype and the corresponding drag torque due to recirculation is about 30% of the total friction torque.

2.3.5 Output Flow Analysis

Due to the rotary valve's non-zero switching time, flow is bypassed through the relief or check valve during transition to limit pressure spikes. Consequently, the valve's normalized axial position does not correspond to the true duty ratio of the valve (i.e.

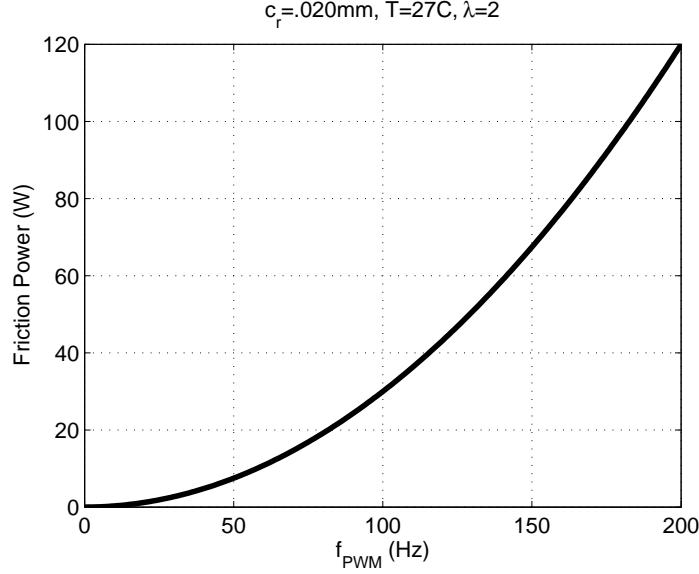


Figure 2.11: Power required to overcome viscous friction. A curve fit of the data yields $f(x) = .003x^2 - 4.8 \times 10^{-16}x + 1.7 \times 10^{-14}$ where $f(x)$ is friction power in W and x is the PWM frequency in Hz . Thus, friction power is essentially proportional to PWM frequency squared even when accounting for the additional effects of fluid recirculation.

50% travel does not equal 50% VVDP output flow). The two can be correlated by finding the volume of fluid bypassed through either the relief (Fig. 2.1(a)) or check valve (Fig. 2.1(b)) during transition. Using the approach and definitions found in Section 2.3.1 and integrating with respect to spool angle, the bypassed fluid volume for a single transition is:

$$V_{by} = \frac{1}{\omega} \int_{\Theta=0}^{\Theta=\Theta_{crit}} (Q_{in} - Q_i(\Theta)) d\Theta = \frac{Q_{in} R_w}{\omega D} \sqrt{\frac{P_{open}}{\Delta P}} \quad (2.38)$$

$Q_i(\Theta)$ is the flow through the rotary valve when the relief or check valve is open and ΔP is the critical angle pressure differential when the relief or check valve closes.

For the relief circuit (Fig. 2.1(a)), the volume of fluid bypassed during the two load transitions decreases the output flow of the system. On the other hand, the two tank transitions have no effect. Accounting for two load transitions and substituting $\Delta P = P_{relief} - P_{load}$, κ from Eq. (2.2), and multiplying by the PWM frequency, the

average flow bypassed is:

$$Q_{relief} = \kappa \frac{Q_{in}}{4} \sqrt{\frac{P_{open}}{P_{relief} - P_{load}}} \quad (2.39)$$

For the check circuit (Fig. 2.1(b)), the bypassed flow is ported to load regardless of whether the rotary valve is transitioning to load or tank. Therefore, the bypassed flow during the two tank transitions will increase the output flow. $\Delta P = P_{check} + P_{load}$ for the tank transitions and the average bypassed flow is:

$$Q_{check} = \kappa \frac{Q_{in}}{4} \sqrt{\frac{P_{open}}{P_{check} + P_{load}}} \quad (2.40)$$

As with the transition loss, the bypassed flow through the relief or check valve is independent of PWM frequency and dependent only on geometric and system parameters. Using Eqs. (2.39)-(2.40), the duty ratio (VVDP output flow fraction) with respect to the valve's normalized axial position z is:

$$s_{relief} = z - \frac{Q_{relief}}{Q_{in}} \quad (2.41)$$

$$s_{check} = z + \frac{Q_{check}}{Q_{in}} \quad (2.42)$$

For the prototype described in Table 2.1 and Section 2.5, $\frac{Q_{relief}}{Q_{in}} = 0.077$ and $\frac{Q_{check}}{Q_{in}} = 0.031$ at a load pressure of $6.9MPa$.

2.3.6 Trade Off and Design Summary

Several design trade offs exist that can be exploited to improve the rotary valve's efficiency. Using the geometric constraints that the sides of the rhombic inlets are parallel to the helical lands and the valve is critically lapped produces the equality $\frac{R_h}{R_w} = \frac{L}{\pi D/2N}$. Using this equality and substituting in κ and P_{open} from Eqs. (2.2) and (2.3) produces the constraint:

$$\kappa^2 \sqrt{P_{open}} = \frac{\sqrt{128\rho}Q_{in}}{\pi C_d DL} = \text{constant} \quad (2.43)$$

Equation (2.43) states that P_{open} and κ cannot decrease simultaneously for a fixed DL . However, since transition losses (Eqs. (2.17)-(2.18)) scale with $\kappa\sqrt{P_{open}}$, Eq. (2.43) suggests that κ should be increased in order to decrease $\kappa\sqrt{P_{open}}$.

Another trade off exists between spool velocity, spool size, leakage, and flow area (pressure drop). Making the simplifying assumption that $R_{in} \approx R_{out} \approx \frac{D}{2}$ in Eq. (2.30) yields:

$$\omega \propto \frac{c_r Q_{in}^2}{D} \left(\frac{1}{A_{in}} + \frac{1}{A_{out}} \right) \propto \frac{c_r Q_{in} \sqrt{\Delta P}}{D} \quad (2.44)$$

ΔP is the combined pressure drop across the inlet and outlet turbines based on their flow areas. Equation (2.44) shows that ω can be increased at the cost of throttling by increasing ΔP , at the cost of leakage by increasing c_r , or by reducing the spool's diameter D which reduces surface area and friction moment arm. Equations (2.43) and (2.44) suggest that the self-spinning velocity can be increased without a penalty in transition loss by increasing the spool length L in Eq. (2.43) to compensate for a decrease in diameter. An additional motive for decreasing D at high speeds, which was not derived explicitly in Section 2.3.2, is that the volume of the inlet pressure rail (shown in Fig. 2.3) scales with D , which accounts for a majority of the compressible inlet volume. Therefore, a smaller diameter spool has the additional benefit of decreasing compressibility losses, which are important at high PWM frequencies and load pressures.

Table 2.1 contains the geometric parameters describing the prototype valve and designs optimized for 15Hz and 75Hz PWM frequency at $P_{load} = 6.9MPa$ and $Q_{in} = 40lpm$ using the design equations derived in Sections 2.3.1-2.3.4 (see [47, 64] for details on the optimization method). A * after a parameter value indicates that the parameter is at the bound specified in the optimization. Note that the total compressible volume, V_{in} , is the volume in the sleeve, V_{sleeve} , plus one half of the pump displacement. As expected, the optimization algorithm drives $\kappa \rightarrow 1$ and L_s , the total spool length, to its upper bound while decreasing D as the desired PWM frequency is increased from 15Hz to 75Hz.

Table 2.2 contains a breakdown of the various forms of loss calculated using the design equations for the prototype and optimized valves. In both cases the transition loss is the dominant form of loss, accounting for as much as 77% of the total losses for the relief circuit and about 67% of the losses for the check circuit. Using the parameters from the optimization for 15Hz reduces all of the losses. Fully open losses no longer exist in the optimized case when $\kappa = 1$ because the spool is always in transition.

Table 2.1: 3-way self-spinning rotary valve parameters

	Prototype	Opt. 15Hz	Opt. 75Hz
D	25.4mm	31mm	17.8mm
L_s	98.0mm	127mm*	127mm*
R_w	3.7mm	8.1mm	4.7mm
R_h	6.5mm	13.3mm*	13.3mm*
L_1	3.2mm	2mm	1.6mm
NA_{in}	36.5mm ²	161.6mm ²	93.8mm ²
nA_{out}	140.5mm ²	120.0mm ²	93.6mm ²
P_{open}	.41MPa	.021MPa	.062MPa
P_{spool}	.205MPa	.081MPa	.318MPa
c_r	.025mm	.020mm	.023mm
κ	.56	1.0*	1.0*
V_{sleeve}	61cc	9.2cc	7.9cc
V_{in}	72.4cc	20.5cc	19.3cc

2.4 Dynamic System Model

A dynamic model of a self-spinning rotary valve based VVDP including the effects of the compressible inlet volume, accumulator, and transition/full open throttling is developed in this section. Several approximations are used to simplify the model: the accumulator gas is assumed to behave adiabatically, line losses are neglected, and the relief or check valve in the circuit opens instantaneously. The pressure drop across the spool, P_{spool} , is also assumed constant.

The VVDP is modeled with two states. The states include the inlet volume pressure P_{in} , governed by compressible oil dynamics, and the load pressure P_{load} , governed by accumulator gas dynamics. Using the definition of bulk modulus, the dynamics of the oil volume can be derived as:

$$\dot{P}_{in} = \frac{\beta(P_{in})}{V_{in}} Q_{vol} \quad (2.45)$$

V_{in} is the inlet volume and $\beta(P_{in})$ is the pressure dependent bulk modulus described by Eq. (2.19). Q_{vol} is the net flow into the inlet volume found by summing all of the input

Table 2.2: Breakdown of VVDP losses using the parameters $P_{load} = 6.9MPa$, $Q_{in} = 40lpm$, $r = .10$. Total output power is $4.6kW$.

	Prototype 15Hz	Opt. 15Hz
$\Pi_{trans,relief}$	1222W	567W
$\Pi_{trans,check}$	725W	368W
Π_{open}	179W	–
Π_{comp}	69W	20W
$\Pi_{leak} + \Pi_{leak,L1}$	113W	55W

and output flows to the volume (refer to Fig. 2.1):

$$Q_{vol} = Q_{in} - Q_{load} - Q_{tank} - Q_{relief} \quad (\text{Relief circuit}) \quad (2.46)$$

$$Q_{vol} = Q_{in} - Q_{load} - Q_{tank} - Q_{check} \quad (\text{Check circuit}) \quad (2.47)$$

The dynamics of the accumulator gas are derived from the ideal gas adiabatic compression equation:

$$\dot{P}_{load} = \gamma \frac{P_{load}^{(1+1/\gamma)}}{P_0^{1/\gamma} V_0} Q_{acc} \quad (2.48)$$

P_0 is the gas pre-charge pressure, V_0 is the initial gas volume, and $\gamma = 1.4$ (the ratio of specific heats for air and nitrogen). Q_{acc} is the net flow of oil into the accumulator (refer to Fig. 2.1):

$$Q_{acc} = Q_{load} - Q_{out} \quad (\text{Relief circuit}) \quad (2.49)$$

$$Q_{acc} = Q_{load} + Q_{check} - Q_{out} \quad (\text{Check circuit}) \quad (2.50)$$

Equations (2.45) and (2.48) are simulated using the Matlab/Simulink software package.

2.5 Experimental Hardware

The prototype rotary valve components (pump housing, valve sleeve, and spools) are shown in Fig. 2.12. The VVDP test stand, shown in Fig. 2.13, consists of a $5.6kW$ AC motor (B) driving a $22.8cc$ fixed-displacement vane pump (C) modified for use with the prototype rotary valve (D). The AC motor is controlled with a variable-frequency drive (A) for testing at different flow rates. Pressure sensors (E) and a cartridge relief or

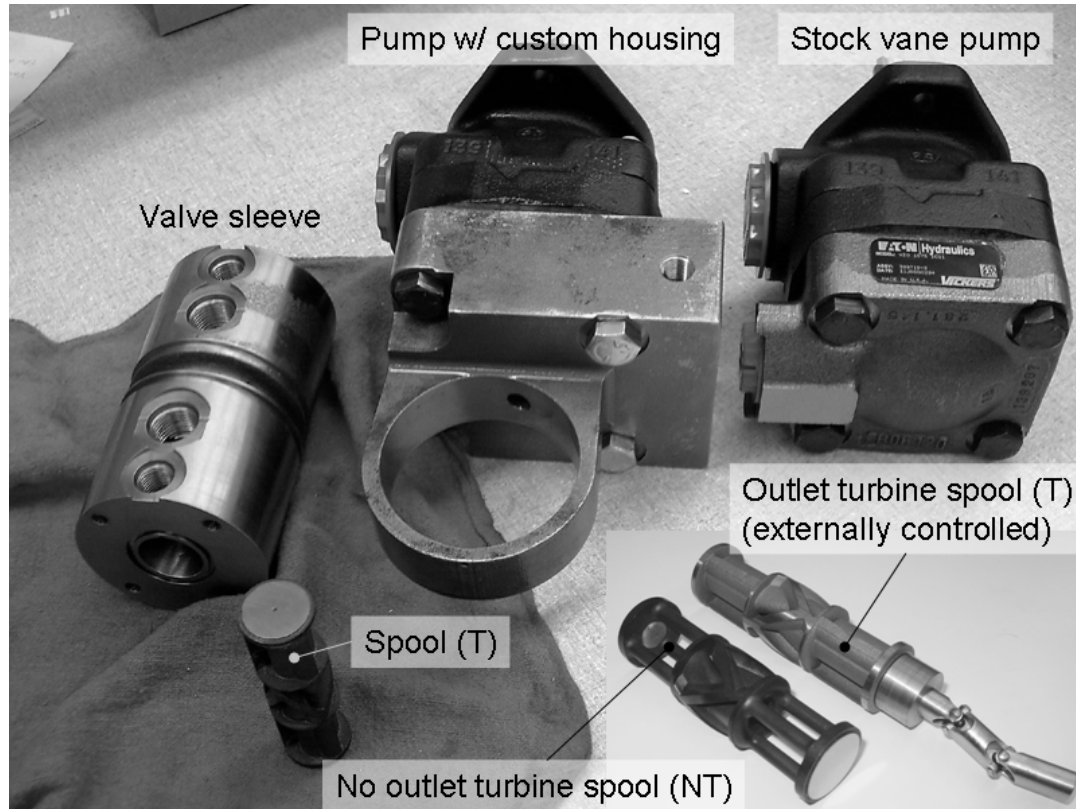


Figure 2.12: Prototype rotary valve hardware

check valve (F) are mounted on the sleeve. The sleeve contains two output ports. One port returns to tank (I). The other port (J) connects to a .16l diaphragm accumulator (G) pre-charged to $2.1MPa$, a flow meter (L), an oil filter (M), and a needle valve load (K). During self-spinning operation, a small gerotor pump (H) is used to control the spool's axial position. A special spool with shaft extension (see Fig. 2.12) is used to control the spool speed externally (N). This spool is used to characterize the valve at different PWM frequencies for a fixed flow rate. Mobile DTE 25 hydraulic oil is used in the test stand with $\rho = 876kg/m^3$ and $\mu = .0387Pa \cdot s$ ($38.7cP$) at $40C$. During operation, both the amplitude and characteristic of the sound produced by the VVDP resembles that of a motorcycle or lawn mower, depending on the PWM frequency.

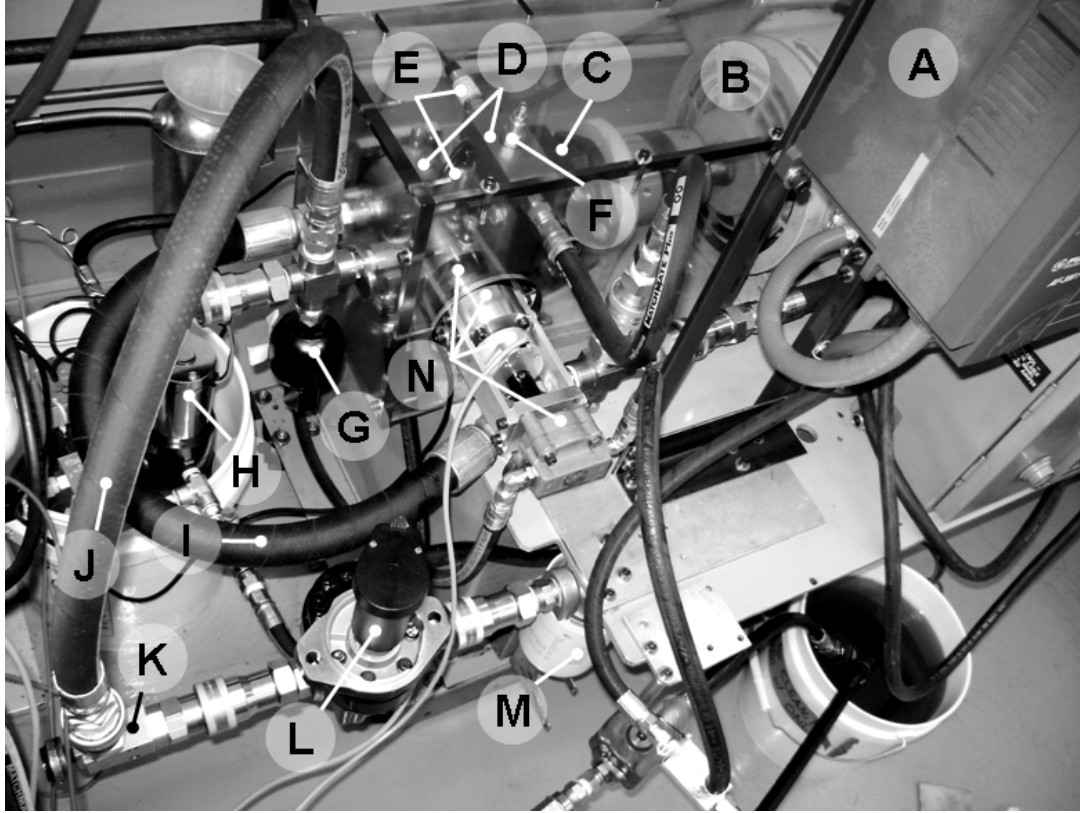


Figure 2.13: Prototype VVDP test stand

2.6 Simulation and Experimental Results

Experimental data was acquired while operating the rotary valve between $15\text{-}75\text{Hz}$ PWM frequency for a fixed axial position, load pressure, and input flow rate ($Q_{in} = 40\text{ lpm}$). $P_{relief} = 8.3\text{MPa}$ and $P_{check} = 1.4\text{MPa}$.⁴ Tests were run at a nominal oil temperature of 30°C with data sampled at 2kHz .

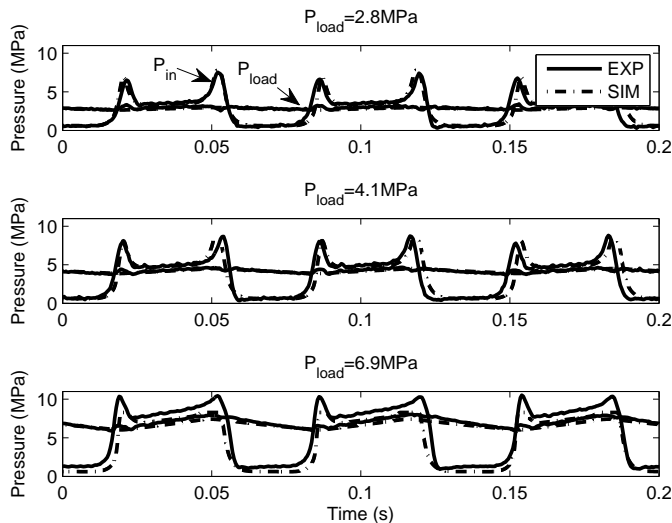


Figure 2.14: 15Hz pressure profiles: 50% travel

2.6.1 Pressure Profiles

Simulated and experimental pressure profiles are presented in Figs. 2.14-2.16. The simulated pressure profiles are matched to experimental data by tuning r , the fraction of entrained air. $r = 0.10$, or 10% air entrainment, was found to provide a reasonable match at 15Hz PWM frequency. While this level of air entrainment is higher than the typical 2%-7% seen in the literature [65] and via word of mouth in industry, it appears possible due to the test stand's unintentional poor reservoir design.⁵

Figure 2.14 shows good correlation between the simulation and experimental data at 15Hz PWM frequency for various load pressures at 50% travel. Spool underlap was included in the simulation after the discovery of an unintentional 26% underlap in the prototype. The underlap decreases the magnitude of the transition peak from load to tank providing a better overall match with the experimental data. The square-wave

⁴ P_{relief} is sized such that $P_{relief} = P_{load} + P_{check}$ at the maximum load pressure tested (6.9MPa). P_{check} is sized such that $P_{check} > P_{open} + P_{spool}$.

⁵ The test stand reservoir is unsealed, contains no baffling, and the return lines are not submerged and are located near the pump inlet. As a result, splashing occurs in the oil at the PWM frequency due to the tank line.

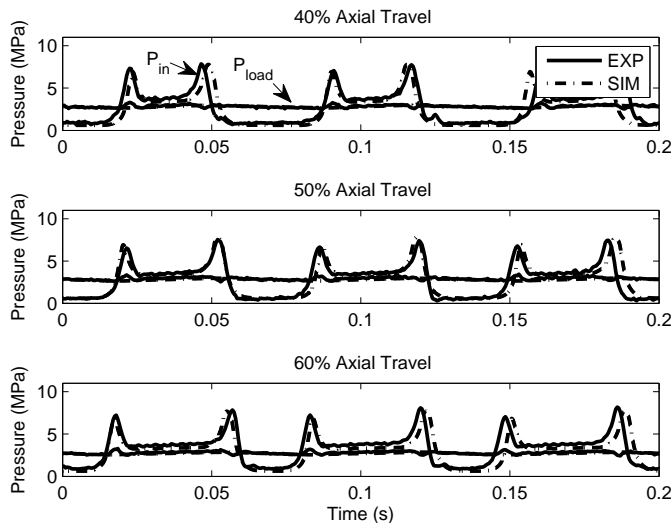


Figure 2.15: 15Hz pressure profiles: $P_{load} = 2.8MPa$

characteristic of P_{in} is clearly visible at 15Hz indicating that the rotary valve is pulsing the flow. Figure 2.14 also shows that the full open pressure drop across the valve spool and sleeve is $0.62MPa$ at 15Hz and $Q_{in} = 40lpm$ (with $P_{open} = 0.42MPa$ and $P_{spool} = 0.2MPa$). This is consistent with the prediction of $.61MPa$ from simulation and CFD. The variation of pulse width with axial position is shown in Fig. 2.15, thereby validating the helical land duty ratio concept.

At 75Hz PWM frequency (Fig. 2.16), more deviation arises between the simulation and experiment although a reasonable match is still achieved. More ripple is evident on the experimental inlet pressure when the on/off valve is connected to the load branch. This may be due to fluid inertia or water hammer effects, which are not modeled. The simulation is able to capture the increasing sluggishness of P_{in} due to compressibility at higher switching frequencies caused by the large inlet volume of the unoptimized prototype and the higher than usual air entrainment. This emphasizes the need for V_{in} to be small and the importance of proper reservoir design for efficient operation at high frequencies.

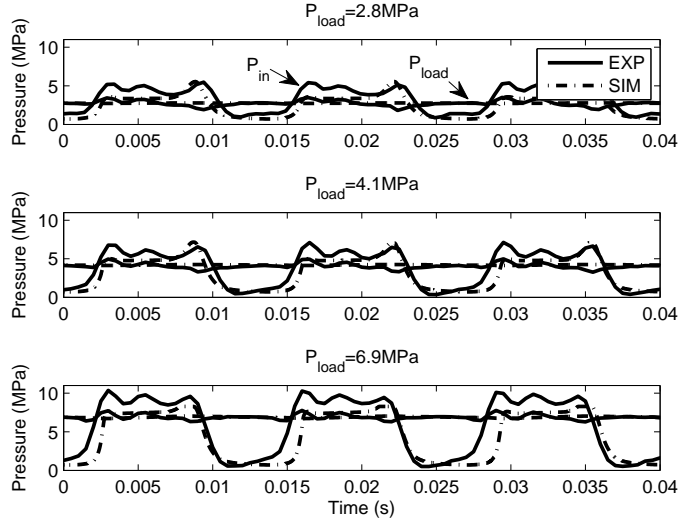


Figure 2.16: $75Hz$ pressure profiles: 50% travel

2.6.2 Self-spinning Validation

The self-spinning concept is validated by controlling the spool's axial position hydrostatically. Using this method, the spool is completely isolated from the sleeve and spun solely with fluid forces. Two spool designs, one with outlet turbines (labeled T in Fig. 2.12 corresponding to Eq. (2.30)), and one without (NT, corresponding to Eq. (2.32)), were tested along with several clearances. Figure 2.17 confirms that ω is proportional to Q_{in}^2 and compares the frequencies achieved experimentally with the prediction from the angular momentum analysis. A_{eff} (see Eq. (2.34)) was calculated with α_{in} and α_{out} based on a spool frequency of $25Hz$ using a correction factor of $\lambda = 2$ on these non-bearing surface area shear ratios. Numerical values of α_{in} and α_{out} are presented in Table 2.3 for different geometries and clearances. Friction due to fluid recirculation in the blade-less outlet section of the NT spool was found to be significant as including α_{out} produced a better match with the experiment (NT_{CALC} in Fig. 2.17).

Figure 2.17 reveals that the inlet turbine contributes a majority of the torque used to spin the spool. The NT spool spins on average 23% slower than a T spool of similar

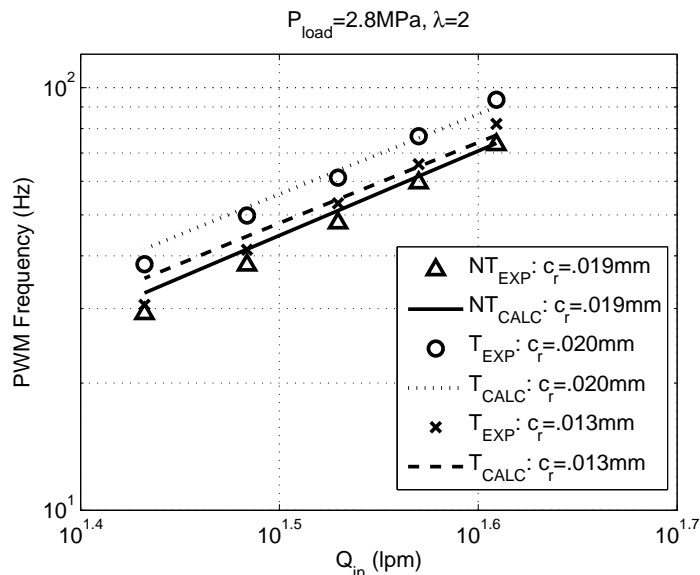


Figure 2.17: PWM frequency vs. Q_{in} (loglog)

clearance. Decreasing clearance has a similar effect. Between the loose clearance ($c_r = .020\text{mm}$) and tight clearance ($c_r = .013\text{mm}$) T spools, the tight clearance spool spins on average 15% slower. Additional experimental data shows that the PWM frequency is independent of axial position, with less than 15% variation in PWM frequency between normalized output flows of .4 to .7.

The corresponding friction (actuation) power estimate used to match the predicted and experimentally observed self-spinning speeds is shown in Fig. 2.18. Approximately 36W is required for 100Hz PWM frequency, 82W for 150Hz , and 143W for 200Hz . To put actuation power into context, the Sturman digital valve [27], with a flow area of 23mm^2 (compared to the rotary valve's 36.5mm^2), requires a fixed 1ms to switch while consuming $.7\text{J}/\text{switch}$. Assuming that the valve must switch twice per cycle, the Sturman valve consumes 140W at 100Hz , 210W at 150Hz , and 280W at 200Hz . Despite consuming nearly twice the amount of power as the rotary valve at 200Hz , the Sturman valve, with its fixed 1ms per switch, spends 40% of the total 5ms cycle time in transition at this frequency. The rotary valve, on the other hand, maintains a fixed ratio between transition time and PWM period which is determined by the valve's geometry.

Table 2.3: Ratio of shear stresses due to fluid recirculation between the spool’s helical lands and turbine structures. The ratio depends on spool section type and radial clearance. Refer to analysis in Section 2.3.4.

Spool Type	c_r	α_{in}	α_{out}
NT	.019mm	.054	.040
T	.020mm	.058	.042
T	.013mm	.036	.026

This property, combined with the reduced power consumption afforded by continuous rotation, enables the rotary valve to effectively operate at higher PWM frequencies compared to linear valves with fixed switching times that are constrained by actuator limitations.

2.6.3 Flow Modulation

Figure 2.19 compares the predicted, simulated, and experimental axial position/output flow relationship for both the relief (top) and check (bottom) circuits. In the relief circuit, increasing P_{load} decreases Q_{out} for a given axial position. Both the analysis and simulation show that as P_{load} approaches P_{relief} , the relief valve is open for a greater part of each cycle since P_{in} reaches P_{relief} earlier in the transition. At $P_{load} = 2.8MPa$, the simulation predicts that the relief valve is open for roughly 1.5ms while this time increases to 9ms when $P_{load} = 6.9MPa$.

In the check circuit, the duty ratio is greater than the corresponding normalized axial position z (i.e. $Q_{out} = sQ_{in} > zQ_{in}$) as predicted in Section 2.3.5, although only at low load pressure. The inconsistency at high load pressure is likely due to compressibility and valve underlap. Compressibility during the tank transitions causes the check valve to open later in the transition, thus leading to less flow bypassed to load. Valve underlap also decreases the flow to load by introducing a leakage path between load and tank.

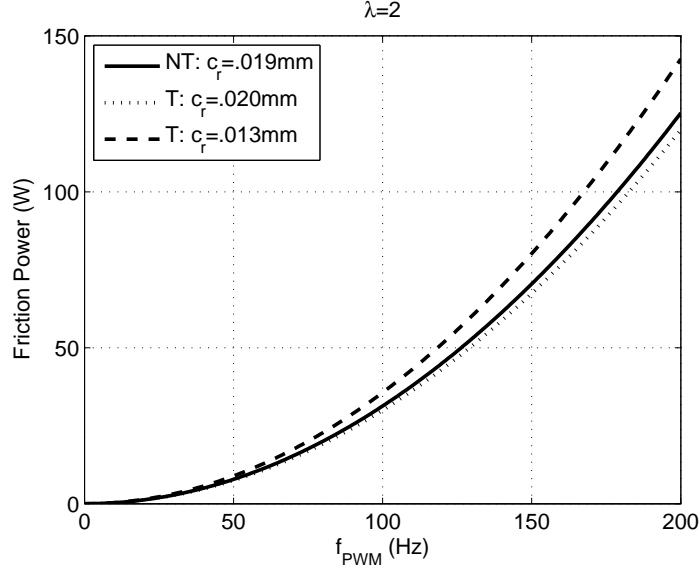


Figure 2.18: Estimated friction (actuation) power used to match self-spinning velocity predictions with test stand data in Fig. 2.17

2.6.4 Hydraulic Efficiency

The hydraulic efficiency of the rotary valve is calculated by comparing the input hydraulic power to the valve to the output hydraulic power of the system⁶ :

$$\eta = \frac{(\sum_{i=1}^n P_{load}(i)Q_{out}(i)\Delta t)/T_{avg}}{(\sum_{i=1}^n P_{in}(i)Q_{in}\Delta t)/T_{avg}} \quad (2.51)$$

$n = T_{avg}/\Delta t$ is the number of time steps over which the summation is performed. Experimental data is averaged over 10 seconds with $\Delta t = .5ms$ while simulation data is averaged over 1 second with $\Delta t = .01ms$. Since leakage is present in the measured flow, it is included in the simulation results. Pump efficiency, however, is not included.

Figures 2.20 and 2.21 compare the experimental and simulated VVDP efficiency at 15Hz PWM frequency with the characteristic efficiency of an equivalent bleed off system (Fig. 1.1(a)). A good match is observed between the experiment and the dynamic model (refer to Section 2.4). In contrast, the efficiency predicted by the analytical

⁶ Efficiency is given on an absolute scale (0-1) rather than percentages.

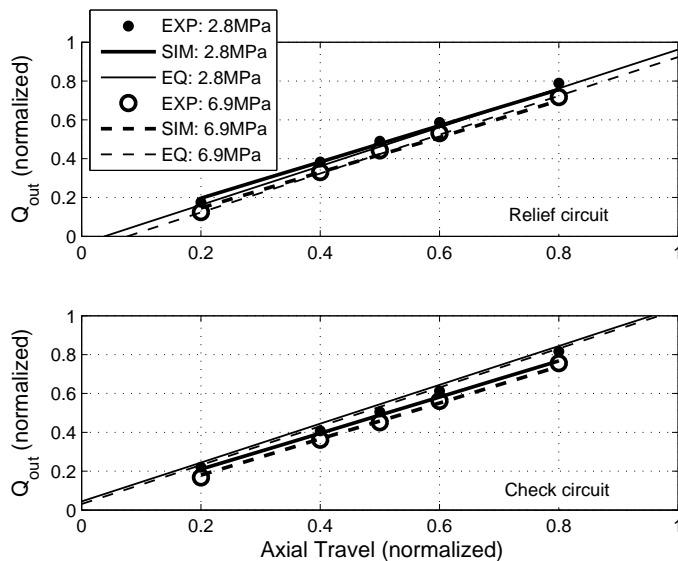


Figure 2.19: Output flow vs. axial position ($15Hz$)

design equations in Section 2.3 is noticeably lower for the relief circuit (Fig. 2.20). This is likely due to the dynamic coupling between compressibility and throttling that is not captured by the design equations, where the two are considered separately. In the actual system (and dynamic model), compressibility slows down the pressure dynamics, i.e. increases the rise and fall time of the inlet pressure during valve transition. Because incompressibility is assumed in the orifice equation used in the transition loss analysis (Section 2.3.1), the analysis predicts that the relief and check valves open sooner in the transition than they do when compressibility is included. Therefore, transition losses are over predicted in the relief circuit since the maximum throttling occurs at the relief pressure. In the check circuit, however, the throttling losses across the check valve are small so there is less impact on efficiency. At $15Hz$, the relief circuit exhibits up to 25% efficiency improvement over the bleed off system for high load pressures and displacements less than 70% (Fig. 2.20). At high displacements, the rotary valve is less efficient due to P_{open} and P_{spool} (see Section 2.3.1), which must be reduced to achieve high efficiency at high displacement. Full displacement efficiency can be further improved by eliminating the transition losses at full displacement in the prototype valve.

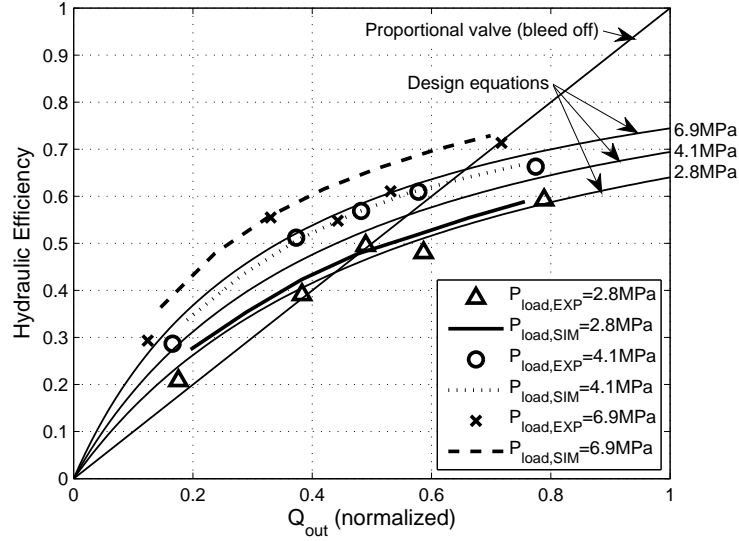


Figure 2.20: Efficiency at 15Hz: Relief

This can be done by increasing the length of the center section of the valve (L_{in} in Fig. 2.5) without modifying the helical lands.

By switching to the check valve configuration shown in Fig. 2.1(b), the efficiency can be further improved up to 5% across a full range of displacements and load pressures (Fig. 2.21). This increase in efficiency is accomplished by limiting transition throttling to $P_{check} + P_{load}$ and also by porting the pressurized bypass flow to load rather than tank. This configuration demonstrates higher efficiency than the proportional valve system for displacements under 75%.

The optimized curve in Fig. 2.21 projects the potential efficiency of the check circuit using the optimized geometry in Table 2.1. Other improvements include reducing the check valve cracking pressure and eliminating spool underlap. Using these enhancements, the simulation predicts up to 22% efficiency improvement including 84% efficiency at 50% displacement. Another 5%-10% improvement in efficiency can potentially be achieved with “soft-switching” (see [48, 49, 47]) which further reduces transition losses by providing an alternate flow path when the valve is opening or closing to tank. These two transitions are not decreased by the check circuit.

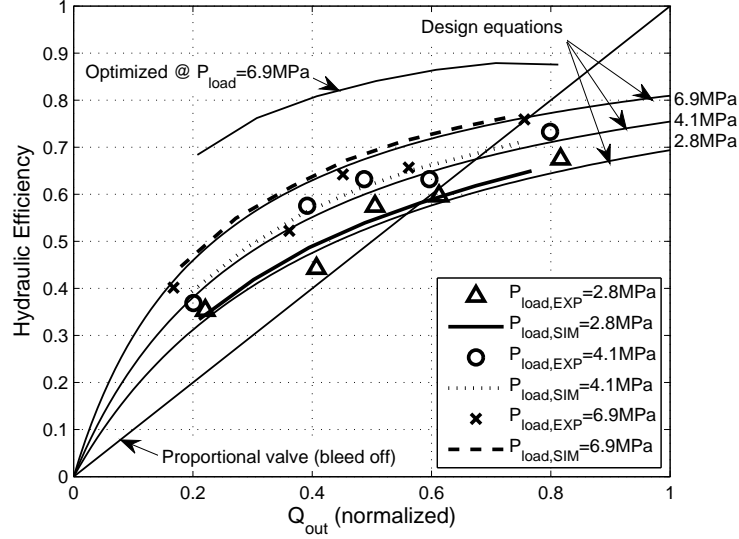


Figure 2.21: Efficiency at $15Hz$: Check

Upon increasing f_{PWM} from $15Hz$ to $75Hz$ (Fig. 2.22), there is more inconsistency between the experiment and simulation. This is due to model mismatch which is observed in the pressure profiles shown in Fig. 2.16. At $75Hz$, the VVDP is only marginally more efficient than the bleed off circuit at higher load pressures and low displacements due to fluid compressibility in the unoptimized prototype. Compressibility increases throttling as mentioned before by slowing the dynamic response of P_{in} such that it no longer transitions as sharply between load and tank pressure. The effect is even greater at high load pressure. If P_{load} is too high, P_{in} may be too sluggish to reach the intended low pressure fully off state. However, upon decreasing V_{in} from $72.4cc$ to $19.3cc$ using CFD [52, 56] and applying the check circuit (with appropriately sized cracking pressure) and optimized geometry, the efficiency of the VVDP can be improved by up to 27% across a full range of displacements at $75Hz$. The optimized simulation predicts an efficiency of 77% at 50% displacement.

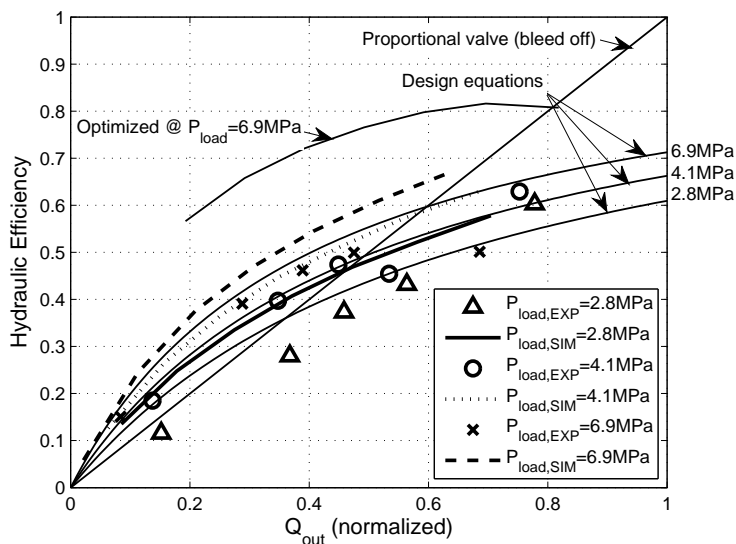


Figure 2.22: Efficiency at 75Hz: Relief

2.6.5 Volumetric Efficiency

The volumetric efficiency defined in this section is based on the leakage across the helical land of the rotary valve separating load pressure from tank (Section 2.3.3). Leakage across the end land (L_1) was not measured because it varies significantly depending on the axial positioning method used. Leakage across the helical land was measured experimentally by holding the spool position fixed with the inlet orifices fully open to load such that ΔP across the land was $P_{load} - P_{tank}$. Each test consisted of measuring the leakage for P_{load} between 1.4MPa-6.9MPa. Figure 2.23 provides a comparison between the measured leakage and the prediction from Eq. (2.22). The temperatures cited represent the average temperature over a single test. Leakage was measured to be within a factor of 3 of the prediction for oil temperatures up to 35C and the results indicate a strong dependence on oil temperature. For a system flow rate of $Q_{in} = 40\text{ lpm}$, Q_{leak} was roughly .5% for the tight clearance spool and less than 1.5% for the loose clearance. At $P_{load} = 6.9\text{ MPa}$, this corresponds to a volumetric efficiency greater than 98.5%.

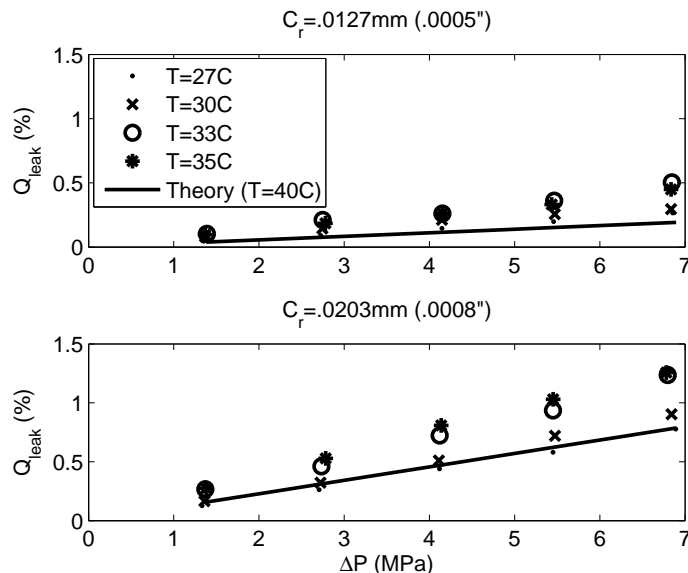


Figure 2.23: Leakage across helical land

2.7 Conclusions

A novel 3-way self-spinning rotary on/off valve designed for pulse-width-modulation of hydraulic flow has been presented in this chapter. A prototype valve based on the proposed design has simultaneously achieved high flow (40 lpm), low full open pressure drop ($.62\text{ MPa}$), high speed (100 Hz self-spinning PWM frequency with 2.8 ms transition time), and low actuation power (30 W). In comparison, a linear on/off valve with slightly smaller flow area consumes 140 W at 100 Hz . This confirms the presumption that actuation power can be reduced by employing continuous rotation to eliminate inertial switching forces. In addition, with self-spinning, the entire rotary actuation power is scavenged from fluid forces and no external rotary actuator is required.

A basic model of the valve suitable for design purposes and optimization has been developed. A two state dynamic model has also been developed and simulated. Both models have been validated by collecting experimental data from a prototype valve utilized in a virtually variable displacement pump. The design equations and dynamic model show good agreement with experimental data at 15 Hz PWM frequency. However,

as the frequency is raised to $75Hz$, the model shows less consistency with experimental data.

The mean output flow of the VVDP has been verified to exhibit a linear relationship with the rotary valve's axial position, thereby validating the helical land concept utilized in the spool. In addition, the self-spinning PWM frequency, predicted to be proportional to Q_{in}^2 , has been confirmed by experiment. A correction factor of 2 on the non-bearing surface area (predicted simplistically) is needed to achieve a good match between the model and the experimental results.

The prototype VVDP has demonstrated efficiency improvements in comparison to an equivalent bleed off system over a large range of displacements at $15Hz$ PWM frequency. At $75Hz$, compressibility negates any efficiency improvement due to the large $72.4cc$ inlet volume of the prototype valve. A CFD analysis of the valve has shown that the inlet volume can be realistically reduced to $19.3cc$ without a significant increase in throttling. Combining the reduced inlet volume with parameter optimization, the validated model predicts that an optimized VVDP at 50% displacement is able to achieve 84% efficiency at $15Hz$ and 77% efficiency at $75Hz$. Proper reservoir design can realistically decrease the entrained air to more common values (2%-7%) which would further improve efficiency.

One limitation of the 3-way self-spinning rotary valve is that it cannot be applied to pump/motors due to the unidirectional flow requirements of the self-spinning design, especially when four quadrant operation is desired (i.e. the ability to pump or motor bidirectionally). In addition, the analysis and design equations presented in this chapter do not provide any guidelines for the mechanical design of the rotary valve, which is important when higher operating pressures are desired. To address these shortcomings, a novel 4-way tandem self-spinning rotary valve is proposed in the following chapter to extend the self-spinning rotary valve concept to pump/motors. A case study is performed to explore the effectiveness of using the proposed 4-way valve in a four quadrant virtually variable displacement pump/motor in a real world application. The selected application is an input coupled power-split hydraulic hybrid passenger vehicle. In addition to using the 4-way valve as an application case study, the valve will also be used to illustrate a proposed design methodology for guiding the mechanical design of the valve for safe and robust operation at high pressures in the presence of cyclic loading.

Chapter 3

Extension of rotary valve to pump/motors and high pressure

The 3-way rotary valve for pump applications presented in Chapter 2 demonstrates that the helical land rotary valve and VVDP approach to displacement control have merit. However, limitations of the 3-way self-spinning valve to pumping (or motoring) only restricts the concept from being implemented in many hydraulic applications where multiple quadrants of operation are desired. This Chapter introduces a new 4-way tandem valve that extends the self-spinning valve concept to pump/motors. The speeder pump/motor of an input coupled power-split hydraulic hybrid passenger vehicle (HHPV) is chosen as a design case study for evaluating the functionality and efficiency of the valve and working through its detailed mechanical design. Section 3.1 provides an overview of the HHPV. Section 3.2 walks through the high level design process of the proposed virtually variable displacement pump/motor (VVDPM) that will be used to replace one of the variable displacement pump/motors on the HHPV. The synthesis of the required 4-way rotary valve is also discussed. Mechanical design considerations are outlined in Section 3.3 for safe high pressure operation. Updated geometric design and loss equations based on the approach used for analyzing the 3-way valve are presented in Section 3.4. A brief synopsis of the valve optimization results over the combined EPA Urban and Highway¹ drive cycles and rationale for migrating to an externally rotated

¹ Refer to work by Rannow [64, 47] for details regarding the optimization procedure.



Figure 3.1: Polaris Ranger hydraulic hybrid passenger vehicle test bed at the University of Minnesota based on an input coupled power-split drive train.

valve are described in Section 3.5. A dynamic model and simulation results of the 4-way valve are presented in Section 3.7 followed by an overview of prototype hardware and experimental results in Section 3.8. Conclusions regarding the 4-way valve are discussed in Section 3.9. The work presented in this chapter has been published in two conference papers [66, 67].

3.1 HHPV Application

Hybrid vehicles, which utilize two or more power sources for propulsion (typically an internal combustion engine (ICE) supplemented by a secondary source that enables energy storage), are becoming increasingly popular due to their improved fuel economy compared to conventional vehicles. The two most common types of hybrids today are electric hybrids (such as the Toyota Prius) and hydraulic hybrids (mainly larger service

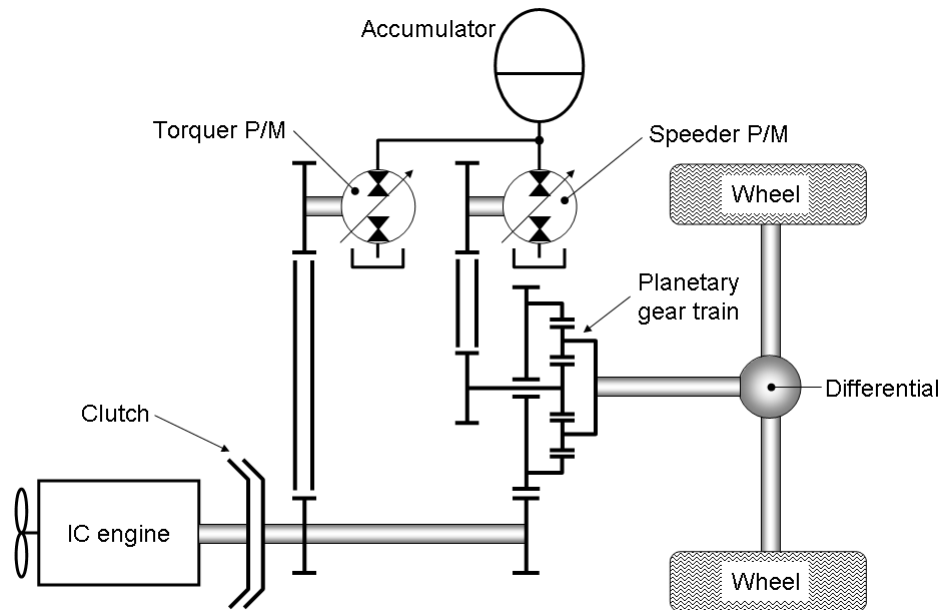


Figure 3.2: Schematic of Polaris Ranger input coupled power-split hydraulic hybrid passenger vehicle. Two variable displacement pump/motors enable full engine management: the torquer, connected to the engine via a fixed ratio, controls the engine torque. The speeder, connected to the engine and wheel via a planetary gearset, decouples the engine speed from the wheel speed.

vehicles such as buses and trucks). Hybridization improves vehicle efficiency primarily by 1) running the ICE at its most efficient operating point (speed and torque) by using the secondary power source to supply or absorb instantaneous demands, 2) downsizing the ICE for nominal loads with the secondary source accommodating peak loads, 3) recapturing and storing energy during braking, and 4) shutting the ICE off whenever possible and driving the vehicle with the secondary source alone. Electric hybrids, to date, have dominated the passenger vehicle segment due to the higher energy storage density of batteries compared to hydraulic accumulators as well as the higher efficiency of electric motor/generators compared to their hydraulic counterparts. Plug-in electric vehicles may have also contributed to the momentum in electric hybrids. However, the low power density of electric systems (approximately an order of magnitude lower than hydraulics [68]) limits energy recovery during braking and also limits performance.

In addition, state-of-the-art batteries and motor/generators are costly, battery performance is affected by temperature, and electric drives do not have the time tested ruggedness of hydraulics systems that have been proven on mobile construction and agricultural equipment.

The Center for Compact and Efficient Fluid Power (CCEFP), an engineering research center established by the National Science Foundation in June 2006, is investigating the viability of scaling down hydraulic hybrid power trains to passenger sized vehicles. Projects include efforts to improve the energy density of hydraulic energy storage (accumulators), improve component efficiency, and explore new avenues of advancing fluid power such as engineered fluids and surface texturing.² The technologies developed by the CCEFP are demonstrated on test beds, one of which is a hydraulic hybrid passenger vehicle (HHPV) based on a Polaris Ranger utility vehicle (shown in Fig. 3.1). Switched-mode hydraulic systems and components, such as the VVDP presented in Chapter 2, are planned for integration on the Ranger test bed and have the potential of making HHPVs practical and competitive with electric hybrids by making use of simple, compact, rugged, and low cost fixed displacement hydraulic components.

The HHPV test bed (Fig. 3.1) is an input coupled power-split hydraulic hybrid.³ A schematic of the vehicle's power train is presented in Fig. 3.2. The Ranger features two variable displacement hydraulic pump/motors (P/M), labeled torquer and speeder in Fig. 3.2, which enable full engine management. The torquer is connected to the engine via a fixed ratio and is used to manipulate the engine torque. The speeder is connected to the engine and wheels via a planetary gearset and is used to decouple the engine speed from the wheel speed. The ability to control the engine's torque and speed independently of the requirements at the wheels allows the engine to be run at its most efficient operating point at all times. As a design case study, this chapter will explore replacing the speeder, currently a variable displacement bent axis machine, with a virtually variable displacement pump/motor (VVDPM) consisting of a fixed displacement bent axis P/M and a rotary on/off valve. The proposed VVDPM and rotary valve are introduced next in Section 3.2.

² Please refer to www.ccefp.org for more information regarding the CCEFP and its research projects.

³ Refer to [68, 69, 70, 71, 72, 73] for details regarding the CCEFP HHPV test bed.

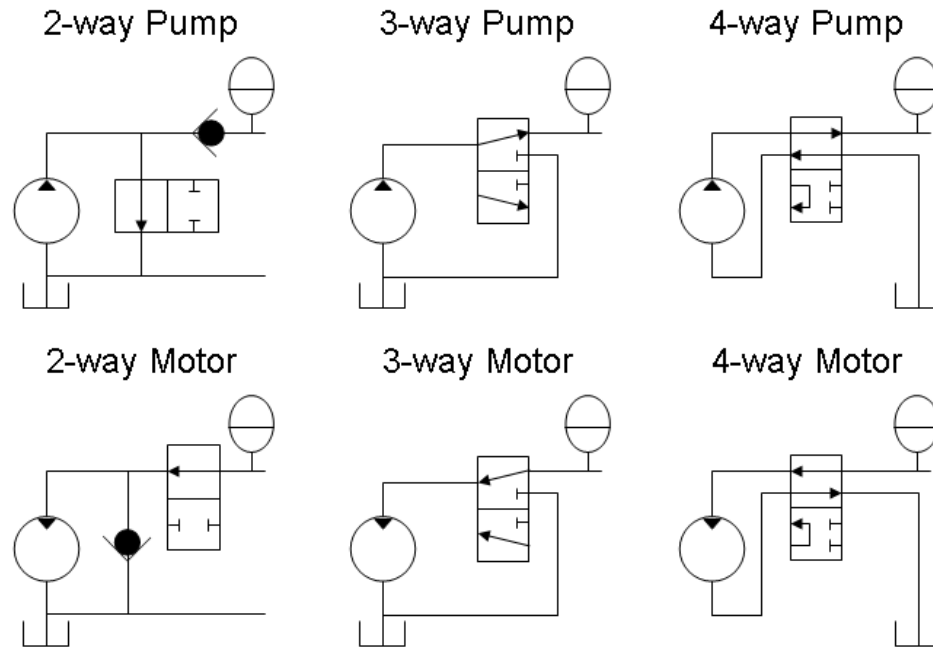


Figure 3.3: Switched-mode pumping and motoring configurations based on 2-way, 3-way, and 4-way on/off valves. Other configurations are possible. Note: check valves for preventing cavitation and reducing transition pressure spikes are not included in these circuit diagrams.

3.2 Proposed VVDPM and Rotary Valve Concept

Switched-mode control of pumping and motoring can be accomplished via a number of configurations based on 2-way, 3-way, or 4-way on/off valves. A selection of example circuits are shown in Fig. 3.3. The design requirements of the VVDPM and the rotary valve that will control it are:

1. The VVDPM must utilize a single on/off valve for both pumping and motoring.
2. The rotary valve must have self-spinning functionality.⁴
3. The VVDPM must be capable of four quadrant operation (bidirectional pumping and motoring).

⁴ The self-spinning requirement was eventually relaxed due to much lower efficiencies compared to externally rotating the valve. See Section 3.5 for details.

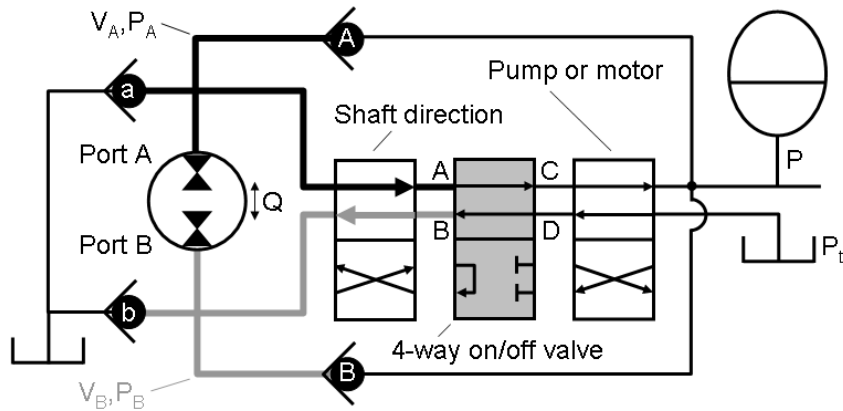


Figure 3.4: Proposed VVDPM utilizing a 4-way tandem on/off control valve. One 4-way directional valve is needed to enable self-spinning by rectifying the flow direction when switching between pumping and motoring. The other is needed for four quadrant operation by controlling the shaft direction of the pump/motor. Check valves a and b prevent cavitation. Check valves A and B reduce pressure spikes when the on/off valve or directional valves are switching. V_A , corresponding to the bold black fluid volume between Port A of the pump/motor and on/off valve, represents the switched volume. P_A is the corresponding pressure in V_A . The volume associated with Port B of the pump/motor is similarly represented by the bold gray lines in the schematic.

The first requirement (single on/off valve) simplifies the device and reduces cost and size. From Fig. 3.3, this eliminates the 2-way configurations due to the difference in location of the valve between the pump and motor circuits. The second requirement (self-spinning) reduces the need for an additional rotary actuator. However, it constrains the flow through the valve to be unidirectional, i.e. inlet and outlet sections of the valve must be consistent between pumping and motoring. Figure 3.3 shows that the 3-way configuration is incompatible with this constraint, since one inlet and two outlets are required for pumping while the opposite is required for motoring. For the 4-way valve circuit, the addition of a 4-way directional valve between the on/off valve and system accumulator and tank enables self-spinning by rectifying the flow direction. The final requirement (four quadrant) is achieved with any of the valve configurations by adding a 4-way directional valve between the pump/motor and on/off valve to enable bidirectional shaft rotation. The final 4-way on/off valve based VVDPM circuit is presented in Fig. 3.4.

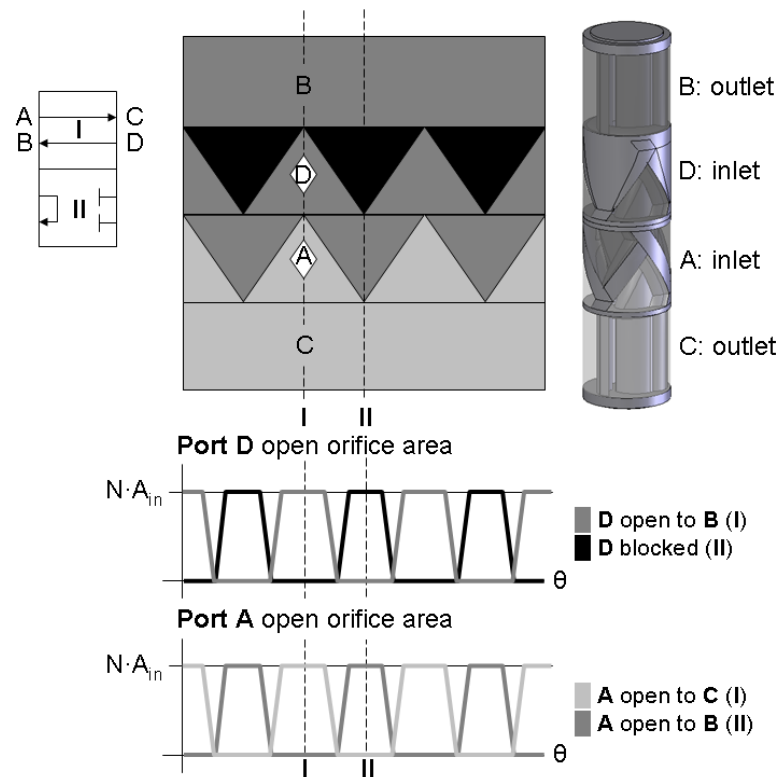


Figure 3.5: Top: 4-way tandem helical rotary valve concept. Bottom: Open area profiles illustrating when Port D is connected to Port B or blocked and when Port A is connected to Port C or B .

An embodiment of the rotary valve that achieves the desired 4-way tandem functionality is illustrated in Fig. 3.5. In comparison to the 3-way valve described in Chapter 2 (see Fig. 2.4), the 4-way valve includes an additional 2-way helical inlet spool section associated with Port D in Fig. 3.5. This section is synchronized to switch in phase with the inlet section corresponding to Port A . This 2-way section either ports flow from Port D to the center of the spool similar to the 3-way valve (Position I), or blocks flow from Port D (Position II). The 2-way inlet section differs from the 3-way section in that a through hole along the axis of rotation allows flow to exit the section axially in either direction, or allows pure axial flow to pass through.

Like-colored sections of the valve (dark gray, light gray) are internally connected. In Position I, the spool connects Port D to Port B via the dark gray flow path. Similarly,

Port *A* is connected to Port *C* by the light gray flow path. In Position II, Port *D* becomes blocked by the solid section of the spool (black sections in Fig. 3.5). Port *A* becomes connected with Port *B* by the dark gray flow path via the axial through hole in the 2-way section. Port *C*, having been disconnected from Port *A*, remains unconnected.

Remarks:

1. Self-spinning is attained at the cost of additional throttling due to the requirement of using a 4-way on/off valve instead of a 3-way valve. As seen in Fig. 3.3, the fluid must pass through the 4-way valve twice (inlet and outlet side of the pump/motor) in comparison to a 3-way valve which only meters the flow once.
2. A side benefit of the 4-way valve, other than self-spinning, is that the decompressing fluid in the switched volume when pumping is ported to the inlet of the pump instead of being dumped to tank. Thus, the energy in the fluid is used to do useful work instead of being lost.
3. The rotary valve embodiment of the 4-way tandem configuration was discovered by recognizing that the inlet and outlet ports of the pump/motor needed to switch in phase. This led to the realization that a second helical section was required. The choice of a 2-way section was motivated by the need to block Port *D* when the valve is in Position II.

3.3 Mechanical Design for High Pressure

The VVDPM is designed for an operating pressure of 21MPa . This pressure is dictated by the HHPV and is considerably higher than the 6.9MPa pressure used in the 3-way valve test stand. As pressure increases, fatigue becomes more of a concern due to the high cycle nature of PWM, especially at high frequencies. Because the spool geometry is complex and failure of the spool presents minimal danger as it is housed in the sleeve, the analysis presented will cover the sleeve only. Additionally, in some valve configurations (such as the 3-way), the pressures in the spool are unchanging and the spool itself does not experience cyclic loading.

Illustrated in Fig. 3.6 are two potential areas of concern. The first concern involves the inlet nozzles, which are essentially cross-holes that create a stress concentration in

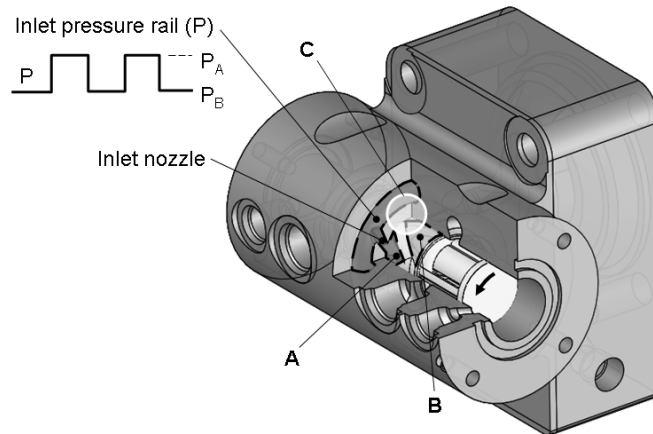
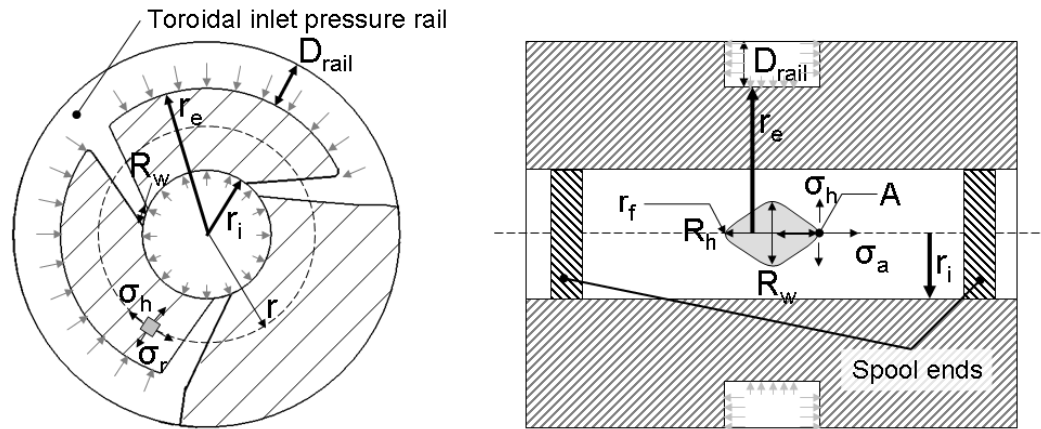


Figure 3.6: Cyclic pressure loading on the valve sleeve occurs due to the switching nature of PWM. The pressure in the inlet rail is continuously switching between P_A and P_B as the valve spool rotates. One area of concern is the inlet nozzle, essentially a cross-hole, which introduces a stress concentration in the sleeve that is then repeatedly pressurized and depressurized. Another area of concern, labeled **C**, is effectively a thick-walled pressure vessel that switches between external pressure loading (**A** = high pressure) and internal pressure loading (**B** = high pressure).

the sleeve. The nozzles are repeatedly pressurized and depressurized. However, the regions of the sleeve neighboring the nozzles do not experience pressure vessel type loading when the valve is fully open. This is because the inner and outer diameters of the sleeve in these regions are nominally at the same pressure since the pressure drop across the nozzle is small compared to the working pressure differential of the valve (about 2 orders of magnitude smaller). During transition, however, external pressure loading scenarios are possible since the pressure drop across the valve can be large as it is opening and closing. Thus, the pressure in the inlet rail can be much higher than the pressure at the bore of the sleeve. Conversely, it is unlikely that the pressure at the sleeve's bore will exceed the pressure in the inlet rail given the direction of fluid flow. Therefore, internal pressure scenarios are improbable.

The regions of the sleeve away from the nozzles (labeled **C** in Fig. 3.6) consistently experience pressure vessel type stresses. Here, the loading scenario switches continuously between external pressure loads (when **A** is high pressure) and internal pressure loads (when **B** is high pressure).



(a) Cross section view of valve sleeve showing orientation of stresses.

(b) Side cross section view of valve sleeve showing the rhombic geometry where the inlet nozzle intersects the sleeve's bore. r_f is the fillet radius at Point A.

Figure 3.7: Schematic of thick-walled pressure vessel representation of the valve sleeve showing variable definitions used in the Stress-Life analysis.

Not accounting for stress risers, the switching load condition between external pressure and internal pressure at **C** is more problematic than the load case at the nozzles between external pressure and equalized pressure. This is due to the compressive nature of external pressure stresses combined with the ability to reduce the magnitude of the stresses by reducing the bore diameter of the sleeve. The external pressure to internal pressure case is more restrictive on the design due to the need to address two load cases. The approach taken in this section to size the sleeve for fatigue will be conservative and will apply the stress concentration at the nozzles to the more limiting external to internal pressure loading scenario encountered in region **C**. A review of the literature is conducted in the next section to devise a strategy for modeling the stress concentration in the sleeve.

3.3.1 Review of Stress Concentration Factors

An examination of the literature provided several methods of evaluating stress risers in pressure vessels with cross-holes. A simple analytical model, proposed by Morrison et

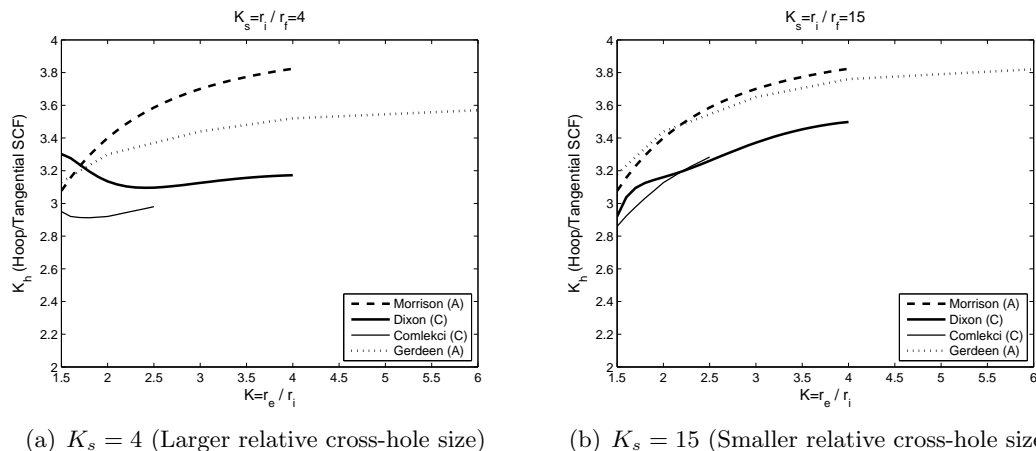


Figure 3.8: Comparison of hoop (tangential) stress concentration factors between several models for a closed-ended thick-walled cylinder with circular cross-hole. (A) denotes an analytical model whereas (C) denotes a computational model. Results from Gerdeen are estimated based on a figure within the paper.

al. [74], models cross-holes as thick-walled pressure vessels perpendicular to the axis of the main cylinder. The stresses where the cross-hole intersects with the cylinder bore are superimposed onto the stresses of the main cylinder. The authors also apply a stress concentration to the main cylinder by using the factor for a hole in an infinite plate subject to uniaxial loads. The analysis determined that the SCF for the Von Mises (Maxwell) equivalent stress in the cylinder was $\frac{5}{\sqrt{3}}$ and independent of the wall thickness ratio $K = \frac{r_e}{r_i}$ (refer to Fig. 3.7, ratio is $K = \frac{b}{a}$ in the paper). This is due to the assumption that the cross-hole diameter is small compared to the inner diameter of the cylinder. Gerdeen [75] proposed a more elaborate analytical model that included shear effects as well as accounting for stresses due to material removal at the cross-hole. This relaxed the small cross-hole diameter assumption used in Morrison's analysis. A figure presented in the paper for hoop SCFs shows that the SCF increases for smaller cross-hole diameters given a fixed cylinder bore diameter. Extrapolating the figure suggests that the minimum SCF is obtained when the cross-hole diameter is equal to the main bore diameter. Figure 3.8 compares the hoop SCF between the model proposed by Morrison

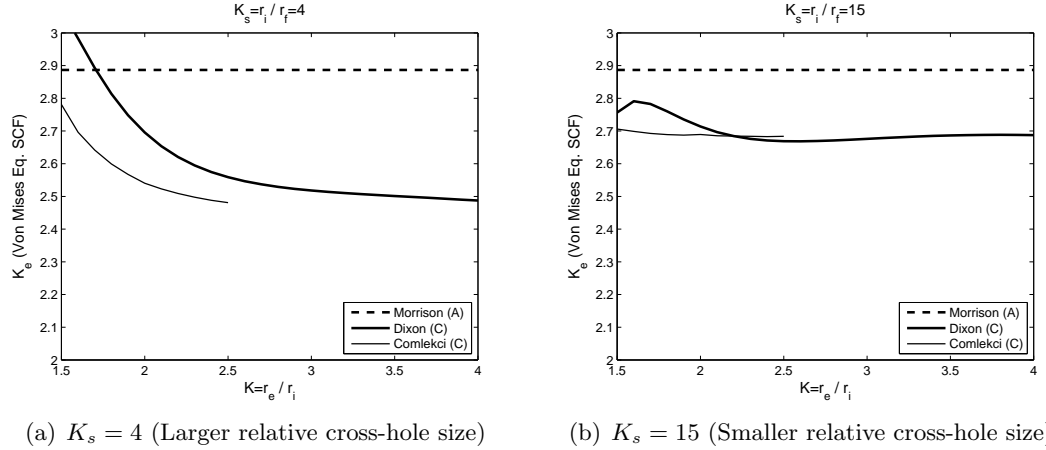


Figure 3.9: Comparison of Von Mises equivalent stress concentration factors between several models for a closed-ended thick-walled cylinder with circular cross-hole. The values presented here are based off of the hoop stress concentration factors presented in Fig. 3.8. (A) denotes an analytical model whereas (C) denotes a computational model.

and the one by Gerdeen and shows the two models converging for small relative cross-holes ($K_s = 15$). This is expected due to Morrison's small cross-hole assumption.

More recent studies have utilized finite element methods to determine SCFs. Dixon et al. [76] used this approach to model closed-ended cylindrical and square block pressure vessels with cross-holes. Sharp corners at the intersection of the hole and main bore are used. The paper presents plots of hoop SCFs derived from finite element results and provides curve fit equations as well. Figure 3.8 compares the curve fits from [76] to results from similar studies found in the literature. While the analytical models predict that the hoop SCF monotonically increases with the diameter ratio K , the finite element results predict a different trend. The behavior also changes depending on whether the cross-hole is large or small. The authors note the discrepancy with Gerdeen's model, however, they do not offer any explanations. A similar finite element study was performed by Comlekci et al. [77]. The study found that the maximum stress generally occurred on the cross-hole surface slightly away from the intersection with the main bore. Simulation results also showed that as the cross-hole diameter increased, the maximum stress decreased and moved toward the intersection point with the two

intersecting when $K_s = 4$. The authors attribute this trend to the inclusion of Poisson's ratio in the analysis. In general, it appears the two computational models begin to converge as the wall thickness of the vessel increases (i.e. higher values of K) as shown in Fig. 3.8.

Figure 3.9 presents the corresponding Von Mises equivalent SCFs based on the hoop SCFs (K_h) shown in Fig. 3.8. The Von Mises SCFs are derived based on the simple analysis performed by Morrison et al. [74] where the hoop SCF is applied to the stresses at the cross-hole. The Von Mises equivalent stresses for the vessel with and without the cross-hole are computed and the SCF, K_e , is obtained by their ratio [75]:

$$K_e = \frac{\sqrt{3}}{3K^2} [K_h(K^2 + 1) + (K^2 - 1)] \quad (3.1)$$

The key finding of this review is exemplified in Fig. 3.9: for thick-walled pressure vessels, the simple model proposed by Morrison provides an upper bound on the Von Mises equivalent SCF with $K_e = \frac{5}{\sqrt{3}} \approx 2.9$. This upper bound is further solidified by studies showing that offsetting the cross-holes from the main bore axis (i.e. making the cross-holes tangential akin to the nozzles) greatly reduces the SCF and improves the fatigue life of the part [78, 79]. While Morrison's analysis only considered the case of a closed-ended pressure vessel with the cross-hole exposed to system pressure, the analysis approach will be adopted and expanded to determine the stresses in the valve sleeve at the inlet nozzles. The key difference will be accounting for both internal and external pressure loading.

3.3.2 Stress-Life Analysis

The sleeve is designed for infinite life using the Stress-Life method described by Norton [80]. Refer to Fig. 3.7 for variable definitions. The location of interest is at the intersection point of the sleeve's ID with the inlet nozzle at the fillet radius r_f corresponding to the rhombus height R_h . This location, marked as point A in Fig. 3.7(b), will encounter magnified hoop or tangential stresses due to the cross-hole. The stresses at A will be characterized by the analytical approach described by Morrison et al. [74]. Note that the sleeve resembles an open-ended pressure vessel since the spool ends support all axial pressure. Beginning with the internal pressure case where the bore of the sleeve is at system pressure P and the toroidal inlet rail and nozzles are at tank pressure (assumed

to be zero for simplicity), the stresses in the absence of the nozzle are (as derived by Lamé in 1833 [81]):

$$\sigma_{ri} = \frac{Pr_i^2}{r_e^2 - r_i^2} \left[1 - \frac{r_e^2}{r_i^2} \right] = -P \quad (\text{Radial, internal no hole}) \quad (3.2)$$

$$\sigma_{hi} = \frac{Pr_i^2}{r_e^2 - r_i^2} \left[1 + \frac{r_e^2}{r_i^2} \right] = P \frac{K^2 + 1}{K^2 - 1} \quad (\text{Hoop, internal no hole}) \quad (3.3)$$

$$\sigma_{ai} = 0 \quad (\text{Axial, internal no hole}) \quad (3.4)$$

where $K = \frac{r_e}{r_i}$ is the wall thickness ratio. The nozzle is approximated as a circle with radius equivalent to the fillet radius (r_f) at the rhombus edge. Morrison et al. [74] describes applying the stress concentration factor for a hole in a flat plate subject to uniaxial stress as an approximation for the cross-hole: the hoop stress σ_{hi} will contribute $3\sigma_{hi}$ to the hoop stress in the presence of the hole and the axial stress σ_{ai} will contribute $-\sigma_{ai}$ to the hoop stress (see Young [82] for a comprehensive list of standard SCFs). The radial stress σ_{ri} at A will remain unaffected by the hole. Also, since the hole is at tank pressure, any axial stress σ_{ai} is relieved (i.e. for closed-ended cylinders). Therefore, the overall stresses due to internal pressure are:

$$\bar{\sigma}_{ri} = \sigma_{ri} = -P \quad (\text{Radial, internal total}) \quad (3.5)$$

$$\bar{\sigma}_{hi} = 3\sigma_{hi} - \sigma_{ai} = 3P \frac{K^2 + 1}{K^2 - 1} \quad (\text{Hoop, internal total}) \quad (3.6)$$

$$\bar{\sigma}_{ai} = 0 \quad (\text{Axial, internal total}) \quad (3.7)$$

Now consider the external pressure case where the bore of the sleeve is at tank pressure and the toroidal inlet rail and nozzles are at the system pressure P . The stresses in the absence of the nozzle are [81]:

$$\sigma_{re} = -\frac{Pr_e^2}{r_e^2 - r_i^2} \left[1 - \frac{r_i^2}{r_e^2} \right] = 0 \quad (\text{Radial, external no hole}) \quad (3.8)$$

$$\sigma_{he} = -\frac{Pr_e^2}{r_e^2 - r_i^2} \left[1 + \frac{r_i^2}{r_e^2} \right] = -2P \frac{K^2}{K^2 - 1} \quad (\text{Hoop, external no hole}) \quad (3.9)$$

$$\sigma_{ae} = P \frac{D_{rail}^2 + 2D_{rail}r_e}{r_e^2 - r_i^2} \quad (\text{Axial, external no hole}) \quad (3.10)$$

The axial stress component is due to the toroidal pressure rail (essentially a groove, see Fig. 3.7(b)) with the simplifying assumption that the rail wraps around the entire

circumference of the sleeve. In addition to the flat plate SCF that was applied in the internal pressure case, there are additional components due to pressure in the nozzle. These are modeled by representing the nozzle as a thick walled pressure vessel with wall ratio $K_s = r_i/r_f$ subject to internal pressure [74]:

$$\sigma_{rn} = -P \quad (\text{Radial, nozzle}) \quad (3.11)$$

$$\sigma_{hn} = P \frac{K_s^2 + 1}{K_s^2 - 1} \approx P \quad (\text{Hoop, nozzle}) \quad (3.12)$$

$$\sigma_{an} = 0 \quad (\text{Axial, nozzle}) \quad (3.13)$$

Since the fillet radius is typically much smaller than the spool radius ($r_f \ll r_i$), the hoop stress can be simplified with the assumption that $K_s \gg 1$. A fillet radius on the order of 1mm is typical. Relative to the main bore of the sleeve at point A , the radial stress of the nozzle σ_{rn} becomes an axial stress, the hoop stress σ_{hn} remains a hoop stress, and the axial stress σ_{an} becomes a radial stress. Combining these with the flat plate contributions from before, the overall stresses due to external pressure are:

$$\bar{\sigma}_{re} = \sigma_{re} + \sigma_{an} = 0 \quad (\text{Radial, external total}) \quad (3.14)$$

$$\bar{\sigma}_{he} = 3\sigma_{he} - \sigma_{ae} + \sigma_{hn} = P \left[\frac{-5K^2 - 1}{K^2 - 1} - \frac{D_{rail}^2 + 2D_{rail}r_e}{r_e^2 - r_i^2} \right] \quad (\text{Hoop, external total}) \quad (3.15)$$

$$\bar{\sigma}_{ae} = \sigma_{rn} = -P \quad (\text{Axial, external total}) \quad (3.16)$$

Note that the contribution of the axial stress σ_{ae} to the overall axial stress $\bar{\sigma}_{ae}$ is relieved by the presence of the nozzle. The overall internal and external pressure stresses in the presence of the nozzle are used to determine mean and alternating component stresses (radial, hoop, and axial) for use in the Stress-Life analysis. Mean (σ_m) and alternating (σ_a) stresses are defined as:

$$\sigma_m = \frac{\sigma_{max} + \sigma_{min}}{2} \quad (3.17)$$

$$\sigma_a = \frac{\sigma_{max} - \sigma_{min}}{2} \quad (3.18)$$

σ_{max} and σ_{min} are the maximum and minimum values of the stress type under consideration, i.e. radial, hoop, or axial. The resulting Von Mises equivalent mean and alternating stresses are:

$$\sigma_{eq,*} = \sqrt{\sigma_{r,*}^2 + \sigma_{h,*}^2 + \sigma_{a,*}^2 - \sigma_{r,*}\sigma_{h,*} - \sigma_{r,*}\sigma_{a,*} - \sigma_{h,*}\sigma_{a,*}} \quad (3.19)$$

* $\in [m, a]$ refers to the mean or alternating component.

The fatigue safety factor is found by plotting the Von Mises equivalent stresses on a Modified-Goodman Diagram with the applicable corrected endurance limit assuming the ratio $\frac{\sigma_{eq,a}}{\sigma_{eq,m}}$ is constant. A reliability of 99.99% ($C_{reliab} = .702$) is used. Notch sensitivity is neglected to insure that the safety factors determined are sufficiently conservative. Results for 1020 and 4140 steel at 21MPa load pressure are plotted in Fig. 3.10 with respect to the outer to inner radius ratio K . The analysis predicts that 1020 steel will not provide sufficient strength for infinite fatigue life regardless of the sleeve's wall thickness. The peak safety factor for 1020 is .96 with the factor reaching a plateau around $K = 5$. The plateau when K is large, i.e. $r_e \gg r_i$, arises because although most of the stresses become small with a thicker wall, the tangential stress due to external pressure approaches a constant. The analysis, however, predicts that 4140 steel will provide a sufficient safety factor even for relatively thin walls with a safety factor of 1 at $K = 1.4$, 1.5 at $K = 1.8$, and 2 at $K = 2.7$. The peak safety factor for 4140 is 2.3.

3.4 Updated Design Analysis

The primary rotary valve loss equations (full open, transition, compressibility, leakage, and friction) can be extended straightforwardly to the 4-way valve. Refer to Section 2.3 for detailed derivations of the various design equations for the 3-way valve. Updated throttling, leakage, switched volumes, bearing surface area, and self-spinning velocity equations are presented in this section using the variables shown in Fig. 3.11.

3.4.1 4-way Valve Throttling Losses

The 4-way valve's throttling loss equations are formulated slightly differently than the 3-way's equations in Section 2.3.1 because of the duty ratio dependence of these losses caused by the new valve structure. For the concept described in Section 3.2 (see Fig. 3.5),

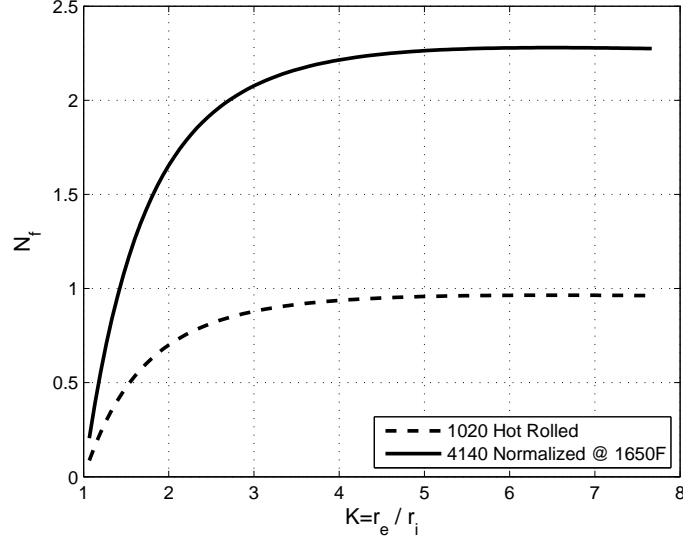


Figure 3.10: Comparison of the sleeve's predicted fatigue safety factor assuming fluctuating external to internal pressure loading at 21MPa for two types of steel. The analysis assumes an uncorrected endurance limit that is half of the ultimate tensile strength of the material as well as a machined surface finish and 99.99% reliability.

when the valve is in Position I, flow passes through the spool and sleeve twice: once from Port A to C and again from Port D to B . When the valve switches to Position II, however, flow only passes through the spool and sleeve once, from Port A to B . Therefore, both the fully open throttling losses and spool/sleeve throttling losses will depend on the duty ratio of the valve, and these losses will be twice as high in Position I than in Position II. Because of this characteristic, the full open throttling losses, spool and sleeve losses, and transition losses are considered separately.

Using the orifice equation, Eq. (2.3), and the fraction of time in transition κ , Eq. (2.2), the full open throttling loss for the 4-way valve is:

$$\begin{aligned} \Pi_{open,4way} &= (1 - \kappa)(2QP_{open}|s| + QP_{open}(1 - |s|)) \\ &= (1 - \kappa)(QP_{open}|s| + QP_{open}) \end{aligned} \quad (3.20)$$

where Q is the flow through the valve and s , the duty ratio, is in the range of $-1 \leq s \leq 1$ depending on the shaft direction and whether the system is pumping or motoring.

The pressure drop due to fluid flow through the spool, $P_{spool} = f(Q, D)$, depends

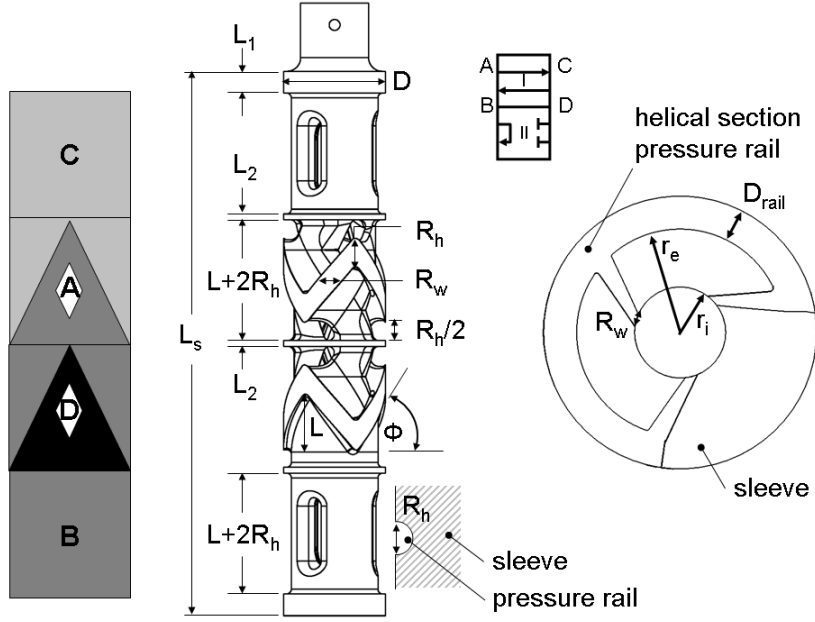


Figure 3.11: Diagram of 4-way valve geometry illustrating variable names used in Section 3.4.

on the flow rate through the valve and its diameter. A CFD generated semi-empirical formula [52, 55, 56] is used to estimate this pressure drop:

$$P_{spool} = \frac{Q^2}{10^{-11.42} \left(\frac{D}{D_o}\right)^{3.02}} \quad (3.21)$$

where Q is flow rate in m^3/s and D_o is a reference diameter in units consistent with D having a value of $25.4mm$.

The pressure drop across the sleeve's toroidal pressure rail, $P_{rail} = f(Q, D_{rail})$, also depends on flow rate but varies with the cross sectional diameter of the rail. Comparisons to CFD work performed by Wang [52, 55, 56] suggest that a minor loss type form is appropriate for the rail pressure drop:

$$P_{rail} = 2K_{rail} \frac{\rho}{\pi^2 D_{rail}^4} Q^2 \quad (3.22)$$

where $K_{rail} = 6$ was found to coincide well with CFD results. To simplify the spool and sleeve throttling losses, it is assumed the pressure drop is equal for all flow paths, i.e.

the pressure drop from Port A to C is equal to the pressure drop from Port D to B and from Port A to B . Additionally, it is assumed that the pressure drop is independent of flow direction, i.e. the pressure drop from Port A to C is equal to the drop from C to A . Using these assumptions and taking into account the duty ratio dependence of the loss, i.e. fluid flows through the spool twice in Position I and only once in Position II , the combined spool and sleeve throttling loss is:

$$\Pi_{spool,4way} = Q [P_{spool}(Q, D) + P_{rail}(Q, D_{rail})] (|s| + 1) \quad (3.23)$$

Note that the loss does not depend on κ since there is flow through the spool regardless if the valve is fully open or transitioning.

The transition throttling loss is calculated assuming no pressure dynamics. The consequence of this assumption is that as soon as the valve opens or closes to Position II, an intermediate freewheeling pressure, P_{fw} , that arises from connecting the high pressure side of the valve to the low pressure side is used immediately where appropriate, i.e., there is no gradual transition of the inlet side and outlet side pressures to the freewheel pressure. Refer to simulated pressure profiles in Section 3.7.1 (Fig. 3.23) to see how the pressures equilibrate when the valve switches to Position II. For the circuit illustrated in Fig. 3.4 that contains cavitation preventing check valves a and b and pressure spike reducing check valves A and B, the transition power losses for pumping and motoring are:

$$\Pi_{trans,pump} = \frac{1}{4} \kappa \sqrt{P_{open}} Q \left[\frac{3(P - P_{fw}) + 4P_{by}}{\sqrt{P + P_{by} - P_{fw}}} + 4 \left(\sqrt{P_{by}} + \sqrt{P_{cav}} \right) - 6\sqrt{P_{open}} \right] \quad (3.24)$$

$$\begin{aligned} \Pi_{trans,motor} = & \frac{1}{4} \kappa \sqrt{P_{open}} Q \left[\frac{3(P - P_{fw}) + 4P_{by}}{\sqrt{P + P_{by} - P_{fw}}} + \frac{3(P - P_t) + 4P_{by}}{\sqrt{P + P_{by} - P_t}} \right. \\ & \left. + \frac{3(P - P_t) + 4P_{cav}}{\sqrt{P + P_{cav} - P_t}} - 6\sqrt{P_{open}} \right] \end{aligned} \quad (3.25)$$

P_{cav} and P_{by} are the cracking pressures of the cavitation preventing check valves (a and b) and bypass check valves (A and B) respectively. P is the system or accumulator pressure and P_t is the tank pressure.

Table 3.1: Leakage paths in 4-way rotary valve based on spool position. In Position I, $P_A \approx P_C$ and $P_B \approx P_D$. In Position II, $P_A \approx P_B \approx P_{fw}$. $P_C = P$ and $P_D = P_t$ or vice versa depending how the ports are connected. Using P and P_t in place of P_A and P_B provides a method of approximating the leakage without needing to calculate P_A and P_B which are flow rate dependent based on the spool's pressure drop.

Spool Position	Leakage Path	Sealing Land	Approximate ΔP
I	$P_C \leftrightarrow P_{axial}$	L_1	$ P_C - P_{axial} $
I	$P_B \leftrightarrow P_{axial}$	L_1	$ P_D - P_{axial} $
I	$P_A \leftrightarrow P_D$	Helical	$ P_C - P_D $
II	$P_C \leftrightarrow P_{axial}$	L_1	$ P_C - P_{axial} $
II	$P_B \leftrightarrow P_{axial}$	L_1	$ P_{fw} - P_{axial} $
II	$P_A \leftrightarrow P_C$	Helical	$ P_C - P_{fw} $
II	$P_A \leftrightarrow P_D$	Helical	$ P_D - P_{fw} $
II	$P_B \leftrightarrow P_D$	L_2	$ P_D - P_{fw} $

3.4.2 4-way Valve Leakage

Leakage is also duty ratio dependent and more complex in the 4-way valve due to the additional spool section and its associated leakage paths. Table 3.1 lists the leakage paths in the 4-way valve along with the corresponding type of sealing land that the leakage is across. In Position I, $P_A \approx P_C$ and $P_B \approx P_D$. In Position II, $P_A \approx P_B \approx P_{fw}$. $P_C = P$ and $P_D = P_t$ or vice versa depending how the ports are connected. The ports will switch if the valve will be used in four quadrant operation. The approximate pressure differential enables estimating the leakage using P and P_t without needing to calculate pressures P_A and P_B which depend on the pressure drop of the spool itself and are therefore flow rate dependent.

The power lost due to the individual leakage components in Table 3.1 are calculated using Eqs. (2.24) and (2.25) which are repeated here for convenience. For leakage across the helical lands:

$$\Pi_{leak} = \frac{L_P c_r^3 (\Delta P)^2}{12\mu R_w \sin \phi} \quad (2.24)$$

L_P is given in Eq. (2.23) and ΔP is the approximate pressure differential in Table 3.1. Losses across the L_1 and L_2 type lands are (adapted from Eq. (2.25)):

$$\Pi_{leak,L_*} = \frac{\pi D c_r^3 (\Delta P)^2}{12\mu (L_*)} \quad (3.26)$$

where L_* is either L_1 or L_2 . The aggregate leakage power loss in the 4-way valve is found by scaling the sum of the total leakage in Position I by the duty ratio $|s|$ and the total leakage in Position II by $(1 - |s|)$:

$$\Pi_{leak,4way} = |s| \sum \Pi_{leak,Position\ I} + (1 - |s|) \sum \Pi_{leak,Position\ II} \quad (3.27)$$

3.4.3 4-way Valve Switched Volumes

The switched volumes V_A and V_B of the 4-way valve can be estimated using the preliminary geometry in Fig. 3.11. Volume V_A associated with helical section A includes the volume of the torus pressure rail assuming N equally spaced rhombic nozzles:

$$V_A = \left(\frac{N-1}{N} \right) \frac{\pi^2}{4} D_{rail}^2 (2r_e + D_{rail}) + \frac{1}{2} N R_w R_h (r_e - r_i) + V_{pm} \quad (3.28)$$

V_{pm} is the internal volume between the P/M and the inlet of the pressure rail. V_B is composed of a semi-circular toroidal rail that accumulates fluid from the end sections of the spool. The volume of the semi-circular rail can be found using the Theorem of Pappus and the centroid of a semi-circular area [83]:

$$V_B = \frac{\pi^2}{8} R_h^2 \left(D + \frac{4R_h}{3\pi} \right) + V_{spool} + V_{pm} \quad (3.29)$$

V_{spool} is the volume internal to the spool from sections A , B , and D which are internally connected. This volume is what enables the recirculation path between Ports A and B in Position II.

3.4.4 4-way Valve Bearing Surface Area

Similar to Eq. (2.33) for the 3-way valve, the bearing surface area of the 4-way valve is:

$$A_{b,4way} = \pi D (2R_h + 2L_1 + 3L_2) \quad (3.30)$$

Likewise, similar to Eq. (2.34), the effective bearing surface area accounting for friction due to fluid recirculation is:

$$A_{eff,4way} = A_{b,4way} + \lambda [2\alpha_{in} \pi D (L + R_h) + 2\alpha_{out} \pi D (L + 2R_h)] \quad (3.31)$$

3.4.5 4-way Self-spinning

The self-spinning velocity of the 4-way valve can be derived using the same torque balance and fluid momentum analysis presented in Section 2.3.4. The primary difference is that the number of turbines producing torque changes depending on the valve position. When the valve is in Position I (on), fluid passes through two sets of inlet and outlet turbines: once from Port A to C , and again from Port D to B . However, when the valve is in Position II (off), the fluid only passes through one set of turbines (from Port A to B). Thus, the inlet and outlet torque equations from Section 2.3.4 (Eqs. (2.28) and (2.29)) need to be modified by the duty ratio s . The total torque from the inlet turbines becomes:

$$\tau_{in,4way} = (1 + s) \frac{\rho R_{in}}{A_{in} N} Q_{in}^2 \quad (3.32)$$

And similarly, the torque from the outlet turbines becomes:

$$\tau_{out,4way} = (1 + s) R_{out} \rho Q_{in} \left(\frac{Q_{in}}{A_{out} N} - R_{out} \omega \right) \quad (3.33)$$

Using Petroff's Law (Eq. (2.27)) as before with the appropriate effective bearing surface area (Eq. (3.31)) to predict frictional torque, the resulting self-spinning spool velocity for the 4-way valve is:

$$\omega_{4way} = \frac{(1 + s) 4\rho}{ND^2 (A_{eff} \frac{\mu}{c_r} + (1 + s) \frac{4R_{out}^2}{D^2} \rho Q_{in})} \frac{R_{in}}{\bar{A}} Q_{in}^2 \quad (3.34)$$

where \bar{A} is an equivalent combined flow area as defined in Eq. (2.31). Note that (3.34) simplifies down to (2.30) when $s = 0$ as expected. This is when the valve is in Position II and fluid only flows through one set of turbines in the recirculation configuration. Accordingly, actuation power due to friction is:

$$\Pi_{f,4way} = \tau_f \omega = \frac{1}{4} A_{eff,4way} \frac{\mu}{c_r} D^2 \omega^2 \quad (3.35)$$

3.5 Drive Cycle Optimization and Actuation Trade Study

The prototype valve is optimized to work with a donated 9.8cc fixed displacement bent axis P/M. This section provides a general overview of the procedure. For details, please refer to work by Rannow [64, 47]. The objective of the optimization is to determine the

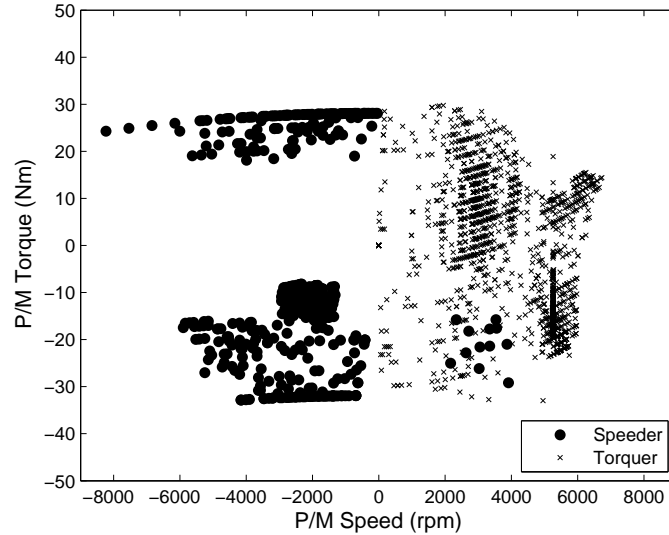


Figure 3.12: Speeder and torquer operating points for an input coupled power-split HHPV with 21MPa working pressure differential.

VVDPM valve geometry that minimizes the total valve losses when implementing the unit as the speeder P/M in the HHPV illustrated in Fig. 3.2. The speed and torque operating points of the speeder over the combined EPA Urban and Highway drive cycles are shown in Fig. 3.12.

While external actuation was not considered when designing the 3-way valve in Chapter 2, it will be compared to self-spinning in this section due to several notable differences with the 4-way valve. The first difference is that the flow rate through the valve is no longer constant and varies across a large range, anywhere between no flow and 82 lpm based on the operating speeds shown in Fig. 3.12. This will make optimizing an efficient turbine difficult. The second difference is the need to operate in four quadrants, i.e. pump and motor bidirectionally. For self-spinning to work, this requires an additional directional control valve that is located in the switched volume between the P/M and on/off valve, as shown in Fig. 3.4. This valve will not only increase compressibility loss due to the larger switched volume, but also add to throttling losses. Because actuation power was low in the 3-way valve at only 30W when switching at 100Hz PWM frequency, separating the actuation problem from the valve design may

provide benefit when designing the 4-way valve.

The cost function used in the valve optimization is:

$$\min_x \left\{ \int_{cycle} [\pi_{open}(x) + \pi_{trans}(x) + \pi_{comp}(x) + \pi_{leak}(x) + \pi_f(x)] dt \right\}$$

where $x = [D, R_w, R_h, L_s, L_1, A_{out}, c_r, D_{rail}]$ is the optimization variable vector. D is the spool diameter, R_w and R_h are the rhombic port width and height, L_s is the spool length, L_1 is the end section land width, A_{out} is the end section flow area, c_r is the radial clearance, and D_{rail} is the cross sectional diameter of the torus pressure rail (refer to Figs. 2.5 and 3.11 for variable definitions). π_f is the friction or actuation power loss which is omitted for self-spinning but included for external actuation.

The speeder VVDPM speed (ω_{pm}) and torque (τ_{pm}) trajectories were chosen to match the optimal points for a typical variable displacement bent axis P/M used on a vehicle driving over the combined EPA Urban and Highway cycles with a working pressure differential of $21MPa$. The optimal points were chosen based on an energy management and vehicle optimization strategy proposed by Cheong et al. [72] that assumes a generalized transmission from which optimal component sizes (gear ratios, pump displacement, etc.) are chosen to minimize total power train losses. Pump displacement is scaled assuming a fixed efficiency map based on normalized torque and flow.

The valve optimization is subject to several constraints:

$$\frac{2R_w}{R_h} = \frac{\pi D}{LN} \quad (3.36)$$

$$\kappa = \frac{4NR_w}{\pi D} \leq 1 \quad (2.2)$$

$$x_{min} \leq x \leq x_{max} \quad (3.37)$$

$$\bar{f}_{PWM} \leq \frac{N\bar{\omega}}{2\pi} \quad (3.38)$$

$$f_{PWM} \leq \frac{N\omega}{2\pi} \quad (3.39)$$

The first constraint, Eq. (3.36), forces the edges of the rhombic ports to be parallel with the helical lands where L is the spool's axial travel. This creates a linear orifice area schedule, i.e. orifice area changes linearly with spool angle, which reduces transition time compared to a circular orifice of equal area [44]. The second constraint, Eq. (2.2),

states that the valve transition cannot exceed one cycle where κ is defined as the fraction per revolution that the valve is in transition. The third constraint, Eq. (3.37), is the result of lower and upper parameter bounds. The final constraints are bounds on the PWM frequency. For self-spinning, Eq. (3.38) is a lower bound on the mean valve frequency based on the self-spinning velocity relationship described in Eq. (3.34). For external actuation, Eq. (3.39) is a constant speed constraint which is used as an input to determine the friction power loss described in Eq. (3.35) when this power must be supplied by an outside source.

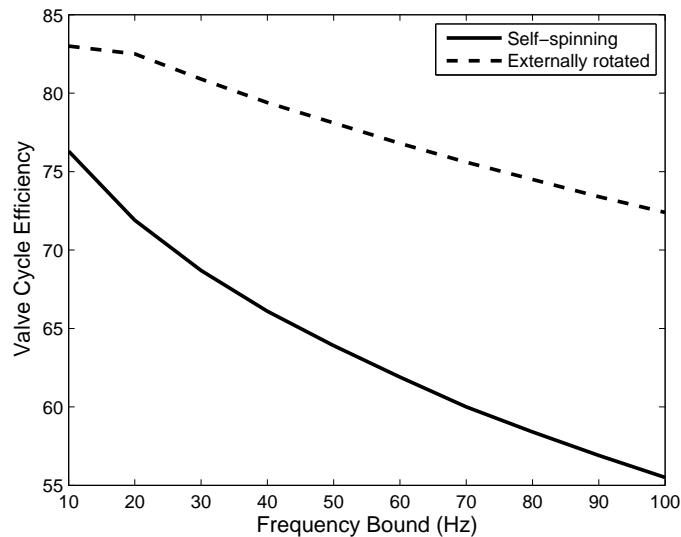


Figure 3.13: Comparison of rotary valve optimized drive cycle efficiencies between self-spinning and external actuation for different frequency bounds (lower bound on mean frequency for self-spinning and constant speed for external actuation). Friction/actuation losses are included for external actuation. P/M losses are not included in either case. The efficiencies correspond to the drive cycle operating points presented in Fig. 3.12.

Valve cycle efficiency over the combined EPA Urban and Highway drive cycles are presented in Fig. 3.13 for both forms of actuation. The efficiency of the externally actuated valve includes the additional actuation power loss. However, the efficiency of the self-spinning valve does not include the additional compressibility and throttling losses

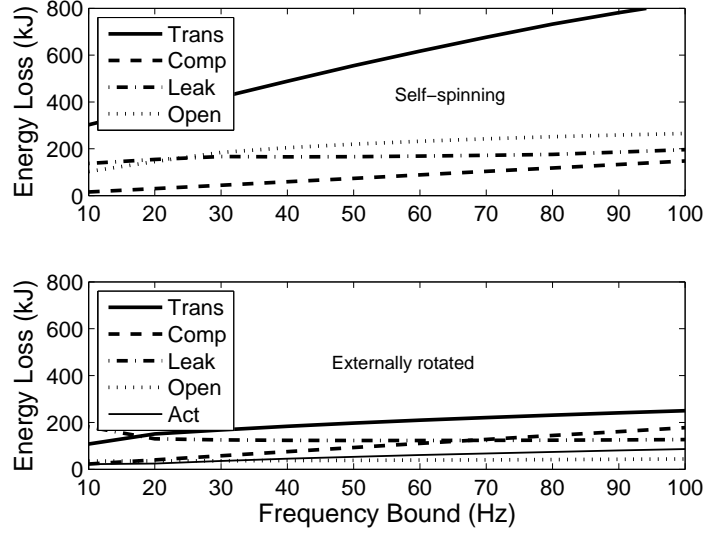


Figure 3.14: Comparison of optimized rotary valve losses between self-spinning (Top) and external actuation (Bottom) for different frequency bounds (lower bound on mean frequency for self-spinning and constant speed for external actuation). Friction/actuation losses are included for external actuation. P/M losses are not included in either case.

associated with the added directional control valve. Including these losses will only decrease self-spinning efficiency further. Figure 3.13 shows that externally actuating the spool improves cycle efficiency by approximately 7% at 10Hz over self-spinning. The improvement increases significantly at higher PWM frequencies to approximately 17% at 100Hz. A break down of losses is presented in Fig. 3.14 for both forms of actuation. Transition losses are dominant in the self-spinning valve, especially as the switching frequency increases. Figure 3.15 illustrates how valve diameter, flow areas, and length compare between self-spinning and external actuation with respect to switching frequency. Recall that transition losses are proportional to $\kappa\sqrt{P_{open}}Q \propto \kappa\frac{Q^2}{A_{in}}$ (refer to Eqs. (3.24) and (3.25)) and that self-spinning velocity is proportional to $\frac{Q^2}{D^2L}\left(\frac{1}{A_{in}} + \frac{1}{A_{out}}\right)$ assuming $R_{in} \approx R_{out} \approx \frac{D}{2}$ (refer to Eq. (3.34)). In order to produce enough torque to satisfy the frequency bound at higher switching speeds, the inlet and outlet turbines of the self-spinning valve are driven to smaller flow areas than the externally actuated valve at the expense of pressure drop, and consequently, transition losses. Smaller flow area

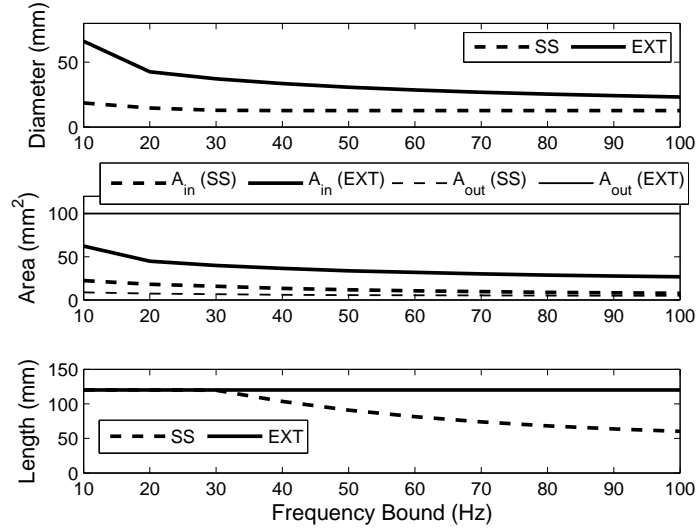


Figure 3.15: Comparison between optimized self-spinning and externally actuated spool geometries. Diameter (Top), inlet and outlet flow areas (Middle), and overall spool length (Bottom) are presented.

also enables decreasing the spool size, and therefore spool diameter, length, and surface area which reduces frictional losses. These trends are revealed in Fig. 3.15. The middle plot of Fig. 3.15 shows that the externally rotated valve's inlet turbine flow area A_{in} is always at least twice the area of the self-spinning valve. The externally rotated valve's outlet turbine flow area A_{out} is driven to its upper bound of 100mm^2 regardless of frequency bound in contrast to the self-spinning valve where A_{out} is consistently smaller than A_{in} . Recall that pressure drop is proportional to $\frac{1}{A^2}$. As a result, full open losses rise from being the smallest loss in the externally actuated valve to becoming the second highest loss in the self-spinning valve. Because actuation losses are small relative to the other primary losses in the externally rotated valve (see Fig. 3.14), the flow areas do not need to be compromised in order to achieve the desired switching speed. In fact, it is less costly from a loss perspective to obtain the actuation power from an independent source. Figure 3.15 also shows how spool diameter and length decrease with faster switching speeds to minimize bearing surface area in the self-spinning valve compared to the externally rotated valve. In fact, the self-spinning valve's spool diameter is driven to its lower bound of 12.7mm between 30Hz - 40Hz .

In conclusion, external actuation enables larger, higher flow valves that do not incur excessive pressure drop and transition loss to achieve desired switching speeds. In applications where a large range of flow rates are demanded, designing the valve for self-spinning requires sizing the spool's turbines for low flow rates to achieve the specified frequency bound which induces excessive throttling at higher flow rates. Due to poor efficiency in comparison to external actuation, self-spinning will no longer be considered for the 4-way valve. Design of the externally actuated valve will be explored in more detail in the following section.

3.6 Externally Actuated Valve

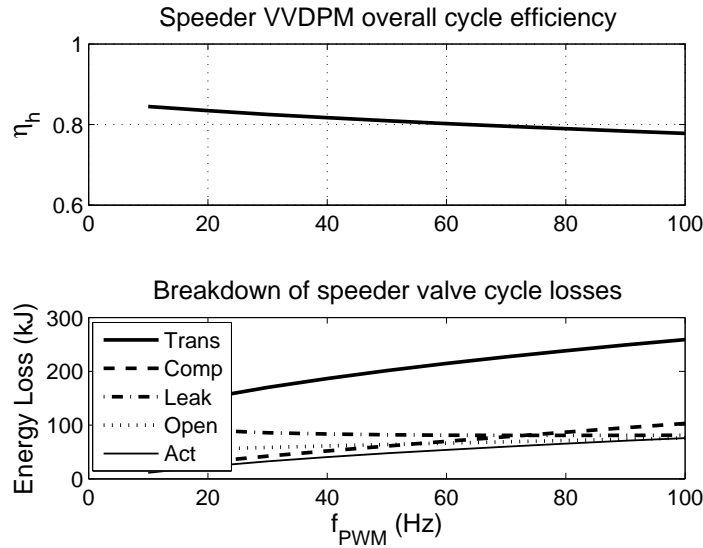


Figure 3.16: Top: VVDPM overall efficiency, defined as $\eta_h = \frac{\sum_{cycle} \tau_{pm} \omega_{pm} dt}{\sum_{cycle} (\tau_{pm} \omega_{pm} + \pi_{tot}) dt}$, optimized and plotted with respect to PWM frequency for 21MPa vehicle working pressure differential. Losses attributed to the fixed displacement P/M are included. Bottom: Breakdown of losses.

Due to its lower efficiency, self-spinning was abandoned in favor of externally rotating the valve for the HHPV. As mentioned in Section 3.5, an additional benefit of migrating to external actuation is that it enables bidirectional flow through the valve spool. This functionality eliminates the need for the directional valve between the P/M and on/off

valve which reduces switched volume and pressure drop in the system. The detailed results from a more refined version of the optimization performed in Section 3.5 is presented in Fig. 3.16 for the externally rotated valve. The reported cycle efficiency in this figure includes P/M losses. Figure 3.16 reveals a linear drop off in efficiency as the PWM frequency is increased from $10Hz$ to $100Hz$ due to the increase in transition losses. While low PWM frequency is beneficial from an efficiency standpoint, high frequency is desirable to reduce torque ripple on the vehicle as well as increase control bandwidth. Since the effects of PWM frequency on vehicle ripple have not yet been determined, a PWM frequency of $40Hz$ will be considered for the remainder of the case study. Of the five dominant systems losses (full open, transition, compressibility, and leakage), actuation power or friction is consistently the smallest loss, even at $100Hz$ as shown in the bottom of Fig. 3.16. Disregarding any frictional effects from fluid recirculation, actuation power due to bearing type friction at the spool lands ranges from $16W$ at $40Hz$ to $101W$ at $100Hz$. Adding in fluid recirculation using the parameters for the loose clearance turbine spool from Section 2.6.2 ($\lambda = 2$, $\alpha_{in} = .058$, and $\alpha_{out} = .042$), the total actuation power is $22W$ at $40Hz$ and $136W$ at $100Hz$.

Optimized valve parameters and efficiency at $40Hz$ are presented in Table 3.2. The true optimal valve is compared to one with an upper bound on the diameter. Since the efficiency difference is minor (1%), the $30mm$ OD spool will be analyzed and designed due to its smaller size. The pressure drops across the various components of the $30mm$ OD valve are presented in Fig. 3.17.

Table 3.2: Speeder valve parameters optimized for a $21MPa$ working pressure differential and PWM frequency of $40Hz$. $L_s = 120mm$, $A_{out} = 100mm^2$, and $c_r = .013mm$ were driven to their respective parameter bounds in both cases. All lengths in mm and volumes in cc .

	D	R_w	R_h	L_1	D_{rail}	V_A	V_B	η_h
Optimal	45.4	11.9	8.7	8.0	9.9	22.7	28.5	.82
D Bound	30	7.85	8.94	6.36	10.4	21.4	25.8	.81

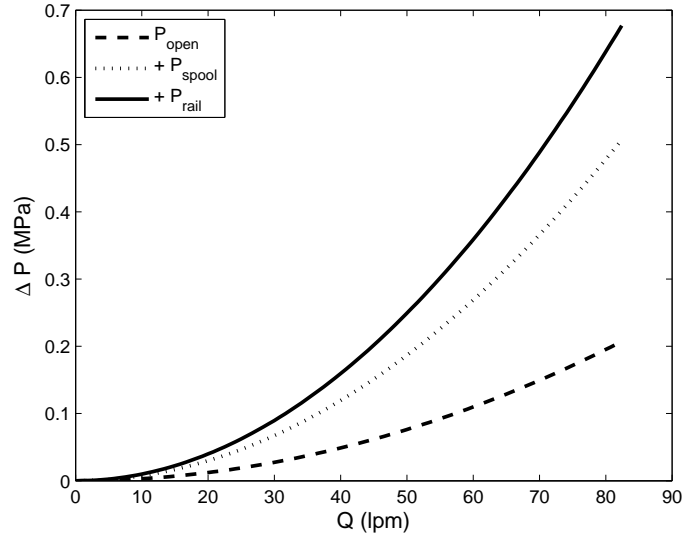


Figure 3.17: Pressure drops across the valve orifice, spool, and toroidal pressure rail based on the 30mm 4-way valve geometry presented in Table 3.2. Note that the traces are additive to elucidate the combined drop as well as the individual contributions.

3.6.1 Drive Mechanism for Realizing External Actuation

A proposed driving mechanism that is capable of achieving the rotational and translational motion requirements of the rotary valve is presented in Fig. 3.18. An exploded render of the mechanism is presented in Fig. 3.19. The concept relies on a decoupled sealing approach that isolates the rotary and translational sealing functions, thereby enabling full sealing using standard o-rings. Decoupling is accomplished via a translating piston and an intermediate shaft. The shaft (see Figs. 3.18 and 3.19) rotates relative to the piston and is supported by a pair of ball bearings. Retaining rings are used to secure the bearings to the shaft and the shaft to the piston. With the retaining rings in place, the shaft is free to rotate relative to the piston; however, the two components are fixed to translate together. The inner diameter of the piston features an o-ring sealing gland. This seal does not experience any translating motion. The translational sealing function is accomplished using a standard reciprocating piston o-ring. The seal gland is located along the outer diameter of the translating piston. A spacer containing a boss that protrudes from the piston wall through the sleeve extension is used to prevent

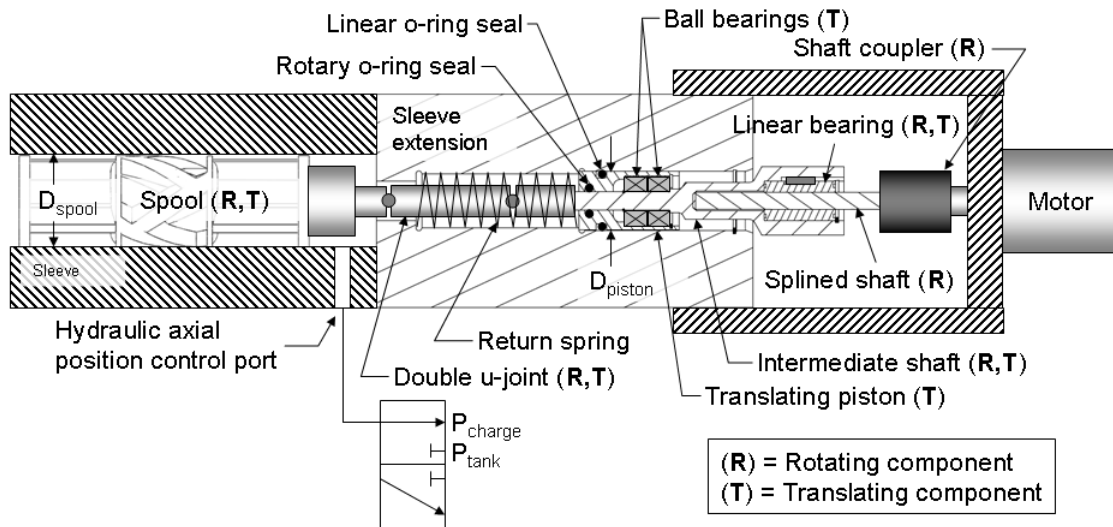


Figure 3.18: Schematic of proposed 2 DOF rotary valve driving mechanism for enabling external actuation. The rotary motion is actuated using an electric motor that is coupled to the spool via a splined shaft and double u-joint. The axial motion is actuated hydraulically by leveraging the area difference between the spool and translating piston using a control valve.

the piston from rotating and provides an alternative means of sensing the spool's axial position. The optical sensor implemented on the 3-way valve was sensitive to leakage, required frequent calibration due to drift issues, and experienced periodic noise from the spool's non-uniform surface finish on the sensing end. The mounting boss, which experiences pure linear motion, enables the use of more repeatable sensing techniques such as linear encoders as well as contacting sensors. In the current design iteration a magnetic linear encoder is used.

The axial position of the spool is controlled hydraulically in the design presented in Figs. 3.18 and 3.19. This is accomplished by utilizing the area difference between the spool and translating piston. With reference to Fig. 3.18, D_{spool} is the diameter of the spool, D_{piston} is the diameter of the piston, and the two are sized such that $D_{spool} > D_{piston}$. When the 3-way control valve connects the axial control port on the sleeve to charge pressure, a net pressure force will be exerted on the system to the left due to the spool's larger area. This causes the spool, connecting u-joint, and piston/intermediate shaft assembly to translate to the left, which compresses a spring.

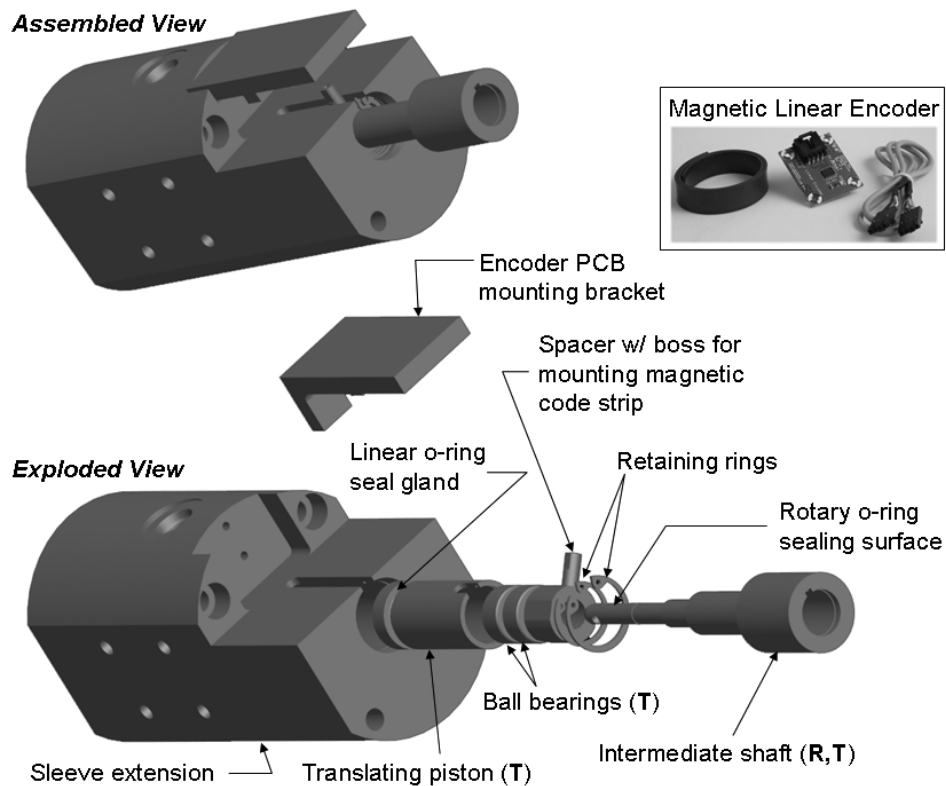


Figure 3.19: Assembled and exploded views of the drive mechanism illustrating its various components. The mechanism shown in this figure uses a magnetic linear encoder to sense the spool's axial position. A boss protruding from the side of the translating piston enables the attachment of a magnetic code strip that is read by the sensor mounted on the sleeve extension.

When the 3-way valve connects the axial control port to tank pressure, the pressure force falls below the spring force, thereby causing the spool to move to the right. Hard stops are incorporated into the drive mechanism to insure the spool remains within its specified range of travel.

The spool is spun with an electric motor. A flexible shaft coupling is used to connect the motor's shaft to a splined shaft that rotates. The splined shaft allows relative translational motion between the spline and a linear bearing while simultaneously transmitting torque to the bearing. A slotted key is used to transmit torque between the

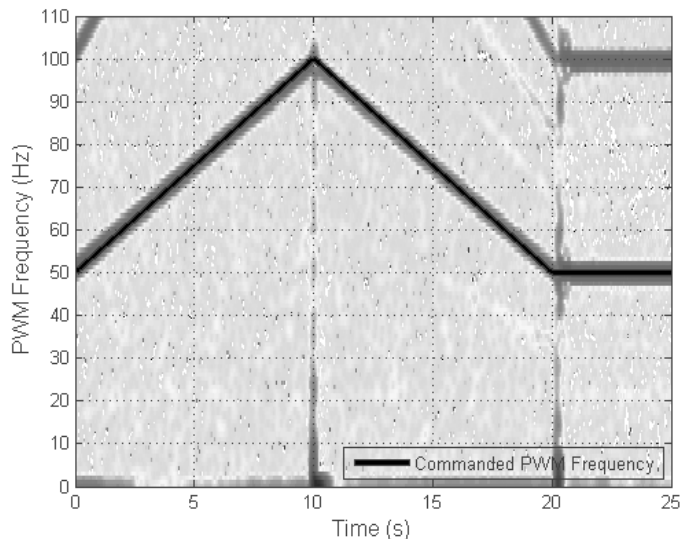


Figure 3.20: Short-time Fourier transform of the VVDP test stand’s inlet pressure (P_{in}) showing its frequency content compared to the commanded PWM frequency trajectory. The PWM frequency ramp trajectory in this figure was commanded concurrently with the step duty ratio trajectory shown in Fig. 3.21. This shows that PWM frequency and duty ratio are independently controllable.

linear bearing and the intermediate shaft which is connected to the spool via a double u-joint (see Fig. 3.18). The double u-joint is used to compensate for angular and parallel misalignment between the spool, which functions as a journal bearing, and the intermediate shaft, which is supported by two ball bearings inside of the translating piston.

Drive Mechanism Validation

A prototype of the driving mechanism illustrated in Fig. 3.18 was fabricated and validated using the 3-way rotary valve test stand described in Chapter 2. Custom components, such as the sleeve extension, translating piston, and intermediate shaft, were machined from low carbon steel. All other components are off-the-shelf parts. The axial motion of the valve is actuated using a servo valve rated for 57 lpm (15 gpm) at a pressure drop of 7 MPa (1000 psi). This valve was selected for demonstration purposes due to lab availability and time constraints. However, in the future, a more appropriate

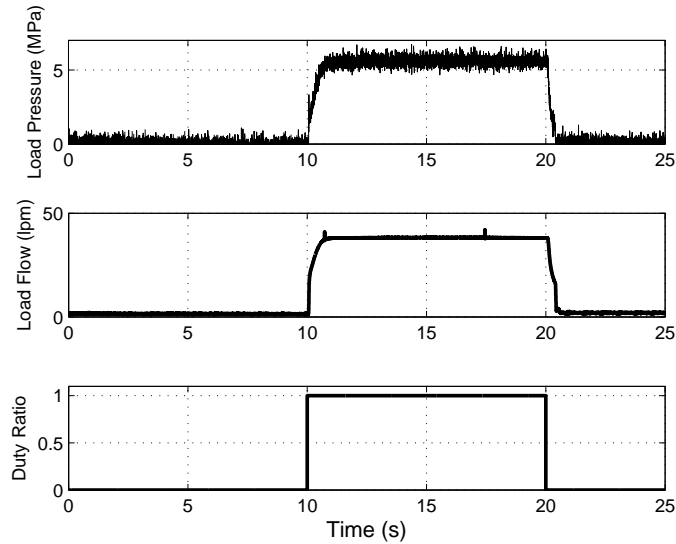


Figure 3.21: VVDP test stand load pressure (top) and flow rate (middle) corresponding to the commanded step change in duty ratio (bottom). The duty ratio trajectory in this figure was commanded concurrently with the ramp PWM frequency trajectory shown in Fig. 3.20. This shows that PWM frequency and duty ratio are independently controllable.

valve, such as a direct acting solenoid proportional valve, will be used. The rotary motion of the valve is actuated using a brushless DC (BLDC) motor with integrated speed controller. Sensing is accomplished using 69MPa ($10,000\text{psi}$) pressure sensors for the inlet and load pressures, and a gear motor with a 1000counts/rev shaft encoder for the output flow rate of the load line. A least squares estimator with a forgetting factor of 150 is used to estimate the flow rate from the encoder's output.

Experimental data validating the drive mechanism's functionality is presented in Figs. 3.20 and 3.21. The plots show data from the same experiment plotted using the same time scale. The experiment consisted of commanding a ramp trajectory in PWM frequency (spool rotational velocity) while simultaneously commanding a step change in duty ratio (axial position). Figure 3.20 presents a Short Time Fourier Transform (STFT) of the inlet pressure, which is pulsed at the PWM frequency, overlaid with the commanded PWM frequency. The STFT uses a window to determine the frequency content of a signal as the signal changes with time. The figure shows that the frequency

content of the inlet pressure is consistent with the commanded frequency.

The step command in duty ratio is performed open loop using a charge pressure of roughly $1.4MPa$ ($200psi$) to drive the spool through its full range of travel. The needle valve in the test stand is set such that a load pressure of $5.5MPa$ ($800psi$) is obtained when the VVDP is at full displacement. Figure 3.21 presents the load pressure and flow rate resulting from the commanded change in duty ratio. Due to the response time of the servo valve and the accumulator dynamics, delay is present before the load pressure and flow rate reach their steady state values. In stepping up from zero displacement to full displacement, a $60ms$ delay occurs before any response to the step command is observed from the pressure and flow data. In total, the VVDP requires a rise time of approximately $500ms$ to reach 90% of its full displacement flow rate. Similarly, the load pressure requires a rise time of approximately $600ms$ to reach 90% of its steady state value. The response of the VVDP is heavily dominated by the dynamics of the accumulator. Faster response can be achieved by either decreasing the accumulator volume or pre-charge, although this comes at the expense of larger output ripple [2].

3.7 VVDPM Dynamic Model and Simulation Results

The proposed dynamic model is based on the pressure dynamics within the two internal volumes of the P/M (V_A, V_B). Included in the model are the effects of fluid compressibility, the rhombic port and helical land geometry, and leakage across the major sealing interfaces. The simulation uses the loss models described in Section 3.4 and is based on the 3-way valve model in Section 2.4. Losses due to the fixed displacement P/M are included based on manufacturer provided efficiency maps. Simplifying assumptions include constant accumulator and tank pressures (P and P_t), no line losses, and no check valve dynamics (instant open/close).

Figure 3.22 presents a flow diagram representing the VVDPM model. Flow subscripts indicate positive flow directions, i.e. Q_{AB} is positive for fluid flow from Port A to Port B . Solid dots indicate flow junctions or pressure connections. $Q_{cav,a}$ and $Q_{cav,b}$ refer to the flows through the cavitation preventing check valves a and b in Fig. 3.4 while $Q_{by,A}$ and $Q_{by,B}$ refer to the bypass flows through check valves A and B that reduce

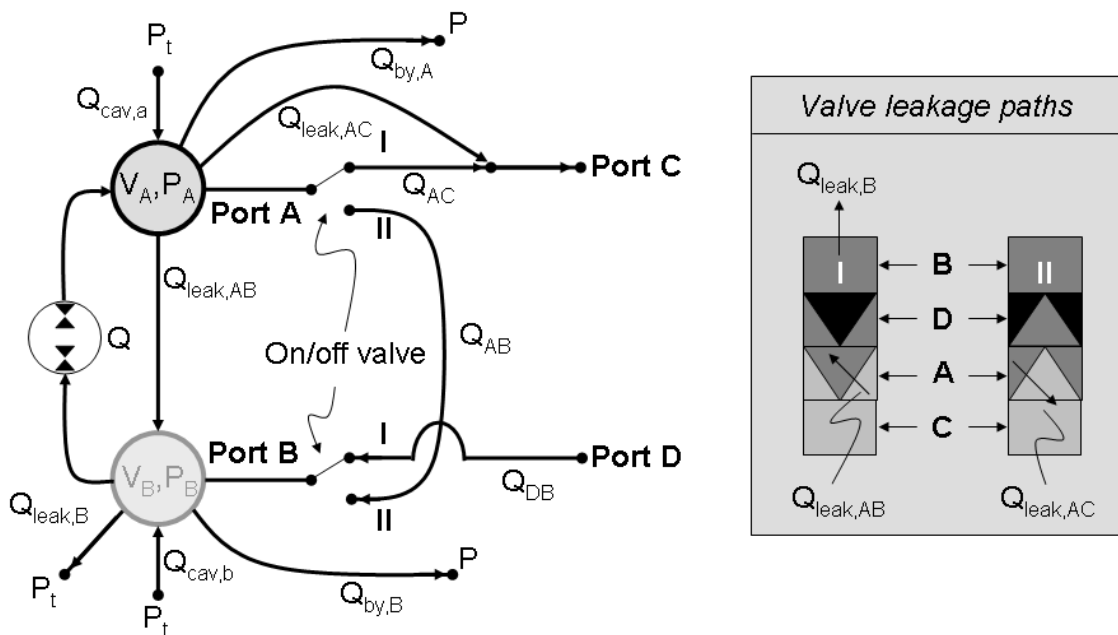


Figure 3.22: Flow diagram describing the VVDPM model including the fixed displacement pump/motor and on/off valve. Arrowheads indicate positive flow directions. Solid dots indicate flow junctions or pressure connections. Inset illustrates leakage paths that affect the pressure dynamics in volumes A and B .

pressure spikes during valve transition. Using Fig. 3.22, the pressure dynamics are:

$$\dot{P}_A = \frac{\beta(P_A)}{V_A} [Q - Q_{AC} - Q_{AB} - Q_{by,A} + Q_{cav,a} - Q_{leak,AC} - Q_{leak,AB}] \quad (3.40)$$

$$\dot{P}_B = \frac{\beta(P_B)}{V_B} [Q_{DB} + Q_{AB} - Q - Q_{by,B} + Q_{cav,b} + Q_{leak,AB} - Q_{leak,B}] \quad (3.41)$$

The model is simulated in the Matlab/Simulink environment using a fixed step size of $.2\mu s$ using the ODE3 (Bogacki-Shampine) solver. System parameters used in the simulation correspond to the HHPV and include accumulator pressure of $P = 22.1MPa$, tank/low pressure accumulator of $P_t = 1.4MPa$, cavitation prevention check valve cracking pressure of $.028MPa$, and bypass check valve cracking pressure of $.76MPa$. The hydraulic oil properties used in the simulation include a density of $876kg/m^3$, dynamic viscosity of $.0387Pa \cdot s$, and 5% air entrainment by volume and no dissolved air.

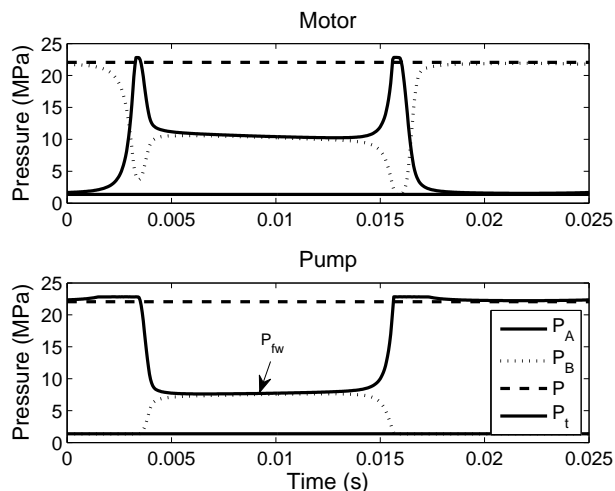


Figure 3.23: Speeder VVDPM pressure profiles for motoring and pumping (one cycle). VVDPM is operating at $4000rpm$ and 50% axial travel.

3.7.1 VVDPM Pressure Profiles

Simulated pressure profiles for the speeder VVDPM are presented in Fig. 3.23. During the time interval from $.004s$ to $.015s$, the on/off valve is in Position II and the VVDPM is idling. Notice that the freewheel pressure (P_{fw}) decreases during motoring but increases during pumping. This is due to whether Port C or D is connected to the accumulator. During motoring for the shaft direction simulated in Fig. 3.23, the accumulator is connected to Port D while Port C is connected to tank. Since Port D is blocked in Position II, it is assumed that no leakage occurs. In contrast, there is leakage across the helical land from Port A (at the freewheel pressure) to Port C (connected to tank). When the VVDPM is pumping, the accumulator and tank connections become switched and there is now leakage from Port C into Port A , which raises the freewheel pressure. Another interesting feature of the pressure profiles is the relatively complex transition during motoring. This is because $P_B > P_A$ when the VVDPM is acting as a motor and $P_A > P_B$ when acting as a pump. When the VVDPM is freewheeling, it is acting as a pump: power is required at the shaft to force flow across the full open pressure drop of the valve. Therefore, when the VVDPM is motoring, P_A and P_B must change relative magnitude (i.e. $P_A - P_B$ changes sign) during every transition. This

switch causes the additional transition effects seen in the top of Fig. 3.23.

3.7.2 VVDPM Efficiency Maps

The efficiency maps presented in Figs. 3.24 (motoring) and 3.25 (pumping) correspond to a valve PWM frequency of $40Hz$ and an operating pressure differential of $21MPa$. The mean efficiency for each point of the map is determined by dividing the total VVDPM output energy by the input energy over a time interval T_{avg} . An interval of $T_{avg} = .25s$ (10 cycles at $40Hz$) was used. The overall efficiency at each combination of speed and valve axial position is:

$$\eta_m = \frac{\int_{T_{avg}} \tau_{pm} \omega_{pm} dt}{\int_{T_{avg}} [(P - P_t)(Q_{DB} - Q_{by,A} - Q_{by,B}) + \pi_{cav} + \pi_{pm} + \pi_f] dt} \quad (3.42)$$

$$\eta_p = \frac{\int_{T_{avg}} (P - P_t)(Q_{AC} + Q_{by,A} + Q_{by,B}) dt}{\int_{T_{avg}} [\tau_{pm} \omega_{pm} + \pi_{pm} + \pi_f] dt} \quad (3.43)$$

$\pi_{cav} = [(P_t - P_B)Q_{cav,b} + (P_t - P_A)Q_{cav,a}]$ is the input power due to the cavitation preventing check valves. η_m and η_p represent overall motor and pump efficiency respectively. Actuation power (π_f) is included in both the motor and pump efficiency calculations. Valve efficiency can be calculated by simply omitting π_{pm} , the power loss due to the fixed displacement P/M, from Eqs. (3.42) and (3.43). The efficiency maps are plotted with respect to the mean shaft torque averaged over the interval T_{avg} normalized with respect to the maximum P/M torque $\tau_{pm,max} = \frac{D_{pm}(P-P_t)}{2\pi}$ (where D_{pm} is the fixed P/M displacement). This represents the corrected displacement fraction of the VVDPM. In comparing the valve efficiency to overall efficiency, the losses contributed by the fixed displacement P/M (a bent axis unit in this study) lead to a reduction in VVDPM efficiency of approximately 5% (i.e. 90% to 85%) across the entire map for both pumping and motoring. Actuation power is predicted to be only $22W$ at $40Hz$ and is independent of whether the VVDPM is pumping or motoring. To put actuation power into context, at $21MPa$ working pressure differential and at $8400rpm$ ($82lpm$), the system hydraulic power is $28kW$.

When comparing motor efficiency alongside pump efficiency in Fig. 3.26, motor efficiency is typically 5% lower across all operating points with an additional drop off in efficiency at higher speeds. For reference, Fig. 3.26 is overlaid with the drive cycle

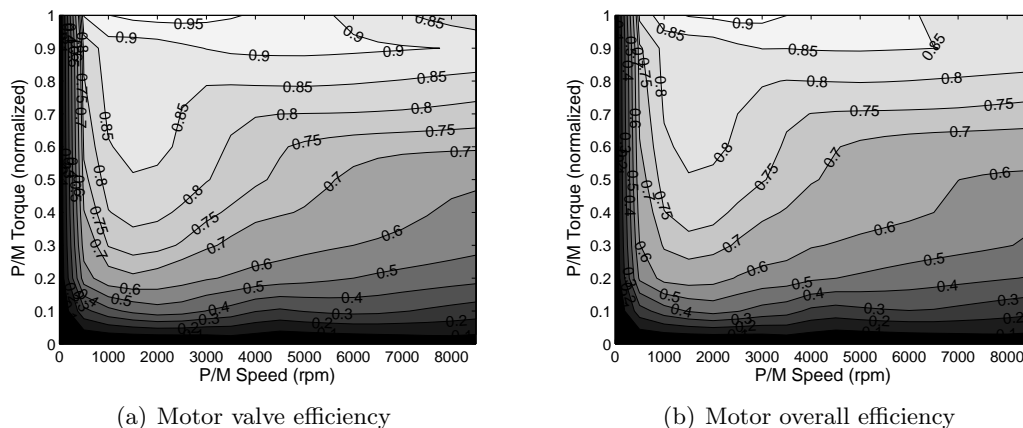


Figure 3.24: Speeder VVDPM efficiency maps for motoring.

Table 3.3: EPA combined Urban/Highway speeder cycle efficiency.

Bent axis	VVDPM (valve)	VVDPM (overall)
0.88	0.83	.77

operating points from Fig. 3.12. The lower motor efficiency is a consequence of transition losses. The bypass and cavitation preventing check valves, which reduce transition losses during pumping, are seldom active during motoring. This is because the intake side of the motor, initially at high pressure, must transition to tank pressure before the cavitation prevention check valves will open. Similarly, the outlet side, initially at tank pressure, must transition to the accumulator pressure before the bypass check valves will open. In contrast, during pumping the outlet side is already at high pressure, which triggers the bypass check valves at the onset of transition (likewise for the inlet side). These effects can be observed in the pressure profiles shown in Fig. 3.23.

3.7.3 Efficiency Comparison with Bent Axis Pump/motor

To benchmark the VVDPM against a variable displacement bent axis P/M, speeder cycle efficiency and overall HHPV fuel economy will be used as metrics. For the cycle

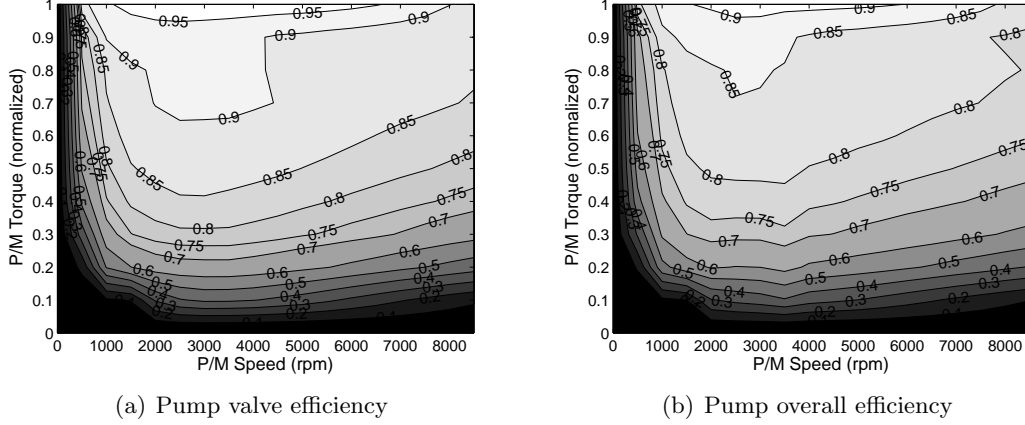


Figure 3.25: Speeder VVDPM efficiency maps for pumping.

Table 3.4: HHPV cycle fuel economy over combined EPA Urban/Highway cycle. **B** indicates bent axis while **V** indicates VVDPM. In all cases, both speeder and torquer sizes are optimized.

	Baseline	Speeder VVDPM	Both VVDPM
Torquer	12cc B	13.1cc B	15.3cc V
Speeder	15.1cc B	22.4cc V	19.9cc V
Mpg	65.6	65.2	62.3

efficiency comparison, the VVDPM will be compared to the bent axis P/M using the optimal bent axis speed and torque operating points that were used to optimize the VVDPM in Section 3.5 (see Fig. 3.12). The cycle efficiency is calculated by determining the losses from the overall VVDPM (or bent axis) efficiency map (π_{tot}) and dividing the total cycle output energy by the cycle input energy:

$$\eta_{cycle} = \frac{\int_{cycle,m} (\tau_{pm} \omega_{pm}) dt + \int_{cycle,p} (\tau_{pm} \omega_{pm} - \pi_{tot}) dt}{\int_{cycle,m} (\tau_{pm} \omega_{pm} + \pi_{tot}) dt + \int_{cycle,p} (\tau_{pm} \omega_{pm}) dt} \quad (3.44)$$

$cycle,m$ refers to operating points where the unit is motoring and $cycle,p$ refers to operating points where the unit is pumping. The speeder cycle efficiencies calculated using Eq. (3.44) are presented in Table 3.3. The results show that losses from the fixed

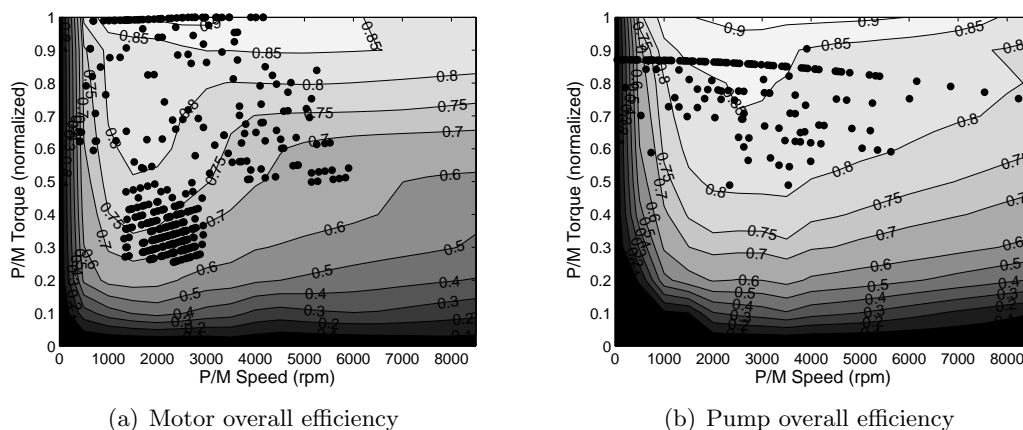


Figure 3.26: Speeder VVDPM overall efficiency maps overlaid with drive cycle operating points from Fig. 3.12.

displacement P/M decrease VVDPM efficiency by 6% over the cycle. The bent axis P/M achieves 11% higher cycle efficiency, likely due to the chosen operating points (optimal for bent axis) as well as the additive nature of the rotary valve losses to the P/M losses.

The impact of lower VVDPM cycle efficiency on vehicle fuel economy is investigated next to assess the viability of implementation on a HHPV. To provide a comprehensive comparison, the VVDPM overall efficiency maps presented in Figs. 3.24(b) and 3.25(b) were input into the vehicle optimization code by Cheong et al. [72], which previously used bent axis maps, to determine the optimal drive train sizing. The HHPV cycle fuel economy is calculated by converting the total input energy required by the vehicle (losses plus cycle work) into fuel consumed using the heating value of diesel ($38.6 \times 10^6 J/L$). Full regenerative braking was assumed (i.e. no friction braking). The fuel economy for the baseline case plus cases where one or both P/Ms are replaced by VVDPMs is presented in Table 3.4. In all cases the P/M displacements are optimally sized. Results show that replacing only the speeder P/M with a VVDPM reduces fuel economy negligibly by $.4mpg$ ($-.6\%$). However, when VVDPMs are used for both the speeder and torquer, the fuel economy decreases by $3.3mpg$ (-5%) from the baseline case.

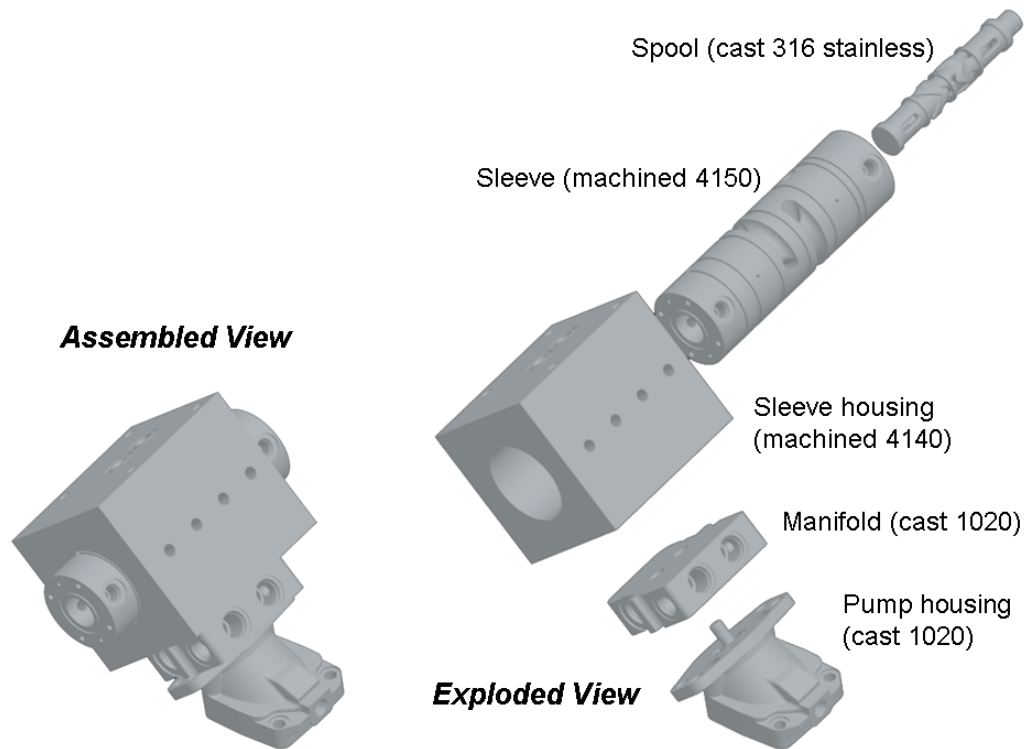


Figure 3.27: Assembled and exploded renders of the 4-way prototype rotary valve.

3.8 Prototype Hardware and Preliminary Testing

A prototype 4-way rotary valve and VVDPM were designed and fabricated to validate the analysis and simulations. Renders of the prototype, shown in Fig. 3.27, illustrate the various components and how they fit together. The actual prototype hardware is shown in Fig. 3.28. The custom P/M housing, which reduces the internal volume of the VVDPM, was cast from 1020 steel with secondary machining of the internal features that interface with the rotating group of the P/M. The manifold, also cast from 1020 steel, houses the cavitation preventing check valves a and b as well as the transition pressure spike reducing check valves A and B (refer to fig. 3.4). The sleeve housing and sleeve were both machined from higher strength alloy steel due to fatigue considerations. The spool was cast from 316 stainless steel with precision grinding on the OD to meet the desired diametral clearance of $.025mm$.



Figure 3.28: From left to right: Prototype 4-way rotary valve sleeve housing, sleeve, and spool.

Modification of the 9.8cc fixed displacement bent axis P/M with the custom housing required considerable disassembly in order access the timing marks on the cylinder barrel and timing gear to insure proper synchronization. Figure 3.29 illustrates various stages of the modification process. Once the modified P/M was reassembled, the unit was run in and tested at pressure. The measured case flow at 21MPa was within the manufacturers specifications, indicating that the unit was functioning properly.

The assembled 4-way prototype rotary valve, including the external driving mechanism and new magnetic linear encoder sensor, is shown in Fig. 3.30. Port plates are used to test the valve as a standalone unit without the need to mount the valve onto the bent axis P/M. Initial benchtop testing of the valve exhibited unusual behavior that was later attributed to internal leakage. Disassembling the valve revealed voids in the spool body that were due to casting defects (see Fig. 3.31). 3M acrylic adhesive was



Figure 3.29: Left: Custom 4-way P/M housing compared to stock housing. Center: Fixed displacement bent axis P/M disassembled to replace housing and insure correct timing. Right: Fully re-assembled P/M with custom housing installed.

used to seal the internal voids. Static testing at $14MPa$ verified that the repair was successful. Further testing validated the new magnetic linear encoder axial sensor as well as the functionality of the rotary valve at low pressure and PWM frequencies up to $40Hz$. In the horizontal orientation shown in Fig. 3.30 with the P/M attached to the valve via hoses, the system was run at $40Hz$ PWM frequency for minutes at a time without issue, with the longest run on the order of 10 minutes.

Once preliminary bench testing was complete, the prototype was transported to Sauer-Danfoss in Ames, IA for more rigorous testing. The test circuit illustrated in Fig. 3.32 was set up in one of their test cells (see Fig. 3.33). Initial testing consisted of characterizing the fixed displacement P/M in pump mode to establish a baseline of the modified unit. Baseline testing was completed successfully with speed and pressure maps recorded. Unfortunately, testing with the rotary valve mounted to the P/M was plagued by seizing. Less than 5 seconds of rotary run time was managed despite numerous attempts to clean and repair the valve. A scanning electron microscope (SEM) was used to analyze particles found after filtering a sample of solvent that was used to clean the disassembled prototype. The SEM detected PTFE, 8620 steel, stainless steel, zinc, and plain carbon steel, as shown in Fig. 3.34. In a last ditch effort, the valve was completely disassembled, the critical diameters of the spool and sleeve were honed, and all of the parts thoroughly cleaned with solvent. The test stand was completely flushed and filters were installed in all upstream lines. Upon reassembly, the spool seized almost immediately as testing resumed.

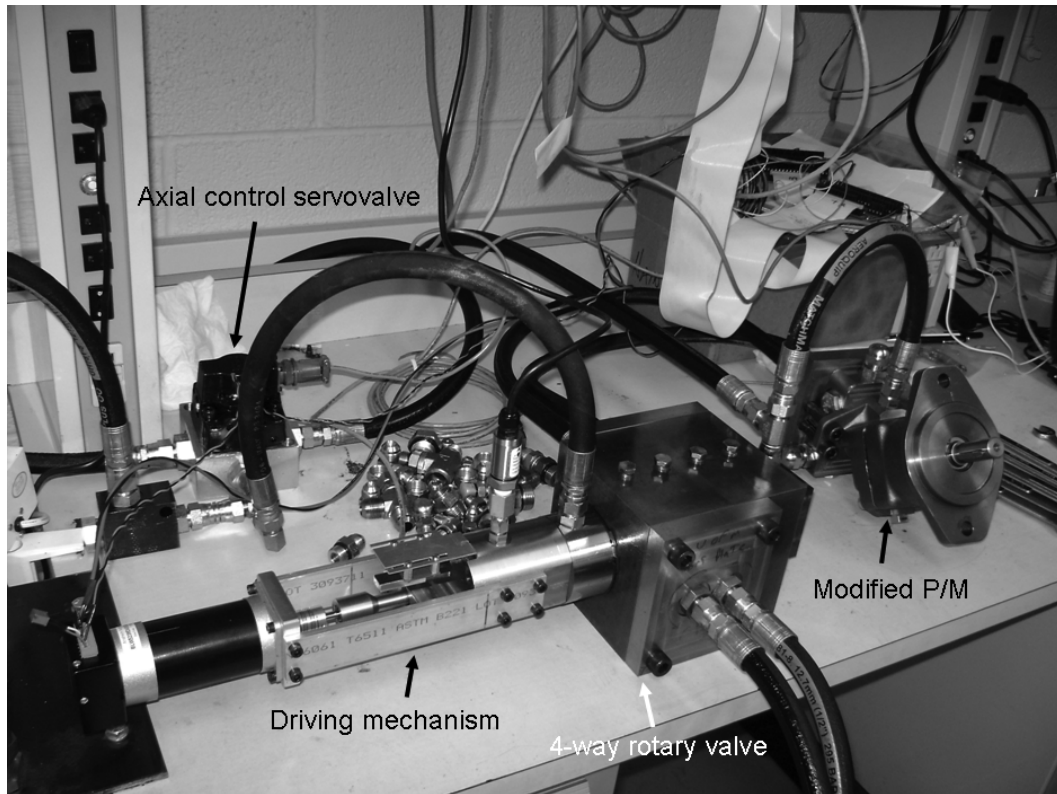


Figure 3.30: Initial benchtop setup for running in the 4-way rotary valve. Port plates enable running the valve as a standalone unit for troubleshooting purposes. The fixed displacement P/M is connected to the valve via hoses.

3.8.1 Full Open Pressure Drop

While seizing prevented investigating the VVDPM's pressure profiles and efficiency characteristics, full open pressure drop data was taken. A diagram of the flow and valve position convention used to describe the data is illustrated in Fig. 3.35. Data was sampled at $1kHz$ using $70MPa$ pressure sensors. Recall that the expected pressure drop across the valve predicted from the analysis in Section 3.4.1 (see also Fig. 3.17) is on the order of $.7MPa$ at $82lpm$. Unfortunately, the sensors used were sized for normal PWM operation at $21MPa$ and improperly sized for measuring the valve's pressure drop. However, it may be possible to glean qualitative information from the data. The flow rates used to generate the plots in this section were calculated by subtracting the case flow from the ideal flow of the P/M based on its speed and displacement. This flow

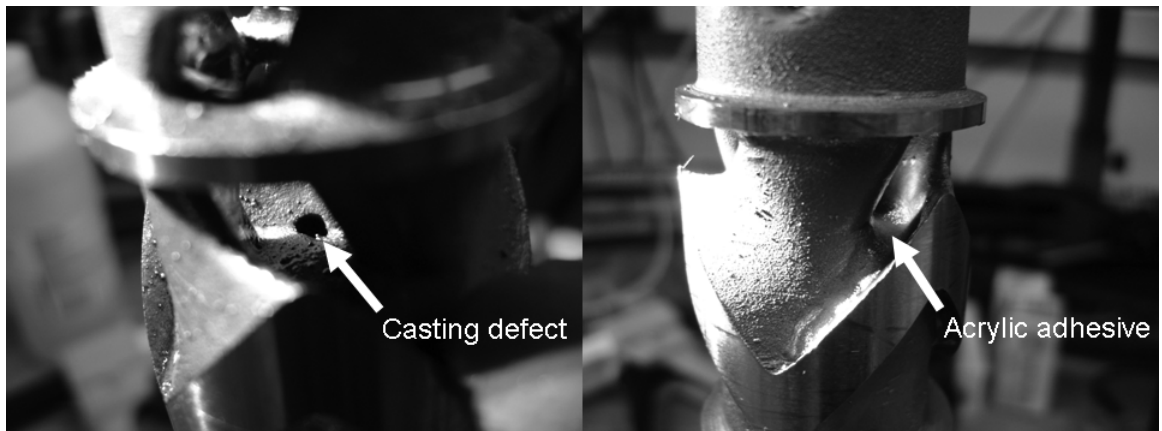


Figure 3.31: Left: Casting defects led to internal voids in the spool which resulted in cross port leakage. Right: Voids were repaired using 3M acrylic adhesive.

Table 3.5: Measured pressure in MPa averaged over $0.5s$ immediately following each test run.

Direction	Position	P_A	P_B	P_C	P_D
CCW	I	1.51	1.63	1.67	1.71
CW	I	1.51	1.63	1.67	1.70
CCW	II	1.68	1.77	1.77	1.86
CW	II	1.66	1.76	1.76	1.84

was used instead of data from the flow meter to keep results consistent between the two valve positions. In Position II, the P/M is recirculating and no flow measurements are available.

The pressures recorded by the pressure sensors at Ports A , B , C , and D for varying flow rates in Positions I and II are shown in Figs. 3.36 and 3.37 respectively. Gage pressure is presented instead of pressure differentials to illustrate several unexpected trends with the data. For example, in Fig. 3.36(a), flow is directed through the valve from Port B to D . However, P_B is less than P_D until the flow exceeds $22lpm$ which would suggest back flow through the valve. Similarly, in Fig. 3.36(b), fluid is flowing from Port A to C even though P_A is less than P_C . In Position II, the same inconsistency is present. Figure 3.37(b) shows that P_A is less than P_B for flow rates less than $25lpm$ even though flow is directed through Port A to Port B .

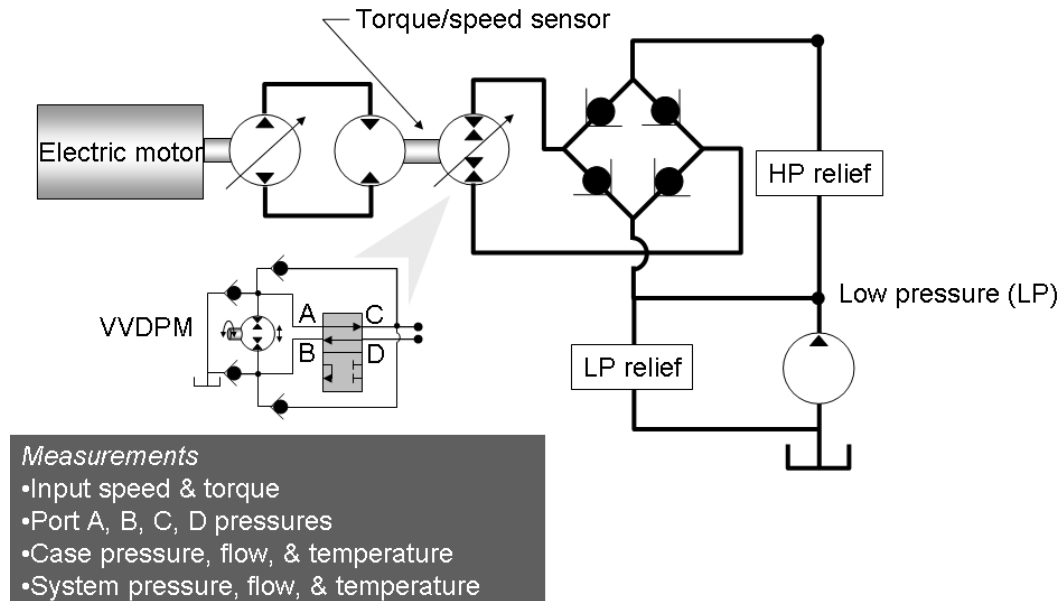


Figure 3.32: VVDPM pump test circuit used in test cell at Sauer-Danfoss in Ames, IA. The 4-way check allows testing both shaft directions of the pump without the need to reconfigure the circuit.

Delving deeper into the data suggests that the inconsistencies are attributable to the improperly sized 70MPa pressure sensors. Table 3.5 lists pressure data averaged over 0.5s for all combinations of P/M direction and valve position after each test run when the P/M is stationary. Although this data is not a true representation of the calibration of each sensor, it provides meaningful insight into the test data. Table 3.5 shows that P_A is consistently $.1\text{MPa}$ lower than P_B and P_C as well as $.2\text{MPa}$ lower than P_D . While $.1\text{MPa}$ is only approximately $.1\%$ of the full scale output of the 70MPa pressure sensors, it is greater than the valve's expected full open pressure drop below 30lpm of flow. While the data does not provide quantitative pressure drop characteristics, it confirms that the full open pressure drop of the 4-way valve is small and within the range estimated in Section 3.4.1 and Fig. 3.17. Figure 3.38 overlays the predicted pressure drop per valve section from Fig. 3.17 with the experimentally measured pressure drops using the 70MPa sensors.

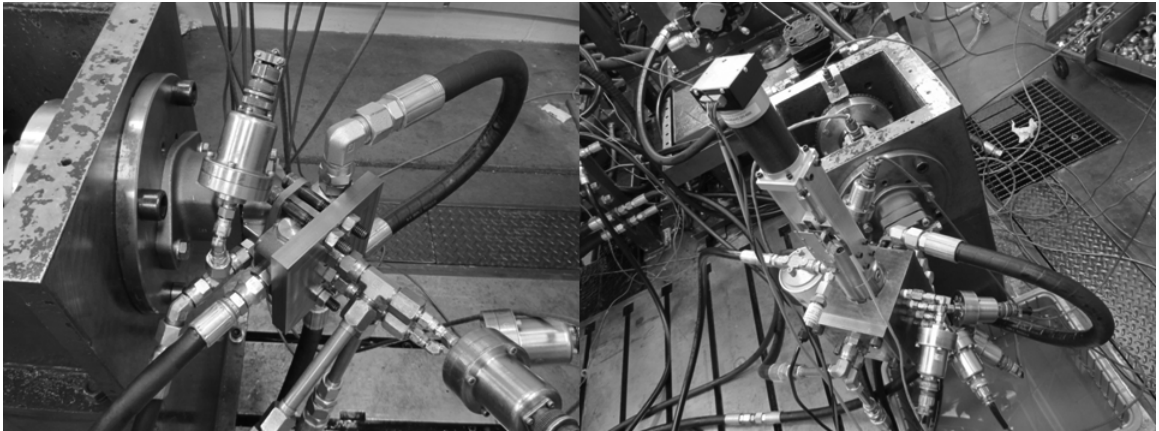


Figure 3.33: Left: Baseline testing of the modified P/M as a standalone unit in test cell at Sauer-Danfoss in Ames, IA. Right: VVDPM assembled for testing with the 4-way rotary valve mounted on the P/M.

3.9 Conclusions

The 4-way tandem rotary valve proposed in this chapter extends the self-spinning helical land rotary valve concept to motors and pump/motors. A design case study of implementing the proposed valve in a virtually variable displacement pump/motor for use as the speeder P/M on a light weight input coupled power-split hydraulic hybrid passenger vehicle was conducted. Due to the high operating pressure required by the HHPV and the cyclic nature of PWM, a systematic approach for sizing the sleeve wall thickness based on fatigue considerations was developed to insure safe operation of the valve. At 21MPa working pressure the analysis suggests that higher strength alloy steel, such as 4140, is required to achieve a reasonable safety factor for infinite fatigue life.

Design equations developed for analyzing the 3-way valve were extended to the 4-way valve and used to optimize the valve geometry over the combined EPA Urban and Highway drive cycles. The optimization revealed that rotating the spool with an external actuator was significantly more efficient than relying on self-spinning, even when considering the additional actuation power. This is due to the large variation in flow rate through the valve which results from the large range of shaft speeds encountered by the speeder over the Urban and Highway drive cycles. For the 30mm diameter spool

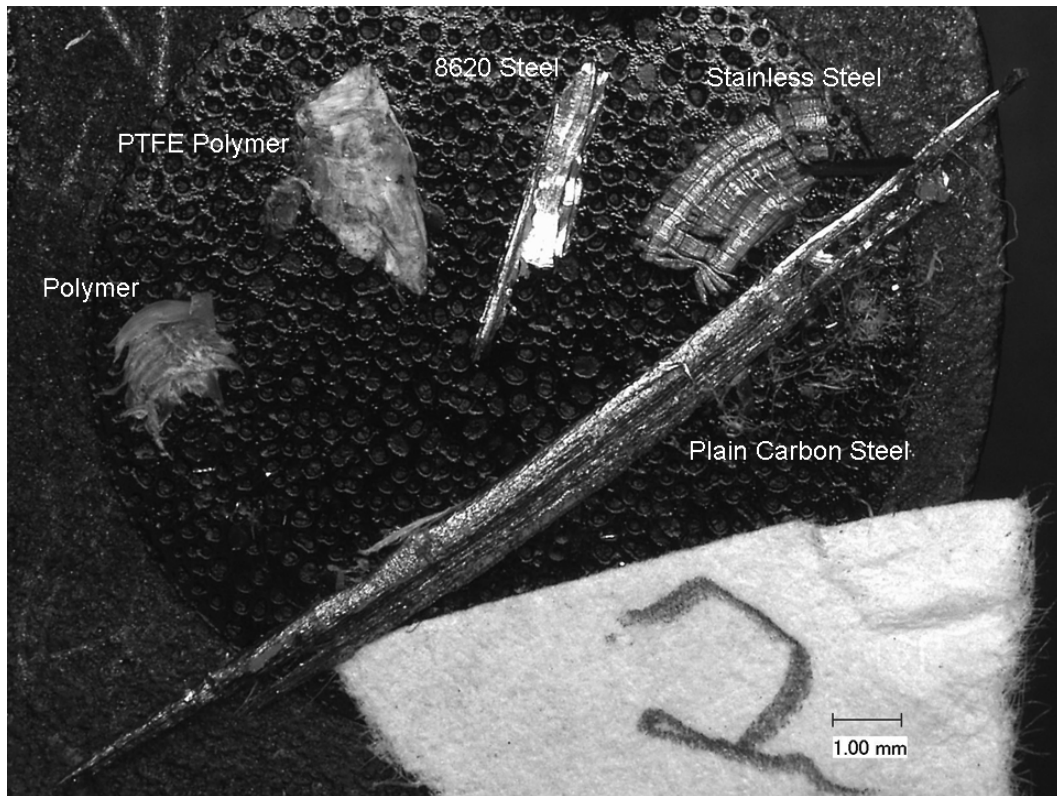


Figure 3.34: Scanning electron microscope analysis of filtered solvent used to clean the prototype valve revealed numerous contaminants.

considered in the analysis with 105mm^2 flow area, actuation power due to bearing type friction at the spool lands is the lowest loss and ranges from 16W at 40Hz to 101W at 100Hz . Adding in friction due to fluid recirculation increases actuation power to 22W at 40Hz and 136W at 100Hz . In context, recall that the Sturman digital valve [27], with flow area of only 23mm^2 , requires $.7\text{J}/\text{switch}$. Assuming two switches per PWM period, the Sturman valve requires 140W at 100Hz . This equates to roughly the same power consumption for a valve that has only one quarter of the flow area of the 4-way rotary valve. This comparison presents a great example of the low actuation power benefit of exploiting rotary motion. To enable externally spinning the valve spool, a two degree-of-freedom driving mechanism that decouples the rotary and axial sealing functions was proposed and experimentally validated.

A dynamic model of the VVDPM was developed based on the pressure dynamics in

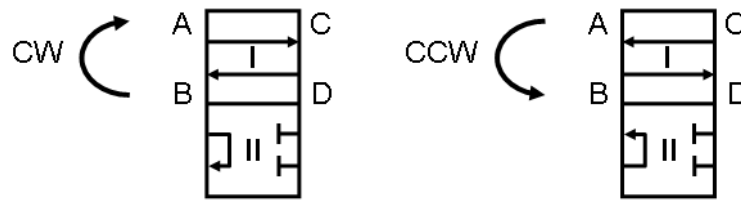


Figure 3.35: Flow direction and position convention used to describe 4-way VVDPM experimental data.

the A and B ports of the P/M which are both switched volumes. The model was used to simulate the VVDPM in both pumping and motoring. Full efficiency maps including losses from the fixed displacement bent axis P/M were generated using the model. For the HHPV case study presented in this chapter, the VVDPM was not able to match the drive cycle efficiency of the baseline variable displacement bent axis machine. However, despite the lower cycle efficiency, replacing the speeder P/M with a VVDPM only results in a slight decrease in fuel economy ($.4mpg$ or $-.6\%$). Replacing both P/Ms results in a slightly larger decrease ($3.3mpg$ or -5%).

A prototype rotary valve was fabricated that included a custom housing for the fixed displacement bent axis P/M to reduce the internal switched volume of the valve. The P/M was successfully modified with the custom housing and preliminary bench testing validated the functionality of the 4-way valve. Unfortunately, seizing plagued the valve during the next stage of testing which prevented meaningful data from being taken. Full open pressure drop data was extracted but pressure sensors sized for the efficiency aspects of the testing proved too insensitive to provide quantitative pressure drop numbers. However, the available data qualitatively suggests that the pressure drop across the 4-way valve is small and within the expected range.

The analysis and simulations performed in this chapter showed that although functional, the 4-way tandem valve, when used in a VVDPM, still lacks the efficiency necessary to make it a compelling alternative to current variable displacement P/Ms. The optimization study found that transition losses were dominant, followed by compressibility losses when the PWM frequency is high. For pumping, bypass check valves connected in parallel with the on/off valve to the system accumulator can provide significant reductions in transition losses. In contrast, there is currently no analogous technique for

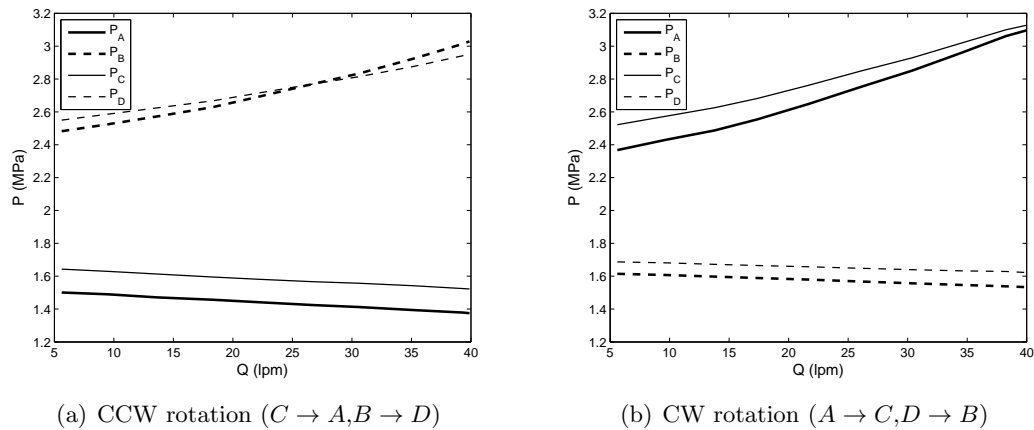


Figure 3.36: 4-way valve Position I pressures. When the P/M is spinning CCW, Port A of the valve coincides with the the inlet side of the P/M and Port B the outlet side. The 4-way check directs the flow such that Port C is connected to low pressure and Port D is connected to high pressure. When the P/M is spinning CW, Port A coincides with the outlet side of the P/M and Port B the inlet side. Port C is connected to high pressure and Port D is connected to low pressure. The cavitation preventing check valves are active on the inlet side of the P/M.

motoring. Several constraints in the rotary spool type architecture, including material and internal switched volume limitations, prevent the valve from operating efficiently at higher pressures and PWM frequencies. The sleeve pressure rail introduces a trade off between compressibility and throttling. A small rail volume is required to decrease the frequency dependent compressibility losses. However, reducing volume by decreasing the cross sectional area of the rail increases throttling. The pressure rail also drives the valve spool to small diameters, which increases the pressure drop across the tortuous internal geometry of the spool. The spool length also increases as a result of small diameter. Long spool length, when combined with the substantial sleeve wall thickness for infinite fatigue life at high pressure, limits the compactness of the design.

The ring valve architecture, described next in Chapter 4, seeks to mitigate the frequency and pressure limitations of the spool valve by eliminating the pressure rail as well as simplifying the flow path of the fluid through the on/off valve. In addition to improving the fundamental geometric structure of the valve, other ideas to improve

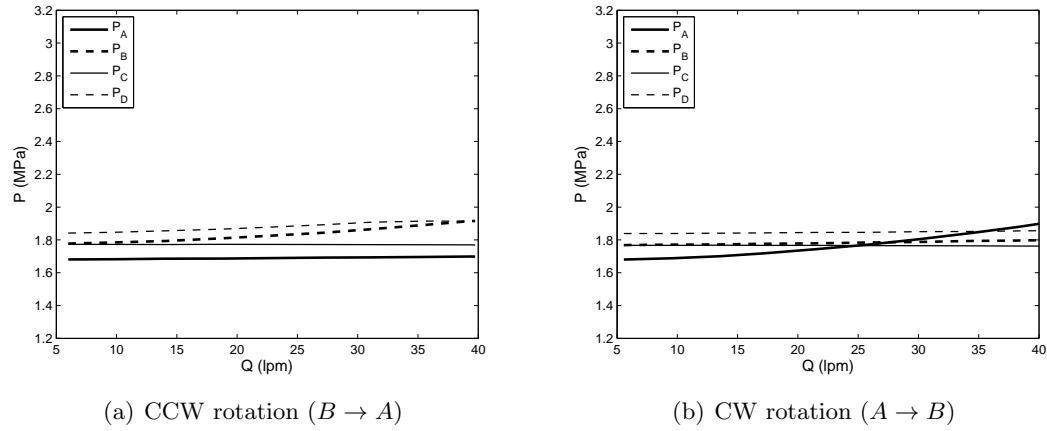


Figure 3.37: 4-way valve Position II pressures. Ports C and D of the valve are blocked in this position. When the P/M is spinning CCW, Port A of the valve coincides with the inlet side of the P/M and Port B the outlet side. Flow is sent through the valve from Port B back to Port A .

efficiency will also be discussed.

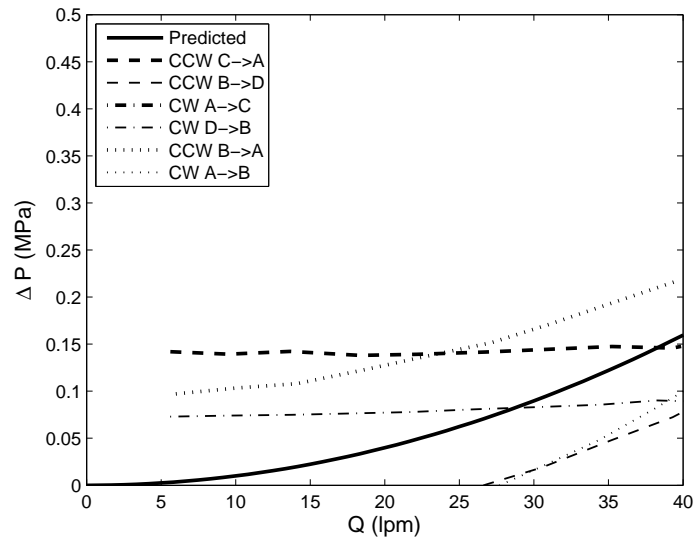


Figure 3.38: Predicted pressure drop across the valve orifice, spool, and toroidal pressure rail compared to measured data from the prototype valve. While the measured data is inaccurate due to inappropriately sized sensors, the pressure drops are qualitatively within the range of the analysis.

Chapter 4

Ring valve concept and other ideas for improving efficiency

The 4-way tandem rotary spool valve presented in Chapter 3 demonstrated the feasibility of adapting the rotary valve concept to four quadrant control of hydraulic pump/motors (P/M). However, the geometric structure of the valve imposed a trade off between compressibility losses and throttling which limited the valve's efficiency. In addition, the use of a 4-way configuration, originally chosen to enable self-spinning (which was later abandoned), also restricted the efficiency of the valve. Consequently, the virtually variable displacement pump/motor (VVDPM) was less efficient than a commercial variable displacement bent axis P/M.

This chapter presents a fresh valve concept that leverages what was learned from the preceding valve generations and starts with a new geometric structure that eliminates many of the trade offs of the spool valve approach. A novel hydraulic circuit for enabling four quadrant control is developed in conjunction with the new valve structure to provide additional efficiency and packaging benefits. Besides geometric and circuit changes, other ideas that have the potential to further enhance efficiency are also presented and discussed.

Section 4.1 presents a trade study that highlights several opportunities for improvement. Leveraging the trade study findings, a valve concept that is based on a ring

control element is introduced in Section 4.2 that realizes the valve requirements established in the study. A detailed simulation is used to compare the ring valve and its 4-way spool valve predecessor in Section 4.3. Section 4.4 introduces several additional concepts besides geometric and circuit changes that have the potential to further improve efficiency. Conclusions are discussed in Section 4.5. The work presented in this chapter has been filed in a patent disclosure.

4.1 Trade Study

The trade study in this section will compare valve configurations, circuit configurations, and valve geometry with the objective of taking a holistic approach to improving on/off valve and VVDPM efficiency.

4.1.1 Valve Configuration

The first aspect of design under consideration is the valve configuration. A 4-way tandem valve was initially selected when designing the first generation four quadrant VVDPM in Chapter 3 (see Section 3.2) in order to meet the self-spinning requirement. Self-spinning was later abandoned due to the inefficiency of relying on the spool's turbine like structure for spinning over a large range of flow rates. One limitation of the 4-way configuration is the additional throttling associated with metering four valve ports instead of three. Check valves can be used to reduce some of the throttling when pumping but not when motoring. For example, in Fig. 4.1, a low cracking pressure check valve can be used at the inlet of the pump to bypass the intake path of the 4-way valve when in Position I. A check valve parallel with the on/off valve with a cracking pressure higher than the full open pressure drop of the on/off valve can also be used to temporarily bypass the on/off valve when it is switching. Both approaches were used in the VVDPM circuit discussed in Section 3.2. One shortcoming, however, is that passive check valves cannot accomplish the same functionality when motoring.

In the 3-way valve, only two ports are active at one time (with the third port blocked) and the flow is only metered once through the on/off valve. Additionally, a check valve can be used with success on the intake side of the motor to reduce transition losses, as shown in Fig. 4.1. The check valve holds the inlet pressure of the motor low when

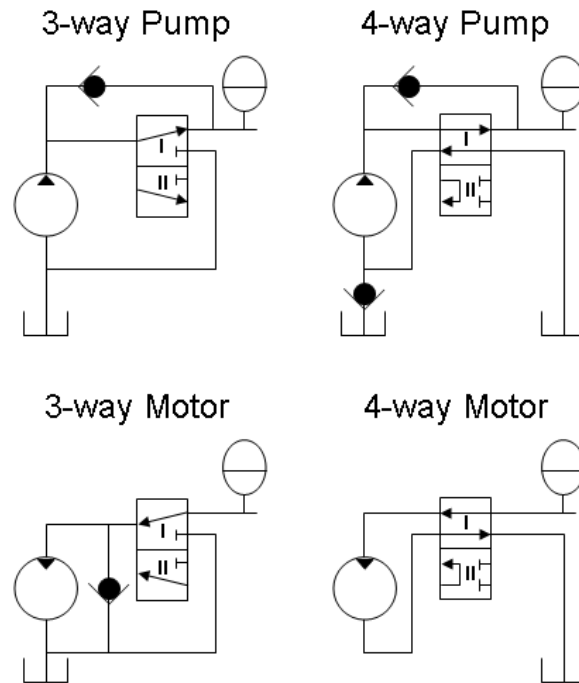


Figure 4.1: Comparison of 3-way and 4-way pumping and motoring circuits showing where check valves can be effectively used to reduce transition losses. Note that check valves are ineffective for reducing losses when motoring in the 4-way configuration.

opening and closing to Position II (to tank), thus bypassing the on/off valve during these two transitions as soon as the valve begins to switch. Comparing the transition loss equations for pumping and motoring between the 4-way (repeated from Section 3.4.1) and 3-way valves reveals a number of extra terms in the 4-way motoring loss that

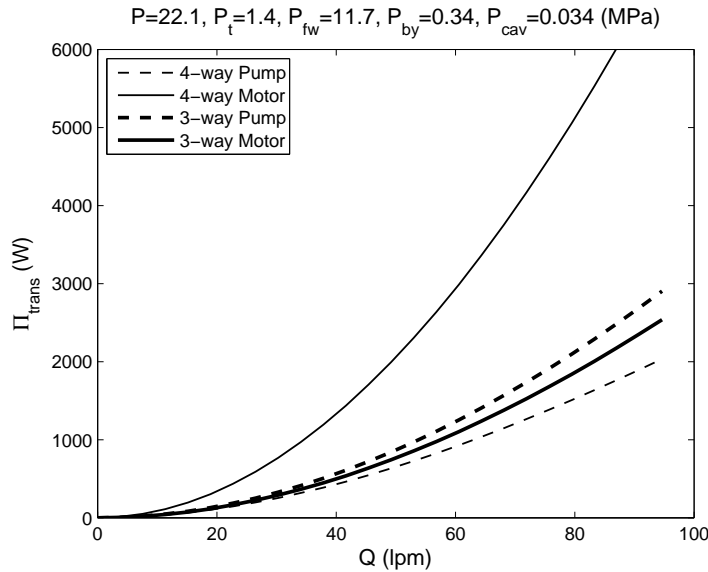


Figure 4.2: Comparison of 3-way and 4-way pumping and motoring transition losses using the 30mm diameter 4-way valve parameters presented in Table 3.2.

are due to the ineffectiveness of the check valves:

4-way Valve

$$\Pi_{trans,pump} = \frac{1}{4} \kappa \sqrt{P_{open}} Q \left[\frac{3(P - P_{fw}) + 4P_{by}}{\sqrt{P + P_{by} - P_{fw}}} + 4 \left(\sqrt{P_{by}} + \sqrt{P_{cav}} \right) - 6\sqrt{P_{open}} \right] \quad (3.24)$$

$$\Pi_{trans,motor} = \frac{1}{4} \kappa \sqrt{P_{open}} Q \left[\frac{3(P - P_{fw}) + 4P_{by}}{\sqrt{P + P_{by} - P_{fw}}} + \frac{3(P - P_t) + 4P_{by}}{\sqrt{P + P_{by} - P_t}} + \frac{3(P - P_t) + 4P_{cav}}{\sqrt{P + P_{cav} - P_t}} - 6\sqrt{P_{open}} \right] \quad (3.25)$$

3-way Valve

$$\Pi_{trans,pump} = \frac{1}{4} \kappa \sqrt{P_{open}} Q \left[\frac{3(P - P_t) + 4P_{by}}{\sqrt{P + P_{by} - P_t}} + 4 \left(\sqrt{P_{by}} - \sqrt{P_{open}} \right) \right] \quad (4.1)$$

$$\Pi_{trans,motor} = \frac{1}{4} \kappa \sqrt{P_{open}} Q \left[\frac{3(P - P_t) + 4P_{cav}}{\sqrt{P + P_{cav} - P_t}} + 4 \left(\sqrt{P_{cav}} - \sqrt{P_{open}} \right) \right] \quad (4.2)$$

P_{cav} and P_{by} are the cracking pressures of the cavitation preventing check valves (connected to tank) and bypass check valves (connected to the accumulator) respectively.

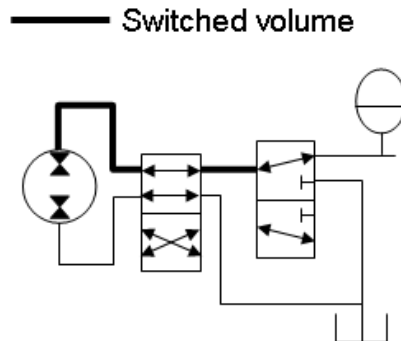


Figure 4.3: Conventional 3-way on/off valve based four quadrant VVDPM. Note that the 4-way directional valve needed for four quadrant operation contributes to the switched volume of the device. Check valves for preventing cavitation etc. are omitted for simplicity.

P is the system or accumulator pressure and P_t is the tank pressure. Figure 4.2 plots Eqs. (3.24)-(3.25) and (4.1)-(4.2) using the optimized 30mm diameter valve parameters in Table 3.2 assuming a working pressure differential of 20.7MPa and a freewheeling pressure halfway between P and P_t for the 4-way valve. The figure reveals that the 4-way motoring transition loss is more than twice each of the other losses and that the freewheeling pressure P_{fw} slightly reduces the 4-way pumping transition loss compared to the 3-way loss. This is because freewheeling enables the transition to start or end at an intermediate pressure instead of transitioning all the way back to tank. Based on the findings in Fig. 4.2, it is clear that the 4-way configuration should only be used if recirculation or self-spinning is required.

4.1.2 Four Quadrant Circuit Configuration

One disadvantage of conventional 3-way valve circuits when considering four quadrant operation is that a directional control valve (DCV) must be used between the on/off valve and the P/M which contributes to the switched volume, as shown in Fig. 4.3. The function of the DCV is to switch the port of the P/M that is pulse-width-modulated depending on the quadrant of operation that is desired. However, with a rotary type valve where the axial position is used to control its duty ratio, it is possible to build the port switching functionality of the DCV directly into the rotary valve's axial travel. This

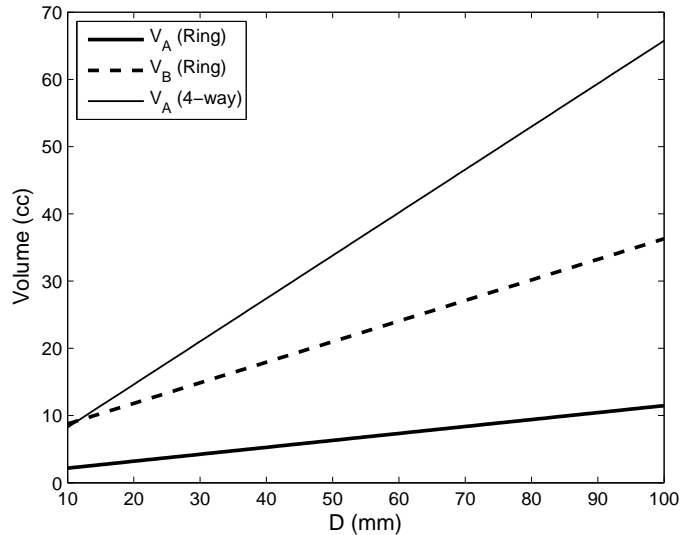


Figure 4.4: Comparison of internal switched volume between ring valve concept and 4-way rotary spool valve for varying valve diameters using the 30mm diameter spool parameters listed in Table 3.2 for $N = 3$. The 4-way valve is assumed to have a wall thickness ratio of $K = 3$. V_{pm} , the volume between the P/M and the valve, is not included in the comparison.

not only reduces the switched volume but also eliminates the DCV entirely and enables full four quadrant operation with just the on/off valve. The concept for embedding the port switching directly into the rotary valve will be presented in Section 4.2, which discusses the ring valve concept.

4.1.3 Valve Geometry

This section explores how switched volume, bearing friction, and leakage compare when inverting the rotary valve structure. The main idea behind the ring valve concept is to invert the rotating spool/stationary sleeve arrangement of the current valve into a structure that consists of a stationary central boss with internal fluid routing (analogous to the sleeve) that has rhombic ports which pass fluid to a rotating outer ring (analogous to the spool) that switches the valve between its on and off states. The idea behind the inversion is to reduce the switched volume by locating the pressure rail in the centermost region of the valve instead of having a toroidal rail that wraps around the

spool which must accommodate sufficient wall thickness for adequate fatigue life. This inversion results in two main benefits: 1) by having the rail centrally located internal to the rotating component, larger valve diameters are more easily achieved, resulting in larger flow areas; and 2) the high frequency pressure pulsing occurs in the central boss, which does not resemble a pressure vessel, and therefore eliminates the limiting internal to external pressure loading that was problematic in the 4-way valve. The rotating outer ring, however, does resemble a pressure vessel, although the 3-way configuration presented in Section 4.2 does not experience pressure pulsing.

The final embodiment of the ring valve concept described in Section 4.2 (see Fig. 4.8) contains two asymmetric pressure rails with internal volumes described by:

$$V_{A,ring} = \frac{\pi}{4} D_{rail}^2 (L + 1.5R_h) + \frac{1}{4} N R_w R_h D + V_m + V_{pm} \quad (4.3)$$

$$V_{B,ring} = \frac{\pi}{4} D_{rail}^2 (5L + 7.5R_h) + \frac{1}{4} N R_w R_h D + V_m + V_{pm} \quad (4.4)$$

where $L = \frac{\pi D R_h}{2 N R_w}$ and V_{pm} is the internal volume connecting the P/M to the valve. $V_m = \frac{\pi}{4} D_{rail}^2 \left(\frac{D_{pc}}{2} + D_{rail} \right)$, which will be neglected in the initial comparison, is the connecting volume for the fluid routing concept shown in Fig. 4.6 that joins the off-center tubular passages to each set of rhombic ports. Recall that the internal volume of the 4-way valve's inlet pressure rail is:

$$V_A = \left(\frac{N-1}{N} \right) \frac{\pi^2}{4} D_{rail}^2 (2r_e + D_{rail}) + \frac{1}{2} N R_w R_h (r_e - r_i) + V_{pm} \quad (3.28)$$

A comparison of the switched volumes between the ring valve and 4-way valve for varying valve diameters is presented in Fig. 4.4 assuming that the 4-way valve has a wall thickness ratio of $K = \frac{r_e}{r_i} = 3$. This is required for a fatigue safety factor of 2 according to Fig. 3.10. Additionally, both valves are sized using the geometric parameters for the 30mm diameter optimized spool valve in Table 3.2 with $N = 3$ switches per revolution. V_{pm} , the internal volume connecting the P/M to the valve, is not considered in the comparison and should be comparable between the two architectures. V_B in the 4-way valve is also omitted from the comparison since it depends on the internal volume of the spool itself which is difficult to project with respect to diameter. Furthermore, since V_B is typically larger than V_A , V_A represents the best case scenario for the spool valve. Figure 4.4 confirms that the ring valve concept drastically reduces the switched volume

of the valve with both volumes significantly less than the 4-way valve for equivalent diameters and cross sectional flow areas.

Bearing friction in the 3-way ring valve is potentially reduced compared to a spool valve of equal diameter since the ring valve only requires two sealing lands. The bearing friction area is:

$$A_{b,ring} = 2\pi DR_h \quad (4.5)$$

For comparison purposes, recall that the bearing friction surface area of the 3-way spool valve is:

$$A_b = \pi D [R_h + 2(L_1 + L_2)] \quad (2.33)$$

Comparing Eqs. (4.5) and (2.33), the bearing surface area of the ring valve will be smaller than a spool valve of equal diameter if $R_h < 2(L_1 + L_2)$.

Power lost due to leakage across the two sealing lands of the ring valve is estimated by making use of Eq. (2.24) (for a single helical land):

$$\Pi_{leak,ring} = \frac{2L_p c_r^3 (P - P_t)^2}{12\mu R_w \sin \phi} \quad (4.6)$$

For comparison, recall that the combined leakage power loss in the 3-way spool valve (Eqs. (2.24) and (2.25)), with the assumption that the axial control chamber is at tank pressure P_t , is:

$$\Pi_{leak,spool} = \frac{L_p c_r^3 (P - P_t)^2}{12\mu R_w \sin \phi} + \frac{\pi D c_r^3 (P - P_t)^2}{12\mu L_1} \quad (4.7)$$

Equating Eqs. (4.6) and (4.7) and solving for L_1 results in the critical end land width:

$$\bar{L}_1 = \frac{\pi D R_w^2 R_h}{(\pi D - N R_w)(R_w^2 + R_h^2)} \quad (4.8)$$

End land widths greater than the critical value \bar{L}_1 will result in the spool valve having less leakage than an equivalent ring valve and vice versa for land widths less than the critical value. Figure 4.5 plots Eq. (4.8) with respect to spool diameter for a fixed rhombus width and height using the 30mm diameter spool parameters presented in Table 3.2.

4.1.4 Trade Study Conclusions

Valve configurations, circuit configurations, and valve geometry were explored in the trade study to identify sources of loss in the current rotary spool valve that could be

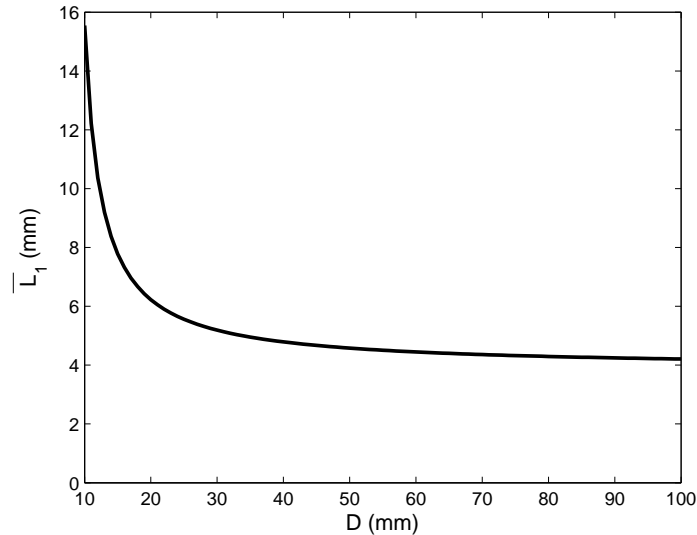


Figure 4.5: Critical end land width \bar{L}_1 with respect to spool diameter (D) for fixed rhombus width ($R_w = 7.85mm$) and height ($R_h = 8.94mm$) using the 30mm diameter spool parameters in Table 3.2. End land widths greater than \bar{L}_1 will result in the spool valve having less leakage than the ring valve.

eliminated with intelligent design changes. Four of the five primary rotary valve losses (transition, compressibility, friction, and leakage) were investigated. Full open losses were not considered due to the considerable dependence of these losses on the actual geometry of the fluid paths within the valve. However, the rhombic orifice geometry (and therefore flow area) was consistent between different valve structures when comparing losses. In addition, analysis conducted when designing the 3-way valve in Chapter 2 and 4-way valve in Chapter 3 has shown that full open losses are typically small (refer to Table 2.2 and Fig. 3.16). Of the four losses studied, two losses can be reduced significantly with little impact on the remaining losses. Transition throttling losses, especially for motoring, can be reduced by using a 3-way valve instead of a 4-way tandem valve. This change reduces the number of valve ports that are metering flow and also enables passive check valves to be used to bypass the on/off valve during transition. Compressibility losses, related to the internal switched volume of the valve, can be reduced by inverting the rotary valve spool and sleeve, which is the basis of the ring valve concept. An additional benefit of the inversion is that the direction control

valve between the on/off valve and pump/motor can be eliminated, thus reducing the switched volume further as well as enabling full four quadrant operation with a single valve. Despite these changes, friction and leakage are comparable between the spool and ring architectures for equivalent valve diameters. However, one caveat is that small valve diameters may be difficult to realize with the ring valve concept due to the requirement of packaging the flow passages within the inner diameter of the rotating ring. The ring valve concept is introduced next in Section 4.2.

4.2 Ring Valve Concept

The 3-way ring valve concept is illustrated in Fig. 4.6. The ring valve is composed of two main components: 1) a stationary cylindrical boss with internal fluid routing that mates to a fixed displacement P/M, and 2) a rotating and translating hollow ring that features two synchronized helical lands along its inner diameter. Figure 4.6 shows a preliminary fluid routing concept. Ports on the end of the boss mate with identical ports on the housing of the P/M. The fluid is then routed through the boss and exits the boss's surface via three sets of rhombic ports (*A*, *B*, and *C*). The ring translates and rotates with respect to the boss with a clearance gap between the innermost surface of the ring's helical lands and the outer diameter of the boss. Port *C* of the boss is connected to high (accumulator) pressure at all times and therefore pressurizes the volume between the helical lands. The ends of the ring are exposed to tank pressure in an open bath of fluid that is connected to tank. Not shown is a housing that surrounds the ring that seals the valve from the outside environment.

Figure 4.7 illustrates the integrated port switching functionality that enables eliminating the 4-way directional valve needed for four quadrant control when using conventional 3-way valves. When the ring is centered in its axial travel, the helical lands do not connect Port *C* with Ports *A* or *B*. Therefore Port *C*, connected to high pressure, is blocked at all times. Ports *A* and *B* are connected to tank and to each other. In this position, the valve is at zero duty ratio and the VVDPM at zero effective displacement. When the ring shifts to the left, one of the helical lands begins to PWM Port *A* between tank and high pressure, similar to the 3-way spool valve discussed in Chapter 2. The axial travel of the ring determines the valve's duty ratio and its rotational velocity

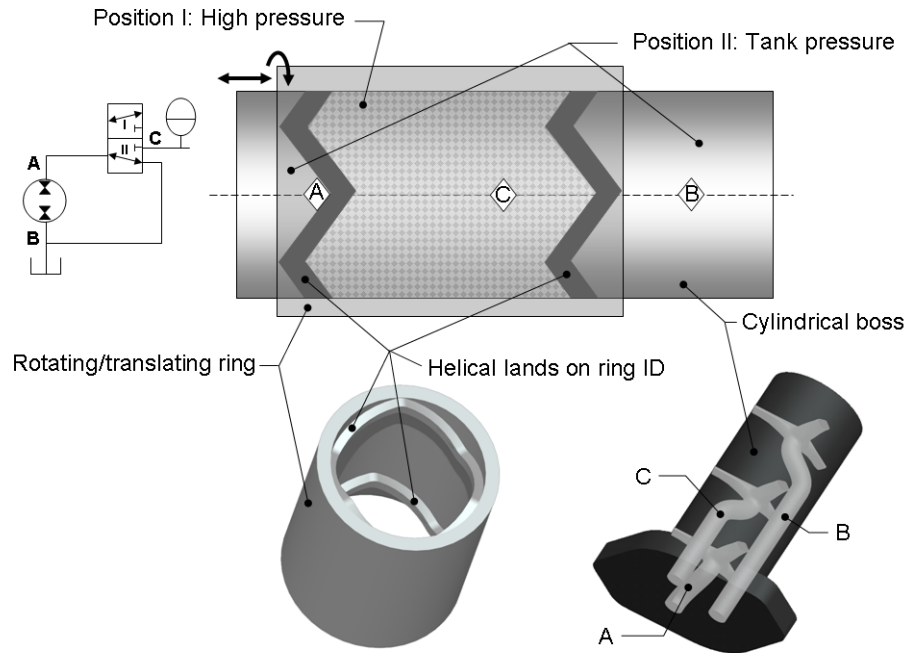


Figure 4.6: The 3-way ring valve consists of a stationary cylindrical boss with internal fluid routing and three sets of rhombic ports on its outer surface corresponding to Ports *A*, *B*, and *C*. A ring with two helical lands on its inner diameter rotates and translates on the boss's surface. Port *C*, located at the center of the boss, is connected to high (accumulator) pressure at all times. Ports *A* and *B*, on either side of Port *C*, are nominally connected to tank via an open bath of fluid that surrounds the ring. When the ring shifts left or right axially, Port *A* or *B* will be pulse-width-modulated between tank and high pressure via the internal cavity formed by the two helical lands. Switching of Port *A* is shown.

determines the PWM frequency. If PWM control of Port *B* is desired, the ring first crosses center (sending the VVDPM through zero displacement), and then shifts to the right which PWMs Port *B*.

4.2.1 Preliminary Sizing and Design Trade Offs

As an initial design study and comparison, a preliminary ring valve will be sized that retains the orifice area and internal flow areas as the optimized 30mm diameter 4-way valve in Table 3.2. A schematic of the geometric relationships defining the valve is

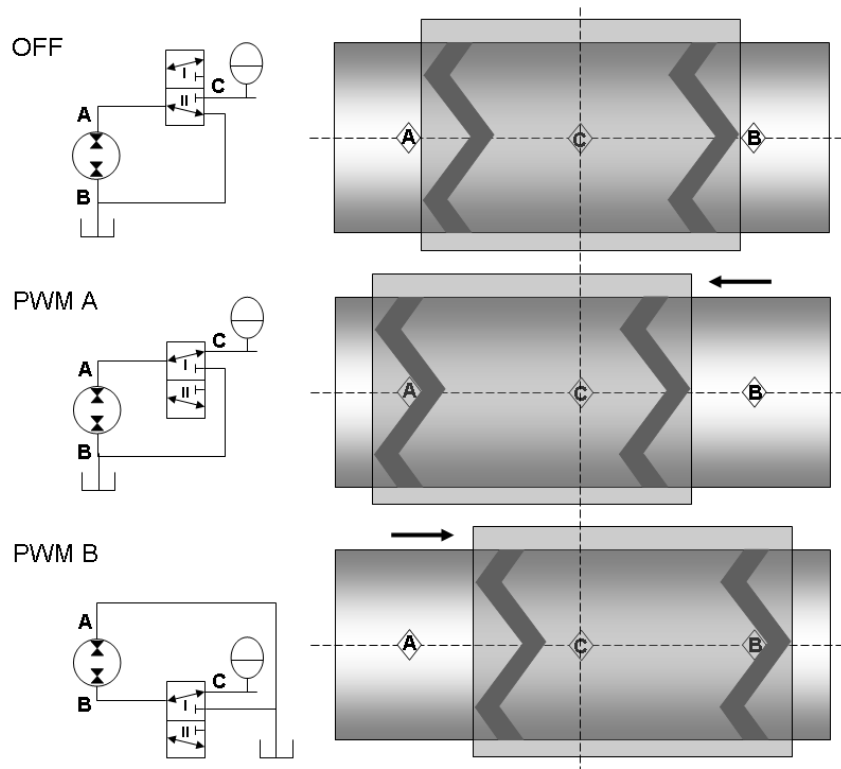


Figure 4.7: Port switching functionality embedded into the axial travel of the ring valve. Note that Port *C* is connected to high (accumulator) pressure at all times. When the ring is centered in its axial travel (top), Port *C* is always blocked. Ports *A* and *B* are connected to each other and to tank by the volume around the rotating ring. Once the ring shifts to the left (middle), the helical land on the left begins to PWM Port *A* between Port *C* at high pressure and tank. When the ring shifts past center to the right (bottom), it begins to PWM Port *B*.

shown in Fig. 4.8. This geometry was used when comparing the ring valve to the spool valve in the trade study performed in Section 4.1. The current concept requires a total axial travel of $2L + 3R_h$.

The ring valve is subject to similar trade offs and constraints as the spool type rotary valve. Because the ring valve uses the same helical land structure as the prior spool valves, it is bound by the same parallel constraint on the rhombic orifices. Recall the constraint equation from Section 2.3.6:

$$\kappa^2 \sqrt{P_{open}} = \frac{\sqrt{128\rho}Q_{in}}{\pi C_d DL} = \text{constant} \quad (2.43)$$

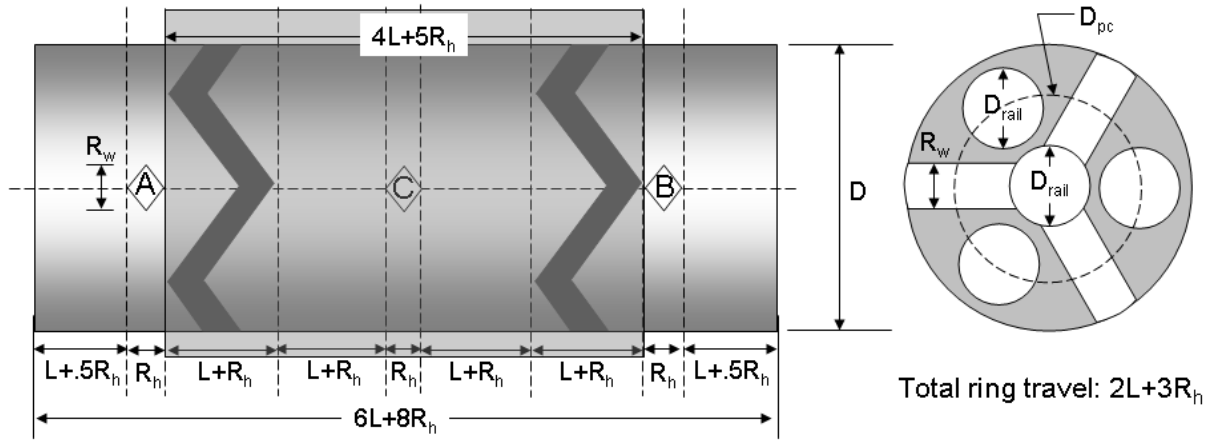


Figure 4.8: Diagram illustrating concept ring valve geometry used in the trade study in Section 4.1.

Equation (2.43) states that maximizing κ (to 1) produces the minimum transition loss for a given spool diameter because transition losses are proportional to $\kappa\sqrt{P_{open}}$. While large valve diameter is desirable from a throttling loss perspective to minimize $\kappa^2\sqrt{P_{open}}$ in Eq. (2.43), small valve diameter is desirable from the standpoint of actuation power (proportional to D^3) as well as compactness. For the ring itself, larger diameter requires a thicker wall to maintain equivalent hoop stress (refer to Eq. (3.3)). However, unlike the spool valve where there is little penalty on valve length, which can be increased to enable decreasing diameter while maintaining orifice area, valve length proportionally increases the switched volume of the ring valve (refer to Eqs. (4.3) and (4.4)).

Since the ring valve by nature necessitates larger valve diameters than equivalent spool valves due to packaging the fluid routing within the central boss, the initial valve geometry will be sized around the smallest ring diameter that maintains the orifice area A_r and internal flow diameter D_{rail} of the 4-way valve. For adequate wall thickness, a ring ID of $D = 60mm$ is chosen. This results in a minimum wall thickness of $4mm$ around the internal flow paths. Setting $\kappa = 1$ results in a rhombus width of $R_w = 15.7mm$ and a rhombus height of $R_h = 4.5mm$. This produces a rhombus aspect ratio of $\frac{R_w}{R_h} = 3.5$. Upon review, an upper bound of 2 on rhombus aspect ratio appears more reasonable and also facilitates better minimum wall thicknesses at the $60mm$ diameter

ring size. This results in $\kappa = .75$ and the valve geometry presented in Table 4.1. A break down of the losses of the preliminarily sized ring valve compared to the optimized 4-way valve are presented in Table 4.2 at the maximum system flow rate of $82lpm$ at $8400rpm$. Port A and B of the ring valve refer to the shorter and longer flow paths respectively as defined in Fig. 4.6. Note that only compressibility and full open losses are different between Ports A and B due to the internal volume and passage length differences. The initial results show that a sub-optimal ring valve exhibits a significant reduction in compressibility, full open, and transition losses compared to an optimal 4-way spool valve at the cost of higher actuation power and leakage. The valve parameters in Table 4.1 will be used in the simulation comparison in the next section.

Table 4.1: Comparison of valve parameters for $40Hz$ PWM frequency and $21MPa$ working pressure differential with $N = 3$. All lengths in mm and volumes in cc .

	D	R_w	R_h	A_r	D_{rail}	V_A	V_B	D_{pc}	L	κ
4-way	30	7.9	8.9	35.1	10.4	21.4	25.8	-	17.9	1
Ring	60	11.9	5.9	35.2	12	9.6	20.7	40	15.7	.75

Table 4.2: Comparison of rotary valve losses at $40Hz$ PWM frequency, $21MPa$ working pressure differential, and $82lpm$ flow rate ($8400rpm$). Total hydraulic power is $28kW$. Loss percentages are based on the total hydraulic power. Ring Port A and B refer to the shorter and longer flow paths respectively as labeled in Fig. 4.6.

	4-way	Ring Port A	Ring Port B
ΔP_{on} (MPa)	.61	.43	.49
ΔP_{off} (MPa)	.61	.14	.20
Π_f (W)	16.2 (.06%)	43.1 (.15%)	43.1 (.15%)
Π_{leak} (W)	62.2 (.22%)	122 (.44%)	122 (.44%)
Π_{comp} (W)	340 (1.2%)	74.8 (.27%)	164 (.59%)
$\Pi_{open,on}$ (W)	827 (3.0%)	589 (2.1%)	667 (2.4%)
$\Pi_{open,off}$ (W)	827 (3.0%)	189 (.68%)	267 (.95%)
$\Pi_{trans,pump}$ (W)	1806 (6.5%)	1548 (5.5%)	1548 (5.5%)
$\Pi_{trans,motor}$ (W)	5420 (19.4%)	1278 (4.6%)	1278 (4.6%)

4.3 Simulation Comparison

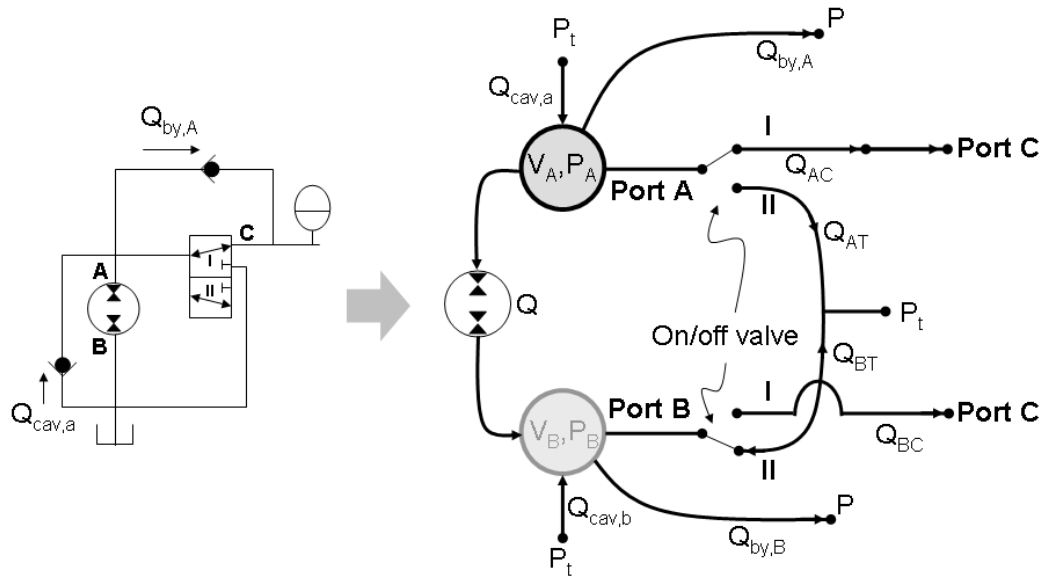


Figure 4.9: Flow diagram describing the ring VVDPM model including the fixed displacement pump/motor and on/off valve. Arrowheads indicate positive flow directions. Solid dots indicate flow junctions or pressure connections. To represent the port switching functionality of the valve, only one switch is active at a time with the other connected to tank when inactive. PWM of Port A is shown including check valves for preventing cavitation and reducing transition pressure spikes. The corresponding check valves for Port B are omitted for clarity.

The ring valve dynamic model is similar to the model proposed for the 4-way valve in Section 3.7 in that the pressure dynamics for the two internal volumes of the VVDPM are modeled (V_A and V_B). The same physical effects are modeled including fluid compressibility, the rhombic port and helical land geometry, and leakage across the major sealing interfaces. Simplifying assumptions include constant accumulator and tank pressures (P and P_t), no line losses, and no check valve dynamics (instant open/close). A flow diagram illustrating the sign conventions used in developing the dynamic equations is presented in Fig. 4.9. Using these conventions, the pressure dynamics in the ring

Table 4.3: Preliminary CFD generated ring valve pressure drop relations for the fluid routing concept shown in Fig. 4.6. The flow rate Q must be in units of m^3/s and A_r is the fully open area of one rhombic port as given in Table 4.1. The pressure drop across the ring is due to the inner cavity connecting flow between Port C and Ports A or B . The pressure drop across Port A is modeled as an orifice with a least-squares fit to determine the equivalent discharge coefficient of .704 based on CFD simulations. The pressure drops across Ports B and C are the pressure drop across A with an additional term to account for the longer connecting pipe length.

	Pressure drop (Pa)
Ring	$\Delta P_{ring} = 3.298 \times 10^{10} Q^{1.88}$
Port A	$\Delta P_A = \frac{\rho}{2} \left(\frac{Q}{.704NA_r} \right)^2$
Port B	$\Delta P_B = \frac{\rho}{2} \left(\frac{Q}{.704NA_r} \right)^2 + 5.167 \times 10^8 Q^{1.34}$
Port C	$\Delta P_C = \frac{\rho}{2} \left(\frac{Q}{.704NA_r} \right)^2 + 2.963 \times 10^8 Q^{1.34}$

valve are:

$$\dot{P}_{A,ring} = \frac{\beta(P_A)}{V_A} [-Q - Q_{AC} - Q_{AT} - Q_{by,A} + Q_{cav,a}] \quad (4.9)$$

$$\dot{P}_{B,ring} = \frac{\beta(P_B)}{V_B} [Q - Q_{BC} - Q_{BT} - Q_{by,B} + Q_{cav,b}] \quad (4.10)$$

Note that the pressure dynamics do not depend on leakage unlike the 4-way valve. This is because the ring valve's leakage is constant across the two helical sealing lands and is lost from the accumulator (Port C) and not the internal volumes (Ports A and B). The flows Q_{AC} , Q_{AT} , Q_{BC} , and Q_{BT} are found by solving the total pressure drop equations for each respective flow path based on the component pressure drops listed in Table 4.3. The component pressure drops are derived using the CFD method described in Sections 2.3.1 and 3.4.1 [52, 55, 56] and consist of three basic types of geometry: 1) the flow path through the ID of the ring that consists of (N) rhombic inlet ports and (N) rhombic outlet ports, described by ΔP_{ring} , 2) the single round inlet port that splits into (N) rhombic nozzles (refer to Port A in Fig. 4.6), described by ΔP_A , and 3) the long cylindrical ports that lead to the rhombic nozzles, described by the second terms in ΔP_B and ΔP_C . Notice that the cylindrical porting for Port B is longer than C , hence the larger coefficient. As an example of solving for flow, the total pressure drop from

Port A to C is $\Delta P_{AC} = \Delta P_A + \Delta P_{ring} + \Delta P_C$. The flow Q_{AC} is the root of the equation and can be found numerically using the Newton-Raphson method.

The dynamic model of the ring valve is simulated in the Matlab/Simulink environment using the same solver, step size, and system parameters used to simulate the 4-way tandem valve including 5% air entrainment (refer to Section 3.7). The only difference is a slightly reduced bypass check valve cracking pressure of $.62MPa$, down from $.76MPa$. This is due to the slightly lower predicted full open pressure drop of the ring valve. The valve geometry in Table 4.1 is used.

4.3.1 Pressure Profile Comparison

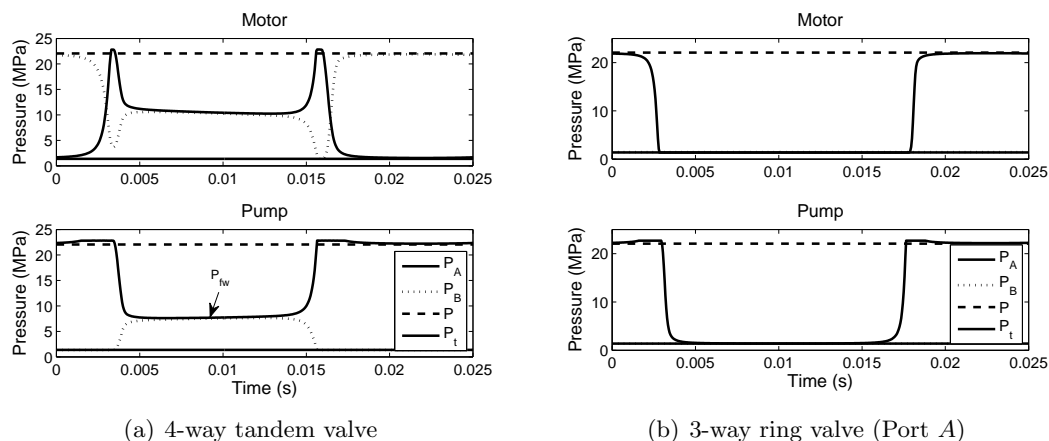


Figure 4.10: Comparison of VVDPM pressure profiles for motoring and pumping (one cycle) between the 4-way tandem valve and the ring valve. The VVDPM is operating at $4000rpm$ and 50% axial travel in both cases.

Pressure profiles for pumping and motoring are presented in Fig. 4.10 for both the 4-way tandem valve and 3-way ring valve for ease of comparison. In both cases the flow rate through the valve corresponds to a P/M shaft speed of $4000rpm$ with the valve at 50% of its axial travel. The ring valve profiles shown reflect the pressure dynamics at Port A which has half of the switched volume of Port B ($9.6cc$ vs. $20.7cc$). The motoring profiles of the ring valve are significantly cleaner than those of the 4-way valve

during valve transition. This indicates that the passive check valves are indeed reducing transition pressure spikes and therefore transition throttling losses.

4.3.2 Efficiency Map Comparison

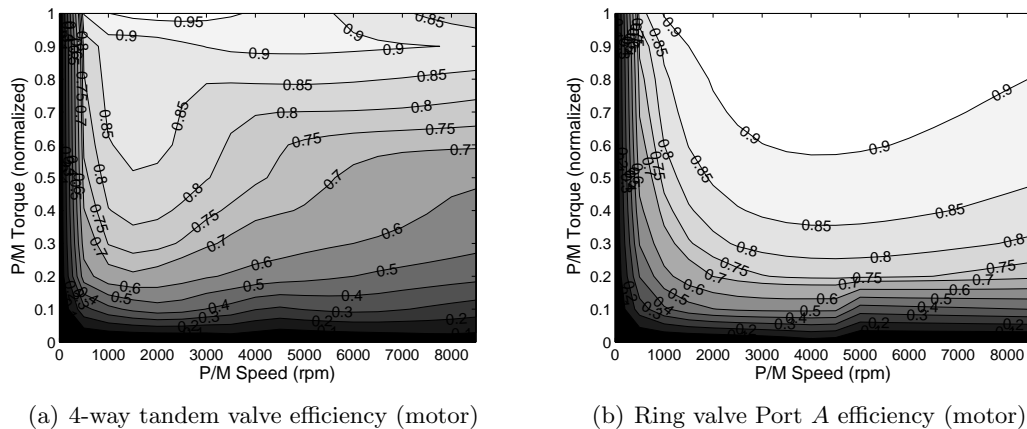


Figure 4.11: Comparison of VVDPM valve efficiency maps for motoring between the 4-way valve and ring valve at $40Hz$ PWM frequency for a system working pressure differential of $21MPa$. Losses from the fixed displacement P/M are not included.

The efficiency maps presented in Figs. 4.11 (motoring) and 4.12 (pumping) compare the 4-way valve efficiency maps (refer to Section 3.7.2 and Figs. 3.24(a) and 3.25(a)) to ring efficiency maps simulated using the same PWM frequency ($40Hz$) and system operating pressure differential ($21MPa$). The simulation results are also averaged over the same time interval ($T_{avg} = .25s$). Neglecting P/M losses, the valve efficiency for the 3-way ring valve at each combination of speed and valve axial position is:

$$\eta_{m,ring} = \frac{\int_{T_{avg}} \tau_{pm} \omega_{pm} dt}{\int_{T_{avg}} [(P - P_t)(-Q_{AC} - Q_{BC} - Q_{by,A} - Q_{by,B} + Q_{leak}) + \pi_{cav} + \pi_f] dt} \quad (4.11)$$

$$\eta_{p,ring} = \frac{\int_{T_{avg}} (P - P_t)(Q_{AC} + Q_{BC} + Q_{by,A} + Q_{by,B} - Q_{leak}) dt}{\int_{T_{avg}} [\tau_{pm} \omega_{pm} + \pi_f] dt} \quad (4.12)$$

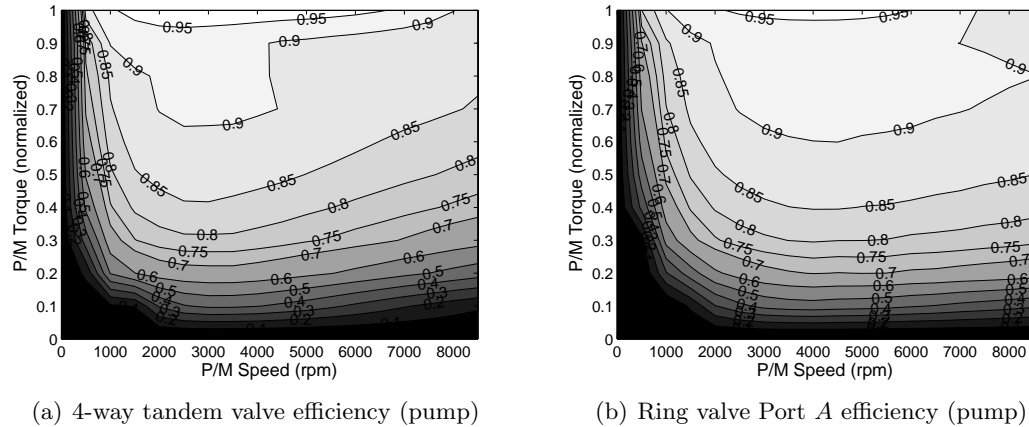


Figure 4.12: Comparison of VVDPM valve efficiency maps for pumping between the 4-way valve and ring valve at $40Hz$ PWM frequency for a system working pressure differential of $21MPa$. Losses from the fixed displacement P/M are not included.

$\pi_{cav} = [(P_t - P_B)Q_{cav,b} + (P_t - P_A)Q_{cav,a}]$ is the input power due to the cavitation preventing check valves.

Comparing the two motor efficiency maps in Fig. 4.11 shows that the ring valve significantly improves efficiency in comparison to the 4-way valve. The most apparent improvement occurs at high shaft speeds (i.e. flow rates) where the ring valve map is appreciably flatter. For example, at an effective displacement (i.e. normalized torque) of $.3$, the ring valve maintains 80% efficiency across a majority of the shaft speeds simulated. In contrast, the 4-way's efficiency is below 70% for most of the range and even drops below 60% above $7000rpm$. The pump efficiency maps presented in Fig. 4.12 show a similar trend, i.e. flatter efficiency with respect to shaft speed, although the improvement is not as remarkable as in motoring. For the most part, the efficiency below $3000rpm$ to $4000rpm$ is comparable between the two valves. However, above $4000rpm$ the efficiency of the ring valve flattens out instead of dropping off like the 4-way. The great improvement in motoring efficiency is likely attributable to the considerable decrease in motoring transition losses as shown in Fig. 4.2, which increase dramatically with flow rate. Since the ring valve shows improved efficiency during pumping as well, especially at higher flow rates, it appears that the lower pressure drops through the

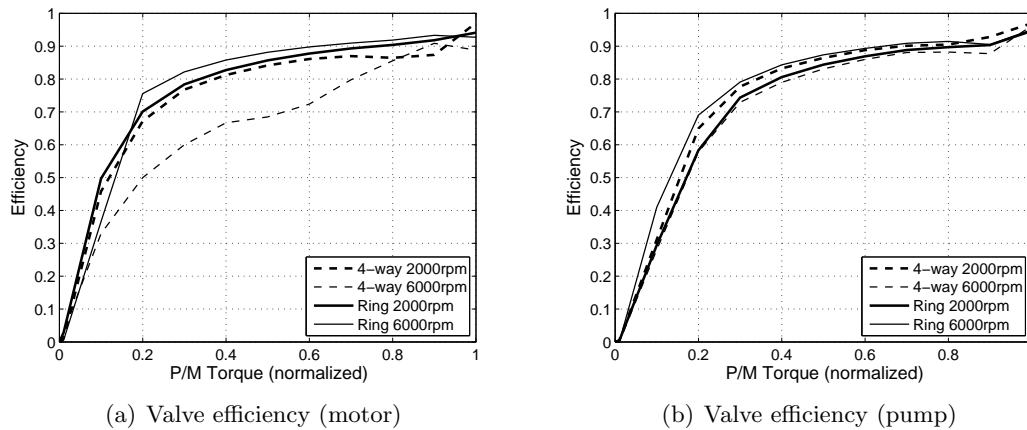


Figure 4.13: Comparison of VVDPM valve efficiency for motoring and pumping between the 4-way valve and ring valve at selected P/M speeds when operating at $40Hz$ PWM frequency for a system working pressure differential of $21MPa$. Losses from the fixed displacement P/M are not included.

valve due to its simpler flow paths is also important.

A comparison of efficiency at selected P/M speeds is presented in Fig. 4.13. Here, differences in efficiency when pumping appear less significant. As a quick check, refer to the losses in Table 4.2. Assuming a duty ratio of $s = 1$ when pumping, adding the relevant losses for the 4-way valve and Port A of the ring valve ($\Pi_f + \Pi_{leak} + \Pi_{comp} + \Pi_{open,on} + \Pi_{trans,pump}$) yields $3.05kW$ of loss for the 4-way and $2.38kW$ of loss for the ring. At $21MPa$ and $82lpm$, the total system power is $28kW$. This equates to an efficiency of 89% for 4-way pumping and 92% for 3-way ring pumping. Even though the ring valve losses are 22% lower, the difference in efficiency is small due to the high system power.

4.4 Other Ideas

This section contains a brief overview of several ideas to further improve efficiency in addition to the valve, circuit, and geometry improvements considered when designing the ring valve. Several of the ideas such as exploiting valve underlap and using higher

bulk modulus fluids are easy to implement and only require more structured analysis to determine the optimal parameters. Others, such as soft-switching, require advances in actuator technology. Underlap will be discussed first in Section 4.4.1, followed by soft-switching in Section 4.4.2, surface texturing in Section 4.4.3, and high bulk modulus oils in Section 4.4.4.

4.4.1 Underlap

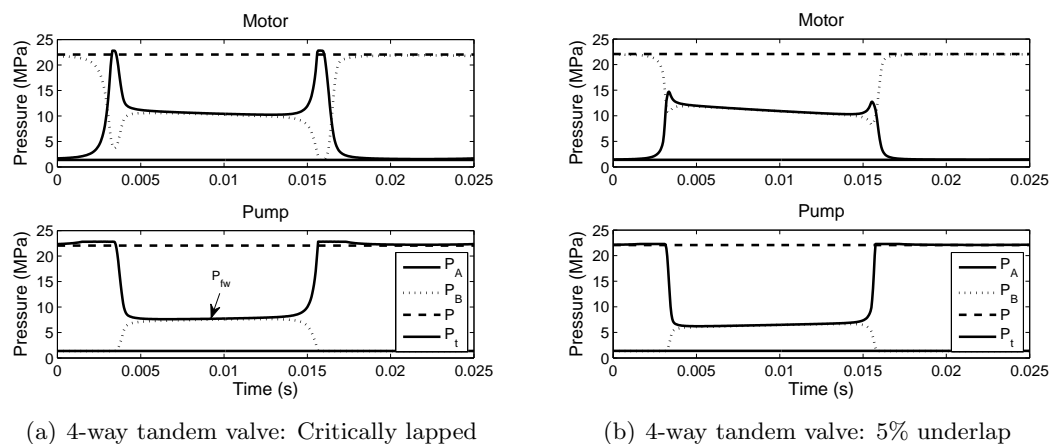


Figure 4.14: Comparison of 4-way tandem valve VVDPM pressure profiles for motoring and pumping (one cycle) with different valve lapping configurations. The VVDPM is operating at $4000rpm$ and 50% axial travel in both cases.

The idea behind valve underlap is to design the width of the helical land to be slightly narrower than the opening of the rhombic ports. With this configuration, the on/off valve never fully closes when transitioning. Instead, the valve will be temporarily open to both Positions I and II (or both load and tank) simultaneously for a short fraction of the transition. The valve open area when cross porting occurs is small and dependent on the amount of underlap. Because the valve never fully closes when switching position, pressure spikes during valve transition are reduced since the flow is never completely blocked. Figure 4.14, which compares pressure profiles for a critically lapped 4-way valve and one with 5% underlap, illustrates this effect. The transition pressure spikes

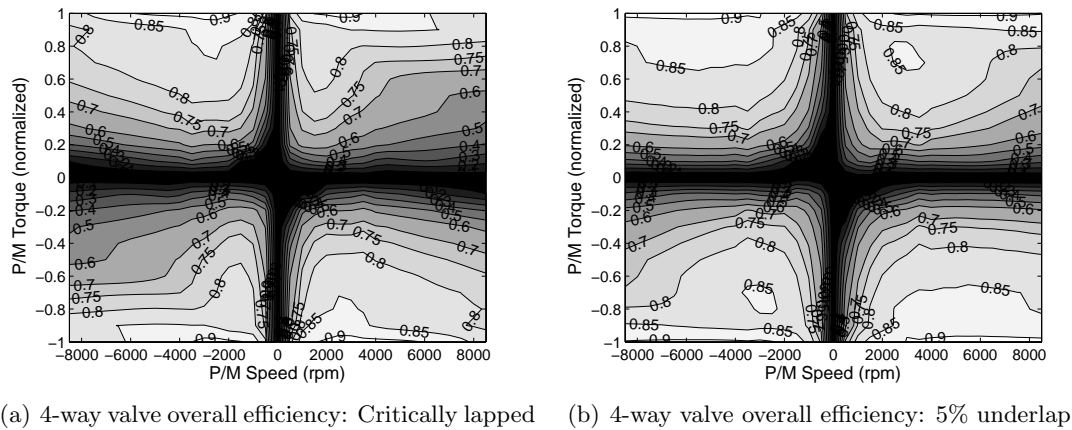


Figure 4.15: Comparison of VVDPM four quadrant overall efficiency maps (including P/M losses) for the 4-way valve with different lapping conditions at 40Hz PWM frequency for a system working pressure differential of 21MPa .

for motoring that could not be reduced with check valves are nearly eliminated with the introduction of a slight bit of underlap. The corresponding four quadrant overall VVDPM efficiency maps are presented in Fig. 4.15. Efficiency improvements are obtained in both motoring and pumping at higher shaft speeds. At lower speeds, especially for pumping, the critically lapped valve is more efficient. Underlap is potentially less effective at lower flow rates due to slower pressure dynamics in the switched volume. Recall Eq. (2.45) where \dot{P}_{in} is proportional to the net flow rate into the switched volume. At lower flow rates when pumping, the switched volume pressure may not have sufficiently risen when cross porting occurs which may lead to unwanted back flow during transition. A comparison of efficiency at selected P/M speeds is presented in Fig. 4.16 which reinforces this hypothesis. The critically lapped valve always exhibits higher efficiency except during low speed pumping. While underlap certainly has benefits for the 4-way valve especially when motoring, it may or may not benefit the 3-way ring valve depending on system parameters. However, when the flow rates are appropriate, underlap can provide additional improvements in efficiency on top of check valves.

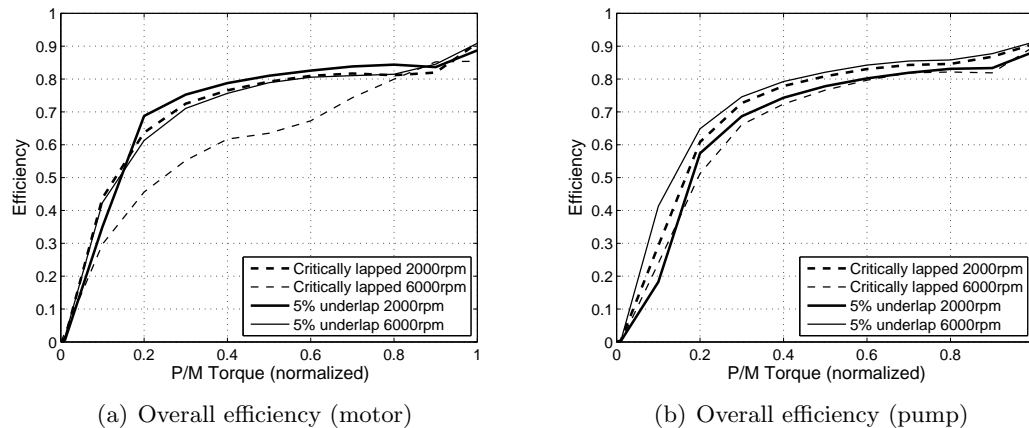


Figure 4.16: Comparison of VVDPM overall efficiency for motoring and pumping between a critically lapped 4-way valve and one with 5% underlap at selected P/M speeds when operating at $40Hz$ PWM frequency for a system working pressure differential of $21MPa$. Fixed displacement P/M losses are included.

4.4.2 Soft-switching

Soft-switching, proposed by Rannow et al. [47, 48, 49], is a method of reducing on/off valve transition losses for switched-mode pump circuits. The concept is to provide a temporary flow path during valve transitions that absorbs and stores fluid when the on/off valve's open flow area is small. This prevents the high throttling losses associated with forcing flow through a partially open valve. The fluid is then released to flow through the on/off valve once it has fully transitioned. The bypass check valves used in the 3-way, 4-way, and ring valve circuits accomplish a soft-switch function for the two load (high pressure) transitions for pumping. For the remaining two transitions to tank, soft-switching is realized using a piston with return spring that can be locked in the middle of its travel via an actively controlled locking mechanism. When opening to tank, the soft-switch works by releasing the locking mechanism as soon as the transition begins. This allows the piston to travel and absorb the pump flow while the valve opening is small, thus dropping and keeping the pressure low. Once the valve is fully open to tank, the return spring, sized to exert a pressure force higher than the full open pressure drop of the on/off valve, expands and forces the fluid out of the soft-switch

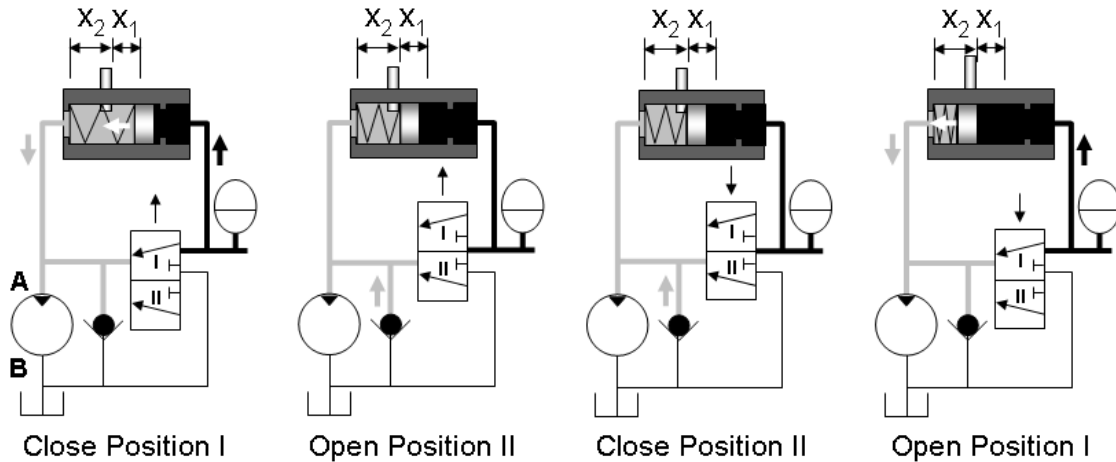


Figure 4.17: Soft-switching concept for 3-way motoring circuit. The soft-switch piston supplies flow rapidly during the two high pressure transitions (open/close Position I) to minimize throttling. The cavitation preventing check valve supplies flow to bypass the on/off valve during the two tank transitions (open/close Position II).

chamber and through the on/off valve. The spring forces the piston to the end of its travel while the on/off valve is open to tank. At this time the locking mechanism re-engages. When closing to tank, the soft-switch piston absorbs flow until it bottoms out against the locking mechanism situated near the middle of its stroke. The piston's travel up to the locking mechanism is sized such that it bottoms out close to when the on/off valve is fully closed to tank. When the piston bottoms out, the pressure in the switched volume rises rapidly and triggers the bypass check valve as the on/off valve begins to open to high pressure. The cycle repeats during the next opening to tank. For pump circuits, simulation predicts that a soft-switch chamber can reduce total valve cycle losses (not just transition losses) on the order of 11% by reducing the two tank transitions [47, 48, 49].

Soft-switching can be extended to the 3-way motor configuration by realizing that instead of absorbing flow during the two tank transitions, as was the case with pumping, flow must be supplied during the two load transitions. Figure 4.17 illustrates the motoring soft-switching concept. Initial travel X_1 is passively actuated. As the valve closes Position I, the additional pressure drop decreases the pressure in *A* which forces the soft-switch piston to translate. This provides additional flow to Port *A* to maintain

it at high pressure and to minimize the pressure drop across the on/off valve. Once the piston reaches the locking mechanism (timed with the opening of Position II), the pressure in A will drop rapidly, thus opening the cavitation preventing check valve and keeping the pressure drop across the on/off valve small (since Position II is connected to tank). The soft-switch piston remains locked in the middle of its travel by the locking mechanism when the on/off valve is open to Position II. As soon as the on/off valve begins to open Position I, the locking mechanism will release. Travel X_2 , actuated by the pressure differential across the piston, is used to supply flow rapidly to Port A to bring it to high pressure as the valve opens to Position I. When the valve is fully open to Position I the spring will return the piston to its opposite end of travel. During the next transition, closing Position I, the piston will translate once again through its initial travel X_1 , thus repeating the cycle.

While the motoring concept has yet to be simulated, due to the similarities between pumping and motoring when using a 3-way on/off valve, it is expected that soft-switching will provide a similar benefit to motoring as it does pumping.

4.4.3 Surface Texturing

Surface texturing at the micro scale has the potential to improve the trade off between leakage and friction at the sealing lands of the rotary valve. The concept is that surface textures at the micrometer-scale with respect to texture width and depth have the effect of increasing the effective fluid film thickness over a portion of the surface area of two sliding surfaces, which reduces the shear stress in Couette flow for constant clearance applications [84]. In essence, the clearance gap between the two surfaces is larger for a proportion of the total surface area which reduces the average shear across the entire area. Preliminary simulations show a reduction in friction with respect to texture depth, density, and width [84]. The optimum texture that exhibited the least friction had a high texture density and a texture width and depth of approximately ten times the nominal clearance [84]. Leakage can potentially be reduced simultaneously with friction by introducing a smaller nominal clearance.

Microtexturing the rotary valve's sealing lands is feasible using techniques such as micro-casting described by Cannon et al. [85, 86].

4.4.4 High Bulk Modulus Oil

Due to the high frequency switching between tank pressure and a high system pressure in switched-mode hydraulic systems, increasing the bulk modulus of the working fluid (or decreasing its compressibility) leads to a direct reduction in the frequency dependent compressibility losses. Compressibility losses are increasingly important at high PWM frequencies. Figure 2.7, presented in Section 2.3.2, illustrates the bulk modulus of a standard hydraulic oil with varying amounts of air entrainment along with the corresponding volumetric energy loss per switch for various load pressures. Decreasing air entrainment via proper reservoir design is an important first step as any air in the oil will dominate the fluid's effective bulk modulus. Various degassing devices are also available to reduce air entrainment. Additional improvements in bulk modulus can potentially be gained with the use of new high bulk modulus hydraulic oils that are currently under development by Tsubouchi et al. at Idemitsu Kosan Co., Ltd. [87, 88, 89]. The concept behind the new oil is to design the molecular structure of the fluid intentionally with high bulk modulus in mind. This is done by creating a thick liquid structure where benzene rings are densely packed close to one another which is unlike conventional oils where the molecular structural regularity is low and molecular free volume is high [87, 88, 89]. The bulk modulus of the new oil is shown to be around 1.8GPa at 40C and 20MPa system pressure whereas the bulk modulus of mineral oil is 1.3GPa at the same conditions. An added benefit of the molecular structure is that gas solubility is low. Experimental tests of nitrogen gas solubility showed that the new oil has one to two orders of magnitude less solubility than mineral oil [87, 88, 89]. Low gas solubility is attractive for switched-mode systems where the rapid switching and pressure fluctuations in the system are likely to agitate gas out of solution.

4.5 Conclusions

Valve configuration, circuit configuration, and valve geometry were revisited in the quest to improve on/off valve efficiency in four quadrant VVDPMs. Since self-spinning is impractical from an efficiency standpoint when the flow rate through the valve varies extensively, the 4-way tandem valve configuration used in Chapter 3 was abandoned in favor of a 3-way valve. Not only did this change reduce the number of times the fluid

is metered through the control valve, it also enabled the use of passive check valves to reduce transition pressure spikes and their associated throttling losses during motoring. Transition losses were the root cause of poor motoring efficiency in the 4-way tandem spool valve.

A new 3-way circuit configuration was also introduced that enables full four quadrant operation without the use of DCVs. The proposed circuit is a significant improvement over conventional four quadrant VVDPMs that use 3-way on/off valves since it eliminates the DCV between the P/M and the on/off valve that contributes to the switched volume of the device. An elegant method of integrating the port switching functionality of the DCV into the axial travel of a rotary valve was introduced to realize the new circuit.

To complement the improvements in valve and circuit configurations, a novel valve geometry based on a ring control element was developed with the goal of reducing the internal switched volume of the valve. For equivalent valve diameters, the ring valve concept significantly reduces switched volume with little impact on friction losses and leakage. However, initial solid modeling of the ring valve revealed that maintaining small valve diameters (favorable for spool valves) with equivalent flow areas was unfeasible at the specified pressure (21MPa) and flow rates (up to 82lpm) due to wall thickness constraints. Regardless, a preliminary solid model of the ring valve with twice the valve diameter (60mm vs. 30mm) had half of the switched volume (9.6cc vs. 21.4cc) of the smaller diameter spool valve.

Simulations of the ring valve revealed cleaner pressure transitions when motoring compared to the 4-way tandem valve. The pressure profiles show that passive check valves are effective in reducing transition pressure spikes during motoring with the 3-way valve configuration which was not possible with the 4-way. This reduces the motoring transition losses by 4142W or 76% for the geometries used. Simulated efficiency maps using the same operating parameters as the maps generated for the 4-way (40Hz PWM frequency, 21MPa pressure differential) confirm significant improvements in motoring efficiency, especially at low effective displacements and high shaft speeds. Pumping efficiency was also improved, although the improvements mainly occur at shaft speeds over 4000rpm . Looking at the other losses in greater detail, analysis predicts that compressibility losses are reduced by 176W (52%), pumping transition losses by 258W

(14%), and full open losses by $160W$ to $638W$ (19% to 77%) depending on the flow path. Meanwhile, leakage only increases by $60W$ (96%) and friction (i.e. actuation) losses only increase by $27W$, albeit this is a 166% increase. Despite the large percentage increase in actuation power, it is still by far the smallest loss, thereby further validating the presumption of low actuation power through continuous rotation and the elimination of inertial forces. The overall improvements in efficiency are remarkable considering leakage and friction are accounted for in the efficiency maps and the ring valve is twice the diameter of the spool valve. Alternately, the gains in efficiency afforded by the ring valve could be applied toward improving bandwidth and performance for a specified efficiency constraint, i.e. enabling faster PWM frequencies compared to a spool valve of equal efficiency.

Accounting for the promising preliminary results, the logical next step in the development of the ring valve is exploring parameter optimization to study the extent of the ring valve's potential and how geometry scaling may differ from the spool valve. In addition to parameter optimization, detailed mechanical design of the ring and its cylindrical boss needs to be performed as well as the synthesis and design of a suitable valve driving mechanism. Hydraulic axial actuation is no longer an option with the current valve concept due to the requirement of connecting Ports A and B to tank in an open bath of fluid surrounding the ring. In addition to the valve, circuit, and geometry improvements proposed, exploiting valve underlap and soft-switching for additional transition loss reduction, surface texturing the valve lands to reduce the trade off between leakage and friction, and making use of higher bulk modulus fluids to reduce compressibility losses should be explored in more detail as well.

Chapter 5

Conclusions

This chapter summarizes the research presented in this dissertation. Section 5.1 reviews the research and the discoveries made. Section 5.2 highlights the contributions to the literature. Section 5.3 discusses several recommendations for future work.

5.1 Review

This dissertation details the design, analysis, and experimental validation of high speed hydraulic on/off valves based on continuous rotary motion. These valves are the hydraulic analogue of transistors in the electrical domain and enable switched-mode digital hydraulics. Unlike traditional forms of resistive valve control in hydraulics that rely on the metering of flow across a variable sized orifice, switched-mode control via pulse-width-modulation (PWM) operates the control valve efficiently in either its fully open state (low pressure drop) or fully closed state (no flow) which eliminates a bulk of the throttling losses in hydraulic control. The advantage of the continuously rotating helical land on/off valve concept that is the foundation for the work in this dissertation is that valve actuation power is reduced from a frequency cubed dependence on switching frequency to a frequency squared dependence. This is accomplished by eliminating the dominant inertial forces associated with oscillatory linear motion for switching valve state in conventional spool or poppet valves. While direct actuation power comparisons to linear valves were not made, the analysis performed on the externally actuated 4-way spool valve and ring valve confirm that actuation power is low. Only $16W$ is predicted

for the 4-way and 43W for the ring valve at 40Hz PWM frequency. Both valves have a large 105mm² flow area which corresponds to a pressure drop of .15MPa at 82lpm. The low actuation power afforded by rotary valves enables high switching speeds and large flow areas, both of which are important in switched-mode hydraulics.

The research in this dissertation extends the pioneering 2-way helical land rotary valve studies by Rajala et al. [41]. First, a novel 3-way self-spinning embodiment was synthesized in Chapter 2 that used the fluid flow through the valve spool to generate angular momentum for rotation. A comprehensive loss and performance analysis was conducted and verified with a dynamic system simulation. The analysis and simulations were then validated using experimental data from a test stand which showed that a fixed displacement pump paired with the rotary valve in a virtually variable displacement pump (VVDP) configuration exceeded the efficiency of an equivalent bleed off circuit for varying output flow rates at moderate PWM frequencies. The self-spinning rotary valve was then extended to the control of motors and pump/motors (P/M) in Chapter 3 with the introduction of the 4-way tandem configuration. This valve, when combined with a fixed displacement P/M to form a virtually variable displacement P/M (VVDPM), was bench marked via simulation with a variable displacement bent axis P/M in a small power-split hydraulic hybrid vehicle. The simulation studies revealed several shortcomings to the 4-way valve which led to higher than anticipated throttling and compressibility losses that prevented the VVDPM from matching the efficiency of the variable displacement bent axis P/M. A mechanical design methodology based on fatigue life considerations was proposed and used to design a prototype 4-way valve. Initial bench top testing validated the valve structure, however, full characterization was hindered by contamination and seizing issues. Lastly, valve configuration, circuit configuration, and valve geometry were reconsidered concurrently in Chapter 4 to improve the efficiency of switched-mode control. A 3-way valve based on a novel ring style control element combined with an elegant integrated port-switching scheme eliminated the directional control valve (DCV) needed for four quadrant operation using the 4-way valve while also enabling the use of passive check valves to reduce transition losses when motoring. Significant improvements in efficiency over the 4-way valve in VVDPM applications was predicted in simulation.

5.2 Contributions

The core contributions of the work presented in this dissertation can be summarized as follows:

1. The development and experimental validation of a systematic analysis and simulation methodology for helical land type rotary on/off valves used in switched-mode hydraulic pump, motor, and pump/motor circuits.
2. The design and experimental validation of solutions for simultaneous two degree-of-freedom linear and rotary actuation using fluid momentum (self-spinning) or generic actuators for rotary motion.
3. The synthesis of helical land rotary on/off spool valves with 3-way and 4-way tandem fluid porting configurations that are self-spinning capable.
4. The development of a mechanical design methodology for spool type rotary valves for infinite fatigue life in the high pressure high frequency operating domain.
5. The synthesis and analysis of a novel ring valve architecture for reducing the conventional trade off between compressibility losses and throttling in rotary on/off valves that simultaneously enables full four quadrant operation of switched-mode hydraulic systems using a single on/off control valve.
6. The extension of the soft-switching approach proposed by Rannow et al. [47, 48, 49] for reducing transition losses in switched-mode systems to motoring circuits.

Summary of publications: The work presented in this dissertation has been published in various conference proceedings and journals [44, 45, 46, 66, 67].

5.3 Recommendations for Future Work

The body of work presented in this dissertation provides a fairly complete look into the design and performance of rotary on/off valves based on the helical land concept. There are, however, several short term and long term directions that are recommended for further study. First, experimental characterization of the 4-way tandem rotary valve

based VVDPM should be completed to confirm the efficiency predicted by the analysis and dynamic simulation. Next, the VVDPM prototype should be integrated onto the hydraulic hybrid passenger vehicle test bed at the University of Minnesota to benchmark its impact on vehicle efficiency and fuel economy in comparison to the results predicted by the analysis. It would also be interesting to experimentally demonstrate the VVDPM prototype in other types of hydraulic systems.

The ring valve concept requires further development. The trade study and simulations presented in Chapter 4 predict a significant improvement in efficiency over the 4-way valve when considering equivalent flow areas and PWM frequencies. Logical next steps include performing parameter optimization to study the scaling characteristics of the concept as well as the mechanical design of a prototype ring valve and its driving mechanism. Experimental validation of the prototype and demonstration on a test bed would be appropriate concluding steps. Formal investigation of the additional ideas to improve efficiency discussed in Section 4.4 including valve underlap, soft-switching, surface texturing, and the use of high bulk modulus hydraulic oil should also be pursued.

Long term future research should investigate appropriate PWM frequencies for different applications with consideration of system inertia. Fast PWM frequencies are desirable for control bandwidth and output ripple reduction, however, a penalty in efficiency is incurred due to the frequency dependent compressibility losses and actuation power requirements. The key question of how fast is fast enough is certainly application dependent but should be explored for typical hydraulic applications. Noise is also a concern in switched-mode hydraulic systems that should be investigated as well as fatigue life of other system components such as hoses, accumulators, manifolds, etc.

With additional development and understanding of application needs, switched-mode control of hydraulic pumps, motors, and pump/motors, enabled by the helical land rotary on/off valve concepts described in this dissertation, could be a viable alternative to metering control using proportional valves or even conventional variable displacement devices in many hydraulic applications. Switched-mode control offers a balance between the high bandwidth capabilities of valve control and the efficiency characteristics of displacement control with variable displacement machines.

References

- [1] Eaton Corporation. *Mobile Hydraulics Manual*. Eaton Hydraulics Training, 2nd edition.
- [2] P. Li, C. Li, and T. Chase. Software enabled variable displacement pumps. In *Proceedings of the ASME Fluid Power Systems and Technology Division 2005*, pages 63–72, 2005. IMECE2005-81376.
- [3] Md. Ehsan, W.H.S. Rampen, and S.H. Salter. Modeling of digital-displacement pump-motors and their application as hydraulic drives for nonuniform loads. *ASME Journal of Dynamic Systems Measurement and Control*, 122:210–215, March 2000.
- [4] J. Cao, L. Gu, F. Wang, and M. Qiu. Switchmode hydraulic power supply theory. In *Proceedings of the ASME Fluid Power Systems and Technology Division 2005*, 2005. IMECE2005-79019.
- [5] J. Cao, F. Wang, L. Gu, and Y. Chen. Research on the principle and characteristic of compounded switch-mode hydraulic power supply. In *Proceedings of 2006 ASME International Mechanical Engineering Congress and Exposition, IMECE2006*, 2006. IMECE2006-13453.
- [6] M. Rannow, H. Tu, P. Li, and T. Chase. Software enabled variable displacement pumps - experimental studies. In *Proceedings of 2006 ASME International Mechanical Engineering Congress and Exposition, IMECE2006*, 2006. IMECE2006-14973.

- [7] M. Batdorff and J. Lumkes. Virtually variable displacement hydraulic pump including compressibility and switching losses. Proceedings of the ASME 2006 International Mechanical Engineering Congress and Exposition, IMECE2006, 2006. IMECE2006-14838.
- [8] J. Lumkes, M. Batdorff, and J. Mahrenholz. Model development and experimental analysis of a virtually variable displacement pump system. *International Journal of Fluid Power*, 10(3):17–27, 2009.
- [9] B. Lehman and R. Bass. Switching frequency dependent averaged models for pwm dc-dc converters. *IEEE Transactions on Power Electronics*, 11(1):89–98, 1996.
- [10] S. Yokota and K. Akutu. A fast-acting electro-hydraulic digital transducer (a poppet-type on-off valve using a multilayered piezoelectric device). *JSME International Journal, Series 2: Fluids Engineering, Heat Transfer, Power, Combustion, Thermophysical Properties*, 34(4):489–495, 1991.
- [11] H. Yamada, G. Wennmacher, T. Muto, and Y. Suematsu. Development of a high-speed on/off digital valve for hydraulic control systems using a multilayered pzt actuator. *International Journal of Fluid Power*, 1(2):5–10, 2000.
- [12] E. Topçu, İ. Yüksel, and Z. Kamiş. Development of electro-pneumatic fast switching valve and investigation of its characteristics. *Mechatronics*, 16(6):365–378, 2006.
- [13] J. Mahrenholz and J. Lumkes. Analytical coupled modeling and model validation of hydraulic on/off valves. *ASME Journal of Dynamic Systems, Measurement, and Control*, 132(1), 2010.
- [14] A. Plöckinger, B. Winkler, and R. Scheidl. Development and prototyping of a compact, fast 3/2 way switching valve with integrated onboard electronics. Proceedings of the 11th Scandinavian International Conference on Fluid Power, SICFP’09, 2009.
- [15] G. Mansfeld. Fast switching ball valves as digital control elements for an electro-hydraulic servo actuator. Proceedings of the 6th International Fluid Power Symposium, BHRA 1981, 1981.

- [16] T. Kajima and Y. Kawamura. Development of a high-speed solenoid valve: investigations of solenoids. *IEEE Transactions on Industrial Electronics*, 42(1):1–8, 1995.
- [17] G. Tao, H.Y. Chen, Y.Y. J, and Z.B. He. Optimal design of the magnetic field of a high-speed response solenoid valve. *Journal of Materials Processing Technology*, 129:555–558, 2002.
- [18] M. Pellikka, V. Ahola, L. Söderlund, and J.P. Uusitalo. Genetic optimization of a fast solenoid actuator for a digital hydraulic valve. *International Journal of Fluid Power*, 12(2):49–56, 2011.
- [19] I. Lee. Switching response improvement of a high speed on/off solenoid valve by using a 3 power source type valve driving circuit. *IEEE International Conference on Information Technology*, 2007.
- [20] K. Krishnaswamy and P. Li. On using unstable electrohydraulic valves for control. *ASME Journal of Dynamic Systems, Measurement, and Control*, 124(1):183–190, 2002.
- [21] Q. Yuan and P. Li. Using steady flow force for unstable valve design: Modeling and experiments. *ASME Journal of Dynamic Systems, Measurement, and Control*, 127(3):451–462, 2005.
- [22] Q. Yuan and P. Li. Robust optimal design of unstable valves. *IEEE Transactions on Control Systems Technology*, 15(6):1065–1074, 2007.
- [23] M. Garstenauer and R. Scheidl. High-speed switching valves actuated by parametrically excited structures. *Bath Workshop on Power Transmission and Motion Control*, PTMC99, 1999.
- [24] B. Manhartsgruber. A hydraulic control valve for pwm actuation at 400hz. *Power Transmission and Motion Control (PTMC 2006)*, 2006. ISBN: 08-6197-135-3.
- [25] J.P. Uusitalo, L. Söderlund, L. Kettunen, V. Ahola, and M. Linjama. Novel bistable hammer valve for digital hydraulics. *Proceedings of the Second Workshop on Digital Fluid Power*, DFP09, 2009.

- [26] J.P. Uusitalo, V. Ahola, L. Söderlund, M. Linjama, M. Juhola, and L. Kettunen. Novel bistable hammer valve for digital hydraulics. *International Journal of Fluid Power*, 11(3):35–44, 2010.
- [27] B. Johnson, S. Massey, and O. Sturman. Sturman digital latching valve. Proceedings of the 7th Scandinavian International Conference on Fluid Power, SICFP'01, 2001.
- [28] J. Ma, F. Fronczak, and N. Beachley. Design of a high speed, high-flow, three-way poppet valve. Proceedings of the 50th National Conference on Fluid Power, 2005.
- [29] B. Winkler and R. Scheidl. Development of a fast seat type switching valve for big flow rates. Proceedings of the Tenth Scandinavian International Conference on Fluid Power, SICFP'07, 2007.
- [30] D. Branson, F. Wang, D. Johnston, D. Tilley, C. Bowen, and P. Keogh. Piezoelectrically actuated hydraulic valve design for high bandwidth and flow performance. *Proceedings of the Institution of Mechanical Engineers, Part I: Journal of Systems and Control Engineering*, 225(3):345–359, 2011.
- [31] B. Winkler, A. Plöckinger, and R. Scheidl. A novel piloted fast switching multi poppet valve. Proceedings of the Second Workshop on Digital Fluid Power, DFP09, 2009.
- [32] B. Winkler, A. Plöckinger, and R. Scheidl. A novel piloted fast switching multi poppet valve. *International Journal of Fluid Power*, 11(3):7–14, 2010.
- [33] P. Cui, R. Burton, and P. Ukrainetz. Development of a high speed on/off valve. *Transactions of the SAE*, 100(2):312–316, 1991.
- [34] F. Brown, S. Tentarelli, and S. Ramachandran. A hydraulic rotary switched-inertance servo-transformer. *ASME Journal of Dynamic Systems, Measurement, and Control*, 110(2):144–150, 1988.
- [35] X. Lu, R. Burton, G. Schoenau, and X. Zeng. Feasibility study of a digital variable flow divider valve. SAE Technical Paper Series, 1991. Paper 911816.

- [36] T. Royston and R. Singh. Development of a pulse-width-modulated pneumatic rotary valve for actuator position control. *ASME Journal of Dynamic Systems, Measurement, and Control*, 115(3):495–505, 1993.
- [37] J. Van de Ven and A. Katz. Phase-shift high-speed valve for switch-mode control. *ASME Journal of Dynamic Systems Measurement and Control*, 133:011003, January 2011.
- [38] A. Katz and J. Van de Ven. Design of a high-speed on-off valve. Proceedings of the ASME 2009 International Mechanical Engineering Congress and Exposition, IMECE2009, 2009. IMECE2009-11189.
- [39] J. Wu and J. Van de Ven. Development of a high-speed on-off valve for switch-mode control of hydraulic circuits with four-quadrant control. Proceedings of the ASME 2010 International Mechanical Engineering Congress and Exposition, IMECE2010, 2010. IMECE2010-37380.
- [40] I. Cyphelly and J. Langen. Ein neues energiesparendes konzept der volumenstromdosierung mit konstantpumpen. *Aachener Fluidtechnisches Kolloquium*, pages 43–61, 1980.
- [41] D. Rajala. Rotary pulse-width modulated valve. Master’s thesis, The University of Minnesota, 2004.
- [42] T. Kobata and A. Ooiwa. Square-wave pressure generator using a novel rotating valve. *Metrologia*, 36:637–640, 1999.
- [43] S.H. Wang, T.T. Tsung, and L.L. Han. Hydraulic square-wave pressure generator with a specific rotating valve. *Measurement*, 42(5):672–677, 2009.
- [44] H. Tu, M. Rannow, J. Van De Ven, M. Wang, P. Li, and T. Chase. High speed rotary pulse width modulated on/off valve. In *Proceedings of the ASME International Mechanical Engineering Congress and Exposition, IMECE 2007*, pages 89–102, 2007. IMECE2007-42559.

- [45] H. Tu, M. Rannow, M. Wang, P. Li, and T. Chase. Modeling and validation of a high speed rotary pwm on/off valve. In *Proceedings of the ASME Dynamic Systems and Control Conference 2009*, 2009. DSC09-2763.
- [46] H. Tu, M. Rannow, M. Wang, P. Li, T. Chase, and J. Van De Ven. Design, modeling, and validation of a high-speed rotary pwm on/off hydraulic valve. *ASME Journal of Dynamic Systems Measurement and Control*, 134:061002, November 2012.
- [47] M. Rannow. *Achieving Efficient Control of Hydraulic Systems Using On/Off Valves*. PhD thesis, The University of Minnesota, 2014 (est.).
- [48] M. Rannow and P. Li. Soft switching approach to reducing transition losses in an on/off hydraulic valve. In *Proceedings of the ASME Dynamic Systems and Control Conference 2009*, 2009. DSC09-2617.
- [49] M. Rannow and P. Li. Soft switching approach to reducing transition losses in an on/off hydraulic valve. *ASME Journal of Dynamic Systems Measurement and Control*, 134:064501, November 2012.
- [50] M. Wang and P. Li. Event based kalman filter observer for rotary high speed on/off valve. In *Proceedings of the 2008 American Control Conference*, pages 1546–1551, 2008.
- [51] M. Wang and P. Li. Duty ratio control of a rotary pwm valve with periodic measurement error. In *Proceedings of the 2009 American Control Conference*, pages 5073–5078, 2009.
- [52] M. Wang. *CFD Analysis, Sensing and Control of a Rotary Pulse Width Modulating Valve*. PhD thesis, The University of Minnesota, Mechanical Engineering, 2014.
- [53] S.L. Dixon. *Fluid Mechanics and Thermodynamics of Turbomachinery*. Elsevier Butterworth-Heinemann, 5th edition.
- [54] H. Merritt. *Hydraulic Control Systems*. John Wiley and Sons, New York, NY, 1967.

- [55] M. Wang, H. Tu, M. Rannow, P. Li, and T. Chase. CFD analysis of a novel high speed rotary on/off valve. Proceedings of the 6th FPNI - PhD Symposium, 2010.
- [56] M. Wang, H. Tu, M. Rannow, P. Li, and T. Chase. CFD analysis of a novel type of high speed rotary on/off valve. *ASME Journal of Fluids Engineering*. Under review.
- [57] H. Gholizadeh, R. Burton, and G. Schoenau. Fluid bulk modulus: Comparison of low pressure models. *International Journal of Fluid Power*, 13(1):7–16, 2012.
- [58] J. Yu, Z. Chen, and Y. Lu. The variation of oil effective bulk modulus with pressure in hydraulic systems. *ASME Journal of Dynamic Systems Measurement and Control*, 116:146–150, March 1994.
- [59] B. Cho, H. Lee, and J. Oh. Estimation technique of air content in automatic transmission fluid by measuring effective bulk modulus. *International Journal of Automotive Technology*, 3(2):57–61, 2000.
- [60] T. Nykanen, S. Esque, and A. Ellman. Comparison of different fluid models. Bath Workshop on Power Transmission and Motion Control, PTMC2000, 2000.
- [61] J. Cundiff. *Fluid Power Circuits and Controls*. CRC Press, 2002.
- [62] A. Cameron. *Basic Lubrication Theory*. John Wiley and Sons, 3rd edition.
- [63] F. White. *Fluid Mechanics*. McGraw-Hill, 5th edition.
- [64] M. Rannow, H. Tu, M. Wang, P. Li, and T. Chase. Optimal design of a high-speed on/off valve for a hydraulic hybrid vehicle application. Proceedings of the 7th International Fluid Power Conference, 2010.
- [65] J. Van de Ven. On fluid compressibility in switch-mode hydraulic circuits - Part II: Experimental results. *ASME Journal of Dynamic Systems, Measurement, and Control*, 135:021014, March 2013.
- [66] H. Tu, M. Rannow, M. Wang, P. Li, T. Chase, and K.L. Cheong. High-speed 4-way rotary on/off valve for virtually variable displacement pump/motor applications.

In *Proceedings of the ASME Dynamic Systems and Control Conference 2011*, 2011. DSCC2011-6109.

- [67] H. Tu, M. Rannow, M. Wang, P. Li, and T. Chase. The advantages and feasibility of externally actuating a high-speed rotary on/off valve. *Proceedings of the 52nd National Conference on Fluid Power*, 2011. Paper 20.3.
- [68] J. Van de Ven, M. Olson, and P. Li. Development of a hydro-mechanical hydraulic hybrid drive train with independent wheel torque control for an urban passenger vehicle. *Proceedings of the 2008 IFPE*, 2008.
- [69] T.P. Sim and P. Li. Analysis and control design of a hydro-mechanical hydraulic hybrid passenger vehicle. *Proceedings of the ASME Dynamic Systems and Control Conference 2009*, 2009. DSC09-2763.
- [70] P. Li and F. Mensing. Optimization and control of a hydro-mechanical transmission based hybrid hydraulic passenger vehicle. *Proceedings of the 7th International Fluid Power Conference*, 2010.
- [71] F. Mensing and P. Li. Sizing and optimal operation of a power split hydraulic hybrid drive train. *Proceedings of the 52nd National Conference on Fluid Power*, 2011. Paper 10.3.
- [72] K.L. Cheong, P. Li, S. Sedler, and T. Chase. Comparison between input coupled and output coupled power-split configurations in hybrid vehicles. *Proceedings of the 52nd National Conference on Fluid Power*, 2011. Paper 10.2.
- [73] K.L. Cheong, P. Li, and T. Chase. Optimal design of power-split transmissions for hydraulic hybrid passenger vehicles. In *Proceedings of the 2011 American Control Conference*, pages 3295–3300, 2011.
- [74] J. Morrison, B. Crossland, and J. Parry. Fatigue strength of cylinders with crossbores. *Journal Mechanical Engineering Science*, 1(3):207–210, 1959.
- [75] J. Gerdeen and R. Smith. Experimental determination of stress-concentration factors in thick-walled cylinders with crossholes and sideholes. *Experimental Mechanics*, 12(11):530–536, 1972.

- [76] R. Dixon, D. Peters, and J. Keltjens. Stress concentration factors of cross-bores in thick walled cylinders and blocks. *Journal of Pressure Vessel Technology*, 126:184–187, 2004.
- [77] T. Comlekci, D. Mackenzie, R. Hamilton, and J. Wood. Elastic stress concentration at radial crossholes in pressurized thick cylinders. *Journal Strain Analysis*, 42:461–468, 2007.
- [78] B. Cole. Strategy for cross-bores in high pressure containers. *Journal Mechanical Engineering Science*, 11(2):151–161, 1969.
- [79] B. Cole, G. Craggs, and I. Ficenec. Strength of cylinders containing radial or offset cross-bores. *Journal Mechanical Engineering Science*, 18(6):279–286, 1976.
- [80] R.L. Norton. *Machine Design: An Integrated Approach*. Prentice-Hall, 2nd edition.
- [81] W.F. Riley, L.D. Sturges, and D.H. Morris. *Mechanics of Materials*. John Wiley and Sons, 5th edition.
- [82] W. Young. *Roark's Formulas for Stress and Strain*. McGraw-Hill, 6th edition.
- [83] J. Meriam and L. Kraige. *Engineering Mechanics Statics*. John Wiley and Sons, 5th edition.
- [84] A. Ramesh. Friction characteristics of microtextured surfaces under hydrodynamic lubrication. Master's thesis, The University of Illinois at Urbana-Champaign, 2012.
- [85] A. Cannon and W. King. Casting metal microstructures from a flexible and reusable mold. *Journal of Micromechanics and Microengineering*, 19:095016, 2009.
- [86] A. Cannon and W. King. Microstructured metal molds fabricated via investment casting. *Journal of Micromechanics and Microengineering*, 20:025025, 2010.
- [87] T. Tsubouchi, H. Kamimura, and J. Shinoda. Development of oily high bulk modulus fluid. Proceedings of the 7th JFPS International Symposium on Fluid Power, 2008.
- [88] T. Tsubouchi and J. Shinoda. Practical performance of high bulk modulus oil. Proceedings of the 8th JFPS International Symposium on Fluid Power, 2011.

- [89] T. Tsubouchi and J. Shinoda. Practical performance of high bulk modulus oil. *Journal of Mechanics Engineering and Automation*, 2:119–123, 2012.

Appendix A

Baseline fixed displacement pump efficiency testing

Baseline testing of the modified fixed displacement bent-axis pump was conducted at Sauer-Danfoss in Ames, IA. The test circuit used to characterize the pump is presented in Fig. 3.32. An adapter plate is used to test the pump as a standalone unit. Data was sampled at $1kHz$ and each data point represents an average over 6 seconds of data. Shell Tellus S2 MA 46 hydraulic oil was used with a kinematic viscosity of $46cSt$ at $40C$, $7cSt$ at $100C$, and a density of $877kg/m^3$ at $15C$. Table A.1 lists the channels and data signals collected.

Volumetric efficiency of the pump is defined as:

$$\eta_{vol} = \frac{Q}{Q_{ideal}} \quad (A.1)$$

where $Q_{ideal} = \frac{D\omega}{2\pi}$ is the ideal flow based on pump displacement D and shaft speed ω . Mechanical efficiency of the pump is defined as:

$$\eta_{mech} = \frac{\tau_{ideal}}{\tau} \quad (A.2)$$

where $\tau_{ideal} = \frac{D\Delta P}{2\pi}$ is the ideal flow based on pump displacement D and pump pressure differential ΔP . Correspondingly, the overall efficiency of the pump is:

$$\eta_{tot} = \eta_{vol}\eta_{mech} = \frac{\Delta PQ}{\tau\omega} \quad (A.3)$$

Table A.1: Data collected during baseline pump testing at Sauer-Danfoss.

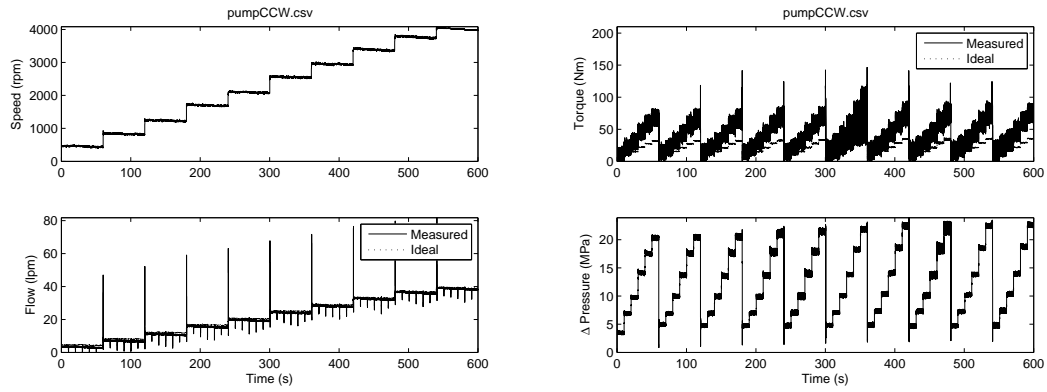
Channel	Signal
1	Input speed (rpm)
2	Input torque (Nm)
3	Case pressure (bar)
4	A System pressure (bar)
5	B System pressure (bar)
6	System flow (lpm)
7	Case flow (lpm)
8	Reservoir temp (C)
9	Case temp (C)
10	Loop temp (C)
11	Time (s)

A sample of raw data collected during a typical efficiency map experiment is shown in Fig. A.1. *A* and *B* system pressures (channels 4 and 5) are the pressures at the inlet and outlet of the pump used for determining the pressure differential.

Four efficiency map data sets were taken, two each for counter-clockwise shaft rotation and clockwise shaft rotation. The resulting volumetric, mechanical, and overall efficiency maps along with oil temperature during each experiment are presented in Figs. A.2 to A.13.

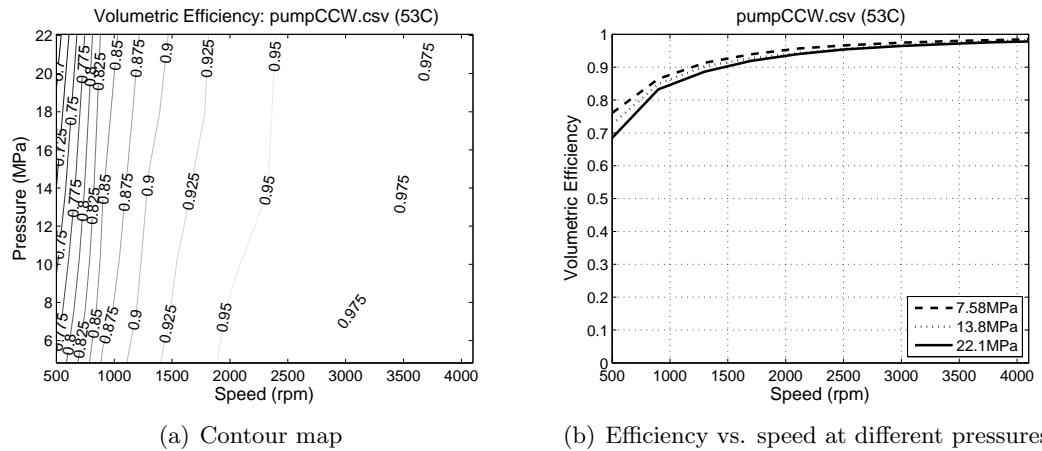
Remarks:

1. The measured mechanical efficiency during all four experiments is excessively poor. The manufacturer provided efficiency numbers claim mechanical efficiency from 94%-99% for pressure differentials ranging from $10MPa$ - $42MPa$ and speeds ranging from $500rpm$ - $4200rpm$. The peak measured mechanical efficiency across all for data sets is roughly 60%. There is also an unexpected peak in mechanical efficiency around $2500rpm$. Looking at the raw data in Fig. A.1 confirms that the measured torque is almost twice the ideal torque based on pressure measurements.
2. Volumetric efficiency looks reasonable compared to manufacturer provided data. Efficiency is slightly lower at low shaft speeds.



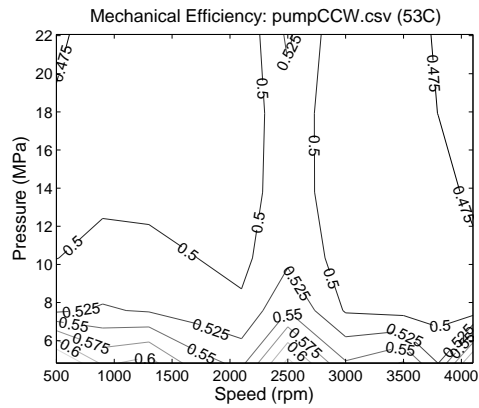
(a) Top: Measured pump speed. Bottom: Comparison of measured and ideal flow rates (based on pump speed). (b) Top: Comparison of measured and ideal shaft torques (based on pressure differential). Bottom: Measured pressure differential.

Figure A.1: Sample of raw data collected. This data set corresponds to the first counter-clockwise experiment.

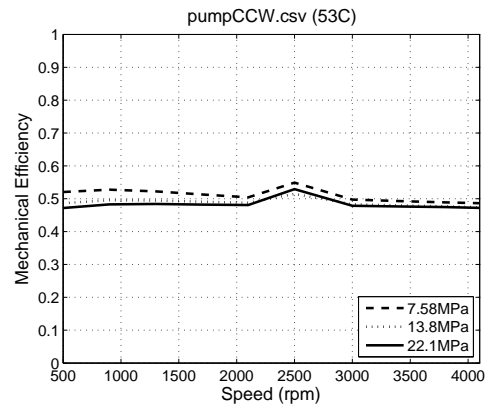


(a) Contour map (b) Efficiency vs. speed at different pressures

Figure A.2: Volumetric efficiency, counter-clockwise shaft rotation, first data set.

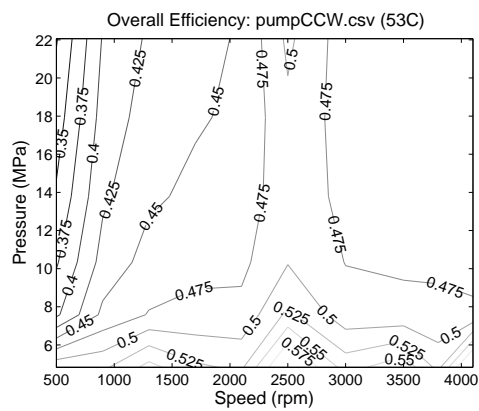


(a) Contour map

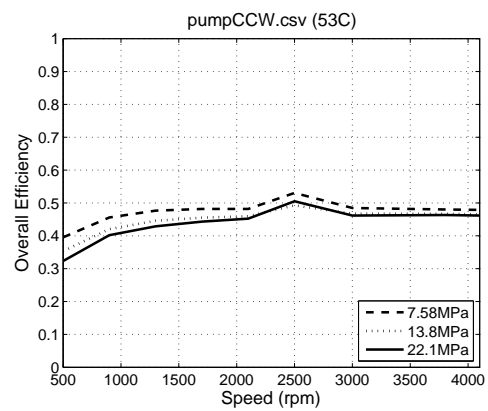


(b) Efficiency vs. speed at different pressures

Figure A.3: Mechanical efficiency, counter-clockwise shaft rotation, first data set.

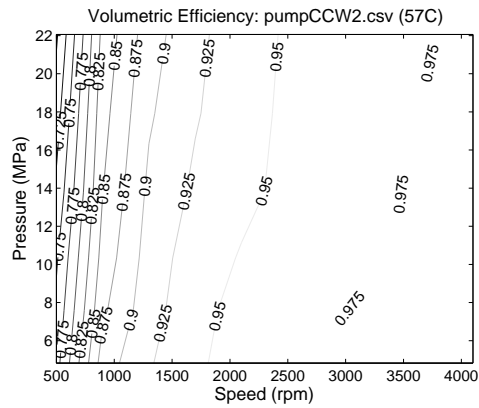


(a) Contour map

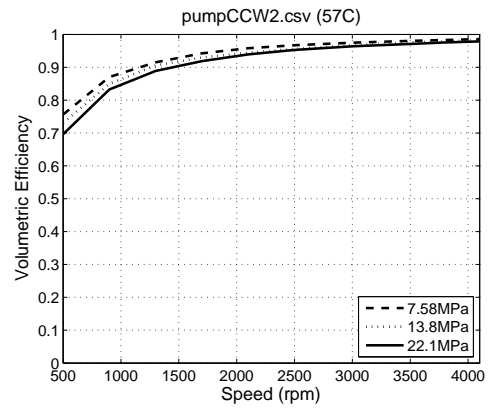


(b) Efficiency vs. speed at different pressures

Figure A.4: Overall efficiency, counter-clockwise shaft rotation, first data set.

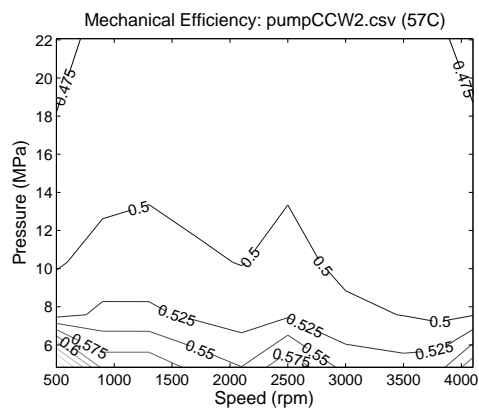


(a) Contour map

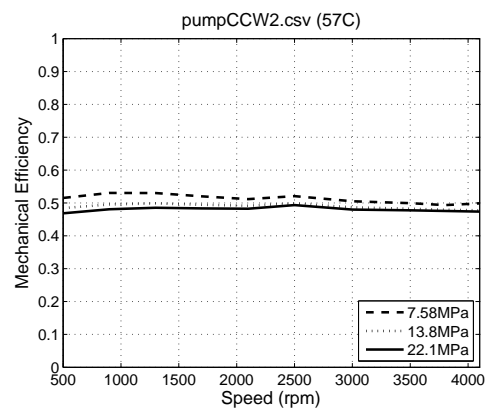


(b) Efficiency vs. speed at different pressures

Figure A.5: Volumetric efficiency, counter-clockwise shaft rotation, second data set.

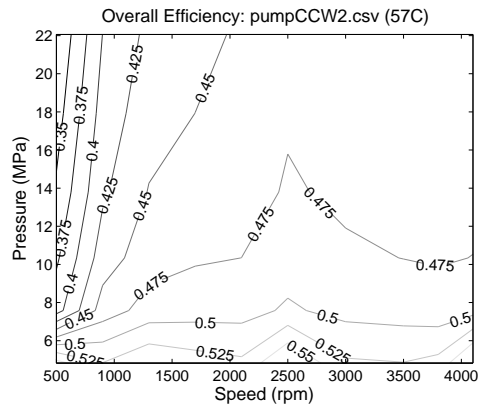


(a) Contour map

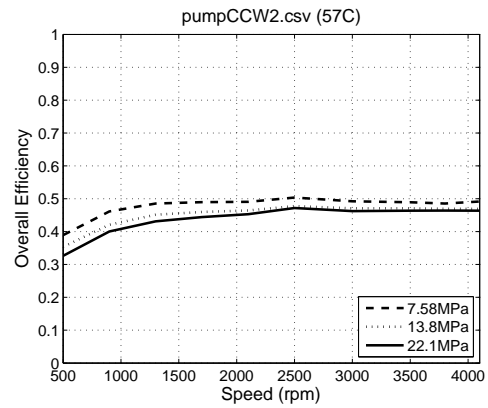


(b) Efficiency vs. speed at different pressures

Figure A.6: Mechanical efficiency, counter-clockwise shaft rotation, second data set.

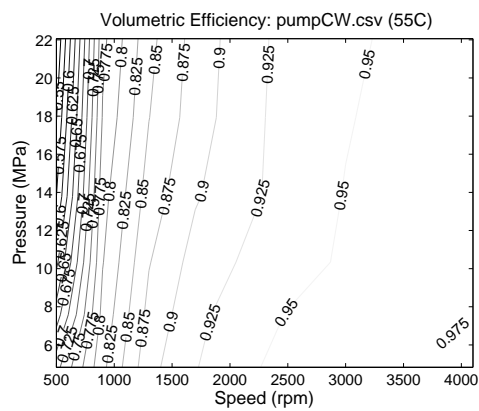


(a) Contour map

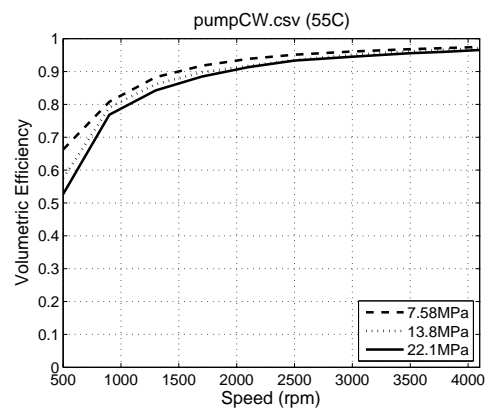


(b) Efficiency vs. speed at different pressures

Figure A.7: Overall efficiency, counter-clockwise shaft rotation, second data set.

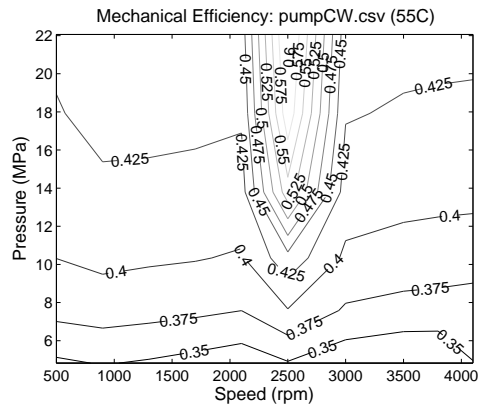


(a) Contour map

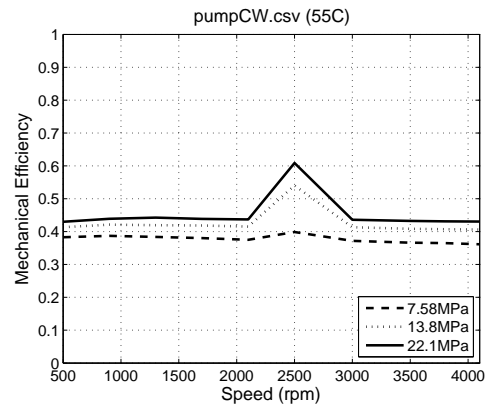


(b) Efficiency vs. speed at different pressures

Figure A.8: Volumetric efficiency, clockwise shaft rotation, first data set.

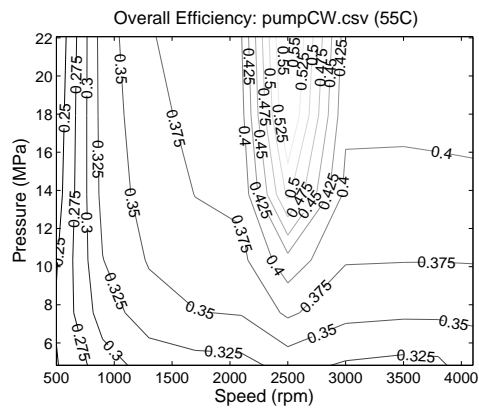


(a) Contour map

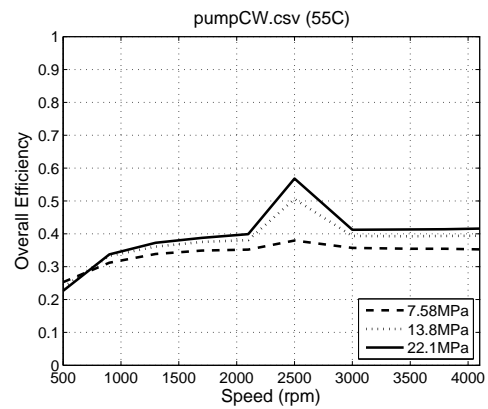


(b) Efficiency vs. speed at different pressures

Figure A.9: Mechanical efficiency, clockwise shaft rotation, first data set.

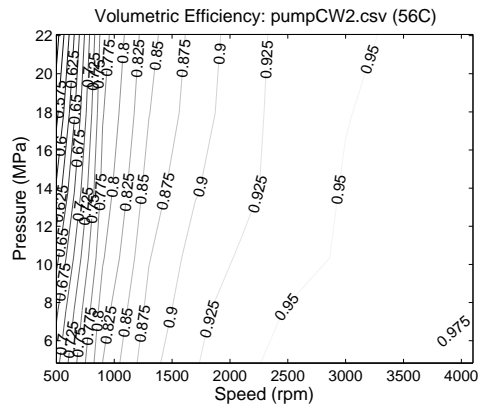


(a) Contour map

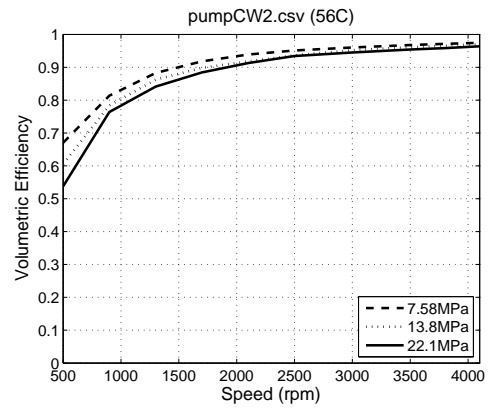


(b) Efficiency vs. speed at different pressures

Figure A.10: Overall efficiency, clockwise shaft rotation, first data set.

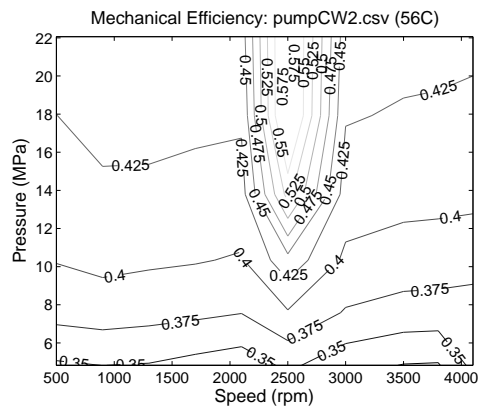


(a) Contour map

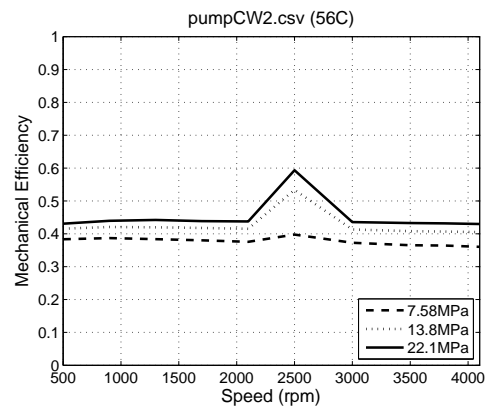


(b) Efficiency vs. speed at different pressures

Figure A.11: Volumetric efficiency, clockwise shaft rotation, second data set.

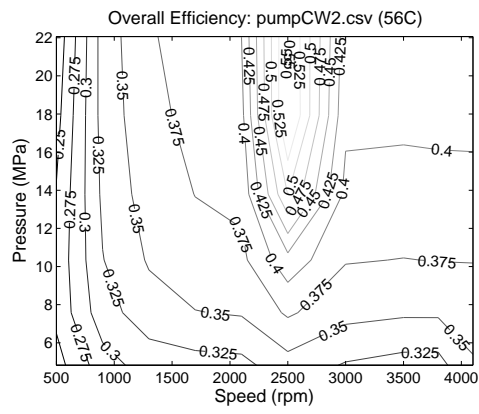


(a) Contour map

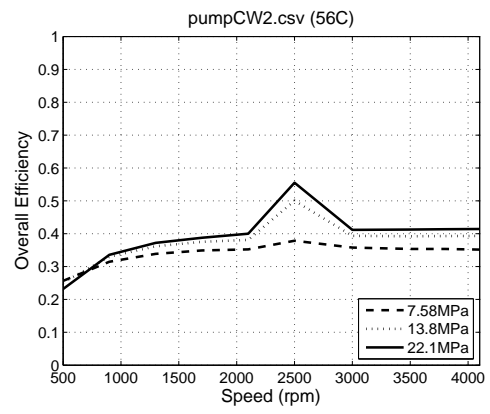


(b) Efficiency vs. speed at different pressures

Figure A.12: Mechanical efficiency, clockwise shaft rotation, second data set.



(a) Contour map



(b) Efficiency vs. speed at different pressures

Figure A.13: Overall efficiency, clockwise shaft rotation, second data set.

Appendix B

4-way rotary valve prototype drawings

This section includes all of the machining drawings for the prototype 4-way rotary valve. Refer to Figs. 3.27 and 3.19 for an assembled and exploded renders of the 4-way valve prototype and driving mechanism respectively. List of drawings:

1. Figure B.1: 4-way rotary valve spool
2. Figure B.2: 4-way rotary valve sleeve
3. Figure B.3: Sleeve housing
4. Figure B.4: Manifold
5. Figure B.5: Pump port plate adapter for stand-alone testing
6. Figure B.6: Valve port plate adapter for stand-alone testing (Ports *A* and *B*)
7. Figure B.7: Valve port plate adapter for stand-alone testing (Ports *C* and *D*)
8. Figure B.8: Valve drive mechanism shaft
9. Figure B.9: Valve drive mechanism piston
10. Figure B.10: Valve drive mechanism housing
11. Figure B.11: Valve drive mechanism guide

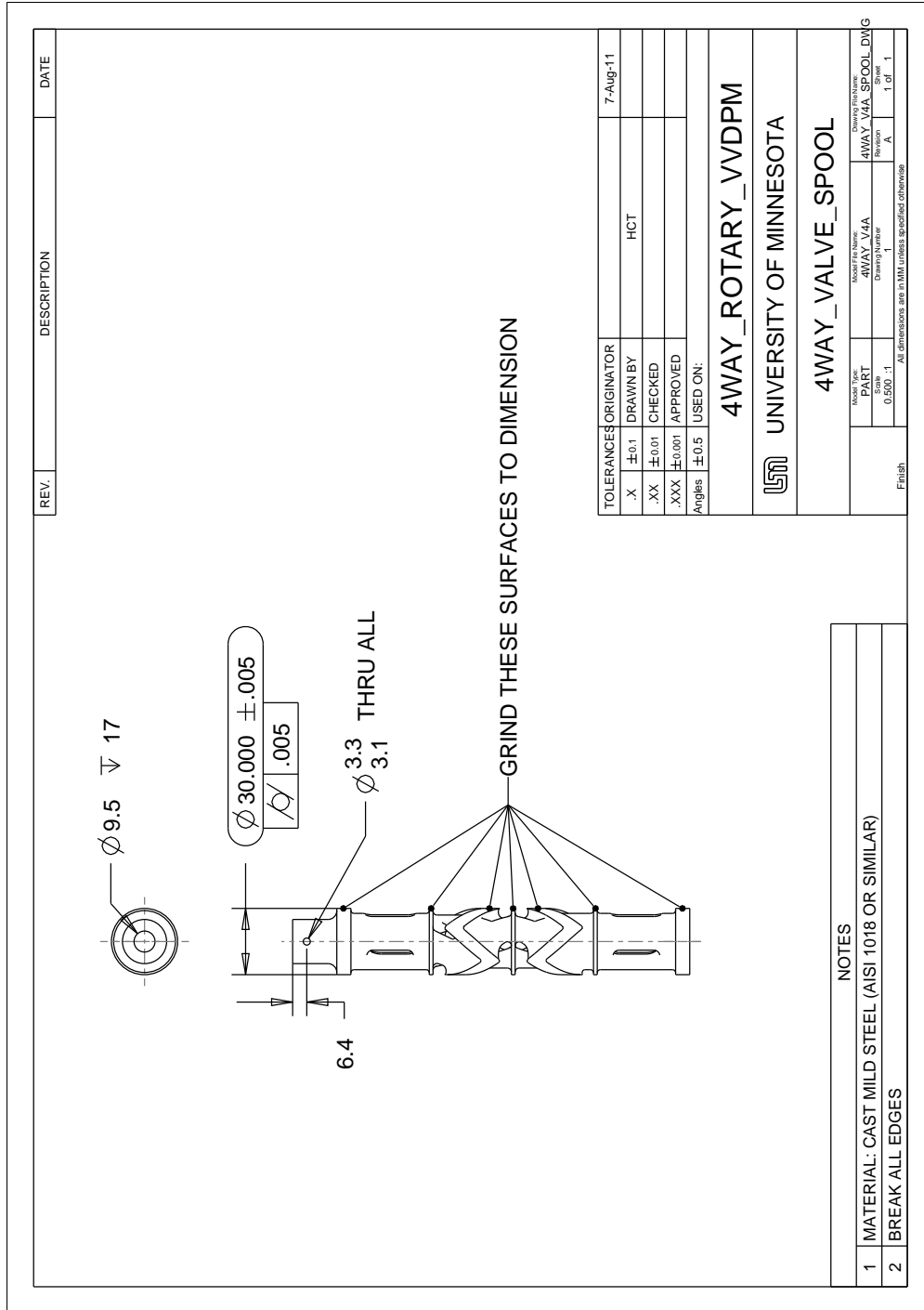


Figure B.1: 4-way rotary valve spool

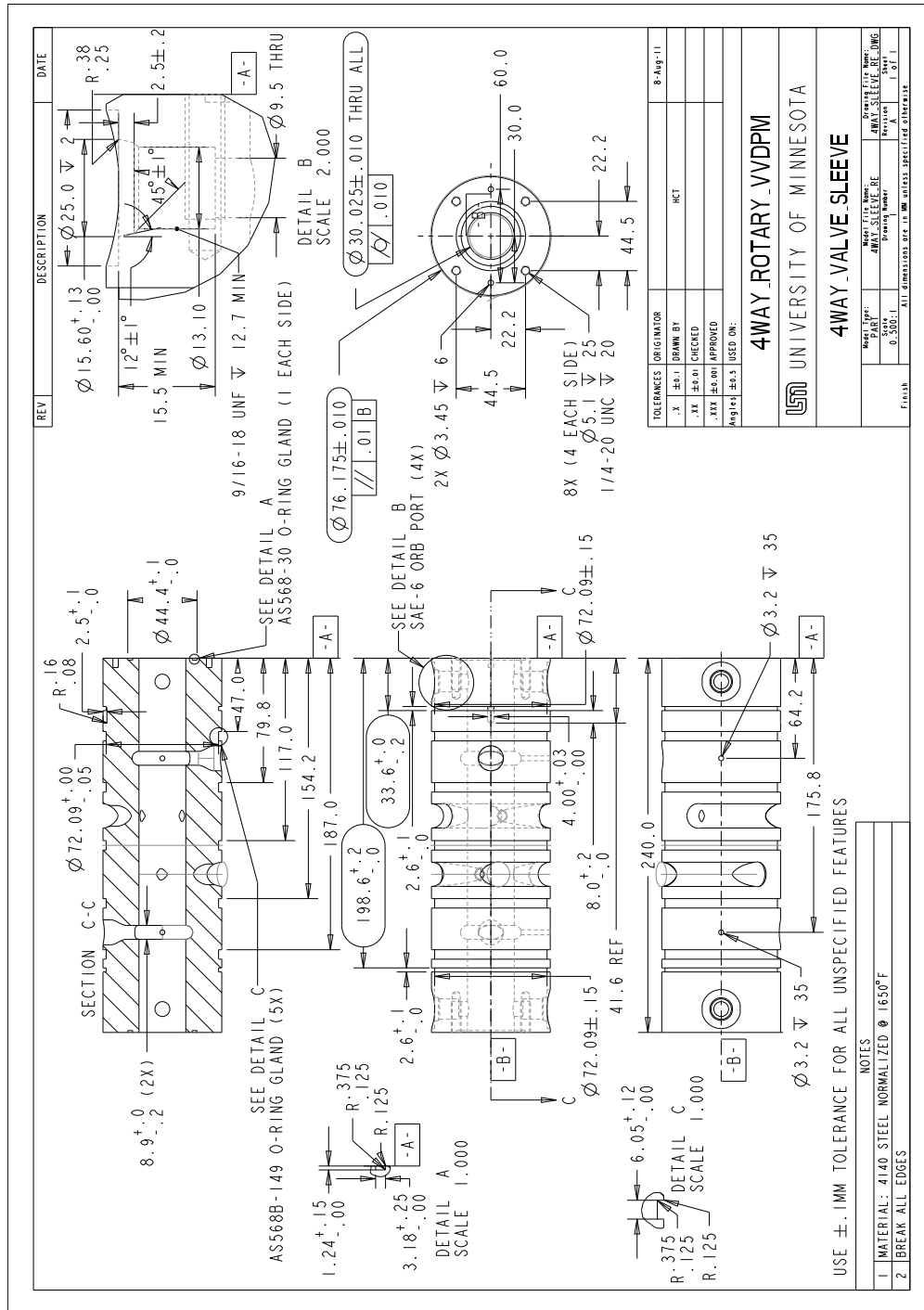


Figure B.2: 4-way rotary valve sleeve

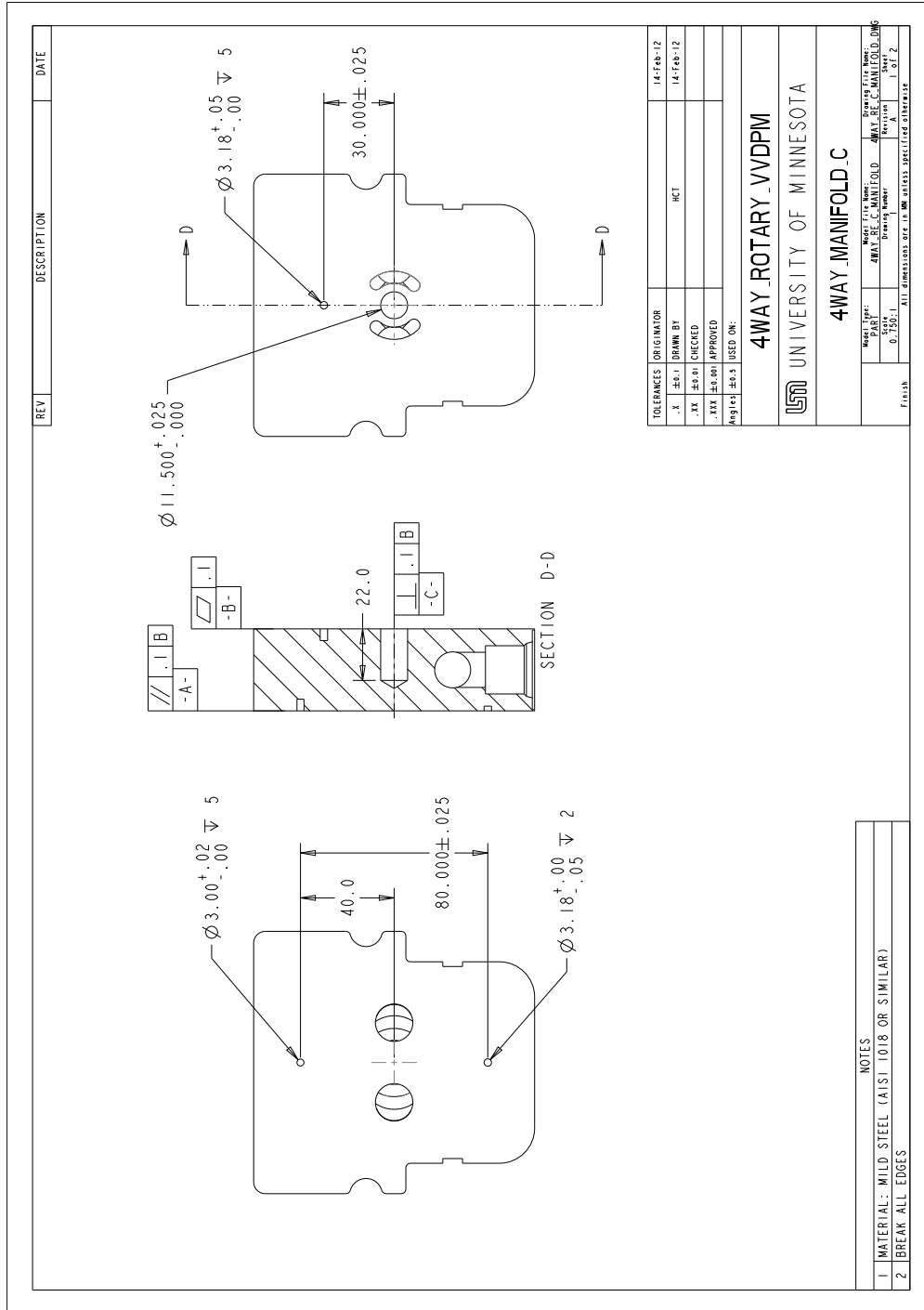


Figure B.4: Manifold

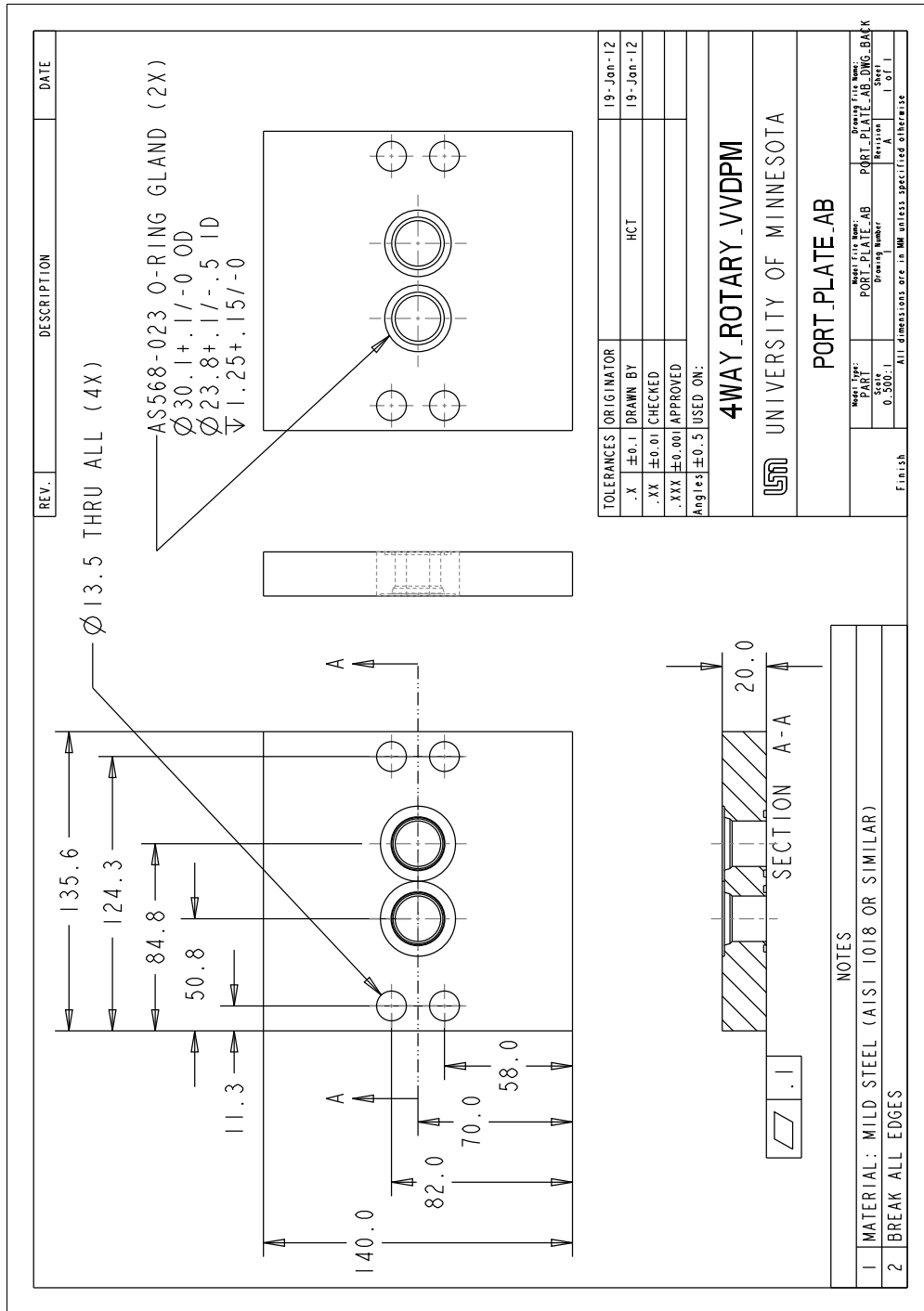


Figure B.5: Pump port plate adapter for stand-alone testing

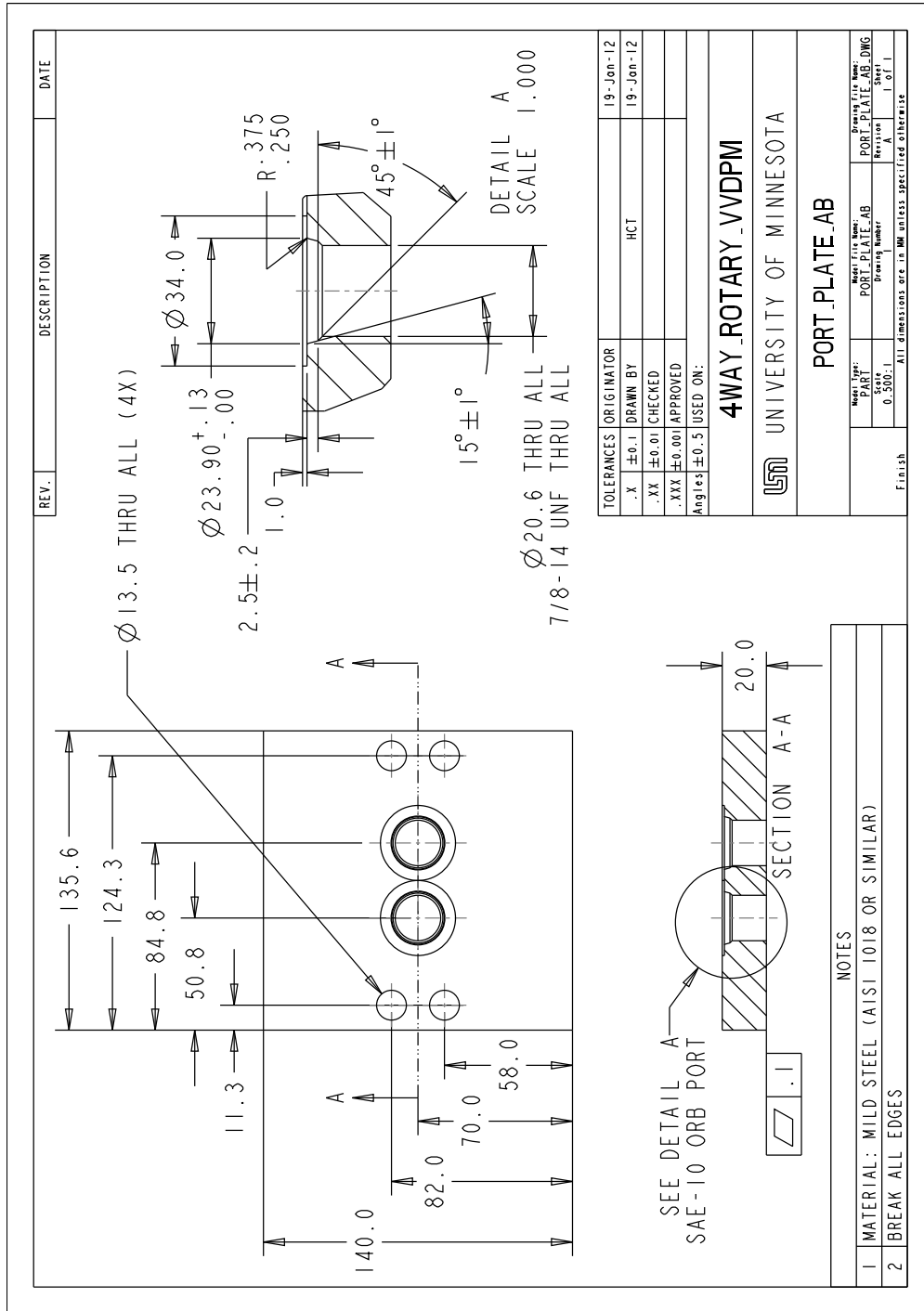


Figure B.6: Valve port plate adapter for stand-alone testing (Ports A and B)

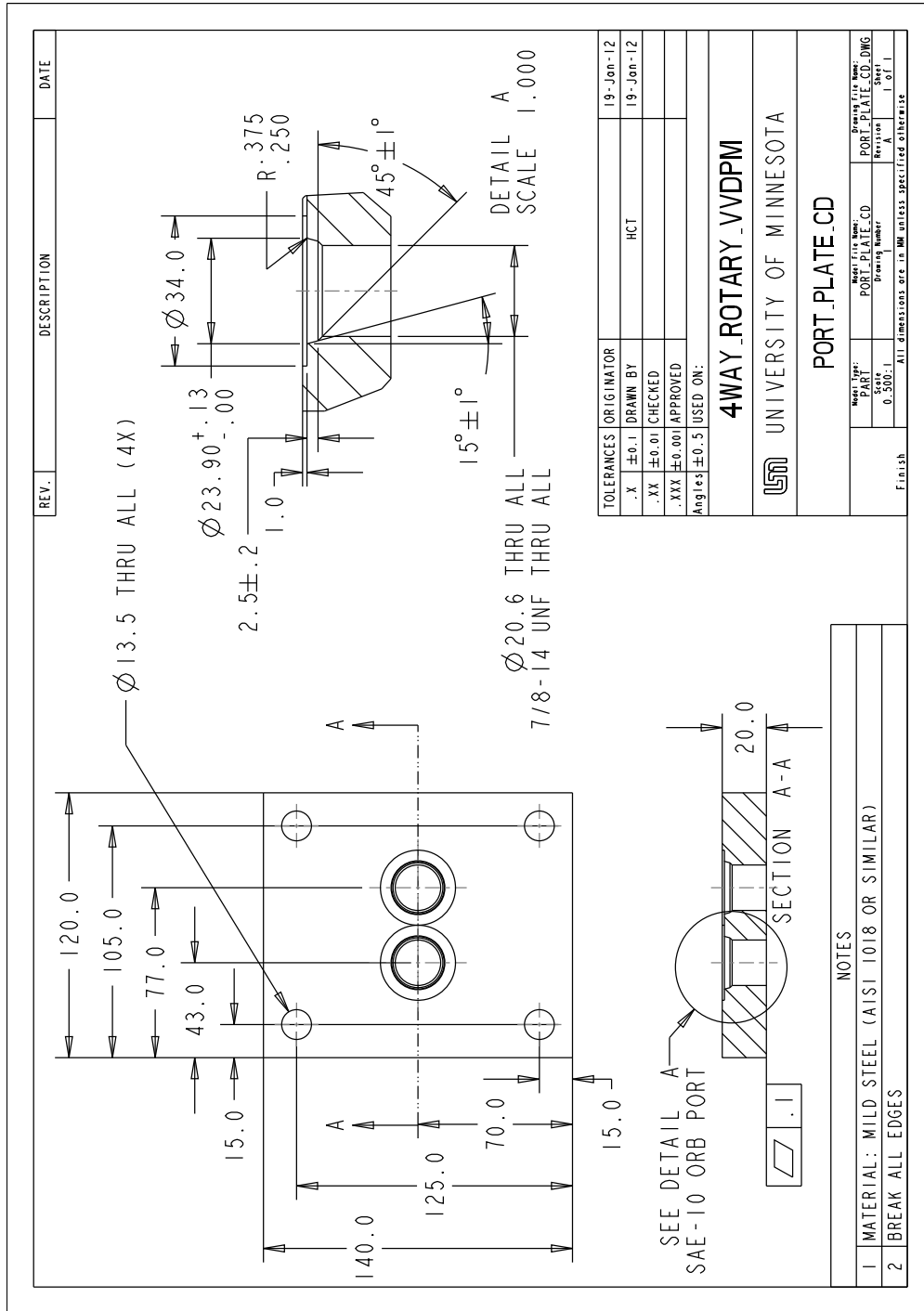


Figure B.7: Valve port plate adapter for stand-alone testing (Ports C and D)

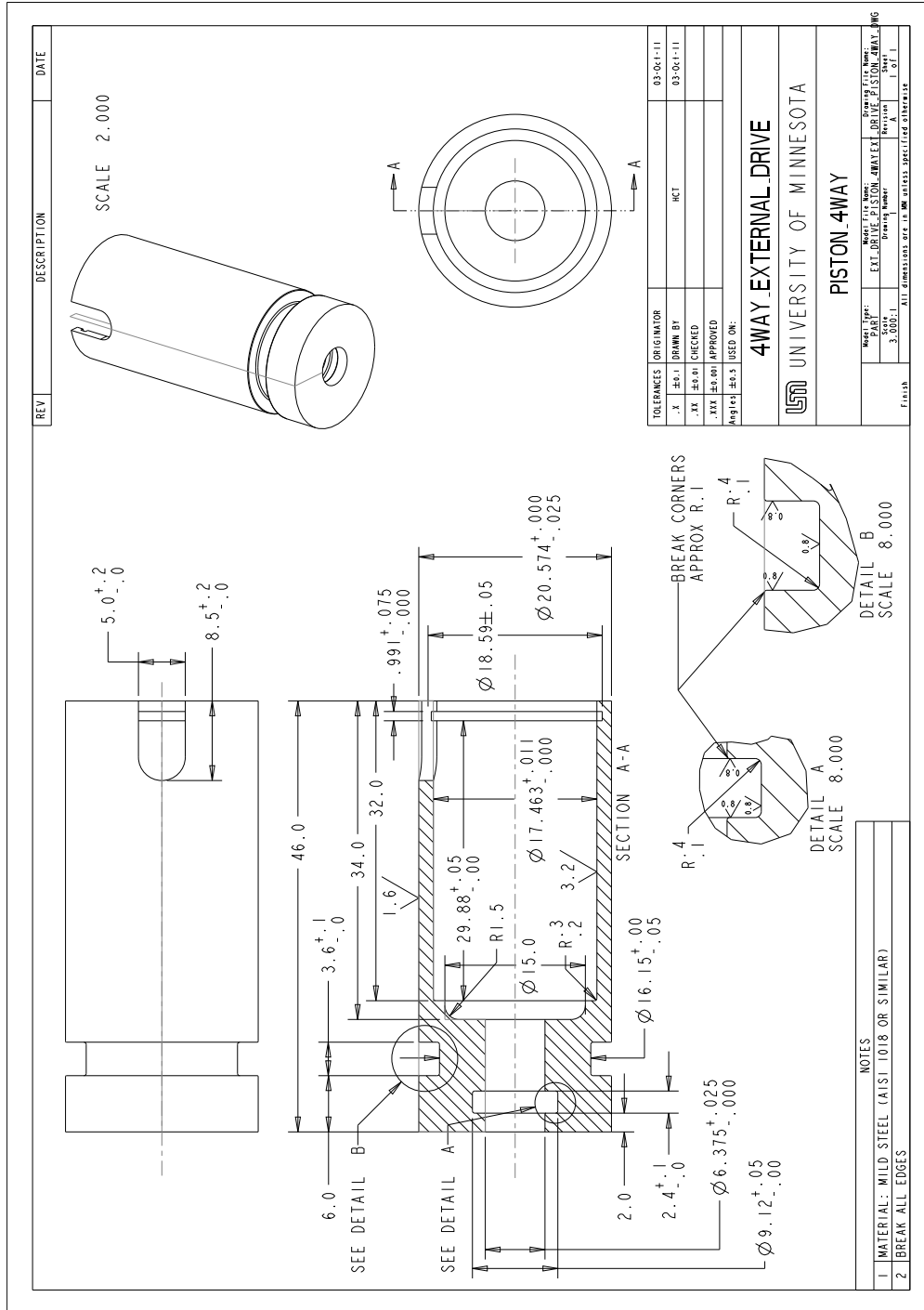


Figure B.9: Valve drive mechanism piston

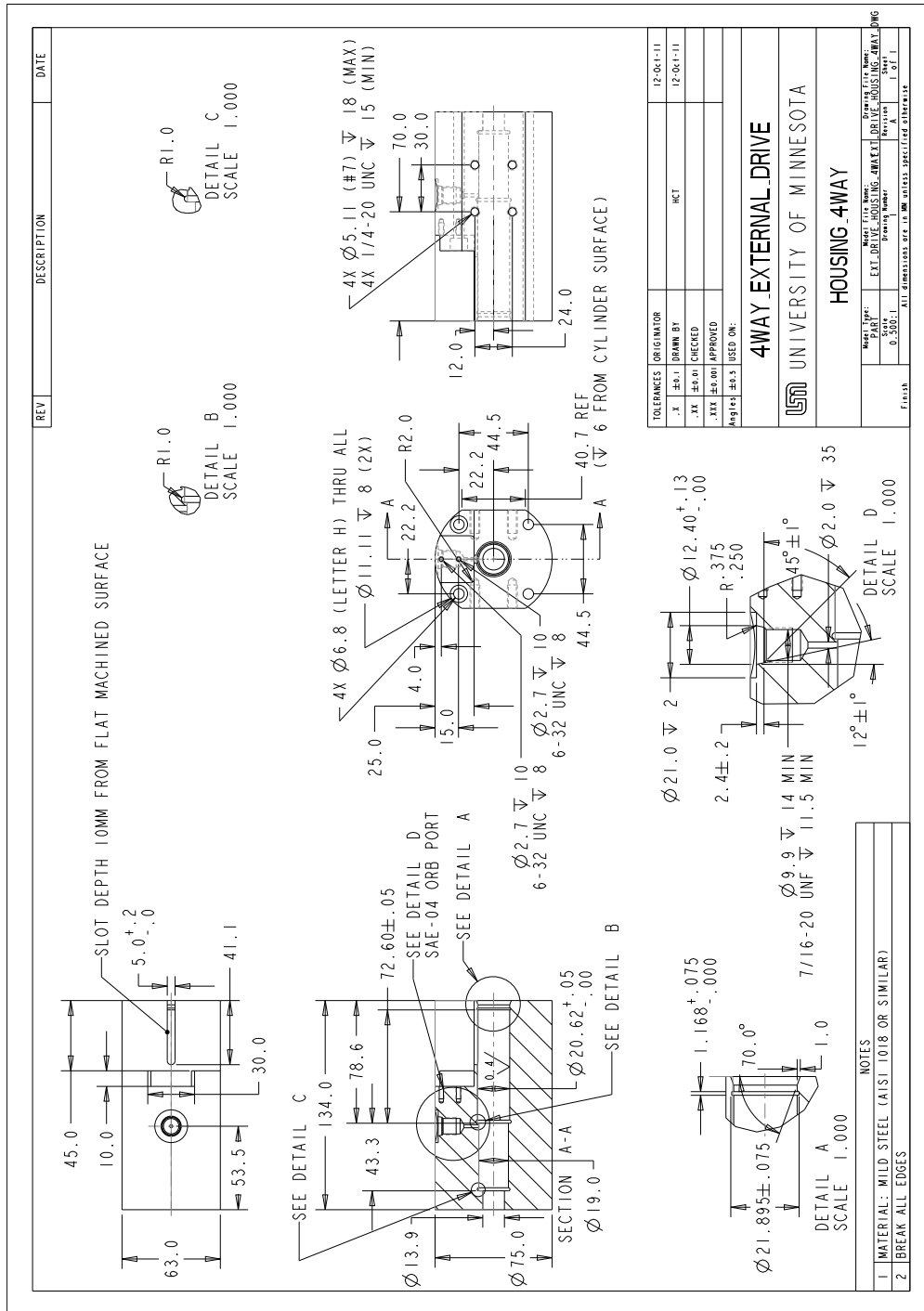


Figure B.10: Valve drive mechanism housing

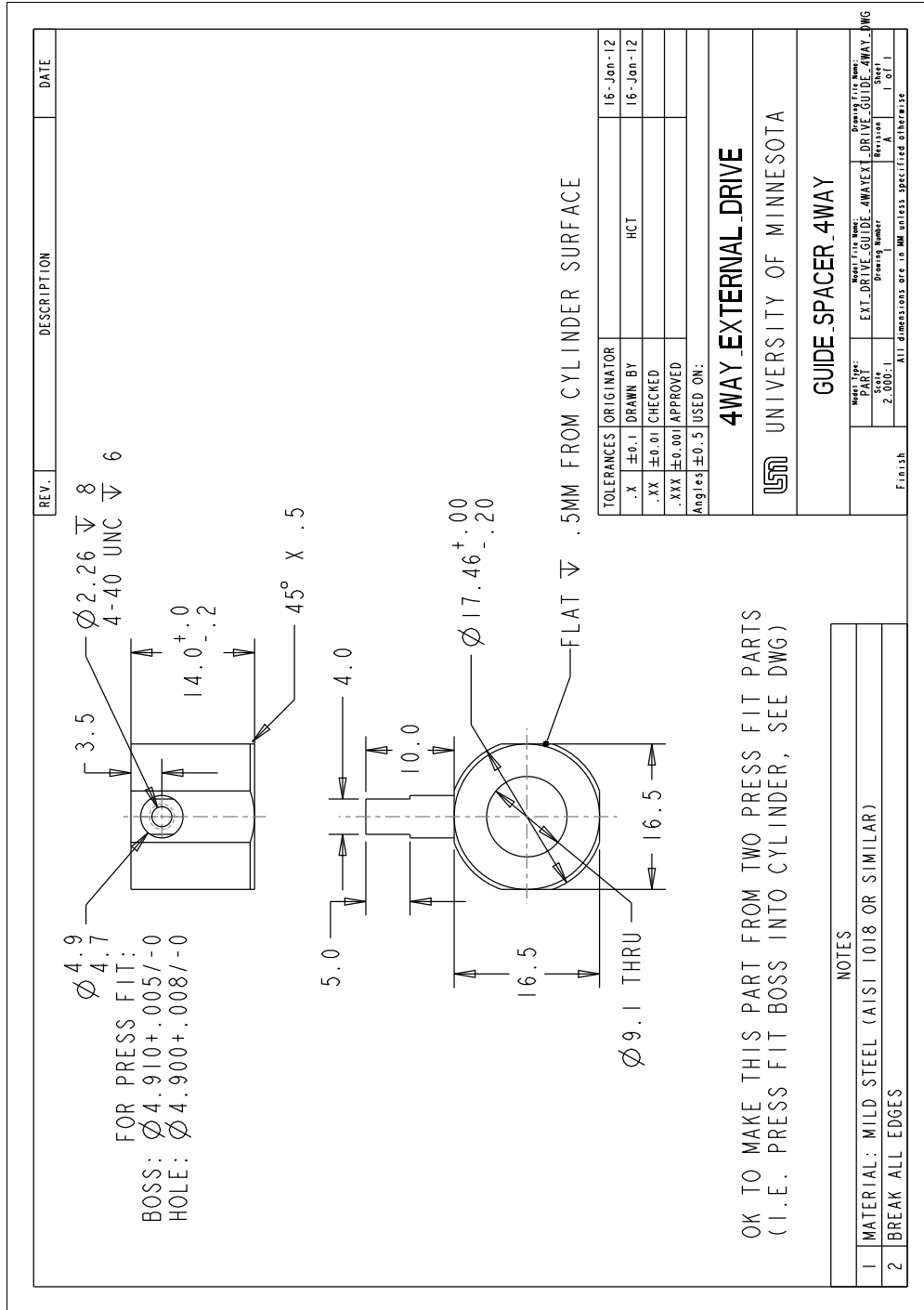


Figure B.11: Valve drive mechanism guide

Appendix C

Pilot operated disc directional valve

This section describes a novel disc style pilot operated directional control valve that was initially conceptualized for the self-spinning 4-way rotary valve. The directional valve is designed to be low profile to package efficiently between the pump/motor and rotary valve. This valve would conceivably be implemented as the valve to control the P/M's shaft direction as shown in Fig. 3.4.

The objective of the proposed disc directional valve is to reduce compressibility and throttling losses in comparison to traditional directional valves. This is crucial to maintaining efficiency since the P/M flow passes through each valve two times (refer to Fig. 3.4) and two valves are needed to operate in all four quadrants. The internal volume of the valve used to control pump/motor shaft direction also contributes to compressibility losses. The proposed disc valve design, shown in Fig. C.1, reduces the port volume compared to a traditional cartridge spool valve from 15cc to 2.5cc. The use of the disc valve is not limited to the 4-way rotary spool valve and can be used in the ring valve as well as other applications.

The disc valve switching concept is illustrated in Fig. C.2. Two sets of ports, $[a, b]$ and $[c, d]$, are machined into housings on either side of the valve disc. These ports are positioned 90° apart. The disc features two through ports that connect housing ports on opposing sides of the disc. To switch position, the valve disc is rotated 90°. Two

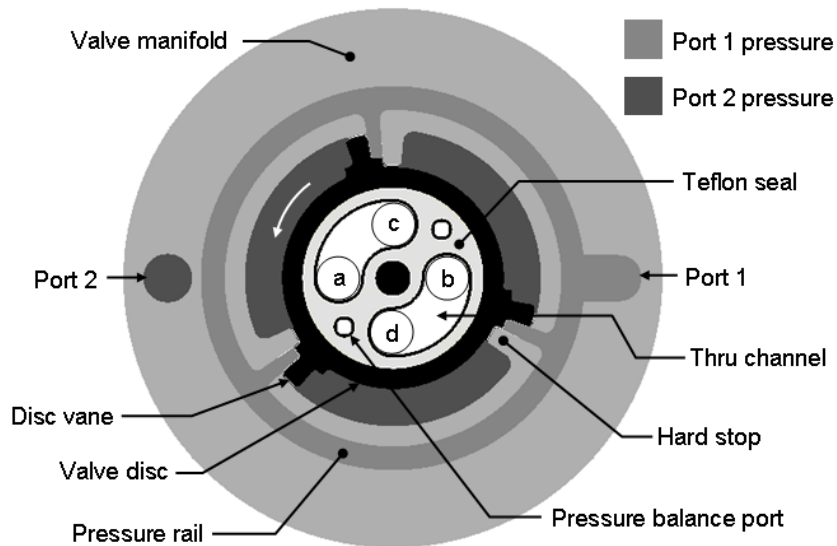


Figure C.1: Disc valve sealing and actuation concepts.

circular through holes, shown in Fig. C.1, pressure balance the disc during switching to reduce pressure induced friction forces.

A Teflon seal, laser cut to fit the light gray cavity in both sides of the valve disc identified in Fig. C.1, provides sealing on both sides of the valve disc. The Teflon seals between the two kidney through ports on the disc and also seals the kidney ports from the Port 1 and Port 2 disc actuation ports. Two pressure rails, connected to Ports 1 (medium gray) and 2 (dark gray), are machined into both sides of the valve manifold. The Port 1 rail (medium gray) is shown in Fig. C.1. Rotation of the valve disc is achieved by using a pilot stage valve to connect either Ports 1 or 2 to pilot pressure and the other to tank. For example, if Port 1 in Fig. C.1 is pressurized, the valve disc will rotate counterclockwise until the disc reaches its limit of travel. One benefit of the disc valve is that no holding power is required once the valve has switched position.

Preliminary leakage testing at a kidney port pressure differential of 6.9MPa yielded an average leakage of $3.36\text{drops}/\text{min}$ or $.24\text{cc}/\text{min}$. In comparison, a typical commercial cartridge spool directional valve exhibits approximately $30\text{cc}/\text{min}$ leakage at the same pressure differential.

Preliminary friction results are presented in Fig. C.3. Friction was measured using a spring scale to measure the force required to actuate the valve disc when pressurized.

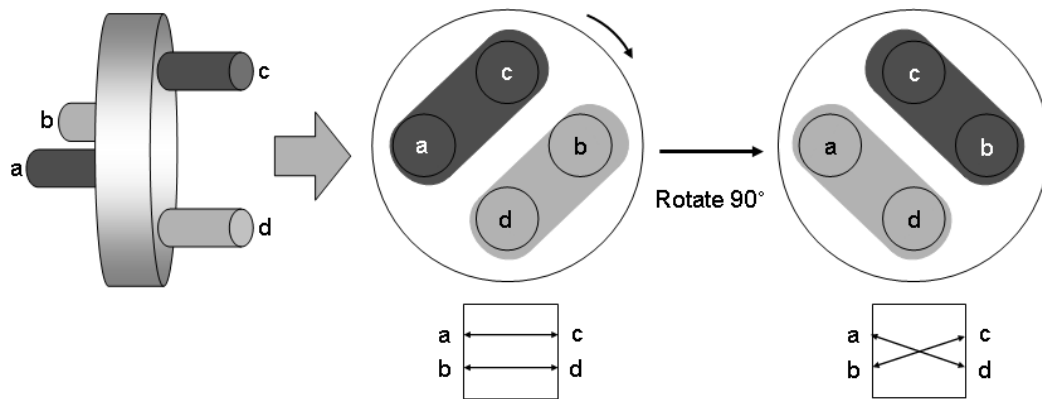


Figure C.2: Switching concept for the disc directional control valve.

The friction results are extrapolated to 35MPa using a least squares fit. A preliminary simulation that includes experimental seal friction as well as viscous friction on the axial disc faces and radial contacts predicts that a pilot pressure of 1MPa is able to actuate the disc through its full range of travel in 12ms for a working fluid pressure differential of 6.9MPa . A peak flow rate of 19.3lpm is required, however, the peak flow rate can be reduced if slower valve transition times are acceptable.

A preliminary CFD analysis of the disc valve predicts that a disc valve sized for 15lpm exhibits a pressure drop of $.06\text{MPa}$, which is half of the pressure drop for a similar cartridge spool valve ($.12\text{MPa}$).¹

C.1 Directional valve machining drawings

Mechanical drawings of the first manually operated prototype directional valve are included in this section. List of drawings:

1. Figure C.4: Disc valve housing base
2. Figure C.5: Disc valve housing cover
3. Figure C.6: Valve disc with initial o-ring seal geometry
4. Figure C.7: Modified valve disc with Teflon seal geometry

¹ CFD analysis performed by Meng Wang.

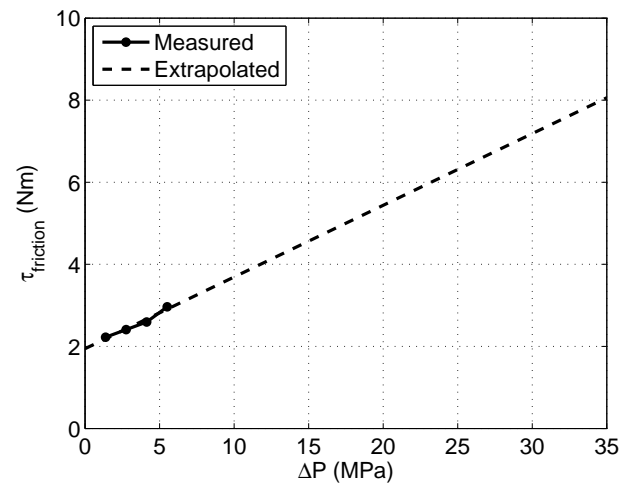


Figure C.3: Preliminary prototype disc valve seal friction. Disc moment arm is 83.3mm .

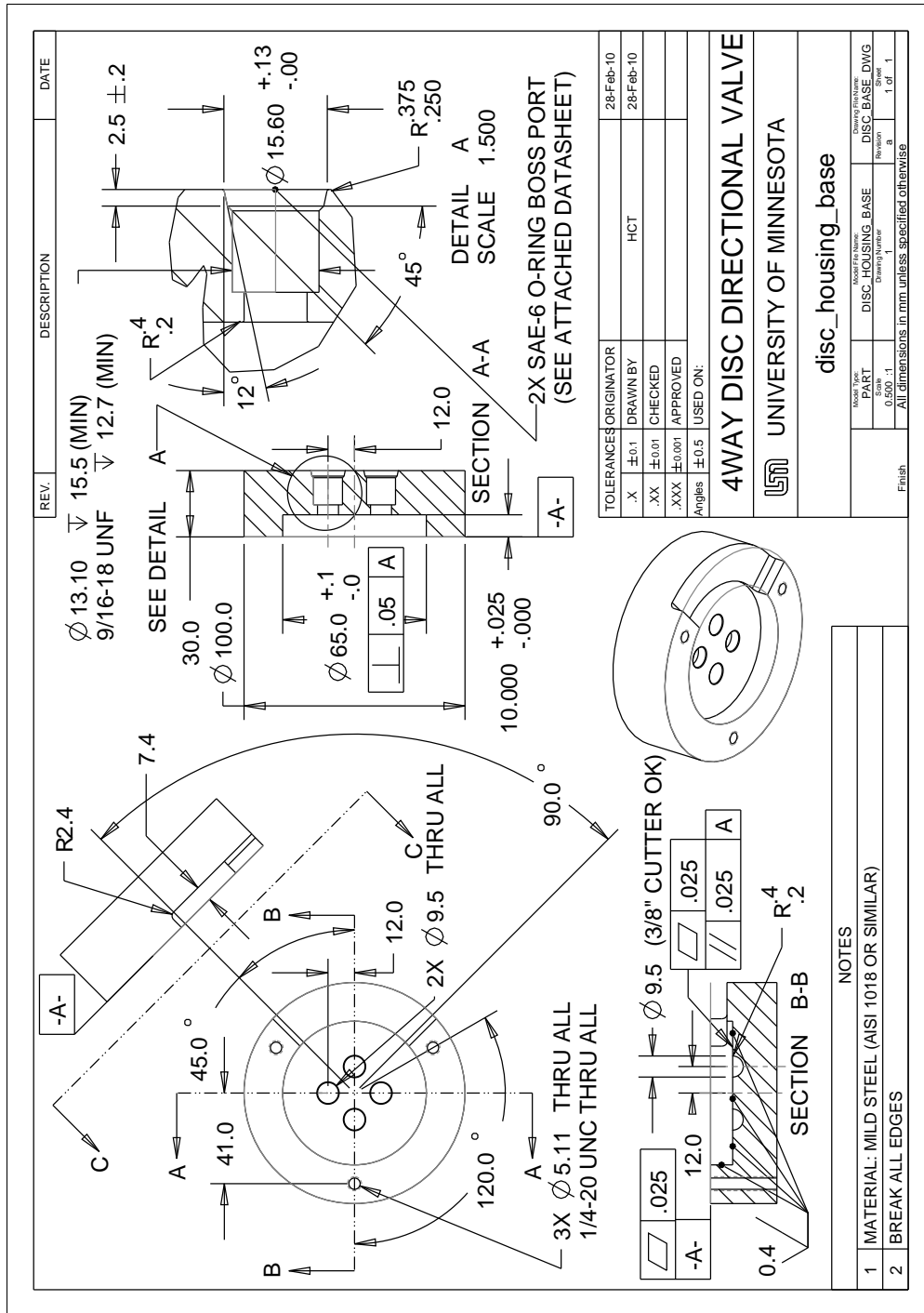


Figure C.4: Disc valve housing base

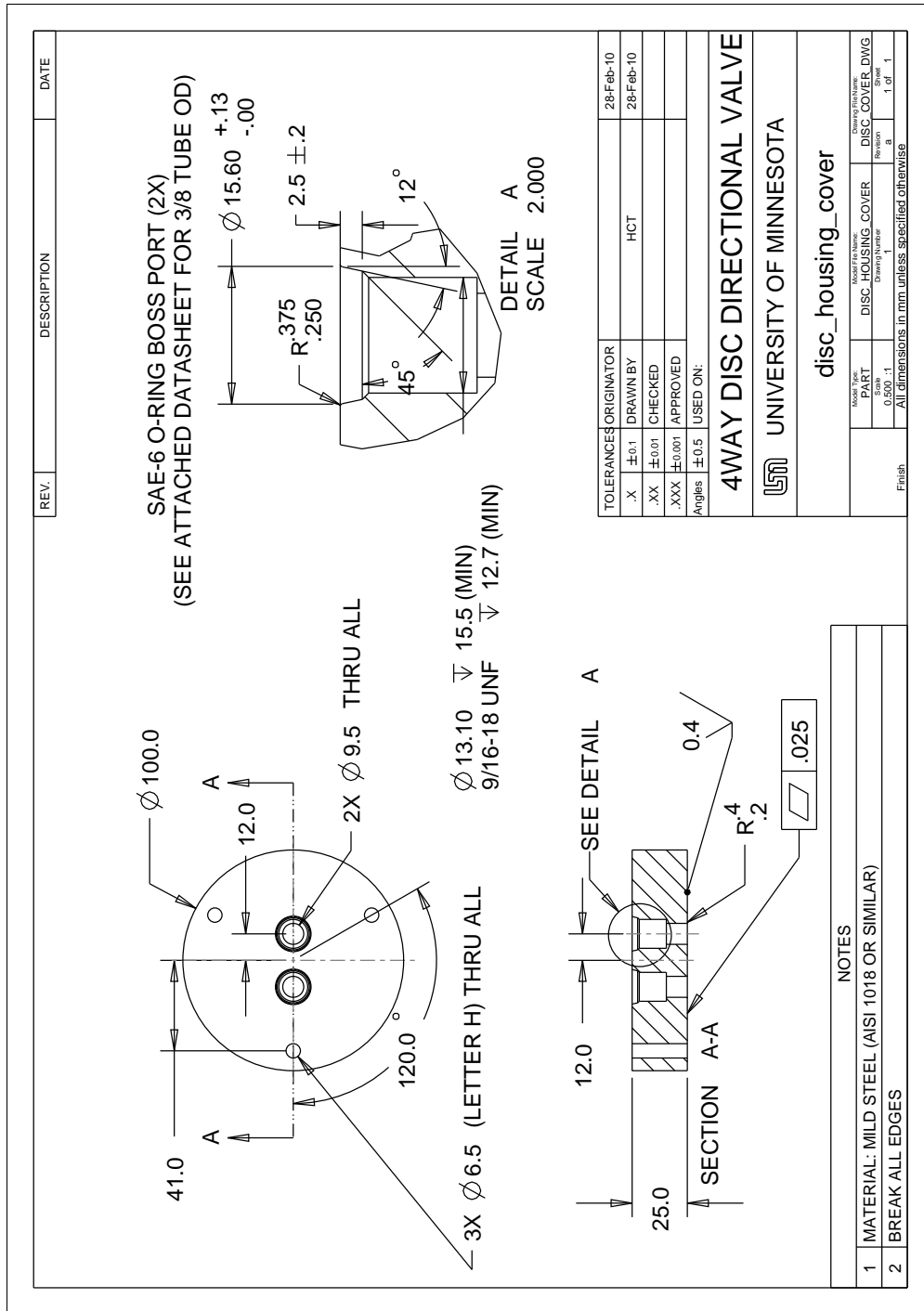


Figure C.5: Disc valve housing cover

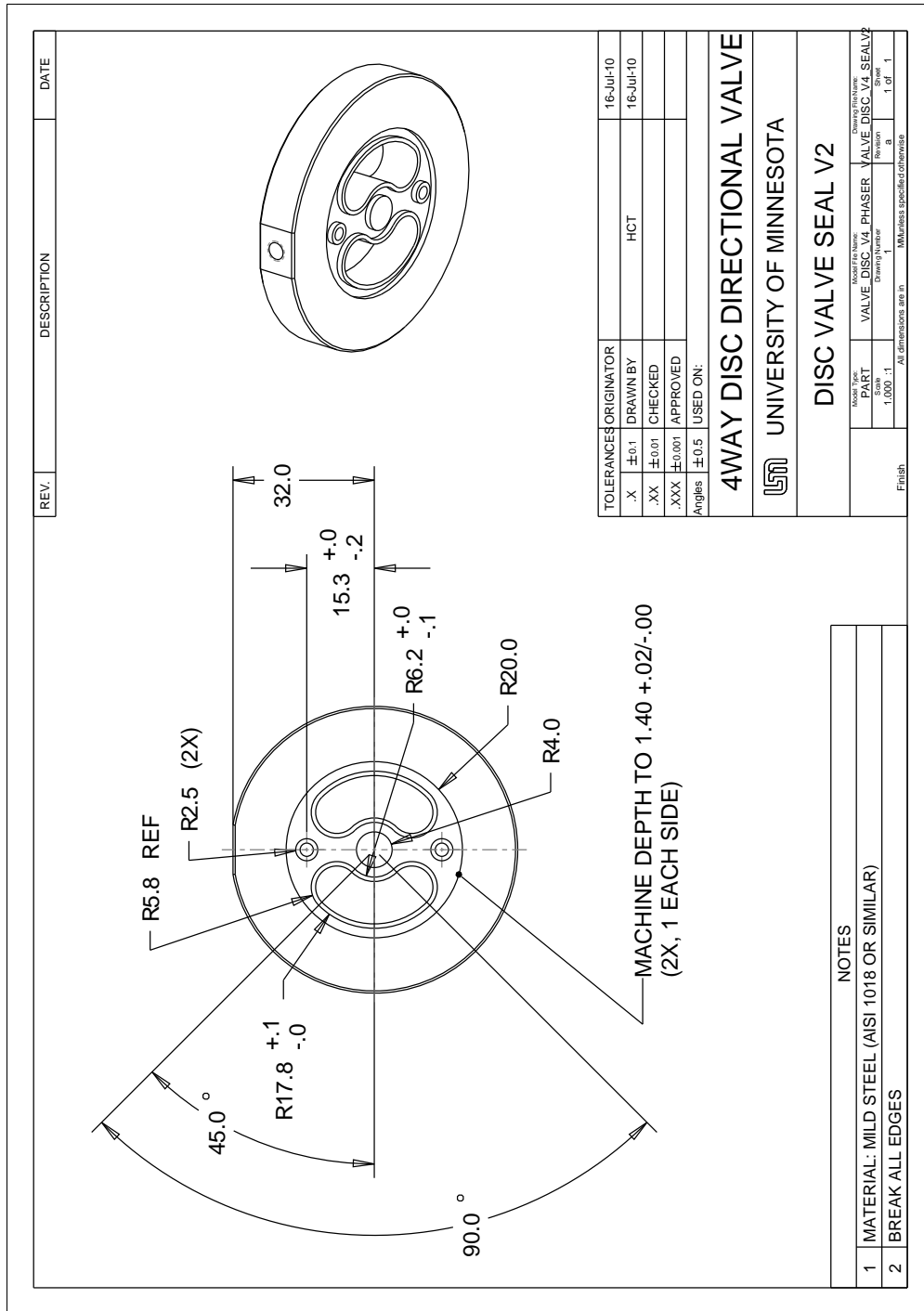


Figure C.7: Modified valve disc with Teflon seal geometry